UNIVERSITY OF COPENHAGEN

PhD Thesis

Vibrational Spectroscopy of Hydrogen Bound Species and Overtone Spectroscopy by Cavity Ring-Down.

Casper Vindahl Jensen

Supervisor: Professor Henrik Grum Kjærgaard

Faculty of Science

Submitted: 31 August, 2024.

Vibrational Spectroscopy of Hydrogen Bound Species and Overtone Spectroscopy by Cavity Ring-Down.

PhD Thesis

Submitted: 31 August, 2024

Casper Vindahl Jensen (cvj@chem.ku.dk)

University of Copenhagen, Department of Chemistry

Universitetsparken 5, DK-2100 Copenhagen Ø, Denmark

This thesis has been submitted to the PhD School of the Faculty of Science, University of Copenhagen.

ACKNOWLEDGEMENTS

Firstly, a big thank you to Henrik. Good bosses, I hear, are not easy to come by, so I am grateful that I have had you as a mentor in science, and as a source of wise words and the occasional beer for when life in, and outside of, science had to be discussed and solved.

I would like to thank the members of the Kjaergaard Group whom I have had the pleasure to work with. You have incredible work-ethics and sharp minds and you motivated me to try and compete with that.

I would especially like to thank Alexander Kjærsgaard who trained me in the lab during my Master´s thesis and made me extremely motivated to chase the slightly improved spectrum of whatever I was measuring. I would also like to give a special thanks to Emil Vogt. All scientific work that I have done in this group started as an idea or a project of yours that you generously included me in. The one quick in-and-out spectrum of *t*-BuOOH turned into a rabbit hole, that kept me occupied for more than three years. It has been a pleasure to contribute some experiments to your awesome vibrational modelling. I am sure you will go far and I will for the rest of time remember the two times I found a mistake in your calculations.

Of past members I would like to thank Jens Wallberg for prefacing the work I have done on the cavity ring-down setup. Thanks for the support in my mission to bring the setup back to life.

Thanks to prof. Martin Suhm and his group in Göttingen. Thanks for inviting me to join your group for my external stay. It was a great experience and a huge pat on

the back to have you acknowledge my work and help me improve it. Also a big thanks to Dan, Anna, Beppo and Laura for making Göttingen an even more beautiful and fun town to be in.

Thanks also to the guys on the fifth, Matthew Johnson and Ole John Nielsen. I don't think I would have had the confidence to take apart all of Henrik's expensive equipment and (sometimes) make it better were it not for the engineering training I received from Matthew. I don't think there exists an obscure tool or adapter that Ole John has not been willing to lend me, and requests of borrowing gases have only been met with the question "which isotope?". I thank both of you for your help.

Lastly, thanks to my proof readers. This was no easy task and I truly appreciate the time you gave me to make this thesis readable. Thank you to Beppo, Dhritabrata, Emil, Nanna and Ružica

ABSTRACT

In this thesis, two somewhat disconnected topics are presented. The first topic concerns the spectroscopic and thermodynamic properties of hydrogen bound complexes. The hydrogen bond strength is probed experimentally for several complexes by analysing the magnitude of the redshift of the OH-stretching oscillator, which occur upon hydrogen bonding. Spectra of the hydrogen bound complexes are recorded at a range of different experimental conditions. Primarily, Fourier transform infrared (FTIR) spectroscopic experiments are done in the gas phase at room temperature. This allows us to investigate spectroscopic properties at conditions relevant to the atmosphere where hydrogen bound complexes have a significant effect on the physical and chemical processes. Other experiments are carried out in a frozen argon matrix and at pulsed helium jet-cooled conditions to elucidate the pure vibrational transitions with minimal rotational structure. The partial pressures and equilibrium constants are determined by an experimental/theoretical hybrid method using the measured integrated absorbance of a known band and a theoretical oscillator strength of the transition(s) associated with the band. I quantify redshifts and equilibrium constants for *tert*-butyl hydroperoxide dimer, which, in my master's thesis, is detected for the first time in gas phase at room temperature, and of methanol dimer, trimer and tetramer. Obtaining the cluster spectra relies on precise subtraction of signals from monomers and solvents. A theoretical model including the interactions between the bound OH-stretch and the low frequency intermolecular modes is developed that quantitatively simulates the temperature effects on the methanol dimer band. Spectra are recorded of methanol dimer and two isotopologues to support the model. The resonance phenomenon is investigated in trimethylamine-water where three different experimental conditions are able to tune the state associated with the bound OH-stretch in and out of resonance with the HOH-bend overtone state.

The vibrational spectra of *tert*-butyl hydroperoxide and isoprene are recorded for the fundamental X-H stretching transitions and extending to the 4th and 5th overtone transitions. The wide range of transition energies demands utilisation of different spectroscopic approaches. The low energy region (< 10000 cm^{-1}) is effectively covered by an FTIR spectrometer and various pathlength gas cells. The high energy region ($12500 - 17000$ cm^{-1}) is recorded with an OPO-pulsed cavity ring-down setup coupled with a FTIR spectrometer, which allows us to obtain overtone-spectra with absolute intensities. The two regions are connected by a conventional scanning UV-Vis-NIR spectrometer. The laser is refurbished and additional optics is installed to match the TEM_{00} mode of the optical cavity. A spectrum analyser is coupled to the setup to calibrate the energy axis at every measurement point and determine the laser line width. A new Python code is implemented to more efficiently fit the ring-downs and differentiate between good and bad laser shots. The effective pathlenth of the 1 meter cavity is re-calibrated. The additions to the setup improves spectral accuracy and the signal to noise ratio significantly. The OH-stretching- and OH/COOH combination bands of *tert*-butyl hydroperoxide are measured from the fundamental region to the fourth overtone region. The spectra show a change in relative intensity and position between the OH-stretching band and the combination band with increasing excitation quanta. The improved setup further reveals a seven-quanta excitation in the spectra. I present a continuous, unbroken spectrum of isoprene recorded from 600 cm^{-1} - 17050 cm^{-1}. The spectrum is recorded with FTIR, UV-Vis-NIR and cavity ring-down and overlapped to give the full spectrum. The spectral data covers the entire region of the James Webb Space Telescope and may act as reference for isoprene detection in exoplanet atmospheres.

DANSK RESUMÉ

I denne afhandling bliver to tilsyneladende afkoblede emner præsenteret. Det første emne drejer sig om spektroskopiske undersøgelser af hydrogenbundne komplekser og deres termodynamiske egenskaber. Komplekserne bliver undersøgt eksperimentielt ved at analysere den rødforskydning af OH-strækningsvibrationen, som sker ved dannelse af en hydrogenbinding. Den primære metode til disse undersøgelser er Fourier transform infrarød (FTIR) spektroskopi af gasfasen ved stuetemperatur. Denne metode giver os informationer om de spektroskopiske egenskaber ved forhold, som er relevante for atmosfæren, og hvorved disse komplekser har stor indflydelse på fysiske og kemiske processer. Andre eksperimenter i frossen argon matrix og ved helium jet-ekspansion bliver også udført for at give information om de rene vibrationelle overgange fra både den vibrationelle og rotationelle grundtilstand. Kompleksernes partialtryk bliver bestemt ved en eksperimentiel/teoretisk hybrid metode, hvor forholdet af et integreret eksperimentielt bestemt absorptionsbånd og en teoretisk bestemt oscillatorstyrke af de overgange, som giver intensitet til båndet giver trykket af komplekset. Jeg kvantiserer rødforskydningen og ligevægtskonstanten ved stuetemperatur for *tert*-butyl hydroperoxide dimer, som i min kandidatafhandling blev detekteret for første gang i gasfase ved stuetemperatur, og af methanol- dimer, trimer og tetramer. Det er kun muligt at se aggregaterne ved meget præcist at trække intensitet fra monomererne, solventer og urenheder fra. En teoretisk model, som beskriver interaktionerne mellem det bundne OH-stræk og de lavfrekvente intermolekylære vibrationer, bliver udviklet og brugt til at simulere temperatureffekter på OH-strækningsbåndet i methanol dimer. Der tages ydermere spektre af isotopologer af methanol dimer, som understøtter den fysiske bund i modellen. Resonanser bliver undersøgt i trimethylamin-vand, hvor målinger i tre

forskellige medier justerer energien af OH-strækket således at det går ind og ud af resonans med omkringliggende energiniveauer.

De vibrationelle spektra af *tert*-butyl hydroperoxide og isopren bliver optaget i den fundamentale region og helt op til den fjerde og femte overtoneregion. Det meget brede energiinterval kræver forskellige eksperimentielle metoder. I den lave energiregion (< 10000 cm^{-1}) kan spektre let blive målt vha. et FTIR spektrometer og et udvalg af gasceller med forskellige vejlængder. Ved højere energier ($12500 - 17000$ cm^{-1}) er intensiteterne af overgangene så lave, at et OPO-laser-kavitetshendfaldseksperiment skal bruges. Sammenkoblet med vores FTIR kan vi lave et eksperiment, der kan bestemme de absolutte intensiteter af disse meget svage overgange. De to regioner er forbundne med spektre som bliver målt med et konventionelt spredningsUV-Vis-NIR spektrometer. OPO-laseren bliver restaureret, og der bliver indsat flere optiske komponenter i eksperimentet for at kunne koble lyset effektivt til den optiske kavitets TEM_{00} tilstand. En spektrumsmåler kalibrerer samtidigt energiaksen og laser-linjebredden for hvert målt spektrum. En ny algoritme som er kodet i Python bliver brugt til mere effektiv databehandling af eksperimentet. Denne kode genkender dårlige laserskud og frasorterer dem i målingerne. Den effektive vejlængde af kaviteten bliver kalibreret. Alle disse forbedringer giver et øget signal-til-støj-forhold og en energiakse med fuldstændig akkuratesse indenfor laserens linjebredde. OH-stræk- og OH/COOH-kombinationsbåndene bliver målt for *tert*-butyl hydroperoxide fra den fundamentale overgang og op til den fjerde overtone. Det observeres at den relative intensitet og position af båndstrukturen ændrer sig med hvert eksitationskvantum. Yderligere bliver et syv-kvante bånd observeret, som ikke før kunne ses pga. for dårligt signal-til-støj-forhold. Jeg præsenterer et komplet sammenhængende spektrum af isopren fra 600 cm^{-1} - 17050 cm^{-1}. Spektrummet er optaget med FTIR, UV-Vis-NIR og kavitetshendfald, som efterfølgende er blevet overlappet for derved at give det sammenhængende spektrum. Spektrummet dækker hele rækkevidden for James Webb rumteleskopet og kan derved bruges som reference for isoprendetektion på exoplaneter.

PUBLICATION LIST

†: Shared first authorship.
*: Corresponding author.
Publications included in this thesis:

Paper 1: Gas-Phase Room-Temperature Detection of the *tert*-Butyl Hydroperoxide Dimer. **Casper Vindahl Jensen** and Henrik G. Kjaergaard*. *The Journal of Physical Chemistry A*, 2023, 127(31), 6476-6485

Paper 2: Effect of Temperature on the OH-Stretching Bands of the Methanol Dimer. Emil Vogt, **Casper Vindahl Jensen** and Henrik G. Kjaergaard*. *The Journal of Physical Chemistry A*, 2024, 128(2), 392-400

Paper 3: Room Temperature Gas Phase Equilibrium Constants of the Methanol Dimer, Trimer and Tetramer. **Casper Vindahl Jensen**, Emil Vogt, Andras Sun Poulsen and Henrik G. Kjaergaard*. *The Journal of Physical Chemistry A*, 2024, 128(31), 6382-6391

Publications not included in this thesis :

Paper 4: Coupling of Torsion and OH-Stretching in *tert*-Butyl Hydroperoxide. I. The Cold and Warm First OH-Stretching Overtone Spectrum. Anne S. Hansen†, Rachel M. Huchmala†, Emil Vogt, Mark A. Boyer, Trisha Bhagde, Michael F. Vansco, **Casper V. Jensen**, Alexander Kjærsgaard, Henrik G. Kjaergaard*, Anne B. McCoy*, and Marsha I. Lester*. *Journal of Chemical Physics*, 2021, 154 (16), 164306

Paper 5: Coupling of Torsion and OH-Stretching in *tert*-Butyl Hydroperoxide. II. The OH-Stretching Fundamental and Overtone spectra. Emil Vogt, Rachel M. Huchmala, **Casper V. Jensen**, Mark A. Boyer, Jens Wallberg, Anne S. Hansen, Alexander Kjærsgaard, Marsha I. Lester*, Anne B. McCoy*, and Henrik G. Kjaergaard*. *Journal of Chemical Physics*, 2021, 154 (16), 164307

Paper 6: Airborne Environmental DNA for Terrestrial Vertebrate Community Monitoring. Christina Lynggaard, Mads Frost Bertelsen, **Casper V. Jensen**, Matthew S. Johnson, Tobias Guldberg Frøslev, Morten Tange Olsen and Kristine Bohmann*. *Current Biology*, 2022, 32(3), 701-707

CONTENTS

LIST OF FIGURES

LIST OF TABLES

LIST OF ABBREVIATIONS

AVTZ aug-cc-pVTZ (basis set)
CRD Cavity Ring-Down
DCM Dichloromethane
DFT Density Functional Theory
DMF Dipole Moment Function
DoF Degree of Freedom
FSR Free cavity spectral range
FWHM Full-Width at Half-Maximum
GDP Gross domestic product
IPCC Intergovermental Panel on Climate Change
IR Infrared
JWST James Webb space telescope
LAM Large amplitude motion
MeOH Methanol
MIR Mid infrared
NCI Non-covalent interactions
NIR Near infrared
PES Potential Energy Surface
SOA Secondary organic aerosols
S/N Signal-to-noise ratio
***t*-BuOOH** *tert*-Butyl Hydroperoxide
***t*-BuOH** *tert*-Butanol
TMA Trimethylamine
TEM Transverse electromagnetic (modes)
UV Ultraviolet
Vis Visible (region of the electromagnetic spectrum)
VOC Volatile organic compound
(G)VPT2 (General) Second-Order Vibrational Rayleigh-Schrödinger Perturbation Theory
WHO World Health Organisation
ZPVE Zero-point vibrational energy

PREFACE

This thesis concerns the vibrational spectroscopy of molecules in the gas phase with two relatively separated angles of incidence. The first main focus of the thesis is on the spectroscopy of fundamental transitions in hydrogen bound molecular complexes and the second on the spectroscopy of vibrational transitions involving many quanta of excitation. The molecules, which are chosen as subjects for this study, have that in common that they represent characteristics and functional groups, which are important in the context of our atmosphere. In the introduction I will discuss the motivation for looking at these specific compounds largely from a climate and environmental perspective.

In the "Theoretical-Computational Background" chapter I will discuss the harmonic oscillator and the theory that goes into improving this simple model. Some general observations and advice is presented for people who like myself are not theoretical chemists but would like to improve on calculations from the harmonic oscillator level.

The core of this thesis is founded in experiments. The "Experimental Methods" chapter includes the theory of absorption spectroscopy and the thermodynamics relevant to the topic as well as an introduction into spectral subtraction. A description of all instruments used in this thesis is given with a focus on their concrete application in my project. It is thus perhaps not a beginners guide but may provide some interesting insights to experimentalists already familiar with the techniques. A large part is also devoted to documenting the improvements made to the cavity ring-down setup, which was the instrument used for the overtone spectroscopy.

The results and discussions thereof are divided into two chapters concerning the hydrogen bound complexes and on determining absolute intensities of OH and CH transitions in two atmospherically relevant molecules.

1

INTRODUCTION

An often heard sentence in science communication is "The world is quantum, but you cant see it." Indeed, our everyday world experience is of not quantum, but rather classical mechanics. The football player, for example, experiences Newton's second law of motion every time they kick the ball. By exerting a certain amount of force on the ball, they will accelerate the ball to a certain velocity. If the player kicks the ball half as hard, the ball experiences half the acceleration. But if the world was shrunk to the size of a ping-pong ball and the football pitch was surrounded by very tall walls, the player would have to deal with the fact that only kicks at some specific velocities would accelerate the ball, while others would make the ball completely intangible to the kick and the player's foot would pass right through it. The 10^{-10} meter sized football can in other words not posses just any energy but instead only discrete, separated energies.

Shrinking football players has proven experimentally challenging and so a much more practical way to experience quantum world is by the use of spectroscopy. In 1852(3), Johan Anders Ångström published one of the first papers describing the phenomenon of absorption of discrete colors of light.[1] Ångström later went on to record the emission lines of hydrogen which lead Johann Balmer to come up with an equation that accounted for the regular spacing of the hydrogen emission wavelengths[2]

$$\lambda = 364.56 \text{ nm} \cdot \frac{n^2}{n^2 - 4} \tag{1}$$

where λ is the wavelength of the n'th emission line. The expression was later generalised by Rydberg to a formula for all hydrogen-like atoms.[3] The major significance of these equations is that the observed energy differences are expressed as depending on integer "quantum" numbers. The earliest modern understanding of quantum mechanics came

with Niels Bohr's atomic model in 1913 and provided a physical explanation for the observed emission lines of the previous 60 years.[4] Bohr formulated that electrons occupy discrete energy levels and can jump from one level to another by either absorbing or emitting a photon with a colour, or photon wavelength, that corresponds exactly to the energy difference between the electronic energy levels.

$$\Delta E = \frac{h \cdot c}{\lambda} \tag{2}$$

where h is the Planck's constant and c the speed of light. It was thus early experimental spectroscopy that guided the discovery of quantum mechanics as we know it today.

Molecular vibrations are, like electronic motion, quantised and the energy levels are separated by energies that correspond to the infrared (IR) part of the electromagnetic spectrum. Light in the infrared spectrum can thus be used to obtain information about the identity and interactions of molecules based on the transition energies of its vibrations. A molecule possesses 3N-6(5) vibrational modes, and many transitions can occur between endless combinations of the modes. The CH- and OH-stretching transitions are highly energetic vibrations with transition wavenumbers ~ 3000 cm^{-1} and ~ 3700 cm^{-1}, respectively. As a rule of thumb, the intensity of vibrational transitions drops by a factor of 10 with each increase in vibrational mode quantum number.[5–12] This means that with increasing energy, the CH-stretches and OH-stretches quickly become the only bright transitions as low frequency vibrations will have gone through many more factor-10 lapses of intensity in the same energy region. The high energy range of the IR spectrum is called the near-infrared (NIR) region. The decluttering of the spectrum in the NIR region presents great opportunity to investigate these high frequency vibrations and experimentally sample high energy ranges of the potential energy surfaces (PES) of these vibrations. The potential energy surface of a vibration resembles a harmonic oscillator in the bottom of the potential. High-quanta excitations can therefore be a good way of measuring anharmonic effects as these often become more pronounced with increasing quantum number.

Another advantage of sampling the high overtones is the increased energy separation of similar but distinct vibrations. In the harmonic picture, each additional quantum of

excitation will add the fundamental transition energy separation between two modes. Anharmonicity may counteract or enhance this effect depending on the oscillator. By going to the high overtones it can, for example, become possible to separate different conformers which may otherwise have overlapping bands in the fundamental region.[12,13] The decluttering and increased energy separation furthermore make the overtone region practical to use for field measurements of compounds that possess these high frequency CH- and OH-stretching modes, as the signals are easy to identify. This can for example be used to detect and quantify species in planetary atmospheres. The James Webb space telescope (JWST), which has been operational since 2022, is recording spectra of exoplanets in the spectral range 350 cm^{-1} - 16666 cm^{-1}. This includes the mid-infrared (MIR) region, the NIR region and part of the visible region. Two of the JWST instruments have a resolving power of $R > 1000$ in most parts of the spectral range,[14,15] and high energy stretching transitions may be excellent targets for the spectroscopic measurements by JWST.

Analyses of XH-stretching vibrations are among the most powerful tools when it comes to obtaining insights into the hydrogen bond. In Figure 1, the potential energy is plotted as a function of the OH interatomic distance for both the free OH and the bound OH in methanol (MeOH) dimer. It is clear that the hydrogen bound OH experiences a stabilisation in potential energy when compared to the free OH. The transition energies likewise decrease resulting in a redshift of the OH-stretch absorption band in the IR spectrum. This redshift is so general for hydrogen bonds that it is part of the latest definition of what constitutes experimental evidence of a hydrogen bond.[16,17] Another fairly general feature of hydrogen bonding is the large increase in intensity of the donor XH-stretching transition. The intensity increase can easily be anywhere between a factor 10-100.[18–20] The magnitude of the redshift and intensity enhancement most often correlate with the strength of the hydrogen bond and these properties are thus excellent probes for determining the hydrogen bond strength.

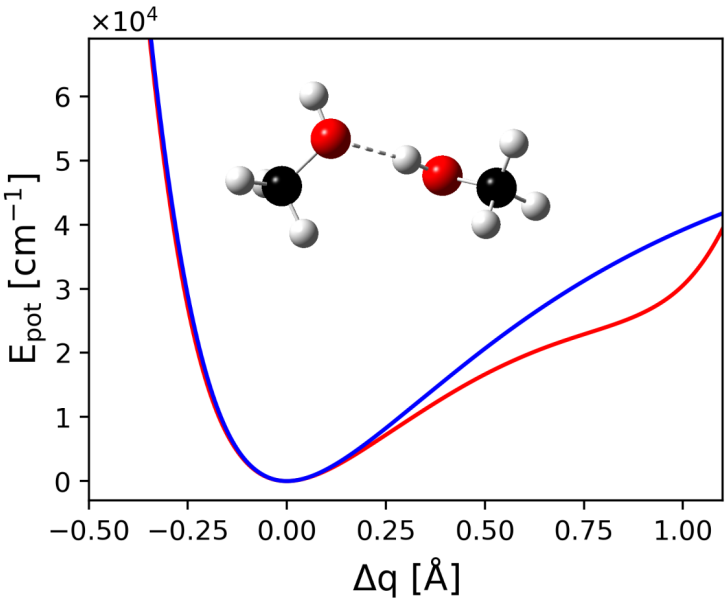

Figure 1: Hydrogen bond change in OH-stretching PES. The PES of $(MeOH)_2$ changes when a H-bond is formed. The blue curve is the free OH-stretch and the red curve is the bound OH-stretch. The widening of the potential decreases the transition wavenumbers.

The hydrogen bond is the strongest non-ionic attractive force between molecules. It is paramount in the folding and final structure of proteins and DNA[21–25] and is one of the most important driving forces of particle formation in the atmosphere.[26,27] OH-functionalities are highly abundant in the atmosphere first and foremost in the presence of water which accounts for up to ca. 5 % of the total number density, depending on temperature and humidity. Alcohols and hydroperoxides are also highly abundant trace species in the troposphere. Alcohols and hydroperoxides are formed in the atmosphere as oxidation products of volatile organic compounds (VOCs), of which there is emitted > 1 Pg C annually from the Earth's surface.[28–31] The main constituent of VOCs in the atmosphere is isoprene which, together with the other VOCs readily reacts with ·OH radicals, ozone and molecular oxygen to form hydroperoxides, carbonyls, alcohols etc. This happens often in a chain reaction-like addition of molecular oxygen to open shell reactants followed by an intramolecular hydrogen shift. This process is known as "autoxidation".[32–37]

Condensation of gaseous species into aerosols is highly disfavoured at room temperature due to the large entropic penalty associated with transforming 3 translational and 3 rotational degrees of freedom (DoFs) into much higher energy vibrational DoFs. Thus, only small amounts of, for example, water dimer will form at any time in the atmosphere and the dimers are likely to exist only for a short time before they again dissociate. The thermodynamics for clustering become more and more favourable the larger the clusters are until a threshold is passed and the change in Gibbs energy becomes negative, such that droplets spontaneously form from sequential condensation of more and more gas-species. In a macroscopic picture this is referred to as the Kelvin effect. As a consequence of this effect, the vapour pressure of a molecule inside a droplet decreases exponentially as the radius of the droplet increases.[28] This means that the initial formations of molecular dimers, trimers and tetramers etc. are the hardest and often rate-limiting steps in clusters growth while sequential addition becomes easier and therefore faster. The initial formation of small dimers, trimers and tetramers is driven by the formation of hydrogen bonds, and the exact strength of this interaction can therefore be determining for whether a small droplet forms or not.

Particles and small clusters act like small seeds for aerosol condensation, which can end up as clouds. They are therefore often referred to as cloud condensation nuclei (CCN). Clouds have a huge impact on the Earth's albedo. Because of this, aerosols are estimated to have an effect on Earth's radiative budget with a magnitude similar to that of methane, nitrous oxide and halogenated species combined.[38–40] The effect of aerosols is, however, associated with large error bars, especially because of the poorly understood initial formation of CCNs from, amongst other things, oxygenated VOCs.

Exposure to fine and superfine particles is further recognised as having a severe impact on human health on a global scale. Several intergovernmental health agencies estimate that 99 % of the global population is exposed to fine particulate matter concentrations above the World Health Organisation (WHO) guidelines. Globally, an estimated 3-7 million people die prematurely due to air pollution annually, about the same number as that of stroke, and the monetary cost of air pollution is estimated at

ca. 6 % of the total global Gross Domestic Product (GDP).[39,41–47]

Although an extremely important mechanism, the amounts of complexes that form at room temperature is miniscule. The properties of these molecular complexes are thus very hard to study experimentally. Much research has been devoted to the characterisation of molecular complexes in molecular jets and matrix isolation experiments, which can operate at very cold temperatures of only a few K. However, the experiments are generally not at thermal equilibrium and even each individual vibrational mode can have its own temperature in a jet expansion. In addition, the hydrogen bonding properties at cryogenic temperatures are also often not representative of those at ambient temperatures.

In order to study these complexes at room temperature, we rely on the two main experimentally observed properties of hydrogen bonds - the red shift and the intensity enhancement. The redshift separates the signal of the complex from its constituent monomer parts, and the intensity enhancement provides sensitivity towards the species which exist in relative minute quantities in the gas mix. Hippler decribed a method in 2007 where the partial pressure, and by extension the formation Gibbs energy of a molecular complex, could be estimated by scaling an experimentally observed band by a theoretically determined oscillator strength for the transition(s) associated with that band.[18,48]

$$p_{complex} \propto \frac{\int A(\tilde{\nu})d\tilde{\nu}}{f_{calc}} \tag{3}$$

By using this technique, very small partial pressures of complexes can be accurately determined and the thermodynamics inferred. Getting the IR spectra of the molecular complexes free from overlapping signals from the dominating monomer species is not a trivial task and in this thesis I will show how subtracting the monomer signals can be done efficiently to provide high quality spectra that can be used to extract thermodynamic data, validate theoretical modelling and probe the strength of the hydrogen bonds in complexes at room temperature. Some of the investigated hydrogen bound species in this thesis are the MeOH dimer, trimer and tetramer. These species have been studied extensively in cold conditions to characterise their formation and

hydrogen bonding networks.[49–59] Until now, few to no previous studies have achieved subtraction of the methanol monomer to a degree sufficient to extract thermodynamic data at room temperature. In this thesis I also bridge the gap between cold and room temperature spectra in a joint effort between high level vibrational simulations and advanced experimental techniques capable of tuning the effective vibrational gas temperature.

Another molecule investigated in this thesis is *tert*-butyl hydroperoxide (*t*-BuOOH). This molecule has previously served as a model organic hydroperoxide in many studies, usually focused on the spectroscopy of the OH-stretching overtones. The overtone spectroscopy has been of interest due to a very distinct feature of tunnelling splitting and a clear combination band from coupling with the low frequency COOH torsion mode.[11,60–65] In my master's thesis I further found suggestive evidence of dimer formation of this molecule[66] and other studies have found hydroperoxides to form stronger hydrogen bonds compared to alcohols.[67] The hydroperoxides are prevalent in the atmosphere and perhaps important for the formation of aerosols. *t*-BuOOH is thus an exciting molecule to study both in the context of overtone spectroscopy and in the context of hydrogen bonds.

As previously mentioned, the flux of isoprene from Earth's surface to the atmosphere is massive. It serves as the foundation for the formation of a large portion of the secondary organic aerosols (SOAs). Isoprene may also be a very good candidate for a biomarker molecule as it has no known abiotic sources on Earth. It is highly abundant wherever there is life, and unlikely to be found where there is not. It is therefore of high interest to obtain good reference measurements in as wide a range as possible with accurate determination of cross sections. This will allow, not only the detection, but also the quantification of isoprene in Earth's atmosphere and perhaps in exoplanetary atmospheres. To allow for the spectroscopic investigation of isoprene and *t*-BuOOH in a wide spectral range, specialised techniques such as cavity ring-down (CRD) spectroscopy is needed. A large part of this thesis is dedicated to the refurbishment and improvement of our CRD setup, which ultimately provided the sensitivity and spectral accuracy

needed to obtain spectra that can be used as reference for satellite and telescope measurements.

2

THEORETICAL-COMPUTATIONAL BACKGROUND

This chapter aims to introduce the theory used in the computational effort in this thesis. Starting from the most fundamental description of a harmonic oscillator, the equations are expanded to the VPT2 treatment which is used in this thesis and is implemented in many popular quantum chemical software packages. A quick introduction to the reduced dimensionality VPT2 scheme along with the most common pitfalls of VPT2 is introduced with examples.

A 1D numerical local mode programme is written in this thesis and used in two of the publicaitons. A short description of the code and discussion about fundamental local mode theory is included.

Lastly, an introduction is given on the analysis of non-covalent interactions and some commonly used software packages that can quantify and illustrate theses interactions.

2.1 NORMAL MODE HARMONIC OSCILLATOR

The Born-Oppenheimer approximation adiabatically separates nuclear motion from electronic motion.[68] This means that the electronic Schrödinger equation can be solved at a given nuclear configuration. By stepwise moving the nuclei and sequentially evaluating the electronic Schrödinger equation, a potential energy surface (PES) is obtained, with the energetic minimum corresponding to the most stable geometry of a molecule, the equilibrium structure. Single, isolated atoms in vacuum have three nuclear degrees of freedom (DoFs). As soon as two or more atoms start to interact with each other, some DoFs become associated with dramatically different amounts of

energy. It can help to partition these DoFs into categories that are intuitive and which can be treated separately based on their associated changes in energy. In a polyatomic, non-linear molecule, we can thus express the atomic motion, in ascending order of energy, as three translational DoFs of linear motion in Cartesian space, three rotational DoFs, one around each principal axis of inertia, and finally 3N-6 vibrational DoFs. In the special case of linear molecules, one rotational DoF is instead transformed into a vibrational DoF.

The different categories of motion in normal modes have the following defining unique properties: Translation changes the center of mass but does not change the orientation of the principle rotational axes relative to the lab frame, nor the potential energy. Rotation changes the orientation of the principle rotational axes but does not change the center of mass nor the potential energy. Vibration changes the relative position of the atoms, but does not change the center of mass nor the orientation of rotation. The translational DoFs are completely separable from the two latter ones.[69] The first two DoFs change only the kinetic energy of the molecule, while the vibrational DoFs have both kinetic and potential energy contributions to the nuclear motion Hamiltonian.

The simplest usable model of molecular vibrational motion is the harmonic oscillator. The harmonic oscillator can be thought of as two point masses held together by a perfect spring. The system has zero friction and the springs act on the masses with a restoring force proportional to the displacement from the equilibrium position $x = R - R_{eq}$. When considering only relative displacement between two or more masses that leaves the center of mass unchanged, the system can be further simplified by contracting the two (or more) masses of the system into a single "reduced mass" $\mu = \frac{m_i m_j}{m_i + m_j}$. This is analogous to a single mass being attached by a spring to an immovable object. In one dimension, the Hamiltonian is:

$$H_{1D} = -\frac{\hbar^2}{2\mu}\frac{\partial^2}{\partial x^2} + \frac{1}{2}ax^2 \tag{4}$$

and the corresponding Schrödinger equation has solutions and energy levels:

$$\Psi_{v,1D} = N_v H_v(y) \exp\left(-\frac{\mu\omega\ x^2}{2\hbar}\right), \quad E_{v,1D} = \left(v + \frac{1}{2}\right)\hbar\omega \tag{5}$$

where N_v is the normalization factor, H_v the v'th order Hermite polynomial as a function of $y = \left(\sqrt{\frac{\mu\omega}{\hbar}}\ x\right)$, a the force constant, $a = \left.\frac{\partial^2 V}{\partial x^2}\right|_{x=0}$, μ the reduced mass and $\omega = \sqrt{\frac{a}{\mu}}$ the angular frequency.

In order to utilize the harmonic oscillator model, we need to define a useful coordinate system. In the following I will assign different symbols for the force constants in different coordinates. The PES can be written as a second order Taylor expansion in mass-weighted Cartesian coordinates. The corresponding Hamiltonian is

$$H(q) = -\frac{\hbar^2}{2}\sum_{i,j}^{3N}\frac{\partial^2}{\partial q_i q_j} + \frac{1}{2}\sum_{i,j}^{3N} f_{ij} q_i q_j, \quad \text{where} \quad q_i = \sqrt{m_i}\ x_i, \quad f_{ij} = \left.\frac{\partial^2 V}{\partial q_i q_j}\right|_{q_i=q_j=0} \tag{6}$$

The variable q is the set of mass-weighted Cartesian displacements of the nuclei from equilibrium and f is the force constant matrix otherwise known as the Hessian. A set of "normal coordinates" Q is introduced. The normal coordinates are linear combinations of the mass-weighted Cartesian coordinates q, which transform the Hessian into a diagonal matrix.

$$H(Q) = -\frac{\hbar^2}{2}\sum_{i}^{3N}\frac{\partial^2}{\partial Q_i^2} + \frac{1}{2}\sum_{i}^{3N} F_{ii} Q_i^2 \tag{7}$$

The normal coordinates thus define 3N decoupled DoFs within the harmonic-oscillator approximation. The three translational and three rotational DoFs can be recognized by having force constants $F_{ii} = 0$. They therefore only contribute with kinetic energy terms to the Hamiltonian. The vibrational Hamiltonian in the normal mode harmonic-oscillator approximation thus consists of the sum of 3N-6 decoupled 1D harmonic oscillators.

2.2 DEVIATIONS FROM HARMONICITY

The harmonic approximation gives analytical 1D solutions, which can be calculated with only three energy evaluations; one at equilibrium and one at a small positive and negative displacement along the normal coordinate. The harmonic potential resembles the true PES only around the bottom of the potential. In the simplest case of a diatomic molecule, the system has 3N-5 = 1 vibration - a stretch. With decreasing interatomic distance, potential energy increases as a consequence of nuclear-nuclear repulsion and approaches infinity as $R \to 0$. The harmonic potential will approach a finite value, which means the PES will not be steep enough on the inner wall. At large interatomic distances, the limiting case is that the two atoms will not interact with each other, thus approaching a potential energy set to 0 as $R \to \infty$. The harmonic potential will have an ever increasing potential energy with R. This incorrect behaviour in the dissociation limit causes stretching mode transition energies in general to be overestimated in the harmonic approximation.

Any deviation from harmonicity is classified as anharmonicity. A vast range of analytical potentials exist, which offers varying degrees of accuracy in different regions of the PES, also depending on the coordinate definition. The Morse potential[70,71] needs only 2 parameters to obtain vibrational transition energies and the potential allows for correct dissociative behavior. The parameters give information about dissociation energy and anharmonicity. However, the Morse potential does not have correct behaviour with $R \to 0$ and goes to a finite value like the harmonic potential. The Deng-Fang potential[71,72] solves this by including the interatomic distance in the energy expression, which gives the correct behaviour in the $R \to 0$ limit as well, and indeed gives more accurate transition wavenumbers for a X-H stretching mode compared to the Morse oscillator.[71]

2.3 VIBRATIONAL PERTURBATION THEORY

One of the most commonly implemented ways of including vibrational anharmonicity in quantum chemical software packages eg. Gaussian16[73] is by expanding the PES in a 4'th order polynomial in the normal modes around the equilibrium geometry. Corrections to the energies are done by Rayleigh-Schrödinger perturbation theory to the second order, and so the theory implemented is referred to as second order vibrational Rayleigh-Schrödinger perturbation theory (VPT2). The expansion demands 2 additional energy calculations along each coordinate in order to obtain numeric derivatives of the Hessian. It is common practice to scale the normal coordinates such that they become unitless quantities. Owing to the fact that the latin alphabet has a limited number of letters, it is also convention to call the unitless normal coordinates q, not to be confused with q from Equation 6. The scaling factors for the normal coordinates and associated momentum operator are[74]

$$q_i = 2\pi \cdot \sqrt{\frac{c \cdot \tilde{\omega}_i}{h}} \cdot Q_i \quad , \quad p_i = \frac{P_i}{h \cdot \sqrt{\frac{c \cdot \tilde{\omega}_i}{h}}} \tag{8}$$

where $\tilde{\omega}$ is the harmonic wavenumber.

The 3rd and 4th order derivatives of the PES allow for coupling between the different normal modes. Cubic and quasi-quartic force constants are evaluated for all the modes:

$$\phi_{ijk} = \left.\frac{\partial^3 V}{\partial q_i \partial q_j \partial q_k}\right|_{q_i,q_j,q_k=0} \quad \text{and} \quad \phi_{ijkl} = \left.\frac{\partial^4 V}{\partial q_i \partial q_j \partial q_k \partial q_l}\right|_{q_i,q_j,q_k,q_l=0} \tag{9}$$

The indices signify the different normal modes and the diagonal cubic and quartic force constants are those where $j, k, l = i$. Quartic force constants involving single derivatives of 4 different modes are not evaluated and do not contribute in the VPT2 equations. The vibrational Hamiltonian is partitioned into the harmonic part, which has an exact solution, and into the first- and second order corrections ordered by the sum of powers of the position and momentum operators (in unitless normal mode space).

$$\begin{aligned} H_{VPT2} &= H_{HO} + H^1 + H^2 \\ H^1 &= \sum \frac{1}{6} \sum_{ijk} \phi_{ijk} q_i q_j q_k \\ H^2 &= \sum \frac{1}{24} \sum_{ijkl} \phi_{ijkl} q_i q_j q_k q_l + H_{Cor} + U \end{aligned} \tag{10}$$

The H_{Cor} is the effect of Coriolis coupling, which in this context describes the coupling between vibrational modes through rotational coordinates.[75] This coupling is most pronounced for small molecules with large rotational constants and for vibrational motion, which has a large displacement away from the molecular axis, such as bending motion. The effect is < 20 cm^{-1} and often negligible for large molecules or molecular clusters.[74,76] U is the Watson pseudo-potential, which has a small kinetic energy correction. The correction is largest for the zero-point vibrational energy ($ZPVE$) but negligible for transition energies.[75,77]

The cubic correction to the potential, interestingly, does not contribute to the first order energy correction as it is an uneven function. The cubic correction does correct the wavefunction to the first order, thus contributing to the second order energy correction by[78]

$$E_v^{VPT2} = E_{HO} + \langle v^0 | H^2 | v^0 \rangle + \langle v^0 | H^1 | v^1 \rangle \tag{11}$$

The VPT2 vibrational energy is conveniently expressed in terms of anharmonicity matrices χ in wavenumber units.[74,75,79,80]

$$\tilde{E} = \frac{E}{hc} = \chi_0 + \sum_i \tilde{\omega}_i \left(v_i + \frac{1}{2} \right) + \sum_{i \leq j} \chi_{ij} \left(v_i + \frac{1}{2} \right) \left(v_j + \frac{1}{2} \right) \tag{12}$$

χ_0 is a correction, which is not dependent on the number of quanta of excitation. It can therefore be left out if one exclusively needs to deal with corrections to transition energies from the same ground state. $\tilde{\omega}_i$ is the harmonic wavenumber and v_i the quanta of excitation in mode i. The in-depth definition of the anharmonicity matrices can be found in references 74, 75, 79, 80 amongst others. Here, we briefly discuss the diagonal terms for mode i:

$$\chi_{ii} = \frac{\phi_{iiii}}{16} - \frac{5\phi_{iii}^2}{48\tilde{\omega}_i} - \sum_{j \neq i} \frac{\phi_{iij}^2 \left(8\tilde{\omega}_i^2 - 3\tilde{\omega}_j\right)}{16\tilde{\omega}_j \left(4\tilde{\omega}_i^2 - \tilde{\omega}_j^2\right)} \tag{13}$$

The important thing to notice is that even in the diagonal anharmonicity terms, cross cubic force constants and harmonic wavenumbers for other modes are included. It can be seen that especially the cubic force constants are important to determine accurately, as they contribute with their squares to the anharmonicity. The harmonic wavenumber appears in all denominators apart from the quartic term. This causes instabilities in the χ_{ii} expression if $\tilde{\omega}$ is very small compared to the cubic force constants. In both the diagonal and off-diagonal χ_{ij} matrix elements, there are denominators that may approach zero at 2- and 3-body resonances of the zeroth order states. This causes the equations to blow up and give unphysical results. There are many routines implemented to circumvent these resonances. The general VPT2 (GVPT2) routine implemented in Gaussian16 removes resonant terms and treats them variationally. It is, however, a well-known problem that the recognition and treatment of resonant terms are far from ideal in Gaussian16 and other GVPT2 implementations. This may cause large problems especially for the calculated intensities where faulty correction to the wavefunctions propagate along with the errors to the PES and dipole moment surface (DMF).[80,81]

The VPT2 equations for properties are slightly more complicated than those for energy and they are largely left out of this discussion. However, it is worth mentioning that in the harmonic approximation the DMF is typically expanded to the first linear term. In the VPT2 treatment it is expanded to the cubic term, which provides second order corrections to 1-quantum excitations and first order corrections to 2- and 3- quanta excitations.[75] The expansion of the DMF above the linear approximation is referred to as "electronic anharmonicity". Wavefunction mixing of states usually happens upon resonance. When treated variationally, states can share and steal intensity from each other. This allows dark states to gain intensity. For bright states, the mixing usually results in a decrease of intensity. This is referred to as "mechanical anharmonicity".[75]

2.4 REDUCED DIMENSIONALITY VPT2

With the increased amounts of displacements and energy evaluations in a 3N-6 dimensional space, the complexity and therefore the computational cost increases significantly when doing VPT2 compared to the harmonic-oscillator approximation. The VPT2 approach is a good compromise between computational cost and accuracy for small and semi-rigid molecules. However, for large systems, and for systems where only a few modes are of interest, it is impractical to use computational resources evaluating force constants for vibrational modes, which contribute only little to the mode(s) of interest. A further advantage of reducing the dimensionality of the VPT2 treatment is avoiding the two major problems that VPT2 suffers from.

The first problem is, as previously mentioned, resonances. With increased dimensionality, it is easy to see that the potential for resonances rise, which may cause problems in the VPT2 treatment. The second problem is associated with large amplitude motion (LAM) modes. Modes with low transition energies and large reduced masses are referred to as such. It is often vibrational motion which is curvilinear in nature and therefore poorly described by a harmonic oscillator in rectilinear coordinates, such as normal mode coordinates. This causes the perturbations to be excessively large in the form of especially large quartic force constants. When paired with small $\tilde{\omega}_i$, Equation 13 becomes very unstable. It is a dogma in perturbation theory, that the perturbations should be small and convergent. With LAM, the zeroth order basis is so far away from the real potential that the perturbations are simply too large and not convergent in a reasonable expansion order.

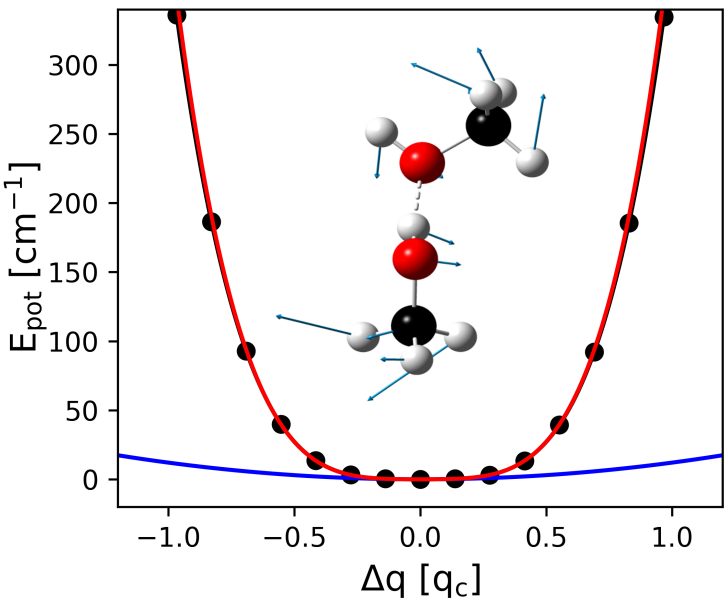

Figure 2: 1D scan of intermolecular torsion mode together with harmonic and VPT2 potential. The blue trace is the harmonic potential, the red trace is the VPT2 potential and the black dots and trace is the manually displaced energy evaluations with interpolation. The displacement is expressed in units of classical turning point, which is $q_c = 0.72$ Å for mode 1.

In Figure 2, the harmonic potential and VPT2 potential are shown together with scanned energy points along the normal mode of the lowest frequency intermolecular torsion mode, which we call ”mode 1” in the following discussion. The harmonic potential is very far away from the true potential, due to the harmonic potential being expanded around the almost flat bottom. The VPT2 potential is deceivingly close to the true 1D potential and one could expect good results. The energy corrections in perturbation theory assumes small, and decreasing higher order force constants. Due to the very large $\phi_{iiii} = 9558$ cm^{-1}, and $\phi_{iii} = 0$, Equation 13 blows up to give a VPT2 transition wavenumber = 1218 cm^{-1} and an oscillator strength of 0.04. This is simply a fault of the perturbative approach. When taking the VPT2 potential and solving the Schrödinger equation variationally, a transition wavenumber of 106 cm^{-1} is obtained, within 1 cm^{-1} of that obtained by the real potential. In conclusion, eventhough the potential is expanded to a high degree of accuracy, the perturbation is too large from the harmonic basis for the VPT2 equations to give usable results.

Inclusion of modes such as mode 1 in a multi-dimensional VPT2 treatment can give unreliable results, not only for mode 1, but also for the modes to which mode 1 contributes cross cubic and cross quartic force constants. In this thesis, the fundamental hydrogen bound OH_b-stretching transition is the focus. From previous studies, in primarily a local mode framework, it has been determined that only a small subset of modes contributes significant perturbations to the OH_b-stretching frequency and intensity. These are namely the intermolecular "rock" and "twist" modes and, to a lesser extend, the intramolecular bend.[82–88] These modes have large amplitudes in the spatial vicinity of the hydrogen bond and partially break the hydrogen bond in their displacements. In the normal mode picture, these modes are reasonably localized and so look like their local mode counterparts. They have a relatively high harmonic wavenumber $600 - 1500$ cm^{-1} and a PES which is close to harmonic in the energy region of interest.[89] Previously, protocols have been suggested for including active normal modes in a reduced dimensional VPT2 treatment based on a quantitative measure of the cross-cubic force constants.[80] Many others have chosen an approach based on a qualitative analysis of the nature of the vibrational motion.[90–92] In our most recent publication, we also show that when two or more OH_b-stretches are coupled, a significant amount of anharmonicity is carried in cross-cubic and cross-quartic force constants. It is imperative to include all modes, which may have a large potential energy coupling, to the mode of interest in a reduced dimensionality VPT2 model.[89]

Inactivation of modes can be done in Gaussian16 in two different ways. Setting a mode to be "inactive" means that it is treated harmonically meaning no 3rd and 4th order derivatives are evaluated along that coordinate. This cuts down the computational cost significantly. Nevertheless, the inactive modes do still contribute to χ_{ij} (Equation 12) with harmonic wavenumber and with cross cubic- and cross quartic force constants, where the inactive mode occurs with up to 2 indices. In the case of mode 1, the harmonic representation is quite bad. An inactive mode 1 will still contribute with perturbations, which are far from ideal, although mitigated to harmonic contributions. Furthermore, unwanted resonances can still occur with the inactive modes, which may cause problems. The alternative option is to "freeze" a mode. In this way all the force constants and harmonic wavenumbers associated with a frozen mode are removed from

all evaluations of χ_{ij}. In Equation 13, this corresponds to a truncation after the second term and a removal of all $\sum_{i \neq j} \chi_{ij}$ in Equation 12. The frozen option also removes the possibility of resonances.[80] Freezing unwanted modes emphasises the reduced dimensionality of the model and is for many applications preferable. It is, however, imperative that the user makes a thorough analysis as to not leave out important modes from the vibrational model. For reference to the curious reader who would like to endeavour in VPT2 calculations of floppy molecular complexes the following advice can be given:

1. Be sure to include all modes in the VPT2 treatment, which have an expected large potential energy coupling with the mode of interest. This could for example be all modes with similar harmonic transition wavenumbers

2. Choose the "Freeze"/"Passive" option for modes that are poorly described by a harmonic potential. Modes that are not expected to be very important for the mode of interest and is expected to be close to harmonic may be included as "inactive".

3. If computationally feasible, do a full dimensional VPT2 calculation and save the force constants in a checkpoint file. The force constants can then be selectively included in new reduced dimensionality computations without new numerical differentiation.

4. Inspect diagonal force constants for convergence with increasing order. If the quartic force constant is much larger than the quadratic and cubic force constants, the mode is likely a troublesome LAM mode.

5. Inspect the cross-cubic force constants to evaluate which off-diagonal couplings may be important.

2.5 1-DIMENSIONAL LOCAL MODE MODEL

When solving the vibrational Schrödinger equation, the choice of coordinates is not restricted to mass-weighted Cartesian coordinates. A perhaps more chemically intuitive way of describing the vibrational motion is in terms of so-called "internal coordinates"

or "local modes". These coordinates are expressed as bond lengths, angles and dihedrals. The definition of a local mode coordinate system is not as straight forward as diagonalizing a harmonic-oscillator Hamiltonian. A Z-matrix has to be constructed such that no unsuitable atom-atom dependencies occur. For high dimensionality this can be a complicated task. It can be assisted by the use of dummy atoms.[85,89]

Local modes are not separated from translation and rotation like normal modes are (in zeroth order). This can cause problems especially for intensities, where vibrational motion, typically bends, can significantly change the orientation of the principle rotational axes, from which the molecular body reference frame is defined. When evaluating the intensity of a vibrational transition, the DMF, which is described in a lab-frame, needs to be correlated with the DMF in terms of the molecular body frame. If this frame changes, the DMF cannot be mapped between the two frames with a linear transformation. To counteract this effect, an Eckart embedding algorithm has to be implemented. The algorithm constructs a matrix that tilts the displaced structure back into a reference frame, typically aligning the molecular axis with that of the equilibrium structure.[69,93] As a final drawback of the local mode description, the Wilson G-matrix, which is a metric tensor that expresses the mass of the oscillators and a transformation between Cartesian and local mode coordinates, is non-trivial for anything but the most simple oscillators at low dimensionality.[18,94,95]

With all of these obvious drawbacks of using a local mode description one may ask, like Edwin Starr did in 1970: "What is it good for?". The automatic inclusion of all $3N-6$ modes in the normal mode description increases computational complexity and imposes a limit on the practically available electronic structure methods. This becomes a problem especially at higher quanta of excitation, due to the high density of states. It has previously been shown, that with high quanta of excitation, the experimentally observed spectra become increasingly simple,[94,96,97] alluding to the fact that only a few localised excitations in high energy modes carry intensity. In order to describe these localized excitations in a normal mode picture, a linear combination of all the normal coordinates have to be taken in order to obtain for example a highly excited localized X-H stretching motion. The full dimensional normal mode description therefore carries

a lot of redundant information. The localization of the vibrational motion justifies a reduced dimensional local mode approach when describing high-quanta excitations.

$$H^{1D} = \frac{1}{2} G_{ii} p_i^2 + V_{AO}(q_i) \tag{14}$$

The zeroth order Hamiltonian for a 1D local mode oscillator i is shown in Equation 14.[94] G_{ii} is the Wilson G-matrix, which is simply $1/\mu$ for motion linear in Cartesian space. q_i is a coordinate describing displacement from equilibrium geometry, which for a stretch is expressed as an interatomic distance. The reduced dimensionality allows for a multi-point scan of the full PES along the coordinate and the Schrödinger equation can be solved in the exact potential, V_{AO}, thus including full 1D anharmonic treatment of the potential energy.

The Morse potential, which has correct dissociative behaviour, has been used with quite accurate results to describe anharmonic local mode oscillators. The analytical form of the Morse oscillator[70] also provides qualitative information about the system in the harmonic wavenumber and anharmonicity parameters, which are directly correlated with the a and D_e Morse parameters.[94]

$$\tilde{E}_{v \leftarrow 0} = v\tilde{\omega} - (v^2 + v)\tilde{\omega}x \tag{15}$$

The transition energy is shown in Equation 15. The harmonic wavenumber and anharmonicity, $\tilde{\omega}$ and $\tilde{\omega}x$, can be experimentally determined by fitting transition energies to a Birge-Sponer expression.[98–101] This provides accurate PESs and consequentially wavefunctions in a Morse oscillator expression. Alternatively, if the PES is determined numerically with a sufficient *ab initio* method, the parameters can be approximated as[7,12,94]

$$\tilde{\omega} = \frac{1}{2\pi c}\sqrt{F_{ii} G_{ii}} \quad , \quad \tilde{\omega}x = \frac{G_{ii} h}{64\pi^2 c F_{ii}} \left(\frac{5F_{iii}^2}{3F_{ii}} - F_{iiii} \right) \tag{16}$$

where F_n is the nth derivatives of the PES: $F_n = \frac{\partial^n V(q)}{\partial q^n}|_{q=0}$. The expression in Equation 16 is derived from second order perturbation theory and indeed bears a resemblance to the expression in Equation 13.

In the context of fundamental transitions, local modes can prove a better basis for describing certain modes. For an OH_b-stretch in a hydrogen bound complex, the vibration is localized even in the normal mode formalism and the interaction with the hydrogen bond acceptor contributes significant diagonal anharmonicity. Therefore, the local mode seems like an obvious choice. Further, the curved motion of many LAMs can be made linear in local mode space, which means that these modes are much better described in local mode coordinates than in normal mode coordinates. The intermolecular modes donor- "twist" and "rock" strongly affect the transition energy and intensity of the OH_b-stretch as discussed in Section 2.4. The inclusion of these modes in a LM model can be done by harmonic or anharmonic coupling in a perturbative approach[18,82–84] or variationally.[85,88,89] In both cases a reasonably robust 20 % - 30 % drop in intensity is observed when including the donor- "rock" and "twist" modes. As such, very reasonable transition intensities can be estimated based on an empirically corrected 1D LM model of the OH_b-stretch.

In this thesis a 1D numerical LM model programme was written in Python3.[89,102,103] The 1D Hamiltonian (Equation 14) is diagonalised in a basis of typically the 50 first m=1 associated Legendre polynomials, P_l^1. The polynomials can be found from the first two polynomials and a recursive formula

$$\begin{aligned} P_1^1 &= N \cdot -\sqrt{1-x^2} \\ P_2^1 &= N \cdot -3x\sqrt{1-x^2} \\ P_{l+1}^1 &= N \cdot \left((2l+1)\, x P_l^1 - (l+1)\, P_{l-1}^1 \right) / l \\ N &= \sqrt{\frac{2l+1}{2l(l+1)}} \sqrt{\frac{2}{q_{range}}} \end{aligned} \tag{17}$$

and for the kinetic energy operator it can be useful to create a set of already differentiated functions. The two first polynomials are trivial to differentiate analytically and the recursive form of the differentiated polynomials is given by

$$\begin{aligned} \frac{\partial}{\partial q} P_l^1 &= N' \cdot \left(l x P_l^1 - (l+1) P_{l-1}^1 \right) \\ N' &= \sqrt{\frac{2l+1}{2l(l+1)}} \sqrt{\frac{2}{q_{range}}} \frac{2}{q_{range}} \end{aligned} \tag{18}$$

The associated m=1 Legendre polynomials are bound on a finite interval $x = [-1, 1]$ and can be mapped onto another range like a q coordinate with a linear function. The normalization factors ensure that $\langle P_l^1 | P_l^1 \rangle = 1$ The choice of basisfunctions does in principle not matter as long as the contracted wavefunctions are converged. The first 4 basis functions are shown in Figure 3

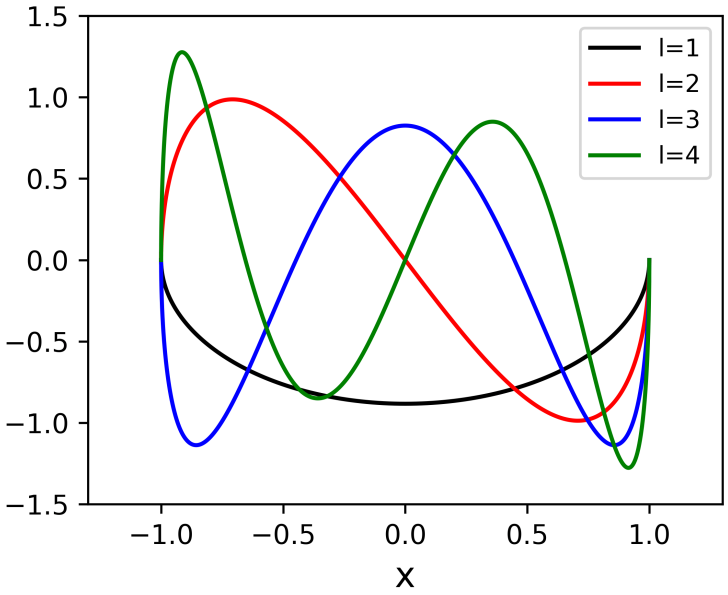

Figure 3: First 4 m=1 Legendre polynomials

The 1D local mode model takes as input a range of potential energies and dipole moment components $\mu_{x,y,z}$ evaluated at different displacements q and finally a reduced mass. The points are interpolated to a reasonable resolution to converge the integrals of the wavefunction with the PES and DMF. The resulting eigenfunctions are shown with the PES of the OH_b-stretch for $(MeOH)_2$ in Figure 4.

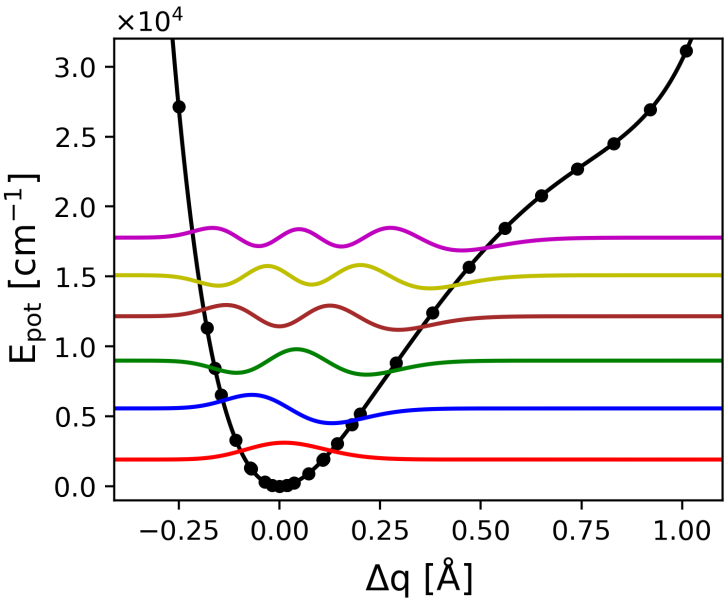

Figure 4: First 6 eigenfunctions of the OH_b-stretch PES in $(MeOH)_2$

The intensity of the transition is expressed as a unitless oscillator strength.[5,104]

$$f_{fi} = 4.702 \cdot 10^{-7} \frac{\mathrm{cm}}{\mathrm{D}^2} \cdot \tilde{\omega}_{fi} \cdot |\langle \Psi_f | \vec{\mu} | \Psi_i \rangle|^2 \tag{19}$$

The oscillator strength expresses the probability of a species absorbing a photon with energy equivalent to an energy gap in the absorber. The oscillator strength is normalized such that a three dimensional harmonic oscillator in a linear dipole has $f = 1$. For real oscillators, the probability is always below 1 and so $f < 1$. The theoretical definition of f in Equation 19 is equivalent to the experimental definition of f in Equation 26.

The script can give numerical solutions to the 1D vibrational Schrödinger equation for all modes that are linear in Cartesian coordinates, or equivalently, where $G_{ii} = 1/\mu_i$. This also means that the script works on normal modes. In this case, the reduced mass can be read directly from the output of the harmonic frequency calculation and the mass-dependent normal coordinate has to be converted to a non-mass-weighted distance coordinate.

2.6 NON COVALENT INTERACTIONS ANALYSIS

Molecular complexes are held together by non-covalent interactions (NCIs). It can be helpful to visualise and quantify these interactions. In the software packages NCIPLOT4[105,106] and NCIMilano,[107] the NCIs are illustrated as isosurfaces of the reduced electron density gradient $s(\mathbf{r})$.[105–110] Typically a value for the isosurface of 0.5 au. is used.

$$s(\mathbf{r}) = \frac{|\nabla\rho(\mathbf{r})|}{2(3\pi^2)^{1/3}\rho(\mathbf{r})^{4/3}} \tag{20}$$

where $\nabla\rho(\mathbf{r})$ is the Hessian of the electron density at point $\mathbf{r}$ in real 3D space. $s(\mathbf{r})$ illustrates a range around the maxima and minima of electron density between molecules. The bonding and anti-bonding interactions are expected to be associated with a certain increase or decrease in electron density. The sign of the second largest eigenvalue of the electron density Hessian, $\text{sign}(\lambda_2)$, shows the curvature perpendicular to the bonding interaction and this quantity is related to the nature of the interaction. A positive sign signifies a deficiency in electron density, thus an anti-bonding interaction and the opposite for a negative sign. In Figure 5, the $s(\mathbf{r}) = 0.5$ au. isosurface is plotted for the rather exotic molecule with 3 intramolecular hydrogen bonds and a trioxide group[111] $(HOOCH_2)_2NCH_2OOOH$.

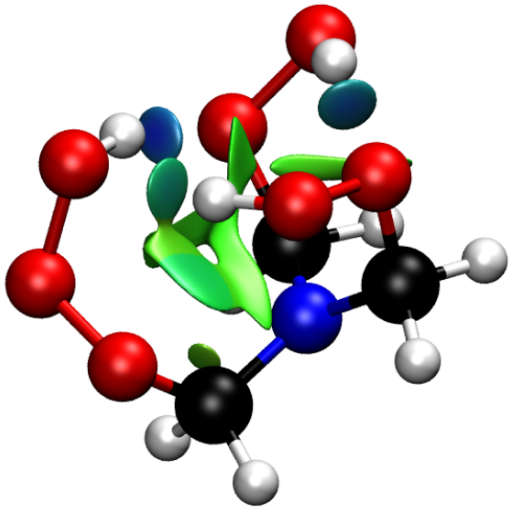

Figure 5: NCI Isosurface of $(HOOCH_2)_2NCH_2OOOH$

The colorscale shows attractive interactions in shades of blue, weak Van der Waal interactions in green and any repulsive interactions as red. The varying shades of blue signifies the electron density at the bond critical points and clearly show the varying relative hydrogen bonding strengths in the molecule. The difference between the interactions can also be visualized by plotting $s(\mathbf{r})$ against $\text{sign}(\lambda_2)\rho(\mathbf{r})$ as is done in Figure 6. Here the dips in $s(\mathbf{r})$ shows the different NCI extrema and the position on the $\text{sign}(\lambda_2)\rho(\mathbf{r})$-axis gives an idea about the strength of the interaction. The three hydrogen bonds are clearly seen with varying strengths [-0.04,-0.02] au. together with secondary interactions [-0.01,0.01] au.

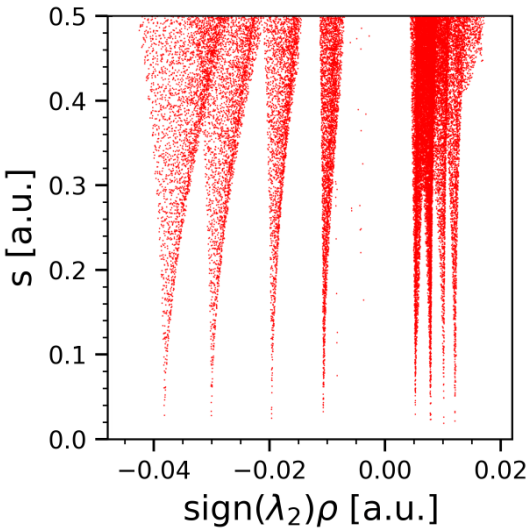

Figure 6: Reduced density gradient plotted against the electron density in $(HOOCH_2)_2NCH_2OOOH$

Different approaches to make a quantitative analysis of the strength of the interactions have been proposed.[109] The observed redshift of an OH-stretch upon hydrogen bonding is in general known to correlate with the hydrogen bond strength.[16,17,67] Therefore, the NCI-analysis can be correlated to this property. The perhaps most straight forward analysis is to read out the $\rho(\mathbf{r})$ at $s(\mathbf{r}) = 0$. In a slightly more involved approach, the $s(\mathbf{r})$ volume is integrated within the $s(\mathbf{r}) = 0.5$ au. isosurface. These two approaches show a reasonable correlation with the observed redshift, but is strongly grouped by the identity of the acceptor atom. The most succesful approach so far is to integrate the electronic kinetic energy within the $s(\mathbf{r}) = 0.5$ au. surfaces. The integrated kinetic energy, $G(s_{0.5})$, is observed to correlate strongly with the observed redshift, thus with

the hydrogen bond strength irrespective of the acceptor-atom.[109] The kinetic energy is expressed from the wavefunctions as[107]

$$G(\mathbf{r}) = \frac{1}{2}\sum_i \alpha_i |\nabla\phi_i(\mathbf{r})|^2 \tag{21}$$

where ϕ_i is the ith natural orbital and α_i the orbital coefficient. If the wavefunction is not obtainable, one can instead use the Abramovs approximate functional[107,112]

$$G(\mathbf{r}) = \frac{3}{10}\left(3\pi^2\right)^{2/3}\rho(\mathbf{r})^{5/3} + \frac{\left(\nabla\rho(\mathbf{r})\right)^2}{72\rho(\mathbf{r})} + \frac{1}{6}\nabla^2\rho(\mathbf{r}) \tag{22}$$

The empirically observed correlation between redshift and integrated electronic kinetic energy is[109]

$$\Delta\tilde{\nu} = 55750\ \frac{\text{cm}^{-1}}{\text{au.}} G(s_{0.5}) - 164\ \text{cm}^{-1} \tag{23}$$

The integrated kinetic energy and the software Bonder was not used in this thesis apart from a small section in Paper 1.[103] However, the equations may be useful for the reader who wants to dig into NCI analyses and are left here as reference for such.

3

EXPERIMENTAL METHODS

In this chapter the background for the principles of absorption spectroscopy and relevant thermodynamics are presented. The different experimental setups that were used in this thesis are presented along with a review of the more fundamental working principles behind the instruments and techniques. A thorough discussion of the FTIR spectrometer is included as this is the most used instrument in this thesis. I further show an in-depth description of the cavity ring-down setup and the improvements and calibrations that I have made on the setup. Additionally, a few examples of the possibilities and limitations of the techniques are given.

3.1 ABSORPTION SPECTROSCOPY

3.1.1 *General Background*

The measured absorption of light is most often expressed in the decadic absorbance A, which is defined from the ratio of the light intensity before and after propagation through an absorber.

$$A = \log_{10} \frac{I_0}{I} \tag{24}$$

The amount of light absorbed at a given energy is dependent on the path length through the absorber l, the concentration of the absorber C and the extinction coefficient $\epsilon(\tilde{\nu})$ which expresses the probability of a molecule absorbing light at the given energy. This gives the Lambert-Beer's law:

$$A = l \cdot C \cdot \epsilon(\tilde{\nu}) \tag{25}$$

The transition dipole moment of a given transition depends on the extinction coefficient integrated over the whole absorption band. The transition dipole moment can only be determined from a single measurement point at peak absorption if the transition is approximately Lorentzian with a known width. In vibrational spectroscopy, clear Lorentzian profiles from individual transitions are almost never observed. Instead, bands are observed consisting of many overlapping vibrational transitions, often coupling with each other and each with their own rotational profile across which the vibrational intensity is distributed. Even partly isolated and cold transitions are further perturbed by Doppler and pressure-broadening effects and instrumental resolution is also often not sufficient. To determine vibrational transition intensities in the gas phase it is therefore the integrated extinction coefficient which is measured. The extinction coefficient is also expressed as the molar absorption coefficient, related by: $\alpha(\tilde{\nu}) = \ln(10)\epsilon(\tilde{\nu})$. The convenient and unitless oscillator strength f can be expressed from the integrated absorption coefficient[5,18]

$$f = \left(\frac{4\ m_e\ c\ \epsilon_0}{N_A\ e^2}\right) \int \alpha(\tilde{\nu}) d\tilde{\nu} \tag{26}$$

where m_e is the electron mass, c the speed of light, ϵ_0 the vacuum permittivity, N_A Avogadro's constant and e the elementary charge. It may be practical to replace the absorption coefficient with absorbance, as this is commonly the directly measured quantity. By inserting Equation 25 into Equation 26 and assuming an ideal gas, we get

$$\begin{aligned} f &= \left(\frac{4\ m_e\ c\ \epsilon_0}{N_A\ e^2}\right) \cdot \left(\frac{c\ \ln(10)\ R\ T}{p\ l}\right) \int A(\tilde{\nu}) d\tilde{\nu} \\ &= 2.6935 \cdot 10^{-9} \frac{\text{Torr m cm}}{\text{K}} \frac{T}{p \cdot l} \int A(\tilde{\nu}) d\tilde{\nu} \end{aligned} \tag{27}$$

where T is the temperature, p the partial pressure of the absorber and l the path length. Alternatively, the absorbance can be converted to the molecular property absorption cross section, usually expressed in cm^2. The oscillator strength is then directly proportional to the integrated cross section by a multiplication factor

$$\sigma(\tilde{\nu}) = \frac{A(\tilde{\nu}) \cdot R \cdot T \cdot \ln(10)}{l \cdot p \cdot N_a} \quad , \quad f = 1.1296 \cdot 10^{12} \cdot \mathrm{cm}^{-3} \cdot \int \sigma(\tilde{\nu}) d\tilde{\nu} \qquad (28)$$

Thus, by constructing experiments where we measure the absorbance of a gas cell with a known path length filled with a known pressure of an absorber and at a determined temperature, it is possible to directly measure the oscillator strength of a transition. At first glance, this seems like not much of a challenge and indeed for intense transitions in pure samples with high vapour pressure, this is an easy task. Unfortunately, nature seldomly conforms to our wishes of simplicity. Often, we want to record a transition that naturally has very low intensity, is associated with a molecule, which has a low vapour pressure and is recorded in a gas mixture together with solvents and impurities. And sometimes all of the above.

3.1.2 *Spectral Substraction*

tert-butyl hydroperoxide (*t*-BuOOH) is analysed in this thesis for many of its interesting properties of e.g. dimer formation and OH-stretch/COOH-torsion combination band- and overtone intensities *(vide infra)*. In all cases, *t*-BuOOH needs to be isolated from the degradation products and solvents, which coexist in the gas mixture together with *t*-BuOOH, thus contributing pressure and absorbance features. A more in-depth discussion of the exact sample preparation and analysis of this compound is given in Section 4.1 and in Paper 1. Here I show an example in Figure 7 of the spectral subtraction that goes into isolating *t*-BuOOH in a sample gas mixture of degradation products and solvents. In panel A, it can be seen that the vast majority of the absorbance is associated with the expected bands from *t*-BuOOH. When zooming in, in panel B, it becomes clear that the degradation product *tert*-butanol (*t*-BuOH) and the solvent dichloromethane (DCM) are both present in the sample. They are identified from the OH-stretching signal at 3642 cm^{-1} and the CH-stretch/HCH-bend signal at 4467 cm^{-1}, respectively. In panel C, the edited spectrum of pure *t*-BuOOH is compared with the original mixture gas sample. The impurities are subtracted with scaled reference spectra of the pure compounds with known pressures. By evaluating the scaling factors needed to subtract the impurity signals away from the mixture

spectrum, the partial pressure contributions can be subtracted from the measured pressure to give the partial pressure of *t*-BuOOH to a high degree of certainty. Thus, a spectrum with associated partial pressure of the pure substance is obtained.

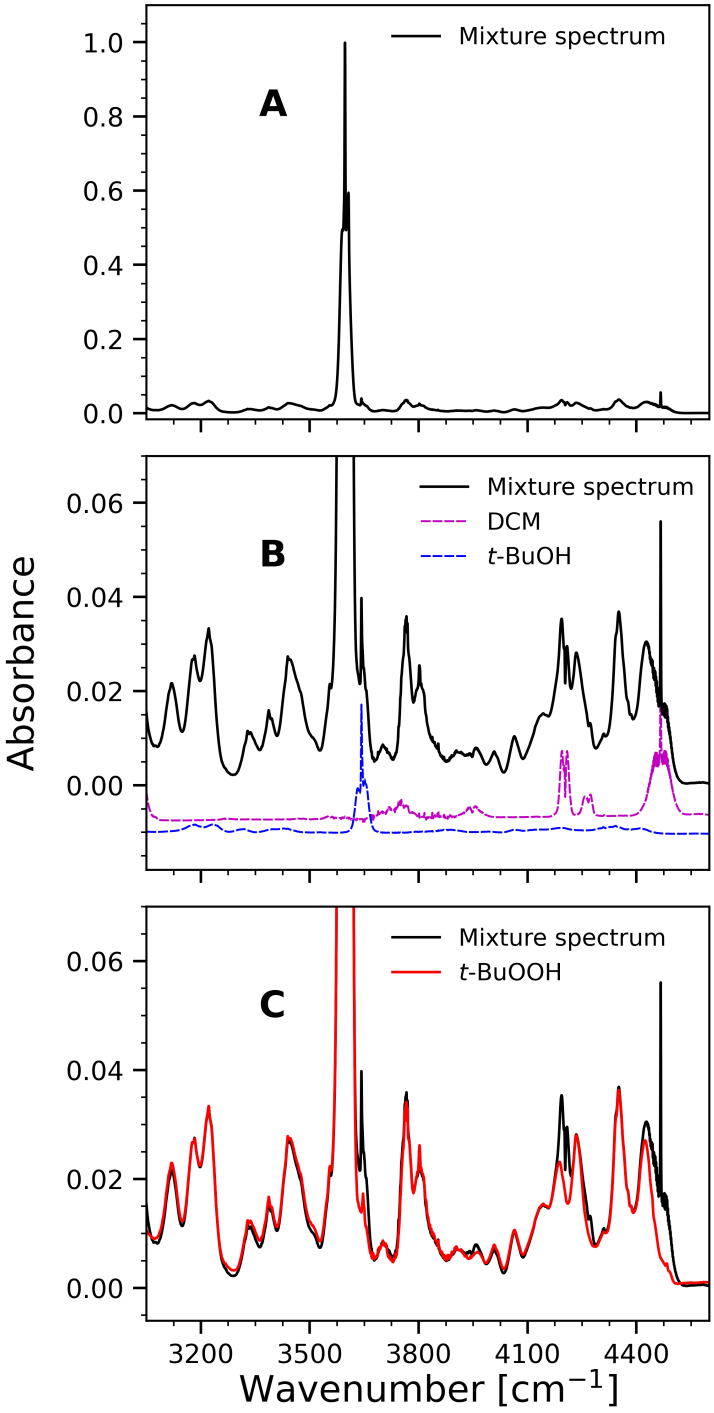

Figure 7: Example of spectral subtraction in a *t*-BuOOH gas sample. The gas sample is a mixture of *t*-BuOOH, its primary degradation product *t*-BuOH and the solvent DCM

As long as unique bands associated with the known impurity species can be identified and reference spectra of the pure unwanted compound be obtained, this technique can be used to "purify gas samples *in post*" as seen in the case of *t*-BuOOH. It is also a useful tool for revealing very small hidden absorbance features, which would otherwise be buried under absorbance bands from other species. In the case of molecular clusters, as discussed in Section 3.1.5, a scaled low pressure monomer reference spectrum can be subtracted from a high pressure sample to reveal absorbance from clusters which does not scale linearly with monomer pressure, but rather with a power corresponding to the order of cluster.

3.1.3 *Pressure Broadening*

When doing spectral subtraction it is important to consider pressure broadening effects. If the reference spectrum is recorded at a different pressure than that of the sample, in some cases, this will lead to insufficient subtraction. The differences in pressure lead to a change in the linewidth of the transitions in a spectrum. Pressure broadening occurs as a consequence of a decreased lifetime of any microstate of a molecule. An uncertainty relation between the lifetime and the energy spread of a state exists (Equation 29), analogously to the Heisenberg uncertainty relation of momentum and position.[113,114]

$$\tau \Delta E \geq \frac{\hbar}{2} \tag{29}$$

where τ is the base e lifetime, often interpreted itself as the uncertainty in time, ΔE the uncertainty in energy, which is often taken as the full width at half maximum of a Lorentzian distribution, and $\hbar$ the reduced Planck's constant. The uncertainty relation means that a decrease in lifetime will increase the energy spread or, in a spectrum, the linewidth of a transition. The exact interpretation of the uncertainty relation is somewhat messy, as there exists no time operator and the interpretation of time varies among physicists, thus the somewhat vague definition of the uncertainty of the property.

With an increase in pressure, an increase happens in the probability of collisions and consequently of energy redistribution between the gas species. The redistribution of

energy results in a depopulation of a given microstate, thus a decrease in its lifetime. The pressure broadening of a transition in gas molecule A by gas molecule B depends on how efficiently the two units A and B can exchange energy upon collision. In general, heavier broadening-gasses B broaden A more efficiently,[115] perhaps due to more closely spaced energy levels. The most efficient broadener for a gas A will always be another gas molecule A because of perfect state overlap resulting in a high coupling element. This also means that if an inert gas like N_2 is used to broaden eg. MeOH, orders of magnitude more pressure is needed compared to adding more MeOH. Differences in pressure broadening are a problem especially for isolated transitions with narrow natural linewidths. In Figure 8, MeOH monomer is subtracted with a scaled low pressure MeOH monomer reference to reveal the aggregated MeOH clusters. Because of the large rotational constants of MeOH, the rotational profile of the OH-stretching band consists of separated sharp rotational-vibrational transitions, which are very sensitive to pressure broadening. Without considerations for broadening the reference, a sufficient subtraction cannot be done. In Section 4.3, spectra are presented where more appropriate broadening dramatically improves the subtraction of MeOH.

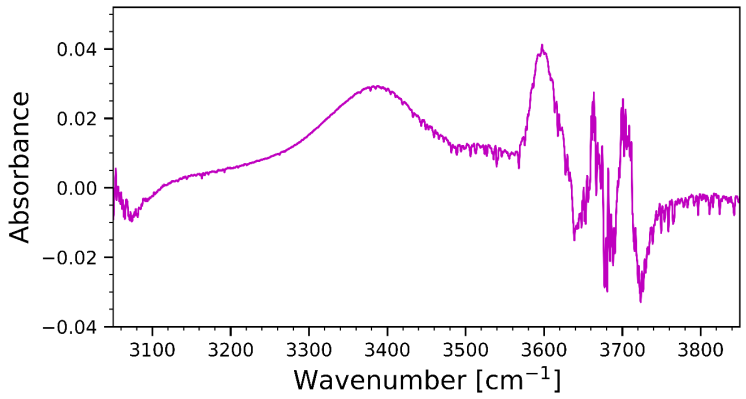

Figure 8: Example of insufficient subtraction due to differences in pressure broadening. A MeOH monomer reference spectrum recorded at 1 Torr pressure is subtracted from a high pressure MeOH spectrum $\sim$ 70 Torr. Large residuals remain for the entire rotational profile due to the large difference in pressure broadening.

3.1.4 *Thermodynamics for Cluster Formation*

A large part of this thesis concerns the formation of hydrogen bound clusters. In the gas phase, when a hydrogen bond donor and acceptor approach each other with correct relative geometry, a hydrogen bond is formed, lowering the enthalpy and entropy of the system. The binding enthalpy is typically between 1-10 kJ/mol for non-charged species, much lower than a covalent bond, which is in the order of hundreds of kJ/mol. The bonding enthalpy for a covalent OH-bond in water at T=0 is, for example, 492 kJ/mol.[116] The low binding energy results in a fast dynamic equilibrium between the monomer and the complex species.

$$\mathrm{XH} + \mathrm{Y} \rightleftharpoons \mathrm{XH{-}Y} \tag{30}$$

Assuming activity coefficients of unity for all species or, in other words, ideal behaviour, we define a unitless gas-phase equilibrium constant of the complex formation for generic species A and B.

$$K_{eq} = \frac{p_{AB} \cdot p^{\ominus}}{p_A \cdot p_B} \tag{31}$$

The reaction Gibbs energy, which determines the thermodynamic driving force and direction of a chemical reaction is defined as

$$\Delta G = \Delta H - T \cdot \Delta S = RT \cdot \ln\left(\frac{Q}{K_{eq}}\right) \tag{32}$$

where Q is the reaction quotient, which is the instantaneous ratio of species activities. When a chemical reaction approaches equilibrium, the reaction Gibbs energy goes to zero, $\Delta G \to 0$, and the reaction quotient goes towards the equilibrium constant, $Q \to K_{eq}$. It is useful to define a constant that allows us to predict the behavior of a chemical system at different starting conditions. Here, we may think of T and Q as the starting conditions and K_{eq} as the constant, which provides prediction power of the system. We can express the reaction Gibbs energy of a system in terms of deviation from the standard state Gibbs energy of formation $\Delta G^{\ominus}$

$$\Delta G = \Delta G^{\ominus} + RT \cdot \ln(Q), \tag{33}$$

where information about the equilibrium constant is contained in the $\Delta G^{\ominus}$ as

$$\Delta G^{\ominus} = \Delta H^{\ominus} - T \cdot \Delta S^{\ominus} = -RT \cdot \ln(K_{eq}) \tag{34}$$

Different approaches can facilitate the determination of $\Delta G^{\ominus}$. The most direct approach is theoretically determining the standard Gibbs energies of the reactant and product units and obtaining the standard Gibbs energy of formation as the difference. For molecular complexes, this approach has difficulties determining the formation standard entropy, $\Delta S^{\ominus}$, accurately, thus compromising the accuracy of $\Delta G^{\ominus}$. This is due to two main issues relating to determining the energy levels in the harmonic oscillator vibrational partition function, which is derived to be

$$Q_{vib} = \exp\left(-\frac{ZPVE}{K_B T}\right) \prod_i \frac{1}{1 - \exp\left(-\frac{\hbar\omega_i}{K_B T}\right)} \tag{35}$$

where $ZPVE = \sum_i \frac{1}{2}\hbar\omega_i$ and ω_i is the angular frequency of a vibrational mode i. The first problem is simply that the determination of the PES is naturally sensitive to the electronic structure method and sufficiently accurate levels of theory quickly become unfeasible for all but the smallest systems. Secondly, in molecular complexes, the vibrational motion of the low frequency LAM modes, to which the partition function is the most sensitive, are often highly anharmonic in normal mode coordinates. The vibration is therefore not well represented in the used coordinates.[117] The theoretical determination of $\Delta G^{\ominus}$ for hydrogen bound complexes is therefore highly erroneous within the rigid-rotor harmonic-oscillator approximation due to the large error on $\Delta S^{\ominus}$. Some work shows promising results on the determination of $\Delta G^{\ominus}$ when treating the LAM modes fully anharmonically,[117] although this requires extensive vibrational modelling and more complicated schemes for counting states.[118]

3.1.5 *Experimental/Theoretical Hybrid Approach*

Experimentally, we can see from Equation 34 that we can determine $\Delta G^{\ominus}$ from determination of K_{eq}. The partial pressures of the monomer and complex species in the gas mix needs to be determined. The main challenge at room temperature is that all but the very strongest bound complexes have a positive standard Gibbs energy of formation $0 < \Delta G^{\ominus} < \sim 20$ kJ/mol.[18] The positive $\Delta G^{\ominus}$ is a consequence of the entropic penalty for transforming three translational and three rotational DoFs into six higher energy vibrational DoFs upon complex formation. This results in relatively minuscule amounts of complex compared to monomers. On the other hand, $\Delta G^{\ominus}$ quickly becomes more favourable for complex formation as T decreases. This is a big motivation for using cold techniques such as supersonic jet expansion and matrix isolation for characterization of weakly bound complexes (*vide infra* Sections 3.2.3 and 3.2.4).

The monomer pressure is usually easily determined from direct reading of a diaphragm pressure gauge attached to the gas-cell. The approximation of $p_{mon} \sim p_{total}$ is accurate to a large degree exactly because of the low equilibrium constants at room temperature. However, to determine the minuscule partial pressures of the complexes in the gas mixture we need some tricks. In Equation 27, we determine the oscillator strength experimentally with all other parameters (pathlength, pressure, temperature and integrated absorbance) known. But, if instead the pressure of the absorber is the unknown, we can determine this quantity provided that we know the oscillator strength, f.[18,19,48,85,89,103,119] I refer to this approach as the experimental/theoretical hybrid approach.

$$p_{complex} = 2.6935 \cdot 10^{-9} \frac{\text{Torr m cm}}{\text{K}} \frac{T}{f_{calc} \cdot l} \int A(\tilde{\nu}) d\tilde{\nu} \tag{36}$$

In Equation 36, the subscript *"calc"* alludes to the fact that we typically have to determine the oscillator strength theoretically. Although we again have to resolve to a partly theoretically determined $\Delta G^{\ominus}$, we obtain a much higher accuracy with this approach. Because K_{eq} has an inverse scaling with f_{calc} through $p_{complex}$ (Equations 31 and 36) the relative error on K_{eq} scales linearly with that of f_{calc}. This is in opposition to the exponential error scaling with $\Delta G^{\ominus}$ directly determined by

calculations. Advanced models like full- and reduced dimensionality local mode models can provide highly accurate descriptions of the bound OH-stretch and the LAM modes to which it is coupled.[82–85,88] Previous studies have shown that a 1D LM of only the bound OH-stretch can to a good extend be empirically corrected for the missing coupling to LAM modes.[84,89,103] Thus, only a minimum of single point energies are needed to determine quite accurate f_{calc}-values. This opens a toolbox for high level electronic structure methods like CCSD(T)-F12a/cc-pVDZ-F12. For larger clusters, DFT methods such as B3LYP-D3/AVTZ also provide reasonable electronic structures, that can likewise be empirically corrected to some degree.[18,89]

FTIR spectra of the molecular complexes are obtained by subtracting a scaled low pressure reference spectrum of the monomers. The low pressure ensures a minimal degree of aggregation. Recording the reference spectrum at an increased pathlength may also be advantageous as the signal-to-noise ratio (S/N) is in general improved with pathlength. In Figure 9, a low pressure reference spectrum of *t*-BuOOH monomer is subtracted in panel A. This quickly reveals the wide band with maximum at 3452 cm^{-1}, which is associated with the antisymmetric OH_b-stretching transition of the *t*-BuOOH dimer (*t*-BuOOH)$_2$. The same impurities are seen as for Figure 7, and here in panels B and C more clearly so, as the dominating *t*-BuOOH species is now removed. In panel D, only the signal from the dimer is left with minimal residuals of the monomer due to an imperfect pressure broadening between the sample and reference spectrum. The dimer has a peak absorbance of only 0.009, less than 1 % of the monomer. By the experimental/theoretical hybrid approach, the dimer pressure is determined to be only 0.0066 Torr compared to the monomer pressure of 3.5 Torr.[103]

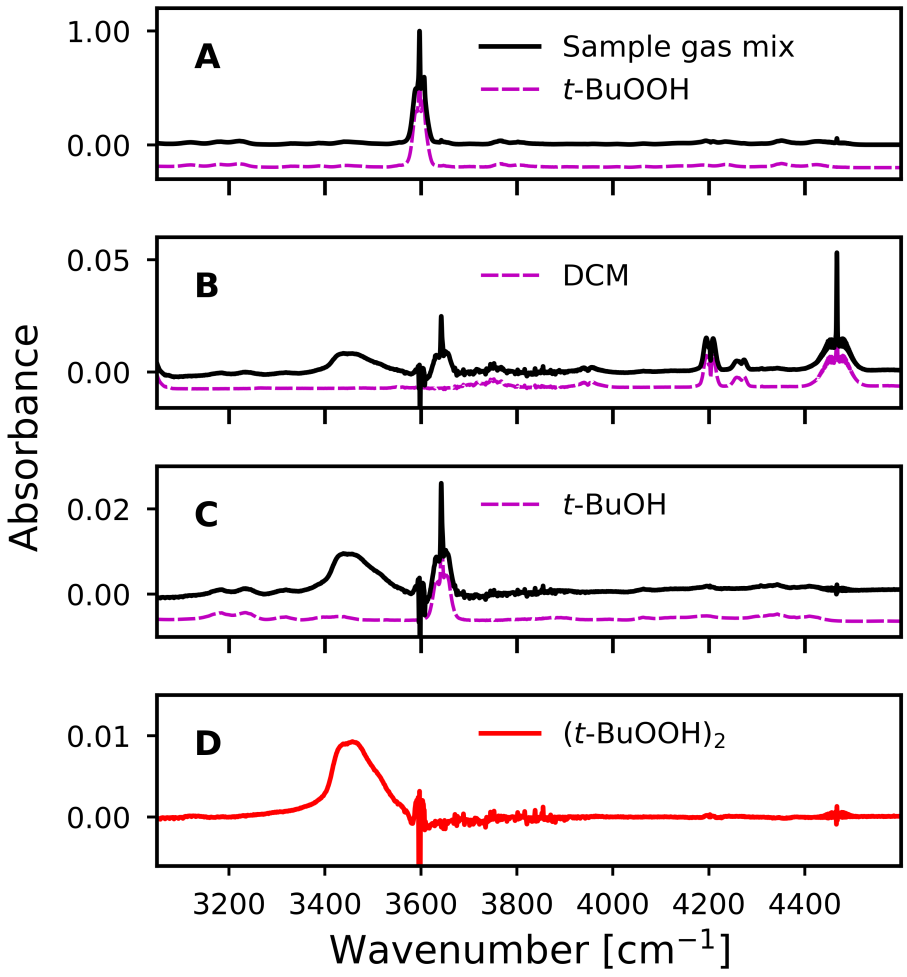

Figure 9: Example of spectral subtraction for $(t\text{-BuOOH})_2$, reprinted with permission from 103.

This approach is extremely well-suited for obtaining spectra of and quantifying hydrogen bound species. Upon hydrogen bonding, the OH-stretching band redshifts, thus separating the monomer signals from the hydrogen bound complex. The band gains intensity due to a change in the DMF and so drastically increases the sensitivity towards the hydrogen bounds species. Combined with a precise spectral subtraction of the monomer signals, these hydrogen bond characteristics are what makes accurate quantification of minute amounts of complex possible despite low formation constants.

3.2 INSTRUMENTATION

3.2.1 *Dispersive Scanning UV-Vis-NIR Spectrometer*

The perhaps most intuitive spectrometer used in this work is the dispersive scanning spectrometer. We use the Perkin Elmer Lambda 1050 NB ultraviolet-visible-near infrared (UV-Vis-NIR) spectrometer with a spectral range of 3030 - 57000 cm^{-1}. The spectrometer consists, in all of its simplicity, of a light source, an optical grating, a slit and a detector. The light source (deuterium or tungsten lamp) produces a spectrum of light, which is then spatially separated by wavelength by the optical grating. The light passes through a slit which, together with the grating, acts as a monochromator of the light. The light passes through the sample compartment where a 15 m multi-pass White cell is seated and afterwards reaches one of 3 detectors. The schematics of the dispersive scanning spectrometer working principles is shown in Figure 10

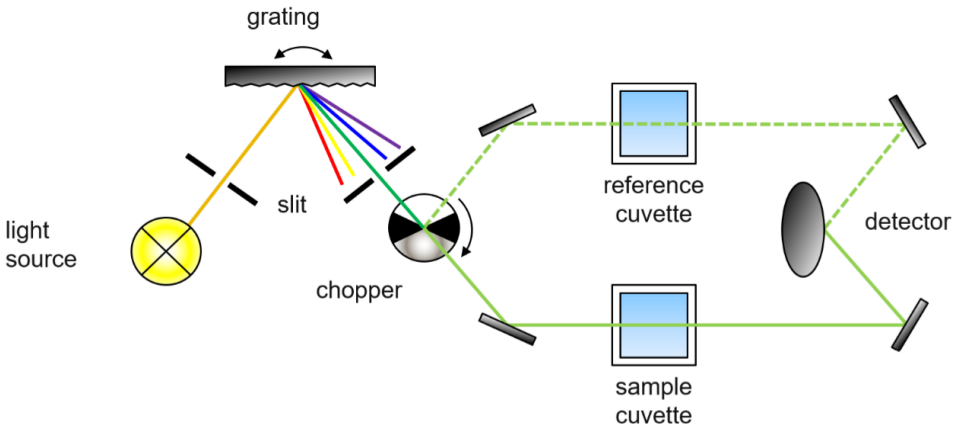

Figure 10: Schematics of dispersive scanning spectrometer. Reprinted with permission by Perkin Elmer.

The more narrow the slit width, the more monochromatic the light. The monochromaticity of the light exciting the slit corresponds to the instrumental resolution of the recorded spectrum. A caveat to the increased resolution is that less light passes through the slit and reaches the detector. This results in a worse S/N. To achieve the same S/N of a slit that is narrowed by half, the integration time would have to be doubled. The spectrum is scanned by step-wise turning the grating, selecting one narrow band of light at a time. Increasing instrumental resolution for a given spectral

range, linearly increases the number of measurement points, which increases the scan time. Building on the previous example of doubling the resolution, this adds up to a factor 4 longer scan time if the S/N is to be maintained with double the resolution. The data interval is set separate from the slit width. A rule of thumb is to choose the data interval smaller than 1/3 the slit width in order to evenly illuminate the spectrum with probe light and not loose spectral information. In Figure 11, a theoretical spectrum is shown, illustrating the difference between intervals that are too large and intervals that are appropriately chosen. The large data interval causes uneven probing of spectral features, whereas the smaller data interval results in an evenly illuminated sample.

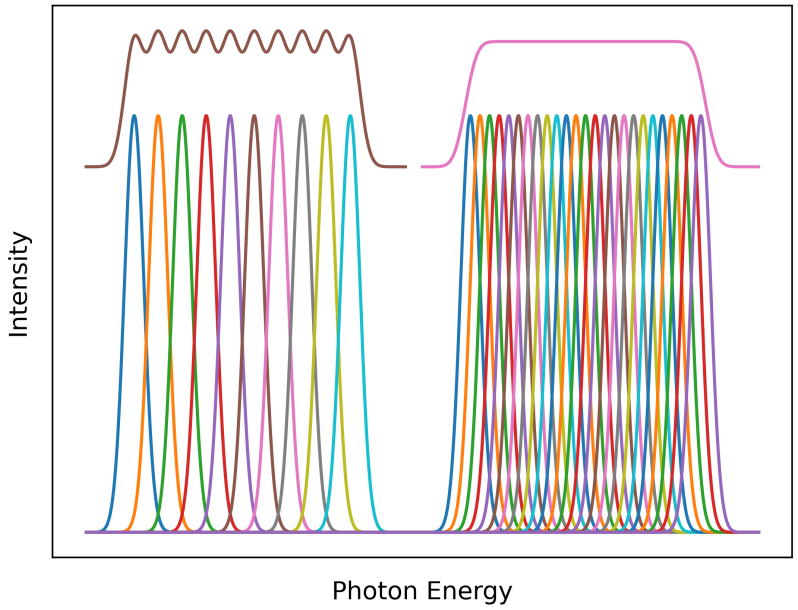

Figure 11: Example of data interval settings on a dispersive instrument. See text for explanation.

A PbS detector covers the region 3030-5550 cm^{-1}, an InGaAs detector the region 5550-11600 cm^{-1} and a PMT detector the region 11600-57000 cm^{-1}. In the region covered by the InGaAs detector the gain of the detector has to be determined in order to obtain linear and reproducible spectra. The detector is only linearly responsive if the detector signal is within a certain interval of intensity pr. time. In Reference 120, a series of test were done on our Lambda1050 NB measuring the electric response function E as a function of slit width and detector gain. The parameters are adjusted such that the entire spectral range of interest has as high an E value as possible while avoided oversaturating (maximum = 100). The response is more or less linearly dependent

on the slit width but more than linearly dependent on the detector gain. The PMT detector automatically adjusts the gain.

The Lambda instrument is operated in the double beam mode. A motor repeatedly switches between the front sample beam and the rear reference beam. The absorbed light of the sample beam is automatically expressed as absorbance with respect to the reference beam intensity. The double beam mode continuously calibrates for fluctuations in the intensity of the light source, minimising noise and drift in the instrument. The rear beam is attenuated by an internal filter with an absorbance of 2. This is close to the amount of light lost by the empty 15 meter multi-pass cell meaning a baseline absorbance close to zero. In the spectral range covered by the InGaAs detector a 0% 100% calibration is performed. This serves to make a baseline correction at each measurement point in the spectrum. This gives the best possible instrumental baseline and provides a good zero for a region, which is used as a bridge between the two other instrumental approaches, FTIR and CRD *(vide infra)*. The 0% 100% calibration makes averaging of multiple cycles impossible and instead a longer integration time is chosen at each point. In the range of the PMT detector the largest drift in baseline comes from scattering from the sample gas and condensation of the sample on the cell optics, which is not corrected for by the 0% 100% calibration. Therefore, for the PMT range, the spectrum is instead recorded without calibration and a baseline is fitted in the data treatment. Spectra are recorded with an increased number of cycles to minimize noise. In Table 1, the selected parameters for the different spectral ranges recorded are listed. Notice that the InGaAs detector is stretched beyond its recommended range to allow for overlap with the PMT detector, ensuring continuity in the spectrum. The transitions recorded in the PMT range are an order of magnitude weaker than those recorded in the InGaAs region. Therefore, more scans are required to maintain a suitable S/N. This substantially increases recording time.

Table 1: Parameters for the Lambda 1050 instrument.

Spectral Range	Detector	Slitwidth	Datainterval	Response time	Gain	Cycles	total time
10470-12270 cm^{-1}	InGaAs	0.6 nm	0.2 nm	5 s	18.5	1	$\sim$ 40 min.
11630-14800 cm^{-1}	PMT	0.6 nm	0.2 nm	3 s	auto	45	$\sim$ 40 h.

For energies where a standard Fourier transform infrared spectrometer (FTIR) instrument can comfortably record spectra ($<$ 11000 cm^{-1}, *vide infra*), a dispersive instrument cannot compete with the spectrum quality and recording speed of a FTIR instrument. At higher energies, the multi quanta excitation of vibrational overtones results in very small oscillator strengths and the 15 meter path length cell and thermal light source do not give a sufficient S/N. Therefore, more advanced techniques are utilized, such as an integrated FTIR-Cavity Ring-down (CRD) setup, to determine absorption features where the optics allow it ($>$ 12500 cm^{-1} *vide infra*). The Lambda 1050 can however provide a bridging of the spectral ranges of the FTIR spectrometer and the CRD setup. Further, the CRD setup is a flow setup, which needs to have several parameters correctly calibrated in order to determine absolute intensities. In spectral ranges covered by the CRD setup, where the Lambda 1050 can still achieve sufficient S/N, the static design of the Lambda 1050 experiment acts as an important check on the more finicky CRD technique. This check is performed on the $\Delta v_{CH} = 5$ transition band of isoprene (See Section 5.2).

3.2.2 *Fourier Transform Infrared (FTIR) Spectrometer*

The undisputed workhorse of the experiments carried out in the first part of this thesis is the FTIR Spectrometer. The spectrometer is based on a 2-beam interferometer, which was developed in the 1880's by Albert Michelson. In the famous 1887 Michelson-Morley experiment, the interferometer was used to disprove the aether theory, which consequentially led to Einstein's theory of special relativity.[121,122] In Figure 12, the schematics are shown of the Vertex 80 series FTIR instrument, which is the primary FTIR instrument used in this thesis. The light of a thermal light source is focused through a pinhole aperture to approximate a point source. The light is collimated and transmitted to a Michelson interferometer before going through the sample compartment and into one of two detectors.

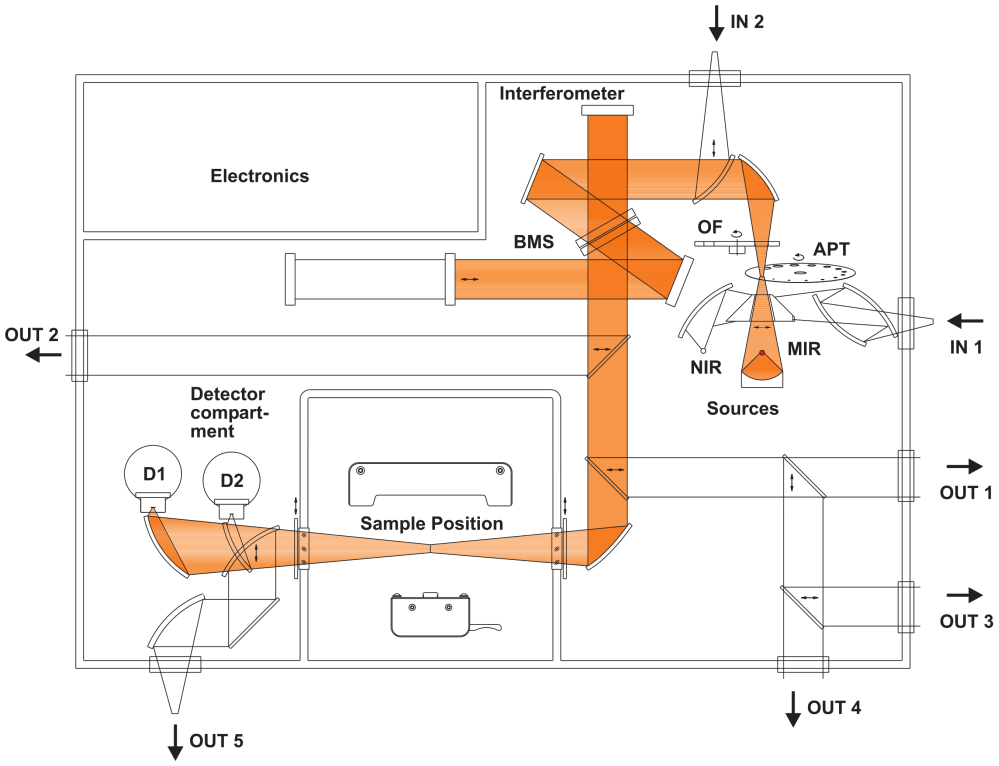

Figure 12: Schematics of Bruker Vertex 80. Reprinted with permission[123]

In the Michelson interferometer, as it is implemented in our FTIR spectrometer, a beamsplitter made of either KBr or CaF_2 splits the collimated thermal light beam equally into two arms towards a stationary mirror and a moving mirror. After a roundtrip the light is recombined at the beamsplitter with half the electric field having travelled L longer in the arm with the moving mirror and thus experiencing a phase-shift corresponding to the product of the time-retardation and the number of periods pr. second (frequency):

$$\Delta\phi = \frac{L}{c} \cdot \nu \cdot 2\pi = L \cdot 2\pi \cdot \tilde{\nu} \tag{37}$$

with ν and $\tilde{\nu}$ being the frequency and wavenumber of the transmitted light, respectively. The phase shift of the light is thus a function of time-retardation and frequency. With a monochromatic light source, the detector would see a signal with intensity $I(L) = \cos(0) + \cos(L \cdot 2\pi \cdot \tilde{\nu})$. The clever design of the interferometer makes it possible to use a polychromatic light source such as a thermal body, which gives light with a continuous intensity distribution as a function of wavelength as governed by Planck's law. The signal $I(L)$ is thus made up of the integral of transmitted

wavelengths, all with different extents of phase shifts. This gives a quite complicated interferogram as exemplified in Figure 13.

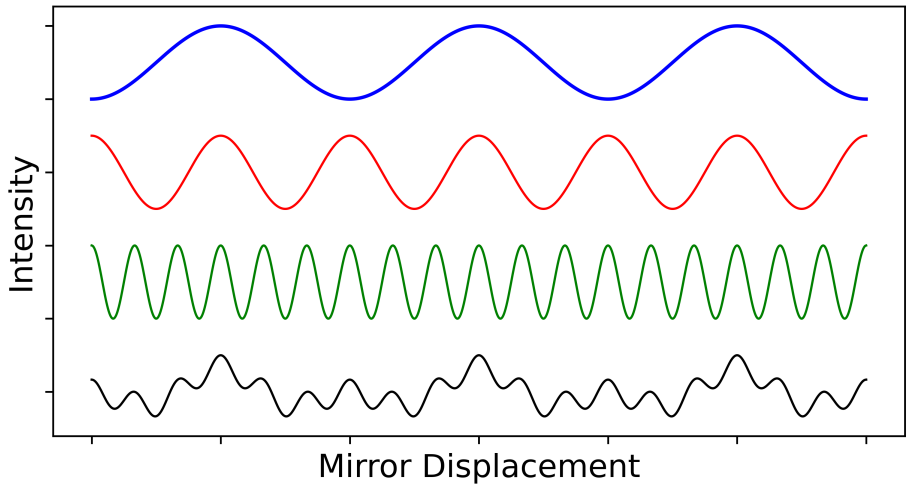

Figure 13: Example of an interferogram. Three different wavelengths of light co-add to give the bottom black trace which is the recorded interferogram.

To determine the components of the light, the signal is transform from a distance domain $I(L)$ into a wavenumber domain $I(\tilde{\nu})$ by applying a Fourier transform.

$$I(\tilde{\nu}) = \frac{1}{L_{max}} \int_{-L_{max}}^{+L_{max}} A(L) \cdot I(L) \cdot e^{i2\pi L \cdot \tilde{\nu}} \, dL \tag{38}$$

The integral should be taken in the interval $[-\infty, \infty]$ but as this is not practical in most laboratory settings, the apodization function $A(L)$ instead ensures that the interferogram goes to 0 in the limits of L. The complex exponential function in Equation 38 can instead be expressed in its real and imaginary parts as

$$e^{i2\pi L \cdot \tilde{\nu}} = \cos(2\pi L \cdot \tilde{\nu}) + i \cdot \sin(2\pi L \cdot \tilde{\nu}) \tag{39}$$

where we realise that the inside of the trigonometric functions are exactly equal to the r.h.s. in Equation 37. We can consider the real part of the expression as a set of basis wavefunctions of wavenumber $\tilde{\nu}$. By taking the product of a basis wavefunction with a certain wavenumber and the interferogram and integrating over L, the Fourier transform gives a coefficient proportional to the amount of transmitted light with that wavenumber. The more the interferogram is in phase with the basis function, the

higher the coefficient. This is done for all wavenumbers and thus a spectrum is created.

Contrary to a conventional dispersive spectrometer (Section 3.2.1), the length of the scanning interval (mirror travel) in a FT-spectrometer does not determine the bandwidth of the spectrum but rather the inverse, or in other words, the resolution of two similar energies. With longer mirror displacement it is possible to differentiate between two waves that have almost the same wavenumber. Mathematically, one can see, that if everything else is identical, two waves with similar wavenumber give almost the same value when evaluating the integral in Equation 38. Two similar but distinct waves $\tilde{\nu}_1 \neq \tilde{\nu}_2$ are separated perfectly when their overlap integral is 0, although a more lenient criteria is often used. When extending L_{max}, the integral will approach 0 as is shown in Equation 40.

$$\lim_{L_{max}\to\infty} \frac{1}{L_{max}} \int_{-L_{max}}^{+L_{max}} \cos(2\pi L \cdot \tilde{\nu_1}) \cdot \cos(2\pi L \cdot \tilde{\nu_2})\ dL = 0 \tag{40}$$

In Figure 14, an example of two waves of nearly the same frequency is shown . It can be seen that the separation of them becomes clear after an increased amount of periods have passed. It is appealing to think based on Equation 37 that higher energy waves with shorter periods would separate faster for a given L. This is, however, more than counteracted by the fact that the number of sampling points pr period decreases with energy, thus making the determination of the phase less precise. And equally important, the collimation of a non-perfect point source becomes a worse approximation with higher energy. One can imagine that for higher energies, the lines in Figure 14 get thicker and more fussy. As a consequence, the spectrometer will warn the user that the resolution is only valid up to a certain energy with a given pinhole aperture.

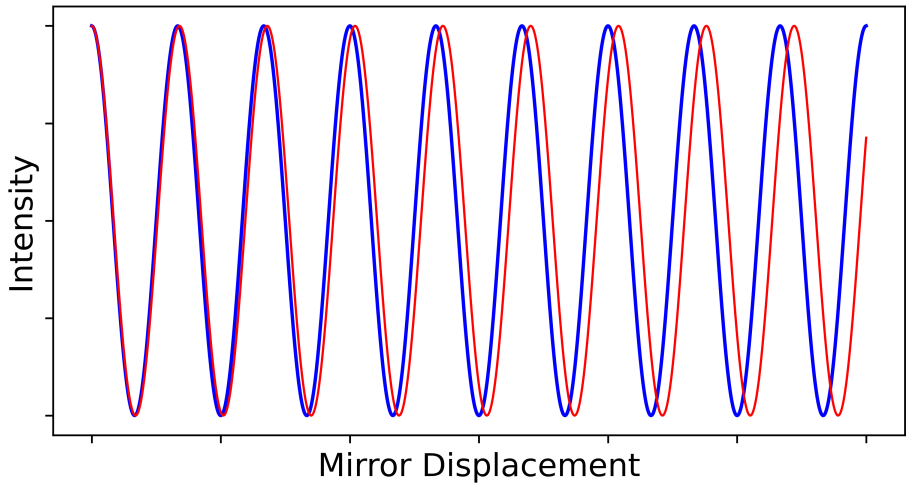

Figure 14: Resolution with mirror displacement L. The frequency difference between the blue and red wave only becomes resolved after a long mirror displacement.

The Fourier transform instruments benefit from very fast spectrum recording speeds and high S/N when compared to conventional dispersive scanning instruments. The exact explanation as to why, the S/N is better for FT instruments is actually somewhat disputed and mathematical arguments are intertwined in a terminology debate[124] (as most of science). One way to think about the S/N advantage is by realising that the FT-instrument does not need a monochromator which severely limits the light that reaches the detector at any time. With same light source intensities and spectral resolution, the signal of the FTIR is thus higher at any measurement point compared to a dispersive instrument.

The perhaps most important spectroscopic advantage of FT-instruments is that the entire bandwidth is recorded simultaneously. This means that instrument drift has a negligible effect on relative intensities, which can be determined to very high accuracy. The biggest limitation of FT-instruments and the reason why they are not commonly used at higher energies such as the UV-Vis range, is that to extend the spectral bandwidth the interferogram sample resolution has to increase. Commonly, the data interval has to be less than half the shortest wavelength. This is known as the Nyquist-Shannon Theorem.[125,126] If the sampling interval is bigger it becomes possible for waves with different wavelengths that are smaller than the data interval to have perfectly identical amplitudes at all sampling points and they can therefore not

be separated. With the smaller data intervals the efficiency of the spectrum recording is negatively impacted. One could say that the advantage of FT-instruments, that the whole spectrum is recorded simultaneously, becomes the disadvantage when only a small range of the spectrum is needed, especially at higher energies.

3.2.3 *Supersonic Jet Expansion*

To obtain spectroscopic measurements of vibrational transitions from the ground state, it is necessary to depopulate the excited low lying rotational and vibrational states, which can be populated at room temperature (~ 200 cm^{-1}). In molecular complexes, especially the low frequency intermolecular modes can be densely populated. In a static gas experiment, heating can be performed by trivial conduction heating. However, cooling to close to $T = 0$ is unfeasible as the vapour pressure quickly approaches 0 at much higher temperatures. Instead, one can take advantage of the cooling in an isentropic adiabatic jet expansion. Here, a gas is expanded from a high pressure reservoir, throttled through a nozzle, and into a low pressure buffer volume with the effect of cooling the gas. The gas is often accelerated through the nozzle to speeds exceeding the local speed of sound making the jet supersonic. The cooling further promotes aggregation making the technique very useful for probing cluster formation.

In an isentropic, adiabatic flow of an ideal gas, the entropy and total energy is constant. We can express the following for the enthalpy:[127,128]

$$H + \frac{1}{2}mv^2 = \text{constant} \tag{41}$$

where H is the enthalpy, m the mass and v the flow velocity of the expanding gas. The high pressure gas is stagnant and often the terms stagnation volume/pressure refer to this part of the setup. As the high pressure gas is stagnant we can set $v = 0$ in Equation 41 and obtain $H_{v=0} = \text{constant}$, which for an ideal gas is equal to the product of the heat capacity and temperature $H_{v=0} = C_p T_{v=0}$. As the total energy is constant we can equate this term to the l.h.s. in Equation 41 and obtain:

$$C_p T + \frac{1}{2}mv^2 = C_p T_{v=0} \tag{42}$$

Equation 42 accounts for the conversion of enthalpy into kinetic energy (velocity) causing the cooling of initially the translational DoFs of the gas. Setting the expansion temperature $T = 0$ gives the maximum expansion velocity in the jet.

$$v_{max} = \sqrt{\frac{2C_p T_{v=0}}{m}} \tag{43}$$

In a supersonic jet expansion the sample or 'seed' gas is diluted, typically ∼0.1% usually in a noble carrier gas. As all noble gasses have the same heat capacity in the ideal gas approximation as they have no internal DoFs ($C_p = C_V + R = \frac{5}{2}R$)[129] it is easy to see from Equation 43 that the heavier noble gasses need to be accelerated to comparably lower velocities to achieve the same cooling. From practical and economic considerations expansions are usually carried out with He or Ne as carrier gasses. The most direct way of controlling the expansion flow velocity and thereby the cooling is by changing the stagnation pressure. The higher the stagnation pressure, the higher the velocity through the nozzle and the colder the expansion. This also means that if a high stagnation pressure is not achievable due to various constrains, one should instead consider using a heavy carrier gas.

The nozzle used for the expansion can be designed in multiple ways with the geometry playing a crucial role on how the molecular beam evolves and cools in the expansion. In the experiments carried out on the *Gratin* jet at the Georg-August-Universität in Göttingen the nozzle consists of a 70 cm long slit with an opening between the blades of 0.2 mm. The slit geometry creates a 1 dimensional expansion perpendicular to the axes of the flow direction and the slit length. In slit nozzles, latteral shockwaves are formed on the edges of the expansion and they converge towards the middle as the supersonic flow is slowed down to subsonic velocities.[127] The shockwaves create large pressure gradients, which perturb the local expansion conditions. By having a long slit the propagation length of the expansion before the lateral shockwaves converge is increased, and a more homogenous pressure is achieved in the region of the expansion, which is probed by the IR beam at around 12.5 ± 2.5 mm from the slit.

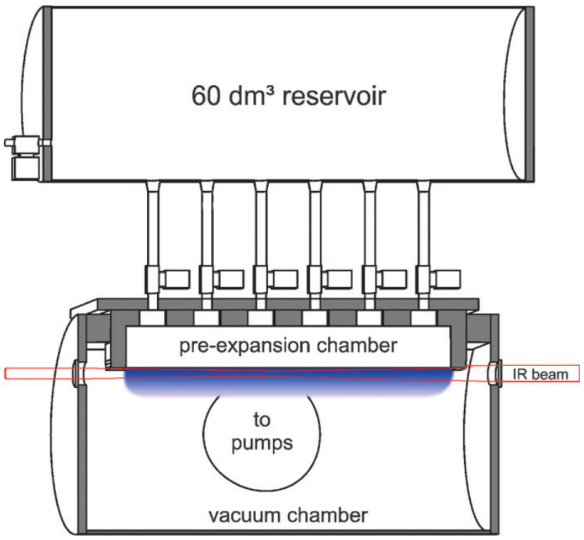

Figure 15: Filet jet expansion schematics. Reprinted with permission from 130.

In Figure 15, the schematics of the expansion in the precurser to the Gratin jet, the *Filet* jet, is shown. Identically between the two jets, the high pressure gas is kept in a reservoir and transferred through an array of 6(7 in Gratin) solenoid valves that open for 133 ms filling a small pre-expansion chamber connected to the wide slit nozzle through which the gas is expanded into the large continuously evacuated vacuum buffer. The 1 dimensional expansion decreases the number density scaling inversely with distance from the nozzle r as opposed to r^2, which is the case for a pinhole nozzle. This increases the possible number of collisions before the IR probing beam, promoting cluster formation and cooling in general.

Thermal relaxation, or cooling, of internal DoFs in the jet is far from an equilibrium process. The cooling of internal DoFs happens by collision energy exchange with other gas species. The energy from the internal DoFs of the seed gas is ultimately transferred into the translational DoFs of the carrier gas. This process requires less than 10^2 collisions for rotational cooling but around $10^2 - 10^4$ collisions for vibrational cooling.[127] The Suhm lab also has a Raman continuous pinhole nozzle jet called the *Curry* jet. In a Raman jet it is possible to accurately determine the vibrational temperature for a particular mode by comparing the Stokes/anti-Stokes transition intensities as the difference only depends on the relative population of the states. The vibrational temperature in the Curry jet has previously been determined to be ca. 100 K[131] which may

be an upper limit on the Gratin jet as more efficient cooling is expected in the slit nozzle.

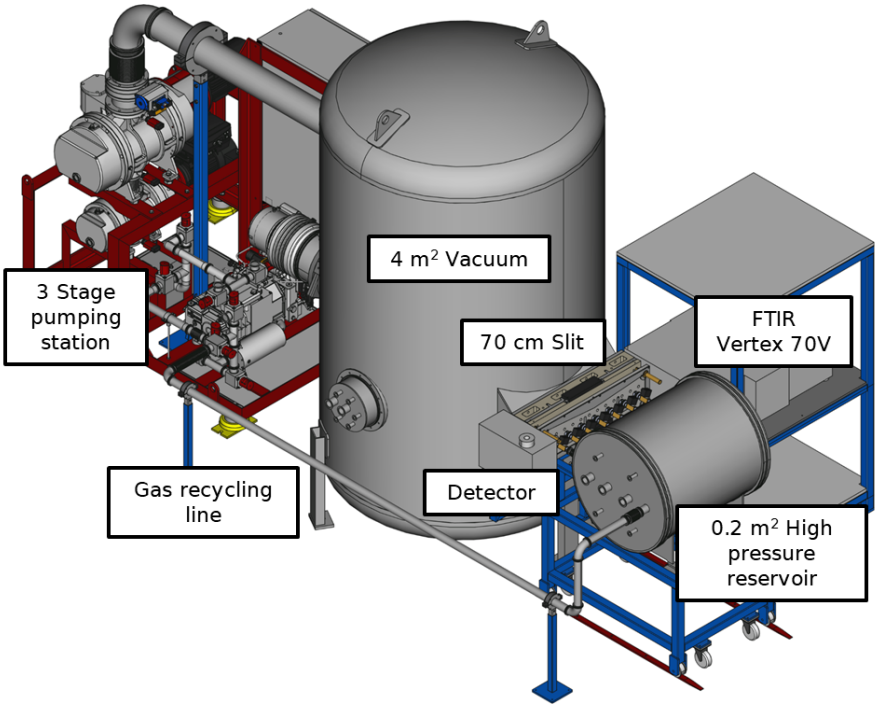

Figure 16: Gratin jet overview. Adapted with permission from 132.

In Figure 16, the overview of the Gratin jet is shown. The expansion similar to that of the Filet jet is probed by a Bruker Vertex 70V spectrometer. The spectrometer is fitted with a Tungsten 20 W external light source at a 3.5 mm aperture and filtered by F20 filters. A CaF_2 beamsplitter is used together with a LN-InSb SW detector scanning double sided in rapid scan mode with 140 kHz and 2 cm^{-1} resolution. The jet is run in a pulsed mode. Compared to a continuous jet expansion, the pulsed setup can expand vastly larger quantities of gas in "macro-pulses" without significantly breaking the vacuum, as long as the time between pulses is used to evacuate the buffer volume.[130,133] The FTIR instrument is synchronized with the solenoid valves with a scan time closely matching the pulse duration of 133 ms, thus getting the maximum advantage of the macro-pulse. The Gratin jet operates in a closed loop system where the expanded gas is re-compressed by two Pfeiffer Okta rotary lobe pumps in series with a Busch Cobra screw pump and is directed to the stagnant volume where-from a new pulse can take place. One pulse uses ca. 10% of the stagnation pressure, or ca. 0.5 moles at 500 Torr stagnation pressure. The re-circulation

is thus an extremely economical solution to the large gas consumption of the experiment.

The supersonic jet expansion coupled with direct absorption spectroscopy whether done with a coherent light spectrometer or FTIR is widely considered as the golden standard for obtaining experimental transition wavenumbers for vibrations. The technique offers limited perturbations from carrier gas effects, condensation, thermal population of states, chromophore-conjugation, ionization etc., which are problematic for many other techniques. It is therefore often the technique to which theory benchmark against when judging their performance of calculating transition energies.[134]

3.2.4 *Matrix isolation*

One of the biggest challenges of a pulsed jet expansion experiment is the low S/N. As the sample is diluted quite extensively in the carrier gas and the number density further decreased by the expansion, the signal is very weak and even with many scans it is not trivial to detect all IR active vibrational transitions. For setups like the Gratin jet, the stability of the compounds measured is also a potential problem as the instrument expands, re-circulates and re-compresses the same sample over and over. To solve these two problems when recording cold spectra one can take advantage of the technique known as matrix isolation.

In matrix isolation spectroscopy a continuous jet expansion through a pinhole nozzle is directed against a CsI window attached to a pumped helium cryostat. Ar, Xe or N_2, which all have reasonably high melting points are often the choice of carrier gas. When the expansion reaches the cold window, usually $\sim$10 K, it freezes, and deposits on the window.

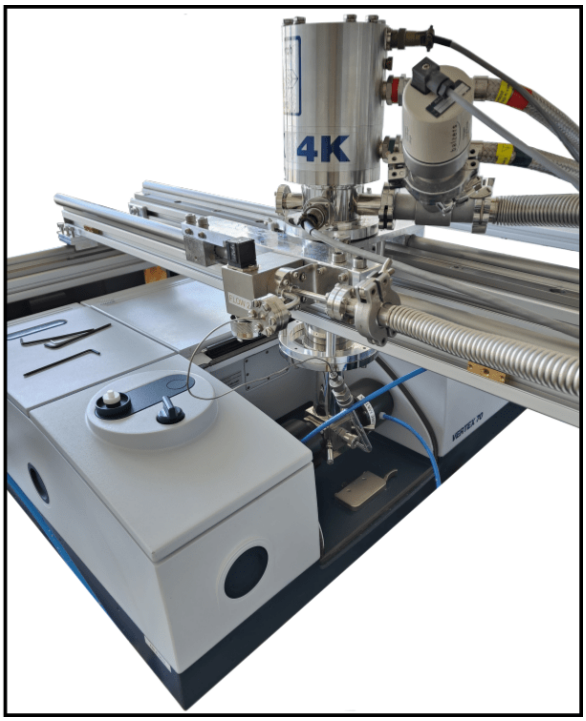

Figure 17: Matrix isolation setup close-up. A CsI window is cooled by a cryostat and kept in a small vacuum chamber and the matrix with seeded sample gas is deposited onto the window. The cryostat and vacuum chamber can be moved in and out of the spectrometer with the rail-system. Purge tubes on either side of the vacuum chamber displaces ambient air with continuous flow of dry N_2.

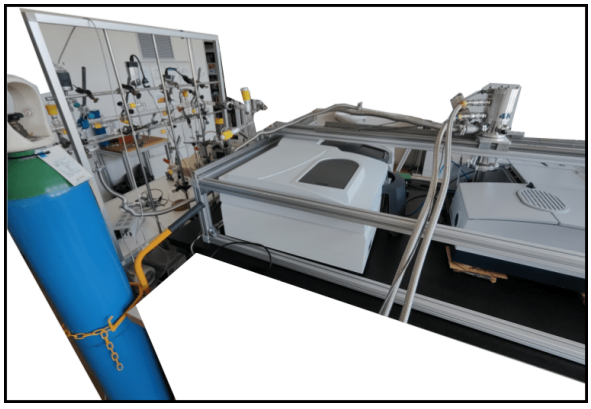

Figure 18: Matrix isolation setup with vacuum line. Cryostat is connected with He-pump-heat exchanger (out of frame). Matrix cell is connected with metal tubing to the vacuum line to the left. Argon matrix gas cylinder is seen in the left corner.

In Figures 17 and 18 an overview of the matrix setup at the University of Copenhagen is shown. The sample is prepared on a J Young glass vacuum line and diluted with Ar gas to a total pressure of $\sim$ 600 Torr corresponding to a ca. 0.1-0.5% concentration. The

vacuum line is connected via Swagelock flexible metal tubing through a needle-valve to the small vacuum chamber where the CsI window sits. The vacuum chamber is continuously evacuated by a turbomolecular pump to a background pressure in the order of 10^{-7} Torr. Deposition of sample should happen at a pace where the vacuum is not broken and the temperature of the window is constant. Too high deposition rates have previously been found to promote formation of large clusters, which might not be desirable in studies of example dimers or other bi-molecular complexes.[135] We choose a deposition rate of roughly 5-10 mmol/h resulting in an increase of the pressure during deposition to around 1-2 $\times 10^{-4}$ Torr. In the current matrix isolation setup at the University of Copenhagen the deposition line is at a 45° angle to the CsI window.

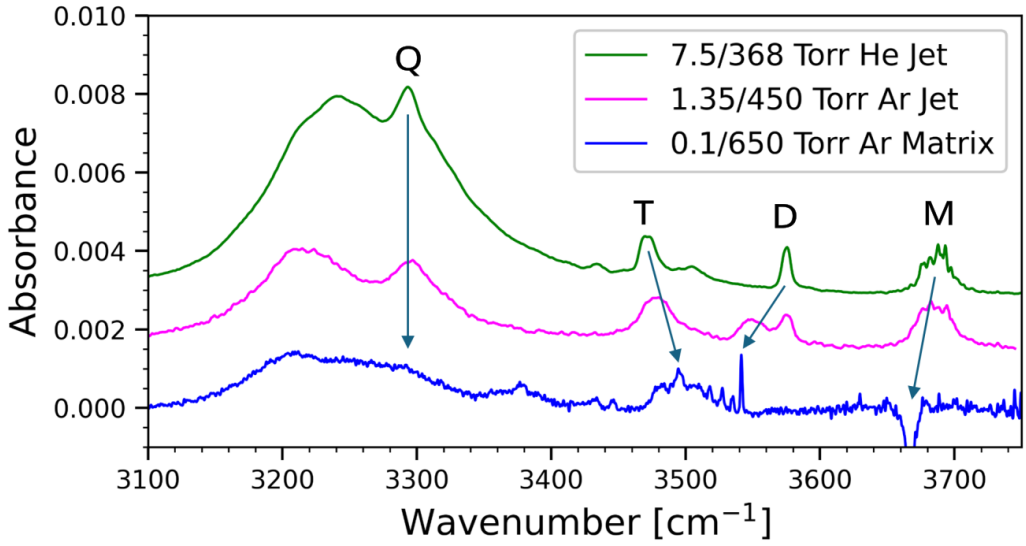

Figure 19: Ar matrix effects compared to supersonic He jet expansion for MeOH. The matrix spectrum is a difference spectrum between initial deposition and after annealing to highlight cluster growth *(vide infra)* This is also the reason why the monomer peak appears as having negative absorbance. Green and magenta traces are He and Ar expansions, respectively, showing the effect of Ar condensation in supersonic jet expansions. The argon jet is scaled $\times 5$ and the traces are shifted from each other for visual purposes.

As the sample/Ar gas mix is deposited on the CsI window the Ar forms a crystal lattice structure. In contrast to the supersonic jet expansion, the carrier gas now quite strongly perturbs the sample as the sample is locked in the carrier gas matrix. In Figure 19, the He supersonic jet expansion spectra of MeOH is shown together with a

corresponding Ar supersonic jet expansion[136] and a Ar matrix spectrum. It is observed that the OH-stretching band from the MeOH monomer and the OH_b-stretching band from the dimer are redshifted by 22 and 34 cm^{-1}, respectively, in the matrix compared to the He supersonic jet. For the trimer a blueshift is observed, which may be due to the more bulky cluster not being efficiently stabilized in the available Ar-matrix sites, but rather 'squeezed' or 'bent' into a matrix site, thereby worsening the hydrogen bonding geometry. Perturbation effects on the tetramer are not clearly observed apart from a diminishing intensity of the band. The diminished intensity may be due to other isomers being more stable in the Ar matrix than the ring-structure, that is observed in the gas-phase. This could also be the source of the signal observed at 3377 cm^{-1}. In the Ar supersonic jet expansion some Ar-atoms condense on the MeOH clusters forming a more amorphous shell around the clusters. The condensation shows a middle point of perturbation between the He jet and the frozen Ar matrix. Ar preferably condenses on the larger clusters. The entire trimer peak therefore appears to be moved from the He expansion to the Ar expansion, signifying that all trimer species are perturbed by Ar condensation. For the dimer, two peaks appear in the Ar matrix showing that only about 50% of the dimer species are perturbed by Ar condensation. No shift in the monomer is observed.

The initial deposition is usually quite inhomogeneous and the sample gets trapped in different matrix sites of varying stability. This causes inconsistencies in the recorded spectrum. In the same way a blacksmith can heat treat their metal to change the lattice structure and obtain different material properties, so can we gently warm the matrix to relax the meta-stable sites into more stable matrix configurations. This is done by raising the temperature of the cryostat to 20-40 K for 10-30 mins before cooling down again to ca. 10 K. This is still below the freezing point of Ar but provides enough flexibility in the matrix for the meta-stable sites to disappear. In Figure 20, the absorbance spectrum of the initial deposition of 0.1:650 Torr MeOH:Ar is shown together with the spectrum recorded after annealing and, in black, the difference spectra. A line of sharp peaks between 3515-3535 cm^{-1} is observed clearly in the initial deposition and after annealing. These are assigned as meta-stable conformers of the MeOH trimer. In the difference spectrum it is observed that these peaks are formed

only very slowly compared to the faster growing signal from a more stable trimer configuration at 3495 cm^{-1}. The annealing time was quite short at 15 minutes. With further annealing the meta-stable sites might disappear all-together.

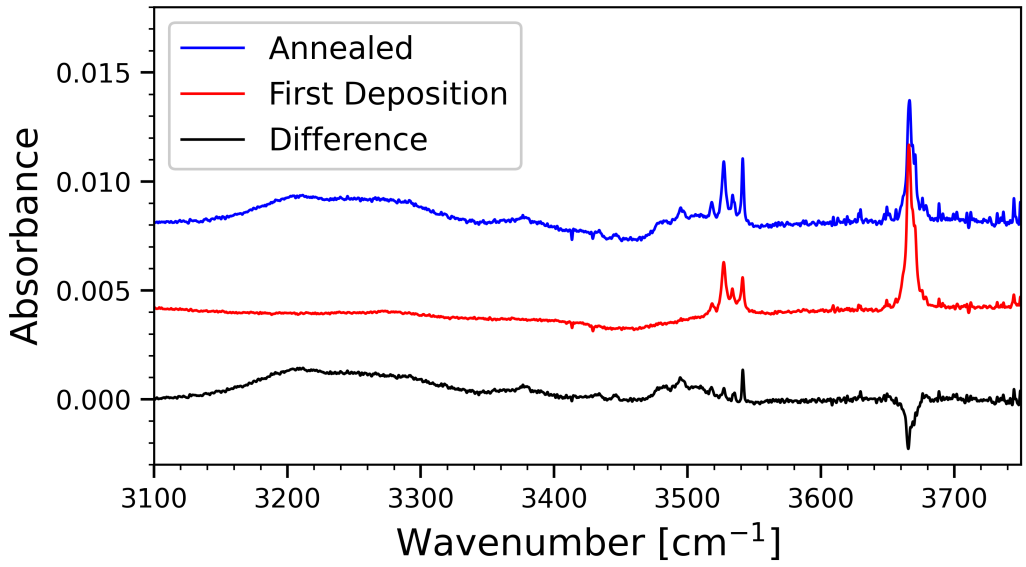

Figure 20: Matrix annealing MeOH. The matrix is annealed at 33 K for 15 min.

When studying molecular clusters the annealing provides another big advantage. The increased mobility within the matrix allows for the solute sample to diffuse and find reaction partners with which they can aggregate. It is thus possible to record absorbance spectra between annealing cycles to identify the peaks that stem from aggregation products. In Figure 20, the black trace shows the difference between annealing and first deposition. The peaks growing are assigned as aggregation products, while the negative peak at 3667 cm^{-1} is assigned as the OH-stretch of the MeOH monomer units which are being consumed in the formation of MeOH clusters.

3.2.5 *Cavity Ring-Down (CRD) Spectroscopy*

A large portion of this PhD has been focused on repairing, rebuilding and improving the coupled FTIR-CRD setup, which was first constructed by Jens Wallberg in 2016 during his master's thesis.[137] The setup consists of many components that each deserves a proper description and so to ease the reading, this section is further sub-divided into small sections. The underlying principles and theoretical background is discussed. The optics setup is shown and a guide for how to best align the cavity with the laser is given. The calibration of the energy axis by an external spectrum analyser is shown and the effective pathlength parameter R_L is determined. Lastly, an overview of the python scripts, which were written to improve the recognition of laser miss-fires and significantly improve the noise level is given.

3.2.5.1 *Theoretical Background*

The oscillator strength of vibrational modes drops by roughly an order of magnitude with every quantum of excitation in that mode.[6] When probing the fundamental XH stretching region of a pure compound, often, sufficient absorbance ~ 1 is achievable with 10-100 cm pathlength given a moderate volatility of the compound. The factor 10 and factor 100 less intense 1st and 2nd overtone transitions can often be compensated for with the use of a folded multi-pass cell, which can easily be designed with a pathlength around 20 meters. The 3rd overtone can become troublesome as optical pathlengths of hundreds of meters are not trivial for most setups. The thermal light sources used in FTIR and dispersive instruments also produces a level of intrinsic noise that starts to compete with the ever weaker signals; and in folded cells, the large losses to mirror absorption limits the intensity of the transmitted light that can reach the detector.

In a CRD experiment, a monochromatic coherent light source is coupled into an optical cavity consisting of two highly reflective mirrors. The light has a small coupling to the outside of the cavity and thus leaks light, which hits a PMT-detector. The intensity of the leaked light is proportional to the light intensity inside the cavity, which has an exponential decay.[138,139]

$$I(t) = I_0 \exp\left(\frac{-t}{\tau}\right) \tag{44}$$

where τ is the natural lifetime or "ringdown time". The mirrors in our setup are plano-concave with a radius of curvature $R = 1$ meter and have measured peak reflectivities $\mathscr{R} = 99.993 - 99.996\%$. The mirrors are separated by 97 cm, which gives a ringdown time of 46 - 80 µs[137] corresponding to an effective pathlength of 14-24 km. It is thus approximately a 3 orders of magnitude increased signal compared to a folded multi-pass cell of 20 meter. The measured ring-down times for the three sets of mirrors used in the isoprene project is presented in Figure 21.

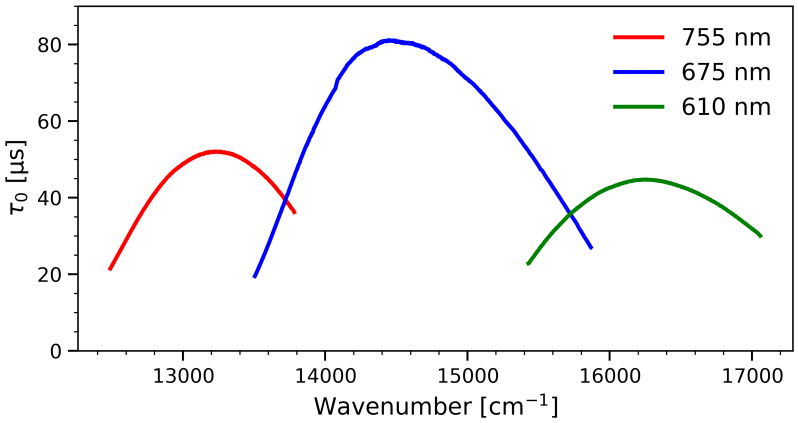

Figure 21: Ring-down time curves for the different sets of high reflective CRD mirrors. The labels denote the mirror center wavelengths. The ring-down times are measured as backgrounds for the isoprene project.

If an absorber is present in the cavity the exponential decay of the light intensity happens more rapidly as light is now lost to the mirrors, to the surroundings and to the absorber. Equation 44 is modified to give

$$I(t) = I_0 \exp\left(\frac{-t}{\tau} - \alpha \cdot c \cdot t\right) \tag{45}$$

where α is the absorption coefficient of an absorber[5] and c the speed of light. The change in the decay is used to express the absorption from a species in the cavity. The absorption coefficient α in units of cm^{-1} is expressed as a function of the natural lifetime of an empty cavity and of a cavity with an absorber.[140]

$$\alpha = \frac{R_L}{c}\left(\frac{1}{\tau} - \frac{1}{\tau_0}\right) \tag{46}$$

where R_L is the effective pathlength of the cavity (*vide infra* Section 3.2.5.4) τ_0 the ringdown lifetime of the empty cavity and τ the ringdown lifetime of the cavity with an absorber. In order to obtain absolute intensities, the absorption coeffient must be converted into a molecular property. A possible choice of molecular property unit is the absorption cross-section which is the absorption coefficient divided by the number density of the absorber, "N". The integrated absorption cross-section is directly related to the oscillator strength by a multiplication factor (Equation 28).

$$\sigma = \frac{\alpha}{N} \tag{47}$$

The number density is determined from an FTIR measurement of a transition with a known oscillator strength. To see how the two are related, the derivation is as follows

$$N = \frac{n}{V} \cdot N_a = \frac{p \cdot N_a}{RT} \tag{48}$$

p is isolated in Equation 36 and inserted into Equation 48

$$N = \frac{c \cdot T \cdot \int A_{FTIR}(\tilde{\nu}) d\tilde{\nu} \cdot N_a}{R \cdot T \cdot f_{FTIR} \cdot l} \tag{49}$$

and the wavenumber dependent σ recorded on the CRD is finally

$$\sigma(\tilde{\nu}) = \frac{\alpha(\tilde{\nu}) \cdot R \cdot f_{FTIR} \cdot l}{c \cdot \int A_{FTIR}(\tilde{\nu}) d\tilde{\nu} \cdot N_a} \tag{50}$$

where $c = 2.6935 \cdot 10^{-9} \frac{\text{Torr m cm}}{\text{K}}$. The oscillator strength of a transition recorded on the FTIR-CRD setup can be determined from a linear fit of measurements at varying absorber concentrations (expressed as integrated FTIR absorbance) following Equation 51

$$\int \alpha(\tilde{\nu}) d\tilde{\nu} = f \cdot \frac{\ln(10)}{f_{FTIR} \cdot l} \cdot \int A_{FTIR}(\tilde{\nu}) d\tilde{\nu} \tag{51}$$

Alternatively, the oscillator strength could be obtained from a direct average of the integrated cross-sections of different measurement following Equation 28. This is, however, not optimal as the direct mean implies that the trend line of a corresponding linear fit intercepts (0,0), which is not necessarily true in experimentally challenging

cases. A non-scaling error will affect the resulting f in this approach, but this is not the case for the linear fit with a free intercept parameter.

3.2.5.2 *Optics, Alignment and Mode Matching*

The schematics of our CRD setup are shown in Figure 22. The design is influenced by that presented by Brown.[140] The laser is a UV-pumped Nd:YAG laser which outputs laser pulses of 1064 nm with a pulse energy of ca. 300 mJ. The laser is frequency tripled to give 355 nm pulses with ca. 1/3 the original pulse energy. The light is then directed into the OPO which down-converts every 355 nm photon into two photons each with half the energy. By scanning the OPO crystal angles, the two photons are tuned in energy to give a photon < 710 nm (Signal beam) and a photon > 710 nm (Idler beam). The OPO provides a large tuning range above and below 710 nm by this approach. The two beams are selected by polarisation gates as the two beams are polarised, off-set by 90 degrees from each other. The OPO outputs pulse energies of ca. < 30 mJ for the signal beam and < 10 mJ for the idler beam.

Following the laser beam path starting from the OPO laser the first component is an iris, which catches scattered light from inside the OPO laser. Next, a polarizer and $\lambda/4$ waveplate works in series to create an optical insulator that restricts back-reflections from the down-stream components back into the OPO. The polariser further filters the laser light such that only the signal or idler beam passes through as these have 90 degrees off-set polarisation. An edgepass filter with cut-on or cut-off at 710 nm further eliminates small amounts of parasitic light from the unwanted signal/idler beam. Two turning mirrors guide the light into the spatial filter consisting of two plano-convex lenses and a tungsten pinhole (*vide infra*). Scattered light from the sides of the pinhole is collected by a telescope connected by a multimode fiber to a High Finesse Laser Spectrum Analyzer UV-I, constantly calibrating the laser photon energy and keeping track of the laser line width. The collimating lens and coupling lens are sat on tilting mounts on XYZ-stages allowing each 5 DoFs. Together with the two turning mirrors in between the two lenses this enables efficient alignment and mode coupling to the cavity. The light exciting the cavity is collected by a PMT detector with a sampling

frequency of 2 MHz.

The sample is introduced by flowing N_2 through a sample holder with a liquid or solid sample. If the sample is a gas, it is throttled through a needle valve before entering a mass flow controller (MFC). The sample gas is then diluted before entering the FTIR with a flow cell installed to continuously measure the number density of the sample. The gas then enters the cavity which is also designed as a flow cell. The cavity mirrors are continuously purged by clean, dry N_2 to avoid condensation on the mirrors.

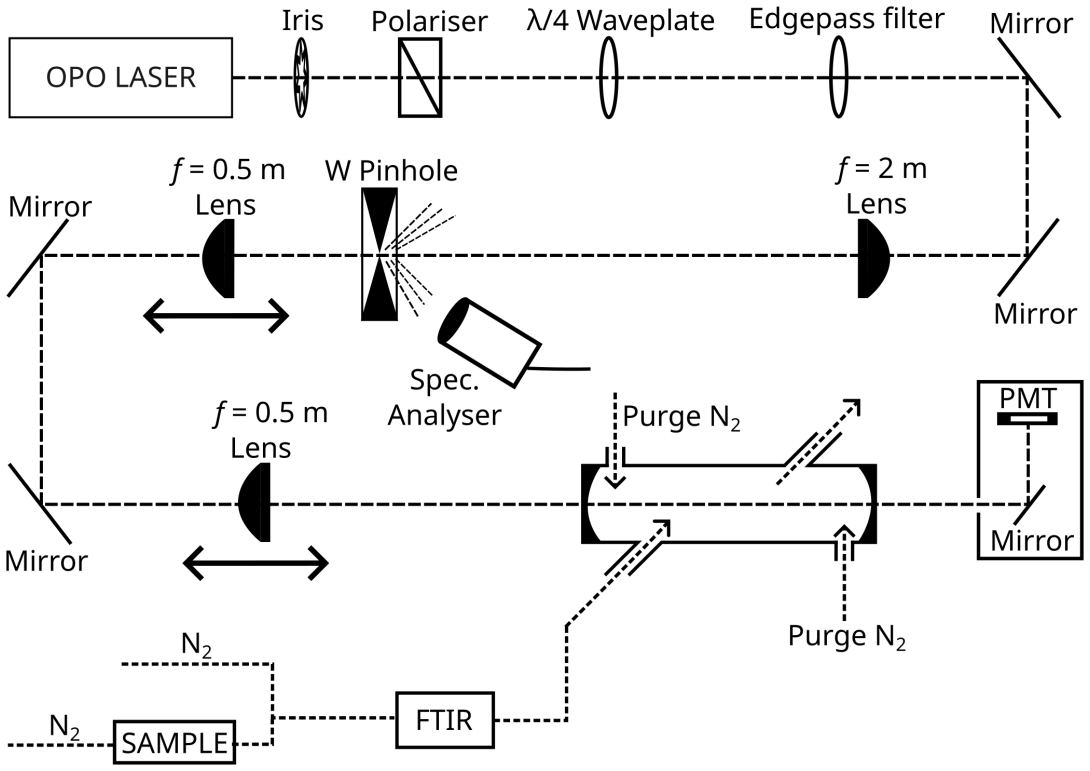

Figure 22: Schematics of cavity ring-down setup

An optical cavity only supports selected spatial modes of light which are determined by the geometry of the cavity. These eigenmodes are the transverse electromagnetic ($TEM_{q,m,n}$) modes. The modes have a longitudinal component q and two transverse components m, n. In order to couple light into the cavity the light has to be shaped to match the geometry of one of these modes. Usually, the modes with no transverse components TEM_{q00}, or just TEM_{00}, are preferred as these modes have the lowest loss rates.[141–143] For a cavity with two identical concave mirrors, like ours, the TEM_{00} modes have a beam waist in the center of the cavity $z = 0$. Cavities can be build in a

multiple of ways and with different combinations of mirrors. Some designs of cavities can even have beam waists outside the cavity.[141] At the beam waist, the wavefront of the beam has a curvature that is infinite. As the beam propagates along the z-axis, the curvature of the beam front evolves as[141,143]

$$R(z) = z\left(1 + \left(\frac{w_0^2}{\lambda z}\right)^2\right) \tag{52}$$

where w_0 is the beam waist radius, defined as $1/e^2$ maximum intensity, in the middle of the cavity ($z = 0$). In order to support the TEM_{00} modes, the beam curvature should match the curvature of the mirrors at the position of the mirrors. From this rule the equation for the beam waist radius at $z = 0$ can be derived and gives

$$w_0 = \sqrt{\frac{\lambda}{2\pi}\sqrt{l(2R-l)}} \tag{53}$$

The beam waist radius is thus wavelength dependent. Since our setup does not have the possibility for ultra precise mode-locking for each wavelength, the optics are adjusted such that the waist fits the center wavelength of the two main sets of cavity mirrors (610 nm and 755 nm). This gives optimal beam waist radii of 311 µm and 345 µm, respectively.

The higher order modes have a shift in frequency associated with them.[144]

$$\Delta\nu = \frac{c}{2l}\left(q + (m+n+1)\frac{2}{\pi}\arctan\left(\frac{l}{\sqrt{l\,(2R-l)}}\right)\right) \tag{54}$$

From this equation it can be seen that the frequency difference between two longitudinal modes is $c/2l$. For our cavity, which is 0.97 meters long, this corresponds to 0.155 GHz or 0.005 cm^{-1}. This is referred to as the free cavity spectral range (FSR). The OPO-laser linewidth (assumed Lorentzian FWHM) is ca. 5 cm^{-1} meaning that at anytime the first 1000 longitutional modes are populated. These cavity modes have a Lorentzian profile with a FWHM, which is determined from the finesse[145] $F = 2\pi\tau c/2l$, which for our cavity is around $F = 60,000$. The FWHM of the cavity modes are then $FWHM = FSR/F = 8.3 \cdot 10^{-8}$ cm^{-1}. Thus, in reality, even though the linewidth of the laser is 5 cm^{-1}, the photon energies supported by the cavity are the cavity modes only which are separated by more than 1000 times their Lorentzian FWHM. This is

analogous to the concept explained in Figure 11 although the defining difference is that the distance between the probing beam peaks (0.005 cm^{-1}) is far less than the spectral features that we are interested in which are 50-100 cm^{-1} wide. Thus, the sample absorption features are probed by 1000s evenly spread out extremely narrow Lorentzian peaks.

In Figure 23, an illustrative example of the cavity modes are shown together with the profiles of a very narrow CW laser and a broader pulsed laser and the absorption profile of a gas-sample. As in our setup, the broad pulsed laser excites many narrow cavity TEM_{00} modes which then probe the absorption profile of the sample. The detected exponential decay is a combination of the many similar decays of the TEM_{00} modes. Alternatively, a very narrow CW laser could be used to excite only one cavity TEM_{q00} mode at the time which would result in a true single exponentiel decay and a much more sensitive experiment. This, however, demands more optics and mode locking of the laser and cavity.

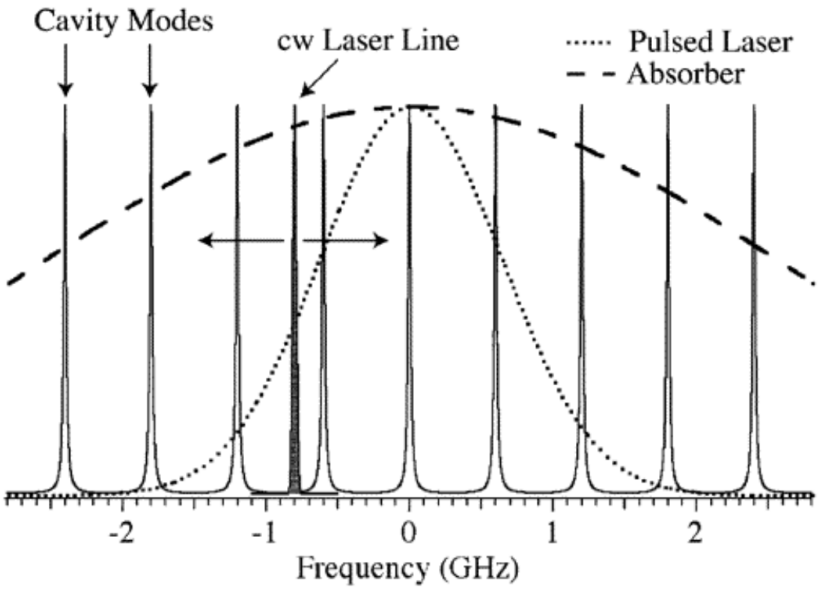

Figure 23: Cavity modes and CW/pulsed lasers. See text for explanation. Reprinted with permission from 140.

The higher order $TEM_{q,m,n}$ modes with excited transverse components m and n have higher loss rates compared to the longitudinal modes. The higher loss rates results in the main exponentiel decay being convoluted with a range of fast exponential decays causing so-called "mode beating". This results in a more uncertain fit of the exponential decay and therefore a more noisy spectrum.[144,146,147] The transverse modes can be

excited if the mode matching is not done correctly and if alignment is not centered on the z-axis of the cavity and/or is tilted compared with the z-axis.[142,143]

In order to achieve efficient mode matching two pieces of optics are implemented: A spacial filter and a coupling lens. The spatial filter consists of a focusing lens, a pinhole and a collimating lens. These are all depicted in Figure 22. The first lens focuses the beam down to close to the diffraction limited spot size directly in front of the pinhole. The part of the light with high angular momentum (high order TEM) cannot be focused to the same small spot. Therefore, a near perfect Gaussian beam exits through the pinhole and is again collimated by a lens. The focusing lens is chosen with a focal length $f = 2$ m for two main reasons. Firstly, the long focusing length means that the tolerance in distances becomes larger, which is more practical for our optical table setup. Secondly, as can be seen in Equation 55, the spotsize is dependent on the focusing length. With a pulse energy of ca. 15 mJ and a pulse length of ca. 5 ns, this turns into a peak power of 3 MW. The power density grows with the inverse square of the spot area and so a focusing lens of 0.5 meter would result in 16 times the power density. At this power density it is not a question of "if" but rather "when" even tungsten cannot withstand the laser anymore. The focused beam spotsize is calculated from Equation 55 assuming a collimated incoming beam.[148]

$$2w_0 = \frac{4M^2 \cdot f \cdot \lambda}{2w_l \cdot \pi} \tag{55}$$

where w_0 is the focused beam spot radius, M^2 is a parameter related to deviations from Gaussian beam propagation, f the focal length of the first lens and w_l the beam radius at the first lens. The second piece of optic used to achieve mode matching is the coupling lens positioned directly before the cavity. By carefully choosing the pinhole size (0.50 mm - 1.00 mm) and the positions of the collimating lens and the coupling lens, the beam focus point position and size can be adjusted to match the TEM_{00} cavity modes. The mode matching is tracked with a Thorlabs Zelux 1.6 MP CMOS camera.

The beam profile that is produced by the OPO laser is sub-optimal for the signal beam and quite horrible for the idler beam. In Figure 24 the beam profile is shown for the signal and idler beam as they come out directly from the laser.

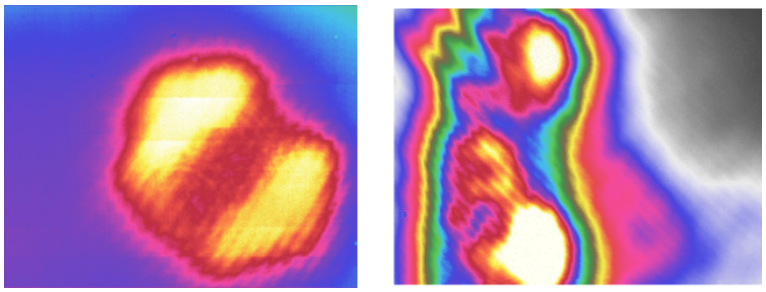

Figure 24: OPO laser profile. Left: Signal beam. Right: Idler beam

Even at the focus point before the pinhole, at first the laser profile could not focus to a single point. It turned out that the OPO crystals had to be adjusted as they were positioned wrongly. In Figure 25 the beam focus point is shown before and after adjusting the OPO crystal and after the pinhole. The spatial filter cleans the beam profile with a power throughput of ca. 20-30% for the signal beam and ca. 10% for the idler beam.

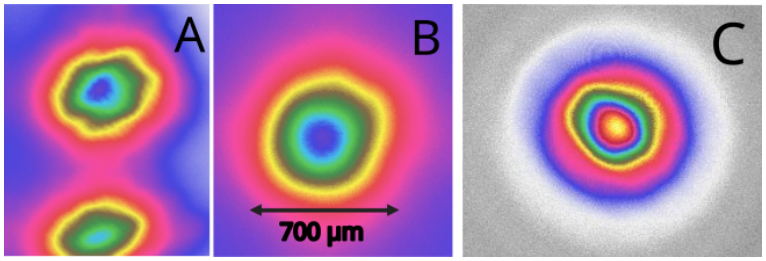

Figure 25: OPO laser profile at focus point before and after pinhole. A: The original signal beam at the focus point. B: Focus point after OPO crystal adjustments. C: Beam after the 500 µm pinhole showing a cleaned up Gaussian beam profile. This profile should be compared to that of the left panel in Figure 24.

3.2.5.3 *Alignment procedure*

The pinhole aperture largely divides the laser alignment into two. The optics before the pinhole are aligned such that the back-reflections from the lens and pinhole coincide and arrive on the backside of the $\lambda/4$ waveplate. After the pinhole, the lenses are removed and the two turning mirrors are adjusted to hit the center of the front and rear of the cavity. This is ensured by installing pinhole apertures in front and behind the cavity. The lenses are then installed. If the lenses are off center, the focusing spot will be shifted as well. They are centered such that light can propagate through the aperture behind the cavity. Finally, their tilt are adjusted such that the back reflection

hits the Tungsten pinhole. If the z-directional positions are not correct for the lenses in order to match the TEM_{00} mode, this needs to be adjusted, and the previous steps may need repeating. Finally, the rough alignment of the cavity mirrors can be done by first installing the rear mirror and adjusting it so the reflection hits the Tungsten pinhole, then installing the front mirror and again adjusting it such that the back reflection hits the tungsten pinhole.

The fine-tuning of the cavity mirrors is done in an iterative procedure, where the CMOS camera is installed behind the cavity and the mirrors are adjusted to best form an output beam that is concentrated and perfectly circular. The camera is then removed and the ringdown time is recorded. The mirrors are then adjusted to maximise the ring-down time. The camera is again installed behind the cavity and the beam profile checked if it is perfectly circular. This is repeated until no further improvements are seen.

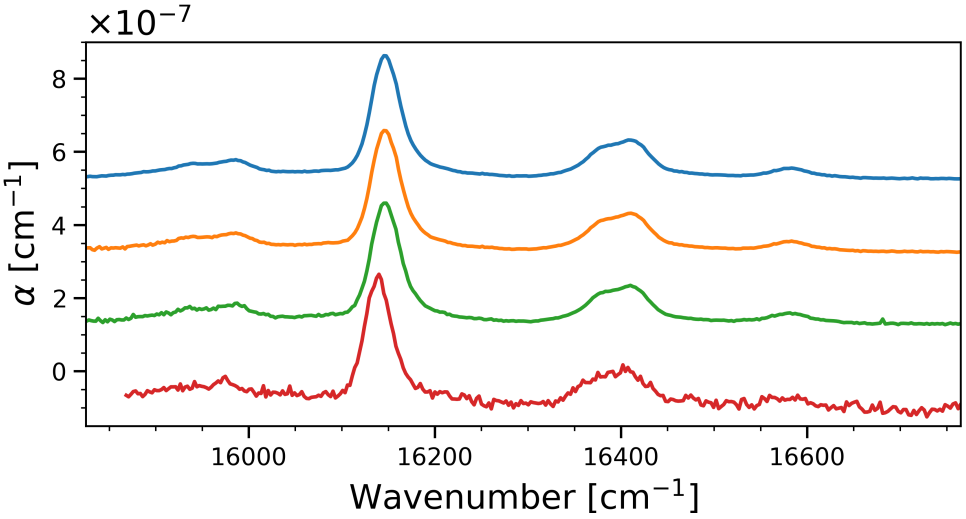

Figure 26: Example of improved S/N by mode-matching. See text for explanation

To highlight the importance of correct mode matching and careful alignment, in Figure 26 the spectrum of the $\Delta v_{OH} = 5$ overtone of *t*-BuOOH recorded by Jens Wallberg is compared to mine. The bottom red trace is Wallberg's spectrum averaged over 400 shots. The green trace, second from the bottom is my spectrum averaged over 360 shots. The data treatment is done with Wallberg's logarithmic fitting algorithm.[137] Already massive improvements are observed. In the orange trace, second from the top,

the same raw data is treated by my own data treatment algorithm.[149] My algorithm recognises bad laser shots discarding them before a direct fit to the exponential decay is done for each shot. The ring-down times are averaged weighted by their individual estimated standard error following Equation 56.

$$C = \frac{\frac{A}{\sigma_A^2} + \frac{B}{\sigma_B^2} + \cdots}{\frac{1}{\sigma_A^2} + \frac{1}{\sigma_B^2} + \cdots} \qquad \sigma_C = \sqrt{\frac{1}{\frac{1}{\sigma_A^2} + \frac{1}{\sigma_B^2} + \cdots}} \tag{56}$$

In the blue top trace, an additional "Chauvenet's Criteria"-filter has been implemented.[149–151] The algorithm calculates the mean and standard deviation of a N large population (or laser shots) and calculates the number of standard deviations needed to account for N-C of the population, where C is the Chauvenet's criteria. Usually C=1/2 is chosen, however I include a more harsh C=5/6. The algorithm throws out data that is classified as outliers and calculates a new mean and standard deviation. This algorithm repeats until convergence or until a maximum of 20% of the data is removed. The algorithm is more robust with larger N. In the *t*-BuOOH spectrum above, minor improvements are seen in the low energy tail of the spectrum when implementing this algorithm.

3.2.5.4 *Calibration of Energy and R_L*

The value of R_L is highly dependent on the flow which in our setup is controlled by four MFCs. Three of the MFCs used operate at less than 10% of their max-flow rate and are therefore likely to be out of calibration in this range after many years of use. The four MFCs are calibrated by a Sensidyne Gilibrator-2 with a 20-6000 SCCM flow tube. The actual flow is found for almost all the MFCs to be ca. 10% too high compared to the reported flow. Calibration functions for the four MFCs are listed below:

1. MFC56: Actual flow $= 1.115 \times$ Read Flow $- 4$ SCCM
2. MFC57: Actual flow $= 1.124 \times$ Read Flow $+ 13$ SCCM
3. MFC58: Actual flow $= 1.103 \times$ Read Flow $- 0.5$ SCCM
4. MFC59: Actual flow $= 1.123 \times$ Read Flow $- 0.4$ SCCM

The efficient pathlength of the cavity, R_L, is then determined. Due to the design of the cavity as a flow cell with purging on the cavity mirrors, the sample gas is not occupying the entire cavity space. To account for this, spectra of a non-condensing gas is recorded with the same number density with a configuration as shown in Figure 22 and one where the sample takes up the entire cavity by dividing the flow equally between the sample inlet and the purge inlets. The number density is validated between the two configurations by the FTIR. Jens Wallberg determined $R_L = 2.78$,[6,152] whereas I determine $R_L = 2.41$ (See Figure 27). The difference might be due to a few different factors. Firstly, R_L may change with the changes made in the overall flow setup as this might change the pressure gradient through the system. Secondly, the sample flow chosen in Wallberg's calibration was only a few percent of the MFC maximum scale. The MFC linearity can perhaps not be strictly trusted in this range. I use double the concentration (propane 10-30 SCCM into total 500-1500 SCCM). The number density was not validated in the FTIR during the Wallberg R_L-calibration. I observed a 12% deviation in number density when going from the standard configuration to going to the full cavity configuration. The difference is most likely due to the non-linear behavior of the propane sample MFC which is operating in the very bottom of the available flow rates. If the same error happened in Wallberg's R_L-calibration without adjustments, then this largely explains the deviation between the two determined R_L-values.

In Figure 27 a few different purging flows were tested to see how R_L changes. The $\alpha'(\tilde{\nu})$ points between 13200 cm^{-1} - 13600 cm^{-1}, where there was sufficient signal, were fitted with a straight line between the cases of a full cavity (α'_2) and the sample flow (α'_1) to give R_L as the slope.[6] With 500 SCCM sample flow and 2×500 SCCM purge flow the R_L was 2.41. with 2×400 SCCM purge flow $R_L = 2.18$ and with 2×300 SCCM purge flow $R_L = 1.97$. The recorded signal increases with smaller R_L. The different flow setups can therefore be used if a sample with low vapour pressure needs to get a signal boost.

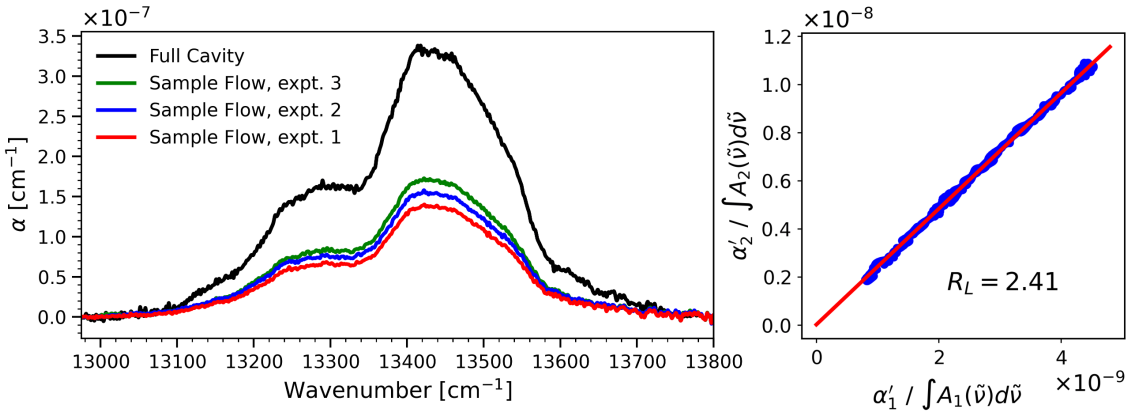

Figure 27: Calibration of R_L at three different purge flows. Left: The absorption coefficient divided by FTIR absorbance is plotted for the same number density and for four different configuration. Black: 1500 SCCM in full cavity. Red: 500 SCCM sample and 2×500 SCCM purge, Blue: 500 SCCM sample and 2×400 SCCM purge. Green: 500 SCCM sample and 2×300 SCCM purge. To the right, the black curve is plotted against the red curve to determine the R_L at the standard configuration used.

The energy axis of the laser was significantly and non-linearly off calibration by the time I took it over. The OPO crystals were at first calibrated using the laser spectrum analyser. This decreased the offset substantially such that the laser was accurate to within ± 4 cm^{-1}. However, the exact photon energy was highly dependent on the temperature in the room. During the warming up period of the laser (ca. two hours) the room temperature would increase by 2-3 K which would results in a drift of 0.2-0.4 nm. Therefore, during each spectrum the photon energy of each laser shot was recorded by the laser spectrum analyser and used as the spectrum energy axis. This means that we achieve complete accuracy of our reported transition energies with a standard error dictated by the linewidth of the laser < 5 cm^{-1}. To experimentally test the calibration a spectrum is recorded of a mixture of H_2O, O_2 and MeOH. The two former has sharp well-documented line-by-line transitions in the Hitran database,[153] and methanol is also a molecule which is experimentally well-studied. The comparison is shown in Figure 28 where a near perfect overlap is shown for both the O_2 and H_2O lines. The transition wavenumbers of MeOH largely match those previously reported, although assignment is a bit tricky in this region for MeOH.[6,154]

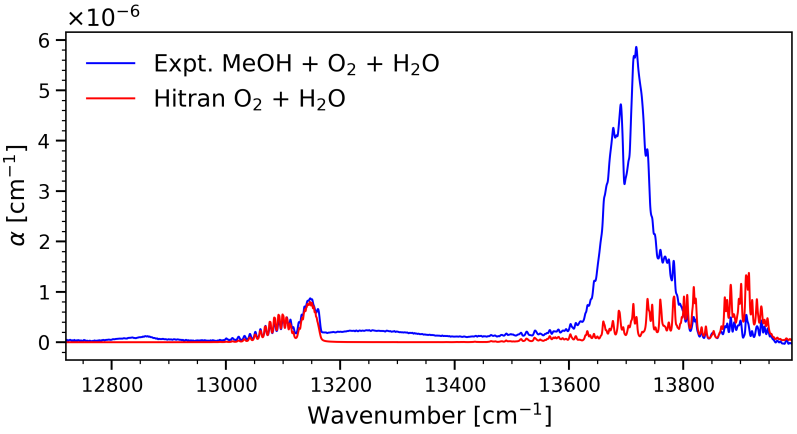

Figure 28: Calibration of energy axis. Spectrum of H_2O, O_2 and MeOH are recorded with the two former compared to the Hitran line-by-line data.

4

RESULTS 1: HYDROGEN BOUND COMPLEXES

In this chapter, the results from the projects concerning hydrogen bound complexes are presented. The projects yielded results, which made it into three separate publications and one manuscript in preparation by the time of writing this thesis. The chapter provides a compilation of the most important results that were published together with some new calculations and experiments, that were done after publication. The projects are presented chronologically. This also means that the experimental protocols and data treatment change for the better in the later projects. In the first paper, for example, the spectral subtraction of *tert*-butyl hydroperoxide monomer, left somewhat large residuals from the monomer due to pressure-broadening effects. The understanding of how to use reduced dimensionality VPT2 calculations came late in the course of this PhD, and is therefore not included in the *tert*-butyl hydroperoxide dimer publication. It is, however, added in this chapter to corroborate the simpler 1D LM calculation that was originally used in the paper.

The methanol dimer paper is a mostly theoretical paper to which I contributed experimental measurements. The project also laid the experimental foundation for the two following projects. Firstly, we understood how to effectively subtract out monomer units from gas phase spectra by counter-acting the pressure-broadening effects. This allowed us to detect and quantify the formation of clusters at room temperature, with an accuracy mostly limited by how precisely we could determine a theoretical oscillator strength. Secondly, we gained an understanding of the effects that temperature have on the OH_b-stretching band, that allowed us to correctly interpret the transition from cold to warm complex spectra. This tied together the spectral assignment in the H_2O·TMA project, where the highly structured OH_b-stretching band of the complex at room

temperature could now be explained from the bands observed at cold conditions. We also present a preliminary temperature calibration curve for the Gratin jet-expansion in Georg-August Universität, Göttingen based on the theoretical model. This may give reasonable estimates for the vibrational temperatures in the jet, which is otherwise near impossible to determine.

I would like to highlight the very reasonable and robust results we obtained by using a reduced dimensionality VPT2 calculation in the methanol cluster project. By reducing the dimensionality based on previous local mode models, we show how to circumvent the problems, which are well-known for VPT2 treatments of especially floppy molecules. GVPT2 is implemented in most quantum chemical softwares and a correct use of a reduced dimensionality scheme may significantly improve the results obtainable by non-experts.

4.1 *tert*-BUTYL HYDROPEROXIDE DIMER

Paper 1 deals with the serendipitous discovery, that *t*-BuOOH forms measurable amounts of dimer at room temperature. $(t\text{-BuOOH})_2$ was detected in the pursuit of determining accurate oscillator strengths for the monomer OH-stretching fundamental and overtone transitions. This is discussed in Section 5.1. The work on OH-stretching oscillator strengths for *t*-BuOOH was started by Jens Wallberg in his PhD-thesis,[152] where the accuracy of the reported oscillator strengths were limited by the solvent (decane or water) and impurities like *t*-BuOH and H_2O, which contributed interfering absorbance bands and partial pressure to the total sample pressure. The purification of the sample was the key to obtain clean enough spectra and accurate sample pressures to allow for the detection and quantification of $(t\text{-BuOOH})_2$.

The H_2O-solvated *t*-BuOOH sample was phase extracted into DCM and dried over $MgSO_4$, removing most of the residual water. The DCM was then evaporated off on a roto-vap at room temperature and at a reduced pressure of ca. 200 Torr. The phase extraction and removal of excess DCM may also have removed most of the *t*-BuOH impurities in the sample as the vapour pressure of the alcohol is about 6-7 times that

of the hydroperoxide. Only small amounts of the corresponding alcohol was observed in the spectra. Lastly, the sample was put in a Produran sample holder and activated 3Å molecular sieves were put in as well, to completely dry the sample.

The purified sample yielded spectra, where upon careful inspection, it was observed that a small region did not scale linearly with pressure. This is exemplified in Figure 29, where a low pressure spectrum is scaled to match the intensity of the monomer OH-stretching band of a spectrum recorded at a higher pressure. The dimer band was not initially expected to be observable at room temperature due to the low monomer pressure. The formation of dimer scales with the monomer pressure squared and divided by a large factor (Equation 31). The dimer would thus only be detectable if the equilibrium constant and the intrinsic intensity of the OH_b-stretching band is of a certain size (Equation 36).

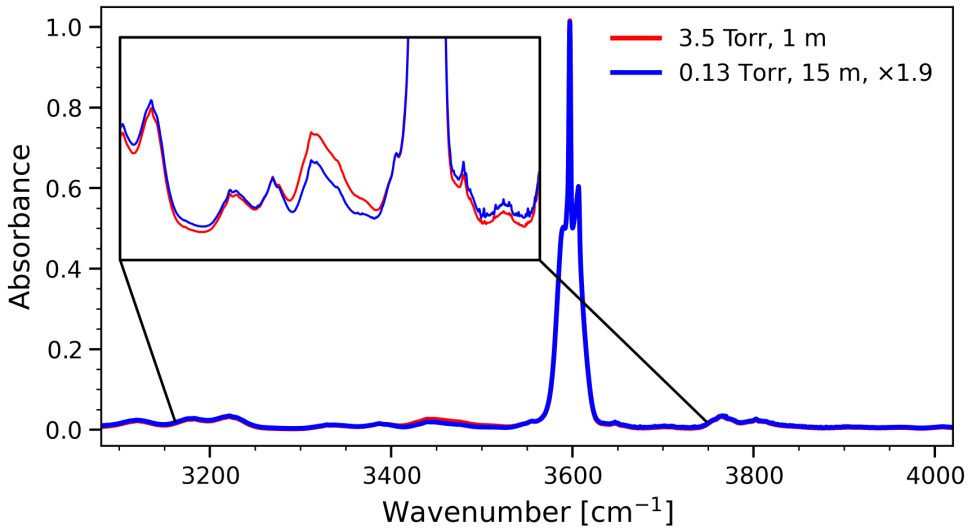

Figure 29: *t*-BuOOH spectra showing non-linear absorbance with pressure variation.

The spectrum of the dimer was obtained by subtracting a low pressure reference spectrum of the *t*-BuOOH monomer along with reference spectra of the solvent used and of the degradation product *t*-BuOH. The process is shown as the example in Section 3.1.5 in Figure 9. In Figure 30, the band associated with the IR-active anti-symmetric OH_b-stretching transition in the dimer is presented at various monomer pressures. The band has a maximum at 3452 cm^{-1}. At 3597 cm^{-1}, residuals remain from the *t*-BuOOH monomer, which is not perfectly subtracted. The monomer reference

spectrum was recorded at a pressure of 0.3 Torr without further pressure broadening. Recording the monomer reference spectrum at slightly higher pressure and pressure broadened with N_2 would probably have increased the quality of the dimer spectra.

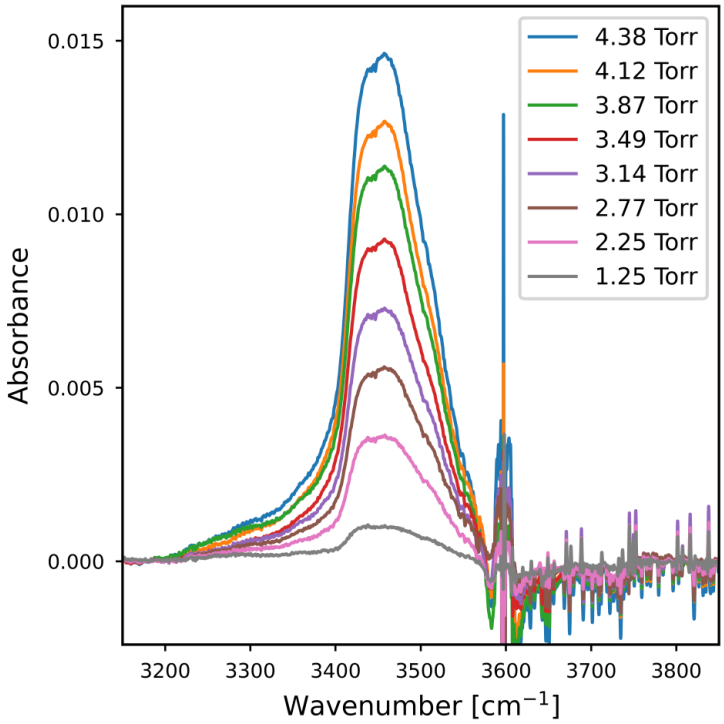

Figure 30: (t-BuOOH)$_2$ spectra at different pressures Reprinted with permission from 103.

The integrated band intensity was converted to a dimer pressure by Equation 36. The oscillator strength was determined from a 1D LM calculation[102,103] using ωB97X-D level of theory[155] and the aug-cc-pVTZ (AVTZ) basis set.[156,157] The two oscillators were assumed to not couple and so the total oscillator strength was taken as

$$f_{calc} = 2 \times f_{1D} \times 0.75 \tag{57}$$

The empirical factor 0.75 is derived from previous studies, where it is shown that the inclusion of the two most important intermolecular modes, "rock" and "twist", decrease the oscillator strength by ca. 20-30%.[83,84] In a later project, a reduced dimensionality VPT2 model (*vide infra* Section 4.2) showed the same trend in MeOH dimer, though to a lesser extent (ca. 15%). The same model is implemented here for (t-BuOOH)$_2$. The results are summarised in Table 2. An important note to the reduced dimensional VPT2 calculation is that the coupling between the two OH$_b$-stretches

is quite large in the normal mode coordinates. This is seen by the obvious missing diagonal anharmonicity, when only using a 1D VPT2 model. The largest reduced cross cubic and cross quartic terms between the two OH-stretches is $\phi_{211} = -1877$ cm^{-1} and $\phi_{2211} = 844$ cm^{-1}, respectively. Although the force constants are large, they are convergent with expansion order, suggesting that the VPT2 equations are valid for the system. In the 10D VPT2 calculation at the ωB97X-D level, one low frequency mode, the anti-symmetric "rock" mode gives a negative VPT2 transition frequency. This is due to several reduced diagonal- and cross- cubic and quartic force constants being much larger than the harmonic wavenumber. The VPT2 series is therefore not convergent.

Table 2: *t*-BuOOH calculated transition wavenumbers and oscillator strengths. The oscillator strengths have been multiplied by factor $\times 10^5$. Value in bold is the one ultimately used for determining dimer pressure. All calculations are performed with the aug-cc-pVTZ basis set.

	Transition wavenumber		Oscillator Strength $\times 10^5$	
	B3LYP-D3	ωB97X-D	B3LYP-D3	ωB97X-D
Harmonic	3538/3499	3640/3609	18.3	15.4
1D VPT2	3643/3384	3758/3515	18.4/0	15.3/0
2D VPT2	3326/3279	3467/3428	20.3	16.8
10D VPT2	3341/3303	3448/3411[a]	17.4	18.5[a]
10D VPT2 adjusted	x	x	11.6[b]	x
1D LM	3283	3413	10.8	9.13
1D LM adjusted[c]	x	x	16.2	**13.7**

[a]Negative wavenumber for LAM mode. Suggests failed/instable VPT2 treatment.

[b]Multiplied by factor $\times 0.664$ found in 89 to adjust for electronic structure and vibrational model.

[c]Adjusted by Equation 57.

The adjusted 1D LM model at ωB97X-D/AVTZ is the one ultimately used for scaling the integrated intensity of the OH_b-stretching band to obtain the dimer partial pressure. The 1D LM model assumes no coupling between the two OH-oscillators. The normal mode calculation shows 32 cm^{-1} and 40 cm^{-1} splitting between the symmetric and

anti-symmetric harmonic oscillators for ωB97X-D and B3LYP-D3, respectively. In a local mode picture, the coupling can be expressed as the harmonic coupling parameter γ':[94,158]

$$\gamma' = -\frac{1}{2}\frac{F_{12}}{\sqrt{F_{11}}\sqrt{F_{22}}}\,\tilde{\omega} \tag{58}$$

where F_{ij} are the second order force constants and $\tilde{\omega}$ is the harmonic transition wavenumber. In a 7×7 2D scan of the local mode coordinates, the PES surface was expanded in a n-1 order 2D power expansion and the force constants were approximated as the 2nd order expansion coefficients. The coupling parameter γ' was determined to be 18 cm^{-1} and 20 cm^{-1} for the two DFT methods used. The difference in energy between the positive and negative combination of the local modes is $2 \times \gamma'$ and corresponds roughly to the splitting of the symmetric and anti-symmetric normal mode stretches.

The 1D local mode calculation does not catch this potential energy coupling. The 10D VPT2 model does include this coupling and also directly include influence of important intermolecular modes. Adjusting by an empirical factor of 0.664 corrects for deficiencies in vibrational model and electronic structure and gives $f_{calc} = 1.16 \times 10^{-4}$. The factor is derived from the methanol dimer[89] but may be applicable in this case as well. The 1D local mode oscillator strength and the 10D VPT2 oscillator strength use very different approximations, but are within 17% of each other. This underlines the relative robustness of the oscillator strength with respect to model and electronic structure used.

The potential energy coupling is further observed experimentally by partly deuterating the dimer, thus decoupling the two OH_b-stretching oscillators. This is done by mixing the H_2O-solvated *t*-BuOOH sample with D_2O before phase extracting it into DCM. The transition associated with the OD_b-stretch is roughly a factor $\sqrt{2}$ lower in energy than that of the OH_b-stretch, minimising the potential energy coupling between the two. In the matrix, the signals associated with the OH_b-stretch are observed to redshift by 17 cm^{-1}, corresponding to the value of γ'. This is shown in Figure 31

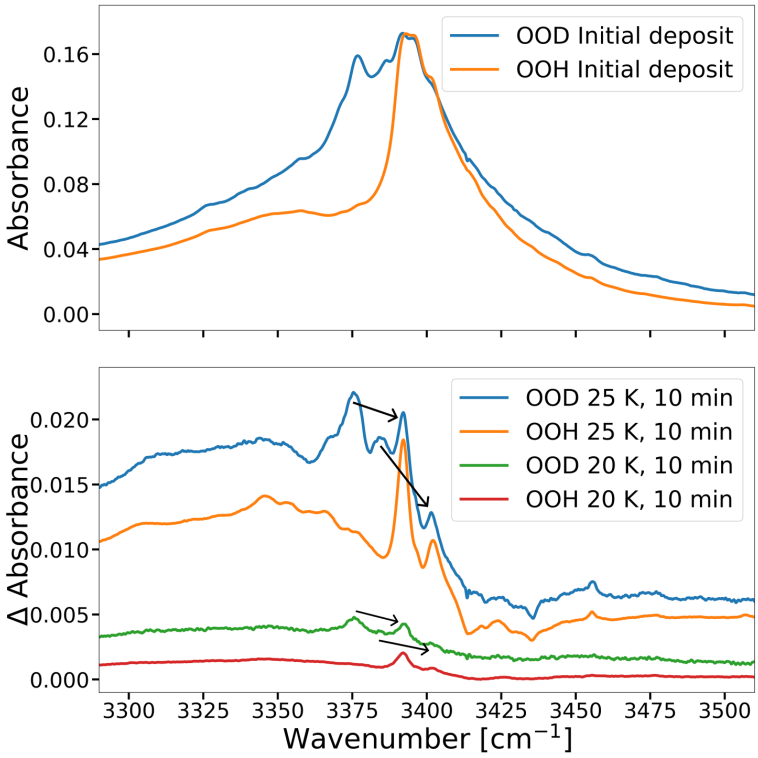

Figure 31: Partly deuterated *t*-BuOOH sample in Ar matrix. In the partly deuterated sample, a mix of non-deuterated and singly-deuterated dimer is present. The singly deuterated peaks are assigned as peaks, which are not present in the non-deuterated sample spectrum. In the bottom frame the difference spectra after annealing are shown. Arrows show the shift of $\sim$ 17 cm^{-1} from *t*-BuOOH·*t*-BuOOD to (*t*-BuOOH)$_2$ Reprinted with permission from 103.

The partial pressures are fitted against the square of the monomer pressures, following Equation 31, to give a linear fit with a slope corresponding to the equilibrium constant K_{eq}. The fit is done in a χ^2-type fit, that include the statistical errors in both integrated area, monomer pressure and temperature. The fit minimises the χ^2 expression in Equation 59,[103] where the sum runs over n=22 measurements.

$$\chi^2 = \sum_{i=1}^{n} \frac{(p^{\ominus} \cdot (p_{dim,i} - p_{dim,fit}))^2}{(p^{\ominus} \cdot \sigma_{p_{dim,i}})^2 + (K_{eq} \cdot \sigma_{(p_{mon,i})^2})^2} \quad p^{\ominus} \cdot p_{dim,fit} = K_{eq} \cdot (p_{mon,i})^2 + b \quad (59)$$

The fit is shown in Figure 32, where the equilibrium constant is determined to be $K_{eq} = 0.41 \pm 0.02$, corresponding to a standard formation Gibbs energy $\Delta G^{\ominus} = 2.2$ kJ/mol (Equation 34). The uncertainty is expressed as 1 σ_{std} and is not including the dominating systematic error introduced by the calculated oscillator strength. In the

paper,[103] the 95% confidence interval on f_{calc} and therefore on K_{eq} was estimated as a factor 2. With the similar results obtained with the new scaled 10D VPT2 calculations a new 95% confidence interval of a factor 1.6 is estimated. This corresponds to a 95% confidence interval for $\Delta G^{\ominus}$ of [1.04, 3.37] kJ/mol.

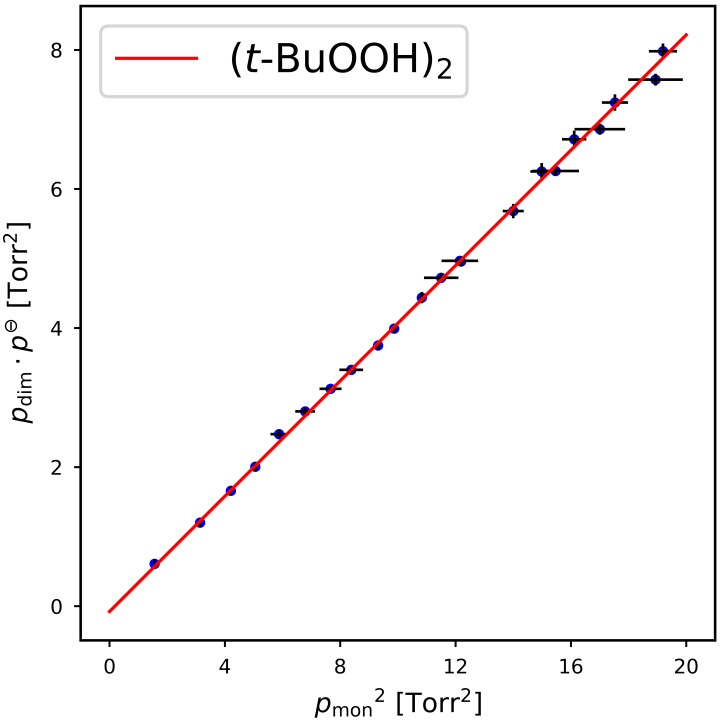

Figure 32: *t*-BuOOH dimer χ^2 fit. Estimated statistical errors in integrated absorbances and monomer pressures are illustrated by error bars corresponding to $\pm\sigma_{std}$. Reprinted with permission from 103.

In Table 3, the formation energy contributions are calculated at various levels of DFT. The functionals B3LYP-D3, M06-2X-D3 and PBE0-D3 perform quite well and give $\Delta G^{\ominus}$ within 0.4 kJ/mol of the experimental value. These functionals should be considered in future studies of similar systems. The importance of including dispersion is clearly seen for the B3LYP functional, where the dispersion correction makes up ca. 40% of ΔE.

Table 3: Calculated thermodynamic values at 298 K for (t-BuOOH)$_2$. All DFT calculations[155–157,159–165] are done with the aug-cc-pVTZ basis set. The CCSD(T)-F12a single point energy calculation[166–170] is done with the cc-pVDZ-F12 basis set. Adapted with permission from 103.

Method	ΔE	ΔE + ZPVE	$\Delta H^{\ominus}$	$\Delta S^{\ominus} \cdot 298$ K	$\Delta G^{\ominus}$
B3LYP-D3	-52.0	-43.9	-44.0	-45.8	1.83
B3LYP	-32.2	-25.3	-24.9	-42.7	17.8
ωB97X-D	-49.7	-41.6	-41.7	-46.5	4.74
M06-2X-D3	-50.4	-42.9	-43.1	-45.3	2.25
PBE0-D3	-50.6	-43.1	-43.0	-45.4	2.37
CAM-B3LYP-D3	-54.8	-46.6	-46.8	-45.4	-1.33
CCSD(T)-F12a //ωB97X-D/AVTZ	-49.5	-	-	-	-
Expt., this work					2.2

(t-BuOOH)$_2$ has a stabilization of 2.2 kJ/mol more than that found for the heteromolecular complex with dimethylether (t-BuOOH·DME) of 4.4 kJ/mol.[67] This modest increase in stabilization was at first surprising as the additional hydrogen bond was expected to add a large bond-enthalpy contribution with only a small additional entropy change as is the case for acid dimers, where equilibrium constants can range up towards $K_{eq} \sim 30 - 2000$.[171–174] Various effects contribute to this difference between the acid dimers and the hydroperoxide dimers. Firstly, the 6-membered ring in the hydroperoxide dimer does not allow for optimal H-bonding angles of 180°. Instead, the theoretically determined H-bond angles of 154° weakens the individual H-bonds. The comparably larger redshift of the t-BuOOH·DME complex, $\Delta\tilde{\nu} = 170$ cm^{-1} vs. $\Delta\tilde{\nu} = 145(162)$ cm^{-1}, further corroborates this analysis. The parenthesis denotes the transition wavenumber of the decoupled OH-stretch. Secondly, the H-bonding in the acid dimer is stabilized by a resonance in the 8-membered ring. Double proton transfer yields the same structure, thus delocalizing the charges efficiently in the whole ring. This cooperative effect[175–178] increases the strength of the already strong hydrogen bonds. In Figure 33, the NCI interactions of (t-BuOOH)$_2$ is compared to that of t-BuOOH·DME. To the left, the $s(\mathbf{r}) = 0.5$ au. isosurface is plotted for the dimer,

showing the hydrogen bond as dark blue disks and the secondary interactions as green surfaces. To the right, the $s(\mathbf{r})$ is plotted against the $\text{sign}(\lambda_2)\rho$ for the dimer and the hetero complex. The electron densities at the hydrogen bonds are $\rho = 0.0265$ au. and $\rho = 0.0313$ for $(t\text{-BuOOH})_2$ and (t-BuOOH·DME), respectively, suggesting weaker bonds in the dimer.

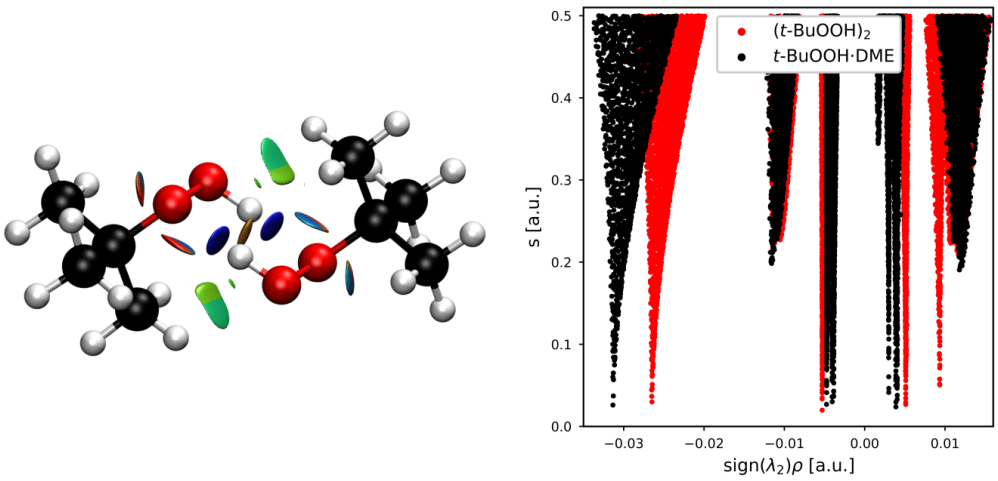

Figure 33: t-BuOOH dimer NCI plot. Reprinted with permission from 103.

In conclusion, the *tert*-butyl hydroperoxide dimer was detected and quantified at room temperature. The ratio of the integrated absorbance of the OH_b-stretching band and an oscillator strength of an empirically scaled 1D LM model gave reliable dimer partial pressures at various measured monomer pressures. The equilibrium constant was determined to be $K_{eq} = 0.41$ corresponding to a standard formation Gibbs energy of $\Delta G^{\ominus} = 2.2$ kJ/mol. The dimer forms a doubly H-bound ring-structure, which weakens the individual hydrogen bonds. The attenuation of the observed redshift, which was only 145 cm^{-1}, was found to be partly due to the weakened H-bonds and partly due to the splitting of the states associated with the symmetric/anti-symmetric OH_b-stretching modes, where only the high energy anti-symmetric mode is IR-active. Partly deuterating the sample gave an experimental γ'-value of 17 cm^{-1}, close to that of LM and NM calculations.

4.2 TEMPERATURE EFFECTS IN METHANOL DIMER

In paper 2, a new vibrational model was constructed by Emil Vogt to give a physical interpretation of the two main observed temperature effects on the OH_b-stretching band in hydrogen bound complexes. These are the blueshift of the band maximum, and the widening of the band. Methanol dimer is chosen as a model system as it is the smallest system that contains an appropriate amount of complexity, which can be generalised to other systems. A smaller and more important system, the water dimer, could seem like a more obvious choice. This system is, though, far more complicated both experimentally and theoretically partly due to the exceptionally large rotational constants and the strong rotational-vibrational coupling and coupling between the intermolecular vibrational modes.[87]

The vibrational model relies on a local mode description of the two OH-stretches and a normal mode harmonic-oscillator description of the eight lowest frequency LAM modes. These are the six intermolecular modes describing the relative motion between each methanol unit and the methyl torsion on each methanol unit. The LAM modes are highly deviant from a harmonic potential in the standard normal mode description (See Figure 2). This is mainly due to the intramolecular deformation that occurs in the MeOH units when displacing along the intermolecular modes in a rectilinear coordinate definition. To solve this problem, the intermolecular modes are partitioned into small displacements with a realignment of the individual MeOH units at each step. This gives more physically representative potentials of the intermolecular motion. The realignment algorithm is shown in Figure 34. After the new LAM mode coordinates are defined, the energy levels are calculated as a sum of energies obtained variationally from a 2D Schrödinger equation including the OH_b-stretch and each one of the LAM modes.

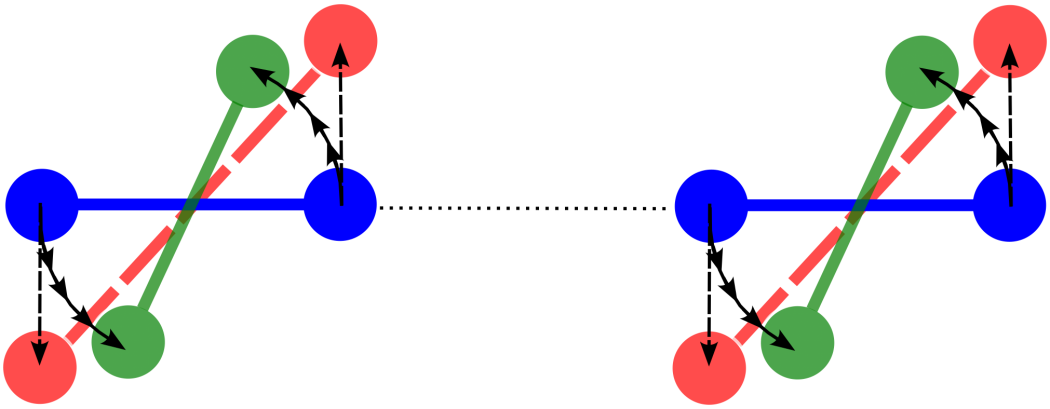

Figure 34: Adjusted normal mode coordinates for $(MeOH)_2$ The red figure shows a rectilinear displacement while the green shows many rectilinear displacements with sequential realignment of the MeOH units, approximating curvilinear motion. Reprinted with permission from 86.

It is well-understood that the intermolecular modes affect the hydrogen bonding transition frequency due to their motion displacing the molecules away from the optimal hydrogen bonding geometry.[18,82–85,87,88] What is perhaps more surprising is the effect that the OH_b-stretch has on the intermolecular modes. Excitation in the OH_b-stretching mode raises the transition energy of the intermolecular modes. This can be explained as follows:

- The intermolecular modes weaken the hydrogen bond, thus the motion is working "against" the hydrogen bond.
- The stronger the hydrogen bond, the more energy the intermolecular motion requires.
- When the OH_b-stretch is excited, the expectation value of the hydrogen bond length, $OH\cdots X$, decreases due to the asymmetric potential (See Figures 1 and 4).
- The H-bond length is related to the strength of the H-bond. The strength increases with a decrease in H-bond length.
- The states associated with the intermolecular modes increase in energy with the number of OH_b-stretching quanta.

If the OH_b-stretch is adiabatically separated from the intermolecular modes, one can imagine the intermolecular modes living on two OH_b-PESs with slightly different energies.

In Figure 35, the transition wavenumber for the eight LAM modes are shown in the $v_{OH} = 0$ and $v_{OH} = 1$ manifolds together with the relative change marked in red.

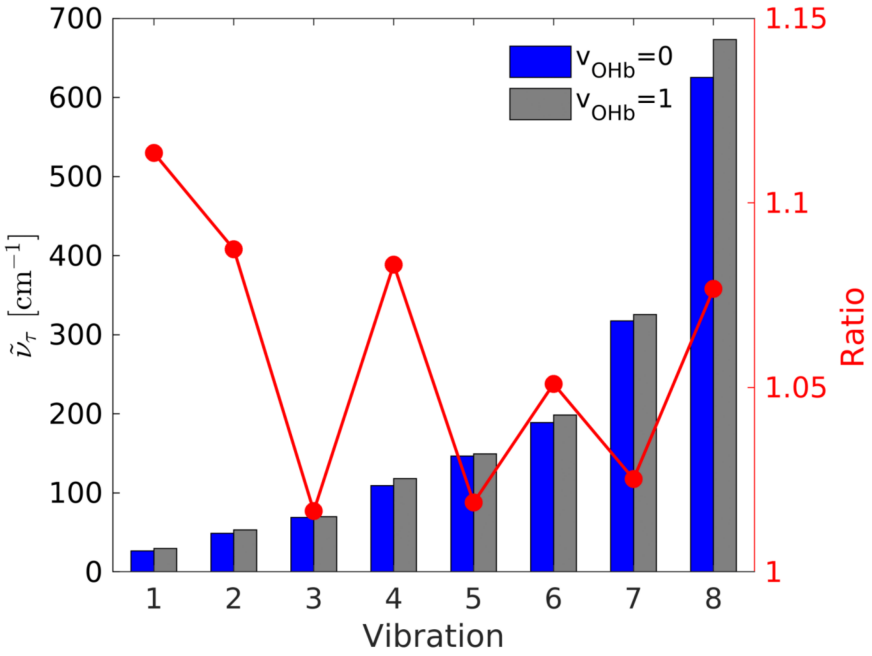

Figure 35: $(MeOH)_2$ LAM modes wavenumber change with OH_b-stretching quanta. See text for explanation. Adapted with permission from 86.

Because the modes are so low in energy, at room temperature (~ 200 cm^{-1}), transitions occur from states associated with many combinations of highly excited LAM modes. The many possible combinations of excitation in the eight LAM modes results in the final states being blueshifted by various amounts in the $v_{OH} = 1$ manifold. This is show in Figure 36. At cold conditions, a 'pure' OH_b-transition will happen from the ground state to the $v'th$ excited state. This is shown as the black lines in Figure 36.

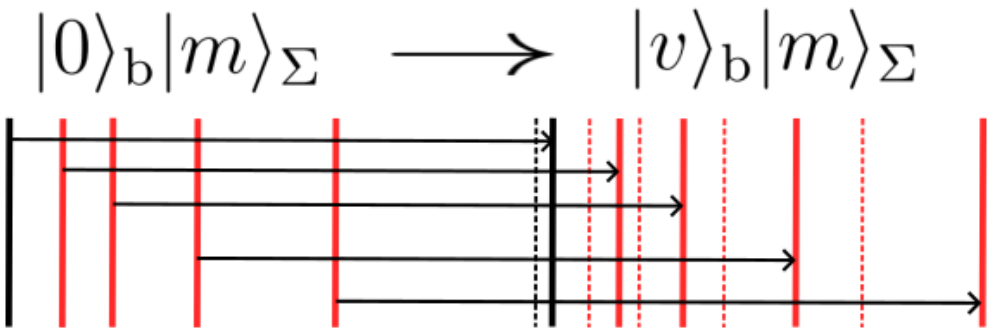

Figure 36: OH_b-stretching transitions in thermally excited $(MeOH)_2$. See text for explanation.

With thermal excitation (red lines) transitions occur from populated excited states associated with the LAM modes. These states are blueshifted in the excited OH_b-stretch states resulting in an increased transition energy. The dashed lines show where the states would be, if the OH_b stretch did not couple to them. At 10 K, no more than 5 transitions are needed to account for the band experimentally observed. At 300 K, more than 10^7 vibrational transitions, each with their own rotational convolution results in the blueshifted wide band observed at 300 K. In Figure 37, the spectrum of $(MeOH)_2$ is recorded at jet-cooled conditions and at room temperature, and the bands are compared to the simulated bands at 10 K and 300 K. The resemblance is striking considering that the simulation is a non-scaled *ab initio* model. To corroborate the model, the dimer spectra of two deuterated isotopologues of methanol were also recorded at room temperature, CH_3OD and CD_3OD. The model correctly captures the very delicate differences in peak positions and full widths at half max (FWHM) between the three isotopologues.[86]

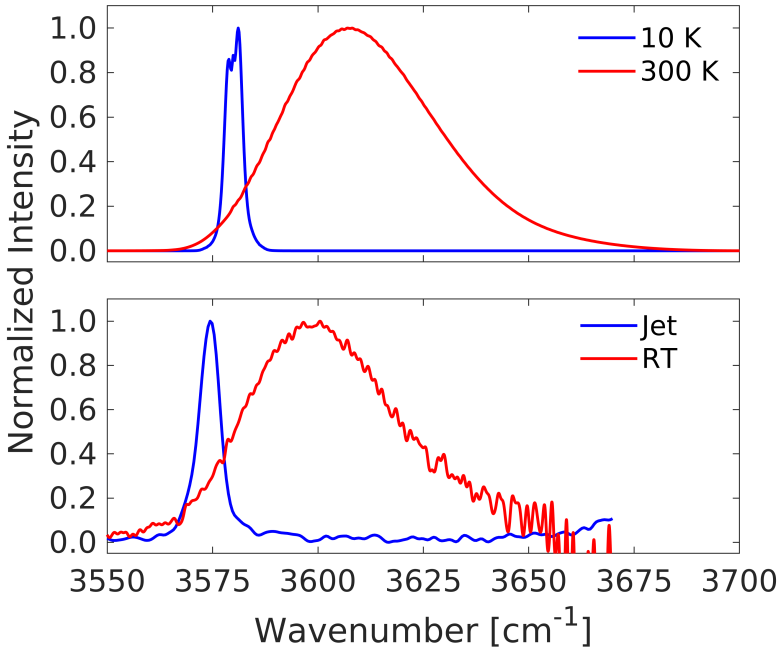

Figure 37: $(MeOH)_2$ simulated at 10 K and 300 K and recorded in jet-cooled conditions and at room temperature. Reprinted with permission from 86.

The model is capable of simulating the OH_b-stretching band of $(MeOH)_2$ at any temperature between 0 and 300 K (or higher). With the close agreement between simulation and experiment, we propose that the methanol dimer OH_b-stretching band together with the simulation may be used as a probe for the vibrational temperature in non-equilibrium experiments. In jet-expansion experiments, the temperature is largely dependent on the choice of carrier gas and the stagnation pressure used (see Section 3.2.3). The rotational temperature is reasonably equilibrated due to the relatively low number of collisions needed (ca. 10^2).[127] The rotational temperature can also more easily be determined by fitting the rotational profile of a known vibrational transition in programmes such as Pgopher.[179] However, the vibrational temperature is often not equilibrated in the jet and also not easily probed. By comparing the change in peak position and FWHM to that of the simulation, the vibrational temperature in a jet-expansion may be accurately determined and calibrated for various carrier gases and stagnation pressures. The effort to record and fit experimental spectra of the MeOH dimer to the theoretical model was started during my external stay in the Suhm lab at Georg-August Universität in Göttingen. This work is very preliminary and is done in collaboration with Post. Doc. Emil Vogt, PhD. student Eaindra Lwin

and bachelor student Mathis Goelz.

A more crude, but user-friendly version of the model is written and implemented in Python as a Jupiter Notebook by Emil Vogt.[180] The variational anharmonic state energies are taken from reference 86 and are assumed to be associated with harmonic potentials. The temperature is simulated in 25 steps from 5 - 85 K. The transitions are convoluted with a Lorentzian profile with FWHM=5.1 cm^{-1} as this is the smallest value reported for the $(MeOH)_2$ band.[53] Reference 53 assumes a rotational temperature of 5 K in their experiments, and we take 5 K as the vibrational temperature corresponding to the FWHM=5.1 cm^{-1}. The simulated change in FWHM is fitted to the input temperature by a polynomial. 7.5 Torr MeOH is expanded in He with total stagnation pressures ranging from 7.5 Torr to 375 Torr. The observed change in FWHM with stagnation pressure is correlated to the simulated FWHM and the theoretical temperature to give a curve that expresses temperature as a function of stagnation pressure. A representative excerpt of spectra at varying stagnation pressures is shown in Figure 38 together with the calibration curve. The change in band maximum was found to be not a good descriptor for temperature as the observed change in more than half of the expansions was below the instrumental resolution of 2 cm^{-1} and at most ca. 6 cm^{-1}. The change in FWHM is a much more sensitive probe but on the other hand more sensitive to baseline corrections and overlapping intensity from other clusters. The vibrational temperature can thus be determined by comparison with the theoretical model. It should be noted that thermal equilibrium is still not ensured and each vibrational mode may have its own effective temperature. The model assumes thermal equilibrium between the vibrational modes, which may cause errors in the results. The IR-beam also have a width, which means that the jet is probed in an interval of temperatures.

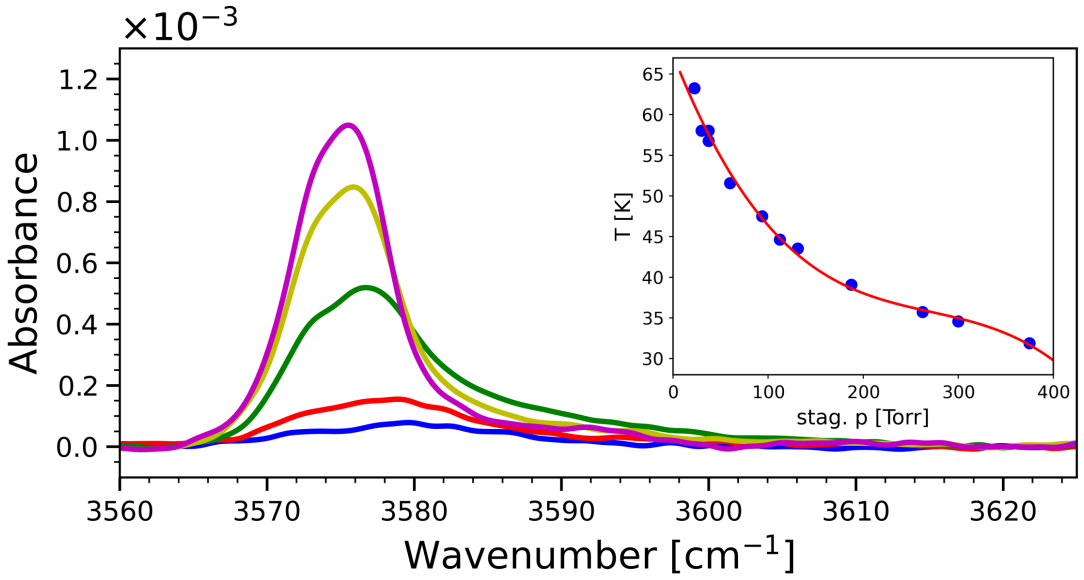

Figure 38: $(MeOH)_2$ in the Gratin jet. See text for explanation.

To obtain spectra of $(MeOH)_2$ at room temperature, two factors had to be considered. Firstly, in order to get a usable signal from the dimer, the monomer pressure had to be reasonably high. However, if the monomer pressure is too high, the formation of trimer and tetramer will contribute intensity in the spectrum. Thus, a moderately low pressure of 25 Torr was chosen. Secondly, due to the very narrow ro-vibrational transitions in the OH_b-stretching band, pressure broadening and drift in the instrument made a huge difference in the quality of the obtained dimer spectrum. After many trials, using a monomer reference of 7.4 Torr recorded directly after the high pressure sample gave the best results. The dimer band was obtained with no interference from higher clusters and with efficient spectral subtraction of the monomer signal. The subtraction is shown in Figure 39.

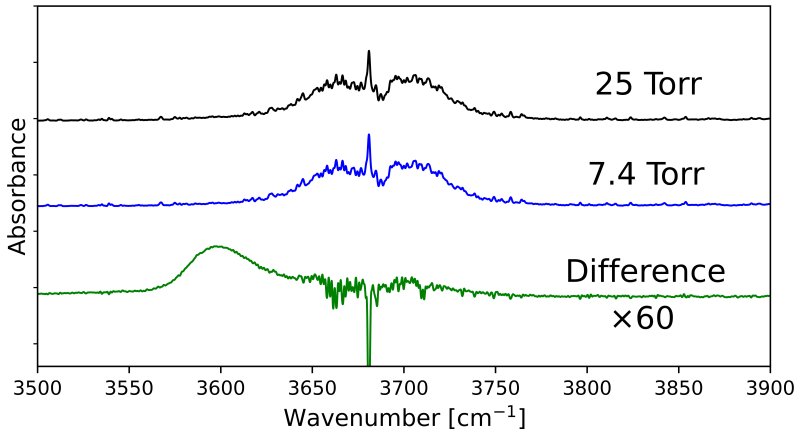

Figure 39: $(MeOH)_2$ spectral subtraction. Reprinted with permission from 86.

In conclusion, the OH_b-stretching band of methanol dimer and two of its isotopologues were recorded at room temperature and compared with a new *ab initio* vibrational model. The clever coordinate description of the model made it possible to accurately represent the LAM modes and capture the change in their transition frequency upon exciting the OH_b-stretching transition. The experiments carried out demanded accurate spectral subtraction, which was achieved by using a relatively high pressure for the monomer reference sample. The predictions of the model together with the experimental calibration curve may be accurate enough to determine the vibrational temperature in supersonic jet-expansions with a reasonable error.

4.3 METHANOL CLUSTERS

Paper 3 builds largely on the experimental findings concerning spectral subtraction in paper 2. In preliminary work, the experimental accuracy was severely limited by the inefficient spectral subtraction of the monomer signals. In the group, we had been focusing on minimising the formation of clusters in the low pressure monomer reference sample. This entailed using a very low monomer pressure and a much higher path length. However, because methanol has very high rotational constants, (128.6, 24.6, 23.8) GHz (B3LYP-D3/AVTZ), the P-Q-R structure of the OH-stretching band consists of separated and very narrow ro-vibrational transitions. These transitions are very sensitive to pressure broadening effects and the high pressure difference between the sample spectra and the monomer reference spectrum resulted in insufficient subtraction. This is shown in Figure 8 in Section 3.1.3. It was later found, that a slightly higher pressure reference sample of ca. 10 Torr (ca. 11-25% of the sample pressures) together with an additional broadening of ca. 300 Torr N_2, resulted in a much better subtraction of the monomer, leaving only the absorption bands from the clusters. The subtraction and the resulting spectrum of clusters is shown in Figure 40. Comparing with the relatively low sample pressure in Figure 39, the dimer and tetramer bands are now visible in the spectrum even before the subtraction of monomer, underlining the cluster formation's non-linear power scaling with monomer pressure.

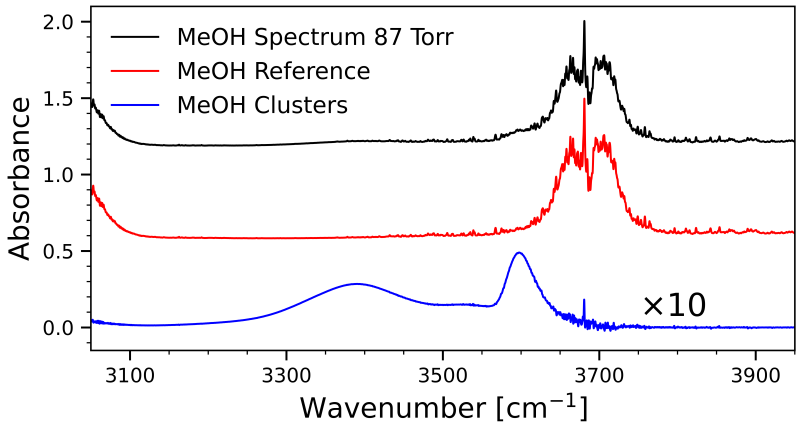

Figure 40: Efficient monomer spectral subtraction leaving MeOH clusters. Reprinted with permission from 89.

The wide cluster band spans 3150 cm^{-1} - 3700 cm^{-1} with peak maxima at 3598, 3527, and 3390 cm^{-1}. We assign the three maxima as the OH_b-stretching bands of the MeOH dimer, trimer and tetramer, respectively. This is at first justified based on the band appearance and location relative to the known cold transitions. As discussed in the previous Section 4.2, the cold bands are located at the onset of the warm bands. In Figure 41, the band max positions of the cold transitions recorded with various experiments[49,53,56–59] are shown as vertical lines, appearing at the onset of each order of cluster. The increased redshift with cluster order is crucial to efficiently separate the clusters from each other. The change in redshift is due to the cooperative effects[175–178] in the hydrogen bonding rings in the trimer and tetramer. The XH$\cdots$YH hydrogen bond makes the acceptor atom Y a better hydrogen bond donor due to the buildup of positive charge on Y. By donating a H to a hydrogen bond, the positive charge buildup is redistributed away from Y making the H-donation more favourable and the resulting H-bond stronger. In general, the effect increases with the system size but with diminishing returns. The separation between the dimer, trimer and tetramer is large enough to separate them, but the higher order clusters are almost completely overlapped with the tetramer band.[56] This is also due to the tetramer forming an especially favourable ring geometry with optimal hydrogen bond angles and minimal steric strain.

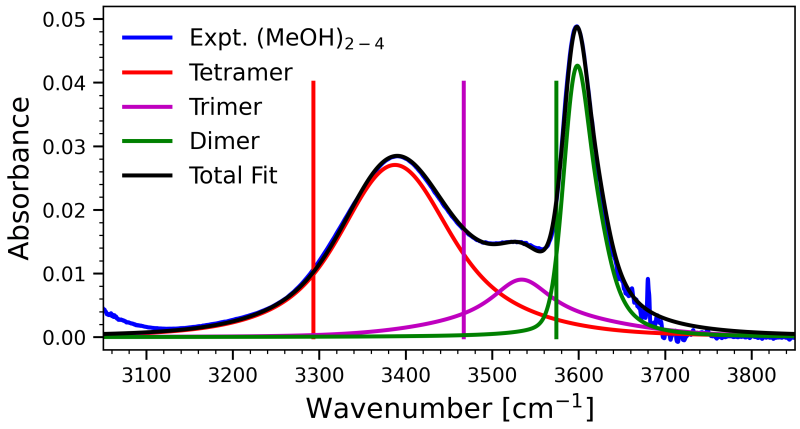

Figure 41: Fitted MeOH clusters and corresponding cold transitions. See text for explanation.

The wide cluster band is partitioned into the three orders of cluster by fitting three band profiles. This is done in python by minimising a sum of squares. Each cluster band profile consists of a sum of two normalised Lorentzian profiles shifted slightly

from each other to allow for some asymmetry as is observed for the dimer band.[86] The fitting expression and further details can be found in the SI of reference 89. Because the monomer reference is recorded at a relatively high pressure of ca. 10 Torr the areas obtained by the fit must be adjusted for cluster signals that are in the monomer reference and therefore is being subtracted out from the samples. The adjustment factors for the dimer, trimer and tetramer areas are derived in reference 89 and are

$$\begin{aligned} A_{D,true} &= A_{D,sample} \cdot \left(1 + \frac{\frac{l_{ref}}{l_{sample}} \cdot SF}{\left(\frac{p_{M,sample}}{p_{M,ref}} \right)^2} \right) \\ A_{T,true} &= A_{T,sample} \cdot \left(1 + \frac{\frac{l_{ref}}{l_{sample}} \cdot SF}{\left(\frac{p_{M,sample}}{p_{M,ref}} \right)^3} \right) \\ A_{Q,true} &= A_{Q,sample} \cdot \left(1 + \frac{\frac{l_{ref}}{l_{sample}} \cdot SF}{\left(\frac{p_{M,sample}}{p_{M,ref}} \right)^4} \right) \end{aligned} \tag{60}$$

where A_{true} is the area adjusted for the error introduced by subtraction, A_{sample} is the measured area, l is the pathlength of the cell and SF, the scaling factor used to subtract the monomer out of the spectrum. The adjustment is largest for the dimer and for the smallest measured pressures as the cluster pressure difference between the samples and the reference is the smallest. The adjustment is 11.4% - 25% for the dimer, 1.30% - 6.21% for the trimer and 0.15% - 1.55% for the tetramer. The difference could potentially affect the band shapes relative to each other, but this is accounted for by fitting the Lorentzian profile parameters to all pressures in parallel with a penalty function that biases the fit to the high pressure spectra, where the error from subtraction is the smallest.

The second and more quantitative proof that the orders of cluster are assigned correctly, is by fitting the cluster partial pressures, which are related to the integrated areas by Equation 36, against the monomer pressure raised to a power corresponding to the order of cluster. This is following Equation 31, which for homomolecular clusters generalizes to Equation 61.

$$K_{eq,n} = \frac{p_n \cdot p^{\ominus n-1}}{{p_{mon}}^n} \tag{61}$$

In Figure 42, the partial pressures are fitted for each order of cluster to the monomer pressure raised to a power corresponding to the cluster order.

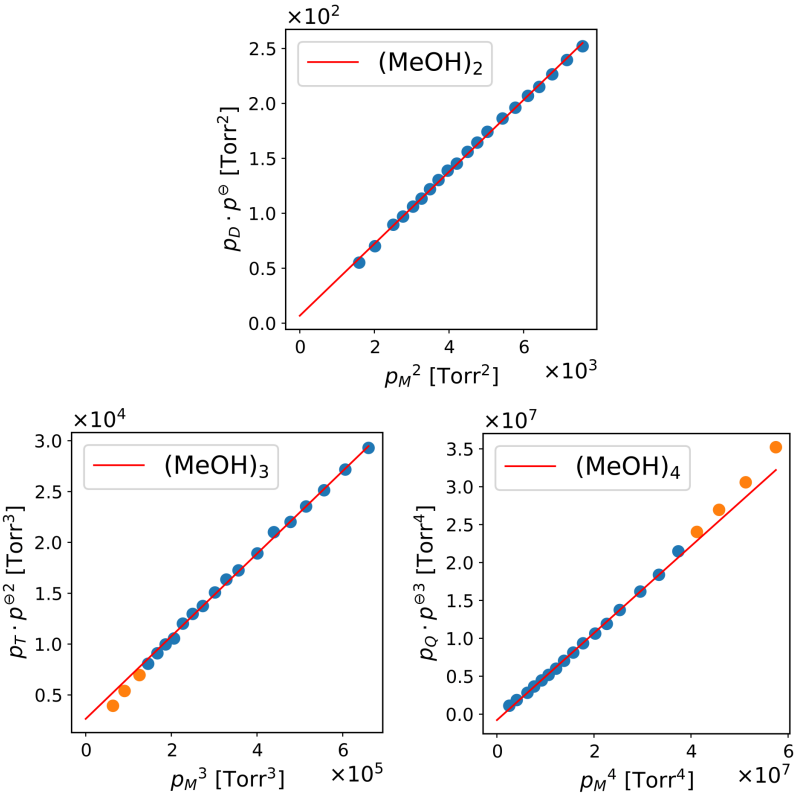

Figure 42: Determination of MeOH cluster equilibrium constants from linear fits. The different orders of clusters scale with the monomer raised to different powers. Adapted with permission from 89.

The linear correlation corroborates the cluster order assignments. A slight deflection downwards for the low trimer pressures indicate that these areas might contain intensity from the dimer. The trimer, in general, contributes lower relative absorbance due to a low abundance and low OH_b-stretching intensity *(vide infra)*. The uncertainty associated with integrating the trimer is therefore larger than for the other two clusters. The three lowest points are therefore excluded from the fit (marked in orange). For the tetramer, the highest pressures deflect upwards, indicating that higher order clusters may contribute intensity to the band. The highest pressures measured are close to saturation and the higher order clusters are expected to be overlapped almost completely with the tetramer. The fits give equilibrium constants and standard errors for the

different clusters of $K_D = 0.033 \pm 0.007$, $K_T = 0.041 \pm 0.023$ and $K_Q = 0.57 \pm 0.25$. The standard error for the dimer is relatively low due to the easy integration of the band intensity and an oscillator strength determined with a highly accurate 4D LM model. The trimer and tetramer have a much larger standard error which is mostly associated with the determination of the oscillator strengths.

In order to obtain the partial pressures of the clusters, which are used to determine the equilibrium constants, the oscillator strengths of the OH_b-stretching transitions with which the recorded bands are associated with, have to be accurately determined. In previous work, reduced dimensionality local mode models at high levels of electronic structure theory have yielded accurate transition wavenumbers and oscillator strengths.[18,82–85,88] We use a 4D variational local mode model with CCSD(T)-F12a/cc-pVTZ electronic structure to get the best possible determination of the methanol dimer OH_b-stretching oscillator strength.[89] The modes included are the OH_b-stretch and the three intermolecular modes "twist", "rock" and "OO-stretch". The oscillator strength is determined to be $f_{calc} = 6.30 \times 10^{-5}$.

Because the local mode coordinates are not easily defined in the larger ring-closed structures of the trimer and tetramer, we instead resolve to using reduced dimensionality normal mode VPT2 calculations. Normal modes are defined in an automated and mathematical fashion (see Section 2.1), reducing the theoretical burden on a primarily experimental chemist. The VPT2 treatment is done on a subset of the normal modes which significantly reduces the computational complexity and, more importantly, excludes the lowest frequency LAM modes which are known to cause significant issues in VPT2 calculations (see Section 2.4). The normal modes, which most closely resemble the local modes: intramolecular OH-stretch, COH-bend and CO-stretch, are included together with the resembling intermolecular modes: "twist" and "rock". This gives 8 dimensions for the dimer, 15 for the trimer and 20 for the tetramer. The oscillator strength is determined for methanol dimer with the 8D VPT2 model and a B3LYP-D3/AVTZ electronic structure as $f_{calc} = 9.49 \times 10^{-5}$. To elucidate how much of the ca. 51% difference from the 4D LM CCSD(T)F12a value is the vibrational model and how much is from electronic structure, the 4D LM model is used with B3LYP-D3/AVTZ

electronic structure. This method gave $f_{calc} = 8.51 \times 10^{-5}$ accounting for 69% of the difference. In other words, this means that the 8D VPT2 vibrational model is within ca. 12% of the 'best' 4D LM model within the same electronic structure. Assuming that the reduced dimensionality VPT2 model is scalable to the larger clusters and that the relative error on the electronic structure is equivalent, we scale all the f_{calc}-values by the factor found in the methanol dimer case ($\times 0.664$). This gives final oscillator strengths: $f_D = 6.30 \times 10^{-5}$, $f_T = 2.35 \times 10^{-4}$ and $f_Q = 5.12 \times 10^{-4}$

Reduced dimensionality VPT2 calculations can, when used correctly, open up a widely accessible toolbox for chemists, who are not specialised in constructing local mode coordinates and vibrational models. The VPT2 code is implemented in a variety of quantum chemical softwares and the option for reducing the dimensionality circumvents the fundamental problem of stability in VPT2 treatment of "floppy" molecules like hydrogen bound species by not including problematic modes.

A NCI analysis of the three orders of MeOH clusters is done in NCIPLOT4.2 and shown in Figure 43. To the left the isosurfaces are plotted with the electron density colour coded from blue to red in the interval [-0.05, 0.05] au. The hydrogen bonds are shown as blue disks and secondary interactions as green surfaces. To the right, the minima in the reduced density gradient correspond to bond critical points and ring critical points in the clusters. The electron density at the bond critical points for the tetramer are significantly larger than for the dimer and trimer, which are similar. This can be interpreted as a stronger hydrogen bond in the tetramer. Despite cooperative effects, the trimer and dimer looks to have similar electron densities at the bond critical points. This is probably due to the ring-strain in the trimer. The trimer further shows a significant secondary repulsive interaction in the ring critical point. This is significantly larger than that of the tetramer, underlining the sub-optimal H-bonding structure for the trimer compared to the much more favourable tetramer geometry.

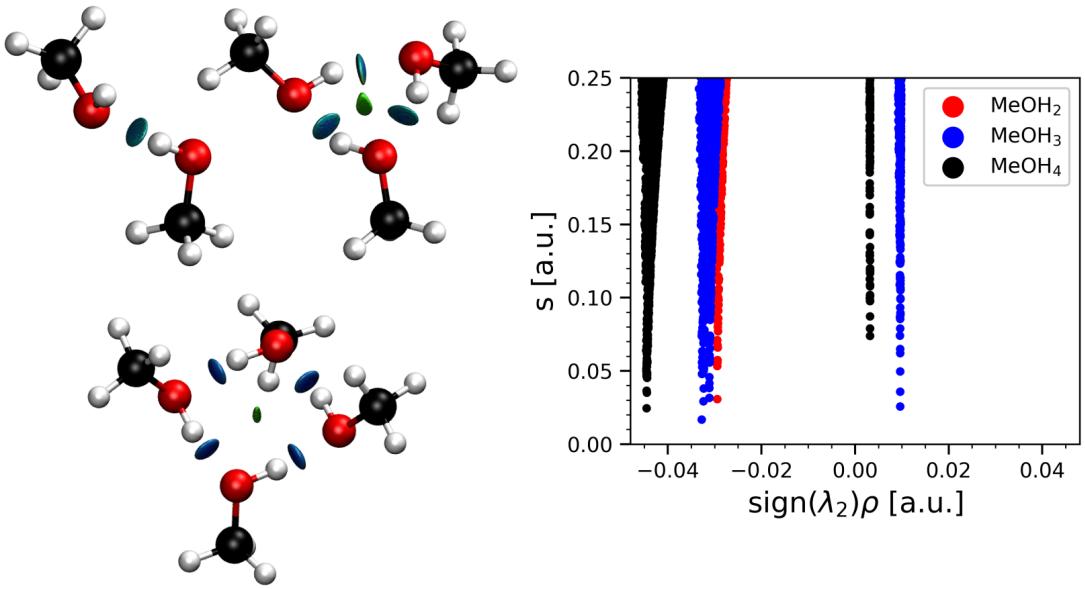

Figure 43: NCI analysis of MeOH clusters. Left: s(**r**)=0.5 au. isosurfaces. Right: Reduced density gradient s(**r**) plotted against electron density sign(λ_2)ρ.

In conclusion, the MeOH dimer, trimer and tetramer are detected and quantified at room temperature using FTIR spectroscopic techniques and precise spectral subtraction. The oscillator strengths of the OH_b-stretching transitions associated with the detected bands are determined using a reduced dimensionality VPT2 model, which is corrected for deficiencies in the electronic structure and the vibrational model. The reduced dimensional VPT2 model is promising for a more automated vibrational analysis of transitions in large and floppy systems, where internal coordinates are not easily defined, and where a full dimensional VPT2 treatment often fails. The NCI analysis shows the intermolecular interactions responsible for the redshifts and stabilization of the clusters and highlights the differences between the trimer and tetramer that results in a relatively low equilibrium constant for the trimer.

4.4 TRIMETHYLAMINE-WATER RESONANCES

Amines are amongst the strongest non-charged hydrogen bond acceptors known.[18,85] The strong hydrogen bonds lead to donor OH-stretching redshifts in the order of ca. 300 cm^{-1}, ca. 3 times that of corresponding O-atom acceptors.[18] Further, the strong intermolecular interactions result in relatively large formation constants making the complexes experimentally approachable. The heteromolecular hydrogen bound complex between trimethylamine and water (TMA·H_2O) has been studied previously at various conditions including room temperature gas phase,[85] matrix isolation[181] and by photo-ionisation size selected action spectroscopy.[182] The room temperature spectrum shows a clear resonance between the OH_b-stretch and the HOH-bend overtone due to the extensive redshift of the very intense OH_b-stretching transition. The bright state associated with the OH_b-stretch shares intensity by mechanical anharmonicity with the bend overtone, making the previously dark state bright. Additional band structure is also observed but is not explained.[85] In the Ar matrix spectrum a somewhat complicated spectrum is observed, and the authors conclude that the primary aggregation product is a much larger cluster consisting of 4 H_2O units and 2 TMA units with little to no 1:1 complex being formed. This seems like an unlikely explanation given the number of assumed reaction partners.[181] The size selected experiment[182] should in principle be able to probe only the 1:1 complex. However, the obtained spectrum shows an unexpected complexity that is far away from former studies done on other hydrated tertiary amines.[183] The authors (questionably) assign all peaks based on a VPT2 calculation as transitions in a 1:1 complex. The group have previously published other alleged size-selective water dimer spectra with an assignment of peaks which, perhaps, is more likely to stem from larger clusters.[87,184] We hypothesise that the spectrum is not as size-selective as reported and that the IR-spectrum is polluted by larger complexes.

In a joint effort between the Suhm-lab in Georg-August Universität, Göttingen and the Kjaergaard-lab, University of Copenhagen, we recorded H_2O·TMA in three different media to better understand the complex structure of the OH_b-stretching band and to right what may be wrongfully assigned spectra in the litterature. In Figure 44, the

H_2O·TMA complex is shown recorded in three different media. The room temperature spectrum is recorded previously by Alexander Kjærsgaard.[85] The He jet spectrum is recorded by Taija Fischer and Eaindra Lwin and the Ar matrix spectrum is recorded by Dhritabrata Pal and myself. In all three media, the OH_b-stretching region is dominated by three major peaks. In a "deperturbed" picture, we refer to the transitions associated with the bands as the OH_b-stretch (v_{OHb}), the HOH-bend overtone (v_{2HOH}) and the combination band of the HOH-bend overtone + the ON-intermolecular stretch ($v_{2HOH+ON}$). Already, it is clear that there is a strong correlation between the three spectra and that the spectra have a much simpler and regular structure than that previously reported in the matrix and size-selective experiments.[181,182] The He jet spectra and Ar matrix spectra look very similar to that previously recorded by the Suhm lab for other tertiary amines.[183]

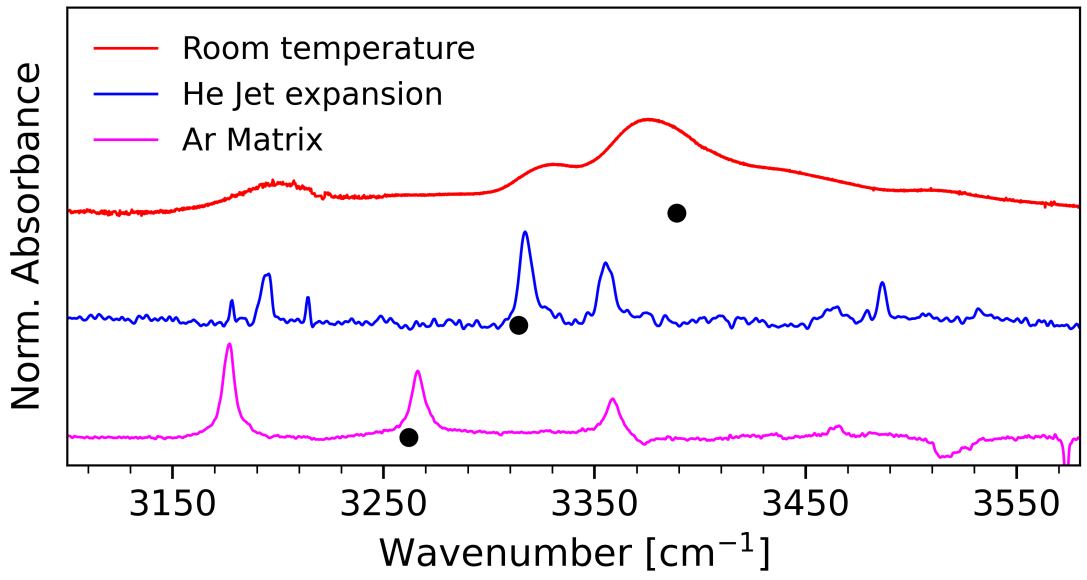

Figure 44: H_2O·TMA spectra in different media. The black dots signify the intensity-weighted band center of each trace. These are: matrix = 3262 cm^{-1}, jet = 3315 cm^{-1} and room temp. = 3389 cm^{-1}. Room temperature spectrum data from reference 85.

Between the three media, the bands are seen to vary in relative intensity with respect to each other and even change order with respect to the intensity. We hypothesise that this is due to a strong resonance between the bright v_{OH} state and the two dark states v_{2HOH} and $v_{2HOH+ON}$. The supersonic He jet expansion is assumed to not perturb the transition energies of the complex and is thus used as a baseline for the band

positions. The central band associated with the OH_b-stretching transition is the most intense as expected from the deperturbed picture. The relative intensities for the three peaks in the spectrum are 0.40/1/0.85. When going from the He jet to the Ar matrix, two main changes are observed. Firstly, the v_{OHb} band is redshifted by ca. 51 cm^{-1}, which is within the normal Ar matrix shift reported for similar transitions.[185] Secondly, the v_{2HOH} band is slightly redshifted and has an increased relative intensity compared to the jet spectrum. The $v_{2HOH+ON}$ band appears smaller. The relative intensities for the bands are 0.95/1/0.47. In the room temperature spectrum, the v_{OHb} transition is now blueshifted due to the thermal effects[86] described in Section 4.2. The order of band intensity shifts and the highest energy band appears the most intense in the spectrum with the relative intensities being 0.20/0.25/1 (using integration limits 3150, 3260, 3343 and 3590 cm^{-1}). The intensity weighted center of the spectrum, which is shown with black dots in Figure 44, corresponds to the position of the "deperturbed" v_{OHb} state, assuming that this transition is the only one carrying intensity. It is seen that the center redshifts in the matrix and blueshifts in the room temperature spectrum, as is expected. The band closest to the intensity weighted center should be assigned as the v_{OHb} state.

The v_{OHb} state is sensitive to the environment and the energy is therefore tuned in the different media resulting in the state going in and out of resonance with the two resonance partners to either side of the band. The states share intensity and repel each other. A bright state can at most share 50% of its intensity to a dark state. This raises the question as to how the intensity order changes with the different media. Assuming that the v_{OHb} state carries all intensity, it is clear that in the jet, more intensity is shared with the $v_{2HOH+ON}$ state which is also the state closest in energy to v_{OHb}. When going to the Ar matrix, the v_{OHb} state is redshifted and therefore gets closer to the v_{2HOH} state. Now more intensity is shared with the v_{2HOH} state rather than the v_{OHb+ON} state.

In the room temperature gas phase spectrum, a large and perhaps unexpected difference is seen in the relative intensities between the three bands. The most intense band, which we associate with the v_{OHb} state, is no longer in the middle. We

explain the phenomenon by an avoided crossings between the deperturbed v_{OHb} and $v_{2HOH+ON}$ states. The v_{OHb} state is now rather a collection of states consisting of 1 OH_b-stretching quantum and a summation of low frequency intermolecular modes alike that of the thermally excited methanol dimer (Figure 36). Some of these summation states are thermally tuned up in energy to the extend that they cross onto the high energy side of the $v_{2HOH+ON}$ state with a following repulsion between the states. The sharing of intensity and repulsion of states are effects of mechanical anharmonicity or "wavefunction mixing". The bands therefore do not have black and white labels as the wavefunctions associated with the states are superpositions of the deperturbed states. The labels can however be helpful to describe which state is dominating in a mixed wavefunction.

In the room temperature spectrum a clear shoulder with maximum at 3510 cm^{-1} is observed. This shoulder is significantly more structured than other warm hydrogen bound bimolecular complexes observed, where a more smooth tailing is often seen.[18,86] We believe that this shoulder is due to a v_{OHb+ON} combination band. The combination band is further visible at 3463 cm^{-1} and 3465 cm^{-1} in the jet and matrix, respectively. Our collaborators were not so sure as to whether a peak was observable or not or if our proposed assignment was correct. The peak was labelled "C" in the manuscript, which is in preparation, for "Casper's peak". In Table 4, the calculated and observed transition wavenumbers are compiled. It is observed that the 6D VPT2 calculated $\tilde{\nu}$ are consistently almost exactly 100 cm^{-1} below that observed in the He jet. The modest and consistent shift supports the assignment.

Table 4: Calculated and observed $\tilde{\nu}$ for H_2O·TMA. Calculations done with B3LYP-D3/AVTZ electronic structure.

	6D VPT2	RT Gas	He Jet	Ar Matrix
$\tilde{\nu}_{OHb}$	3226	3375	3317	3266
$\tilde{\nu}_{2HOH}$	3095	3200	3195	3177
$\tilde{\nu}_{2HOH+ON}$	3257[a]	3330	3355	3359
$\tilde{\nu}_{OHb+ON}$	3341	3510	3463	3465
$\tilde{\nu}_{HOH}$	1589	-	-	-
$\tilde{\nu}_{ON}$	162	-	-	-

[a]Transition not included in VPT2 calculation. $\tilde{\nu}_{2HOH+ON}$ estimated as $\tilde{\nu}_{2HOH} + \tilde{\nu}_{ON}$

To simulate the avoided crossing in calculations, a "dirty trick" is applied.[186] The mass of the bound H is changed, resulting in a change of transition wavenumber proportional to $\sqrt{(1/\Delta\mu)}$. The calculation is set up as a 6D VPT2 calculation including OH_b-stretch, OH_f-stretch, HOH-bend and the three intermolecular modes that resembles "twist", "rock" and ON-stretch. The calculation is done on a B3LYP-D3/AVTZ electronic structure. The calculation outputs the transition energies before "deperturbed" and after the variational treatment, which is activated in GVPT2 when the transition energies are within a certain threshold. As the three quanta state $v_{2HOH+ON}$ is not included in the VPT2 treatment, the resonance between v_{OHb} and v_{2HOH} is used as the example instead. In Figure 45, the transition energy is plotted for the deperturbed and variational states as a function of H mass. It is seen that as H gets heavier, the deperturbed OH_b-stretching transition energy drops below that of the bend overtone. The variational states approach each other but can only reach a minimum energy difference of 118 cm^{-1} before they repel each other with their labels switched around.

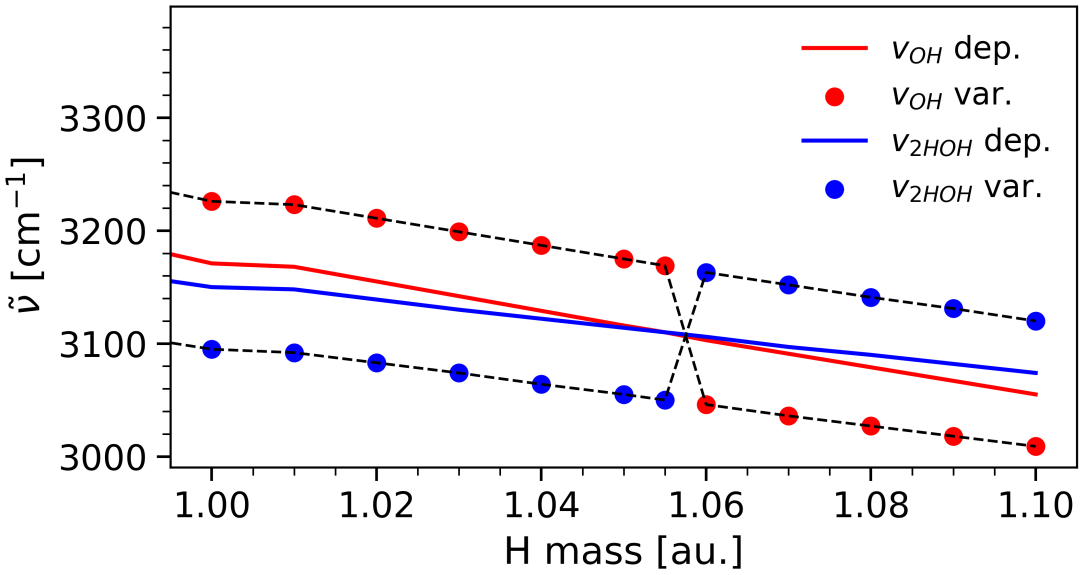

Figure 45: H_2O·TMA mass tuning. The theoretical mass of H is changed to tune the OH_b-stretch energy. As the deperturbed states converge, the variational states repel and can only reach a minimum distance of 118 cm^{-1} before diverging again with switched labels.

In conclusion, H_2O·TMA is experimentally observed in three different media. The cold spectra show a simple structure of three strong peaks, which is in line with that observed for other hydrated tertiary amines. An additional much smaller signal was assigned as the ν_{OHb+ON} state. Previous studies of H_2O·TMA incorrectly assign what can only be noise or larger cluster peaks as originating from the bimolecular complex. We do not observe these transitions in any media. The jet spectrum, which is the media with the smallest perturbation of the transitions are in close agreement with a 6D VPT2 calculation, which accounts for the three main observed features. The states in the He jet and Ar matrix share intensity based on the proximity of the dark states to the bright ν_{OHb}-state. In the room temperature spectrum, the order of intensity is switched, which suggests that an avoided crossing has occurred. The resonance model offers a likely interpretation for the highly structured OH_b-stretching band observed at room temperature.

5

RESULTS 2: ABSOLUTE INTENSITIES

5.1 *tert*-BUTYLHYDROPEROXIDE

The recording of absolute intensities of *t*-BuOOH was the main objective of my master's thesis.[66] The spectra have since been re-recorded and the data treatment refined. The presentation of the results in the $\Delta v_{OH} = 1 - 3$ regions will be presented rather swiftly as the spectra have been reported before.[66] This thesis builds on the previous findings from my master's thesis and additionally, absolute intensities of the $\Delta v_{OH} = 4 - 5$ regions were obtained by the use of the newly refurbished FTIR-CRD spectrometer. The determination of the partial pressure was hindered by the solvent in which the hydroperoxide was kept and by the degradation products of *t*-BuOOH. The procedure for phase extracting the sample into DCM and spectrally subtracting remaining solvent and impurities is described in Sections 3.1.5 and 4.1 and in reference 103. In previous publications,[60,61] the band appearance and relative intensities are described by two different vibrational models, and by experimental spectra. The two main features in all OH-stretching regions are the pure OH-stretching band and the OH-stretching / COOH-torsion combination band. In this thesis, I will present the absolute intensities in the $\Delta v_{OH} = 1 - 5$ regions for the pure OH-stretch as well as for the combination band.

5.1.1 *Fundamental OH-stretch region*

The spectra recorded are the same as reported in reference 103 and so the spectrometer settings and sample preparations are equivalent to those described in said paper. To

determine the OH-stretching band intensity, 13 measurements with a determined *t*-BuOOH pressure in the range of 1.3 - 3.5 Torr are used. This gives a peak absorbance of the OH-stretching band between 0.37 and 1.00 ensuring linear absorbance with pressure. For the must weaker combination band, a total of 21 measurements were used in the range of 1.3 - 4.4 Torr corresponding to a peak absorbance between 0.014 - 0.041. In Figure 46 a representative excerpt of recorded spectra in the fundamental region is presented. The OH-stretch has a peak absorbance at 3597 cm^{-1}. Difference bands from thermally excited torsional states are observed around 3444 cm^{-1} and the combination band is centered around 3786 cm^{-1}. As presented in references 60, 61, 66, the COOH-torsion potential is a symmetric double well with a $v_{OH} = 0$ barrier of ca. 290 cm^{-1}. This gives rise to tunnelling splitting which is especially pronounced in the combination band, as the tunneling splitting increases with excitation quanta in the COOH torsion. The high energy shoulder at 3607 cm^{-1} is assigned as an OH-stretching transition from a thermally excited torsional state. The transition energy is higher due to the lessened tunneling splitting in the $v_{OH} = 1$ state compared to the OH-stretching ground state.[60]

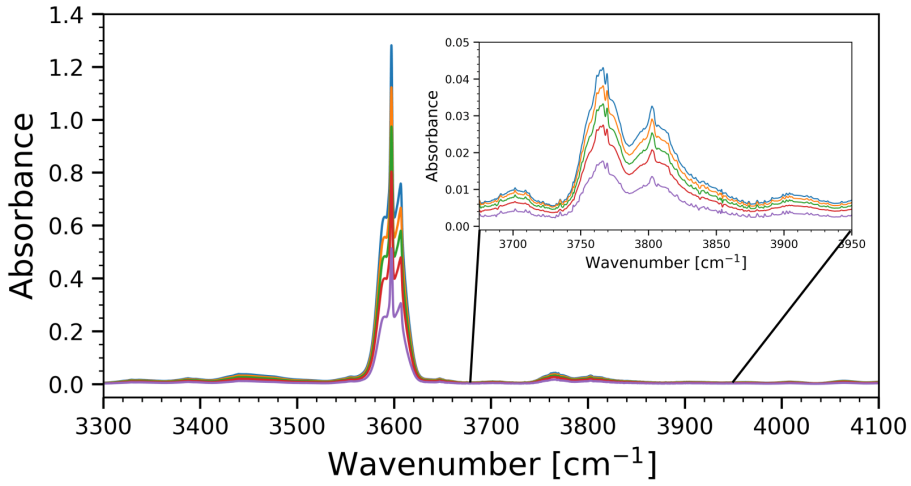

Figure 46: *t*-BuOOH $\Delta v_{OH} = 1$ spectrum

The OH-stretching band is integrated from 3527 - 3675 cm^{-1} and the combination band from 3731 - 3875 cm^{-1}. The baseline is difficult to determine in the fundamental region, as the bands associated with v_{OH} is overlapping with a whole manifold of CC, CH and CCH-bend combination bands. Therefore the integration is done with two linear baselines, one slightly high [3292 cm^{-1}, 4035 cm^{-1}] and one slightly low

[2443 cm^{-1}, 4550 cm^{-1}], and a mean is taken of the two. The determined areas are fitted by Equation 27 by minimizing a χ^2-expression analogous to Equation 59. In the χ^2-expression, the standard error on the pressure and temperature are considered along with the estimated standard error introduced by varying the integration ranges. The collected standard errors for the pressure and temperature are combined as

$$\frac{p \cdot l}{c \cdot T} = x \quad , \quad \sigma_x = \sqrt{\left(\frac{\partial x}{\partial p}\right)^2 {\sigma_p}^2 + \left(\frac{\partial x}{\partial T}\right)^2 {\sigma_T}^2} \tag{62}$$

Fits are shown in Figure 47. For both fits, the intercept with the $\int A(\tilde{\nu})d\tilde{\nu}$ -axis is 0 within one and two standard errors for the OH-stretch and combination band, respectively.

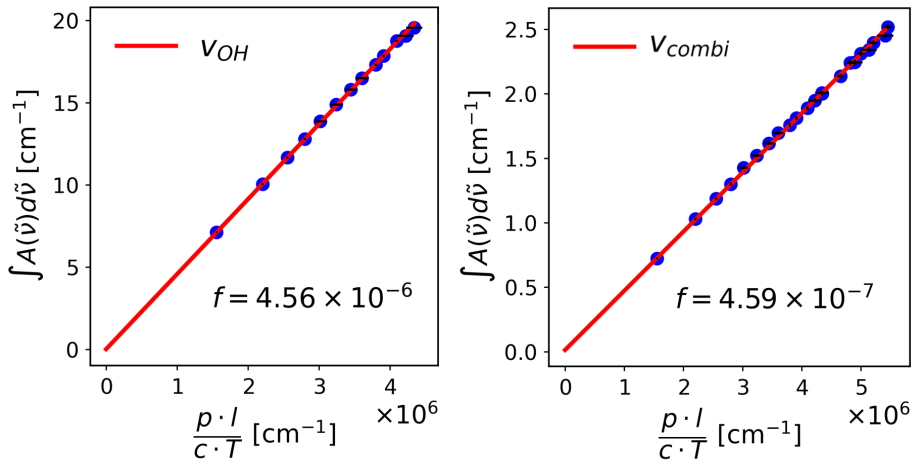

Figure 47: *t*-BuOOH $\Delta\nu_{OH} = 1$ linear fit. To the left: ν_{OH}. To the right: $\nu_{OH/COOH}$

The error bars are marked with black, but are hardly visible in the plot. Systematic experimental errors are combined with the χ^2-statistical error in the final reported standard error on the oscilllator strength. These are approximately additive in a Euclidian norm if the errors are added as relative errors.[187]

$$\sigma_f = \sqrt{{\sigma_{stat}}^2 + {\sigma_{baseline}}^2 + {\sigma_l}^2 + {\sigma_{p-gauge}}^2 + {\sigma_{pathlength}}^2} \tag{63}$$

The final f-values with collected errors are $f_{OH} = (4.56 \pm 0.15) \times 10^{-6}$ and $f_{OH/COOH} = (4.59 \pm 0.58) \times 10^{-7}$

5.1.2 $\Delta v_{OH} = 2$ *Region*

In the $\Delta v_{OH} = 2$ region, the band is recorded using a 16 PA, IR Analysis, Inc. White-cell with a measured path length of 15 meters. The spectrometer is fitted with a CaF2 beamsplitter, 2.5 mm aperture and spectra are averaged over 8000 scans. The 8000 scans are much more than that needed for a sufficient S/N in the region. However, the large number of scans makes it possible to simultaneously get high quality spectra of $\Delta v_{OH} = 3$. The spectra recorded for the fundamental region using a 1 meter path length cell also provide sufficient signal in the $\Delta v_{OH} = 2$ region for determination of the oscillator strength. Thus, good coherence between the three FTIR regions and two different path length cells is achieved.

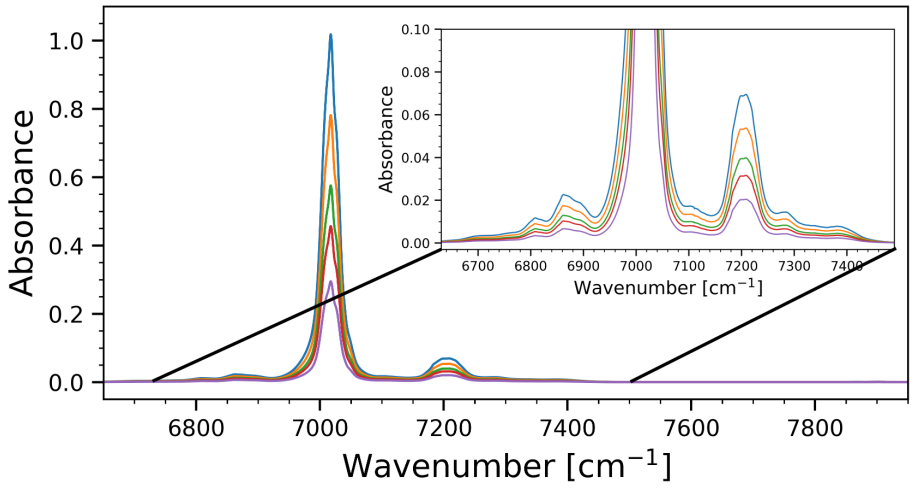

Figure 48: *t*-BuOOH $\Delta v_{OH} = 2$ spectrum

The $\Delta v_{OH} = 2$ region is presented in Figure 48. The OH-stretch has a peak absorbance at 7017 cm^{-1} and the combination band at 7204 cm^{-1}. Noticeably, the fine structure is more limited compared to the fundamental region. This is due to the rapidly increasing density of states, which speeds up relaxation through dark internal conversion processes reducing the lifetime of the excited state. Due to the time/energy uncertainty relation (Equation 29), the individual rotational-vibrational transitions broaden and overlap to form the observed band without rotational features. The oscillator strengths obtained by the 1 meter cell and the 15 meter cell are identical within standard error for both the OH-stretching band and the combination band. The two measurements are combined to give a final value by taking a mean weighted by

their individual estimated standard errors following Equation 56. The individual values and the final value are reported in Table 5.

Table 5: Oscillator strengths for *t*-BuOOH $\Delta v_{OH} = 2$ with 1 meter and 15 meter cell. Values are multiplied by $\times 10^7$.

	1m	15 m	Final result
OH	8.25 ± 0.43	8.30 ± 0.29	8.28 ± 0.24
Combi	1.13 ± 0.21	1.08 ± 0.07	1.08 ± 0.06

The linear fits for the 15 meter cell measurements are shown in Figure 49. For the OH-stretch, 9 measurements are included with a peak absorbance between 0.30 and 1.0. For the combination band 17 measurements are included. The intercept with the $\int A(\tilde{\nu})d\tilde{\nu}$ -axis is 0 within 0.5 standard errors for both bands. For both bands, all 21 measurements with the 1 meter cell are included (not shown). The spectrum is baseline corrected by a 4th order polynomial fitted in a wide region around the bands. When comparing with a linear baseline fitted [6465 cm^{-1}, 7630 cm^{-1}] the difference was less than 1% for the more sensitive combination band at the lowest pressure. The difference was propagated as an error on the band areas. The bands were integrated between 6923 - 7137 cm^{-1} and 7137 - 7282 cm^{-1}.

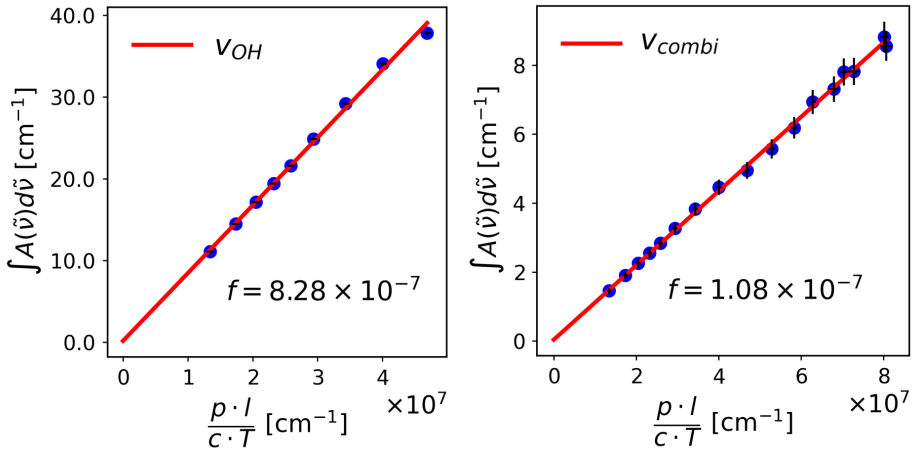

Figure 49: *t*-BuOOH $\Delta v_{OH} = 2$ linear fit. To the left: v_{OH}. To the right: $v_{OH/COOH}$ Data shown for the 15 meter cell experiments.

5.1.3 $\Delta v_{OH} = 3$ *region*

The $\Delta v_{OH} = 3$ region is recorded simultaneously with the $\Delta v_{OH} = 2$ region. Spectra at different pressures are shown in Figure 50. The bands are approaching the practical linear limit of the FTIR spectrometer. The baseline above ca. 10800 cm^{-1} is hard to correct and the spectrum is noticeably more noisy. The spectrum around the $\Delta v_{OH} = 3$ transition is baseline corrected by a 4th order polynomial. The OH-stretching band has peak absorbance at 10249 cm^{-1} and the combination band is centered around 10448 cm^{-1}. In this region, the high energy shoulder, also observed in the fundamental region, is visible at 10293 cm^{-1}. The OH-stretching band and the combination band are integrated between 10161 cm^{-1} - 10374 cm^{-1} and 10390 cm^{-1} - 10541 cm^{-1}.

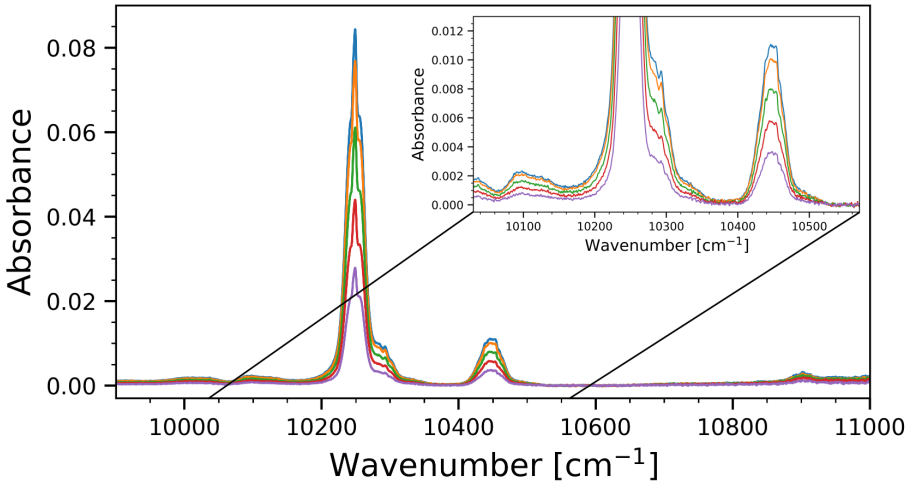

Figure 50: *t*-BuOOH $\Delta v_{OH} = 3$ spectrum

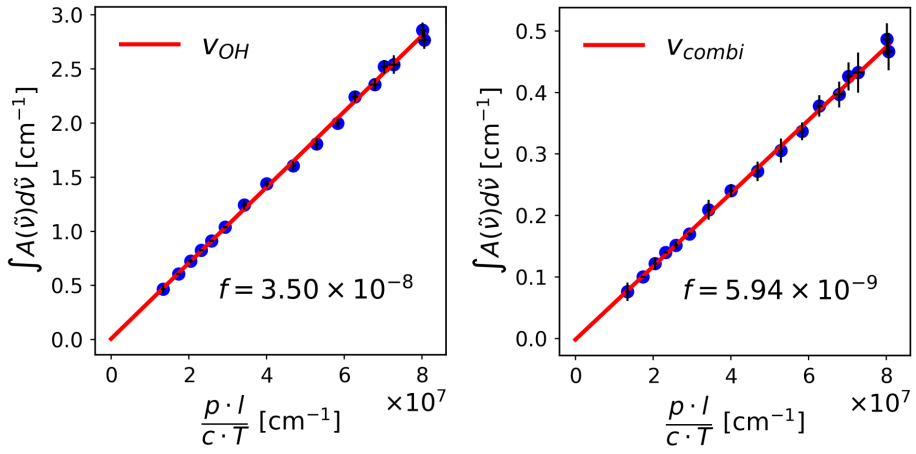

Figure 51: *t*-BuOOH $\Delta v_{OH} = 3$ linear fit. To the left: v_{OH}. To the right: $v_{OH/COOH}$

The final reported oscillator strengths are $f_{OH} = (3.50 \pm 0.11) \times 10^{-8}$ and $f_{OH/COOH} = (5.94 \pm 0.58) \times 10^{-9}$

5.1.4 $\Delta v_{OH} = 4$ *region*

This region is recorded on the FTIR-CRD coupled flow setup. The gas flow is directed through the previously described 1 meter cell, which was also used to determine the oscillator strength of the fundamental transitions. The fundamental spectrum is being recorded continuously during the CRD spectrum scan to measure the number density and consistency of the gas mixture throughout the CRD scans. The CRD scans from 724 - 769 nm in steps of 0.1 nm with 60 shots at each step. Each spectrum is averaged from two scans. The background was taken in a single scan of 120 shots pr. step. The measured laser linewidth is ca. 5 cm^{-1}.

The FTIR spectrum also ensured purity of the sample. It was observed that the solvent DCM completely disappeared from the spectrum after ca. 1 hour at the maximum flow of 200:300 sample/carrier gas ratio. Only a small amount of *t*-BuOH was observed. A FTIR-CRD reference spectrum was recorded of *t*-BuOH and the CRD reference spectrum was subtracted from the sample CRD spectrum by the same scaling factor as determined by the FTIR spectra. The amount was scarce but made a small absorption contribution especially in the combination band region. The subtraction is shown in Figure 52.

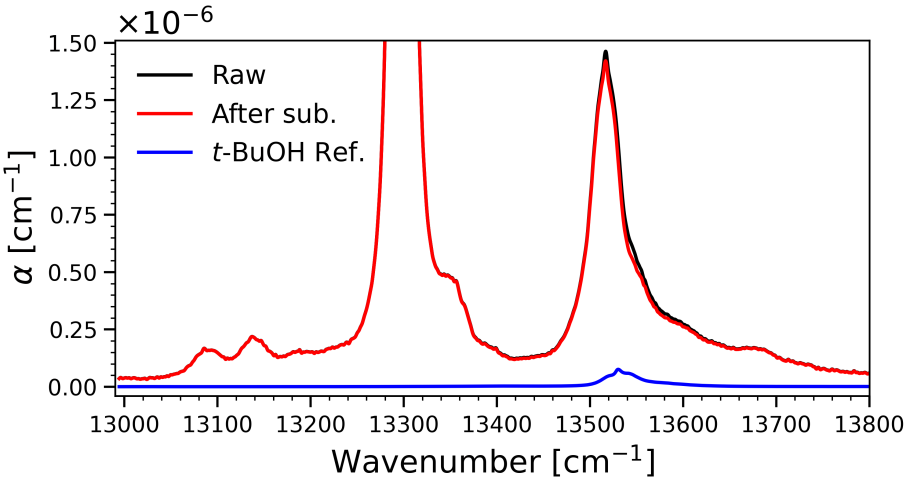

Figure 52: *t*-BuOOH $\Delta v_{OH} = 4$ subtraction of *t*-BuOH. The *t*-BuOH makes up only a small fraction of the total sample pressure. Here, the spectrum of 200 sccm *t*-BuOOH is shown before and after subtracting *t*-BuOH

The meticulous protocol for determining experimental errors for each measurement point in the regions $\Delta v_{OH} = 1 - 3$ does not really make sense in the FTIR-CRD setup. The determination of R_L, by which all values are scaled, is estimated to have a 5% standard error. This is an order of magnitude larger than the statistical errors introduced by fluctuations in pressure and temperature in the static experiments. Not a lot of wiggle room is left for determining different baselines as the spectral bandwidth is limited to either side of the absorption bands. The spectrum is, however, naturally quite flat due to the very limited number of bright transitions, and an excellent S/N. An estimated standard error of 2% is added due to baseline correction. The baseline is corrected by a straight line from 13007 cm^{-1} - 13772 cm^{-1}. The standard error based on integration limits is determined as 2.2% and 3.5% for the OH-stretching and the combination band, respectively. The optimal integration limits are 13245 cm^{-1} - 13394 cm^{-1} and 13453 cm^{-1} - 13684 cm^{-1} for the OH-stretching and the combination band, respectively. The collected standard errors are thus determined as

$$\sigma_f = \sqrt{{\sigma_{RL}}^2 + {\sigma_{baseline}}^2 + {\sigma_{int}}^2} \tag{64}$$

In Figure 53, the CRD-spectra are shown for a range of sample mixing ratios. The total flow is always 500 sccm of which 0-200 sccm is bubbled through the sample holder, thus diluting the sample gas. The linear fits of the integrated absorption coefficients of

the CRD recorded bands vs. the integrated fundamental OH-stretching band recorded on the FTIR are also shown.

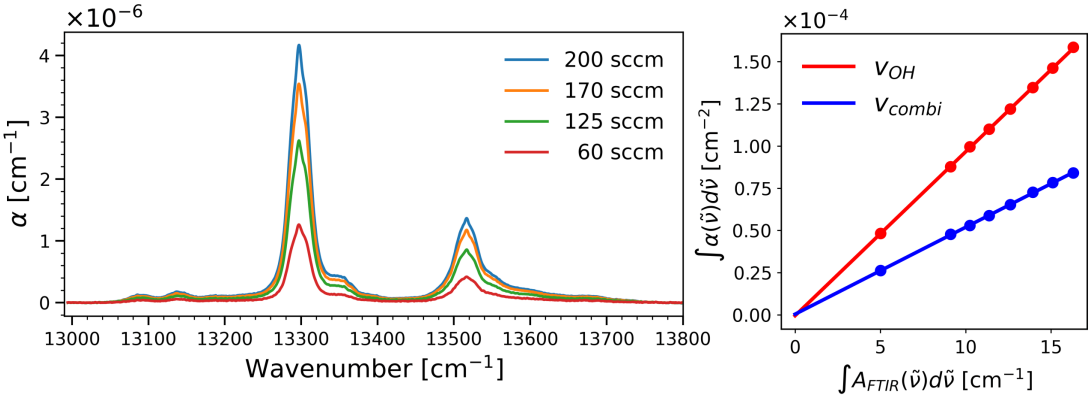

Figure 53: *t*-BuOOH $\Delta v_{OH} = 4$ spectra and linear fit at different sample concentrations. To the left, the spectra are recorded with different mixing ratios of sample/carrier gas. The label denotes the flow through the sample holder. To the right, the integrated absorption coefficient is plotted against the integrated fundamental OH-stretching band recorded on the FTIR.

In reference 60, it is shown that at the higher overtones ($\Delta v_{OH} \geq 4$), the OH-stretch is the transition that carries most of the intensity and shares it by Franck-Condon mechanisms to the surrounding states. This means that in order to compare directly with the theoretical band oscillator strengthfor models that do not include the combination bands, the whole band must be integrated. Thus, the band is also integrated from 13025 cm^{-1} - 13785 cm^{-1}, assuming that all spectral features arise from the OH-stretch as a consequence of intensity redistribution. The final reported f-values are summarised in Table 6 where a comparison is also made to the "direct mean" of integrated cross sections, which, as discussed in Section 3.2.5.1, implies that the linear fit is forced through (0,0). The difference is within standard error for all bands validating the baseline.

Table 6: Oscillator strengths for *t*-BuOOH $\Delta v_{OH} = 4$ by FTIR-CRD. Values are multiplied by $\times 10^9$.

	Free fit	Direct mean
Total	3.29 ± 0.19	3.30
OH	1.92 ± 0.11	1.92
Combi	1.02 ± 0.066	1.03

5.1.5 $\Delta v_{OH} = 5$ *region*

In the $\Delta v_{OH} = 5$ region the intensity is significantly more spread out compared to the other regions. The relative intensities of the difference bands centered around 15960 cm^{-1}, and the combination band centered around 16340 cm^{-1} are now quite a lot larger in comparison to the OH-stretch with peak absorption at 16147 cm^{-1}. Interestingly, a new band appears at 16582 cm^{-1}, which is assigned as a combination band of 5 quanta in the OH-stretch and 2 quanta in the COOH-torsion mode. A (3+1)D model predicts the transition wavenumber of this combination band at 16655-16700 cm^{-1}.[60] The model overpredicts the transition wavenumber of the pure Δv_{OH} by ca. 60 cm^{-1} in this region. The combination band is previously observed in photo-acustic experiments.[62] The band is also observed to grow in the next $\Delta v_{OH} = 6$ region[64] corroborating the theoretical finding that the intensity sharing processes become more efficient with increasing OH-stretching quantum number.[60]

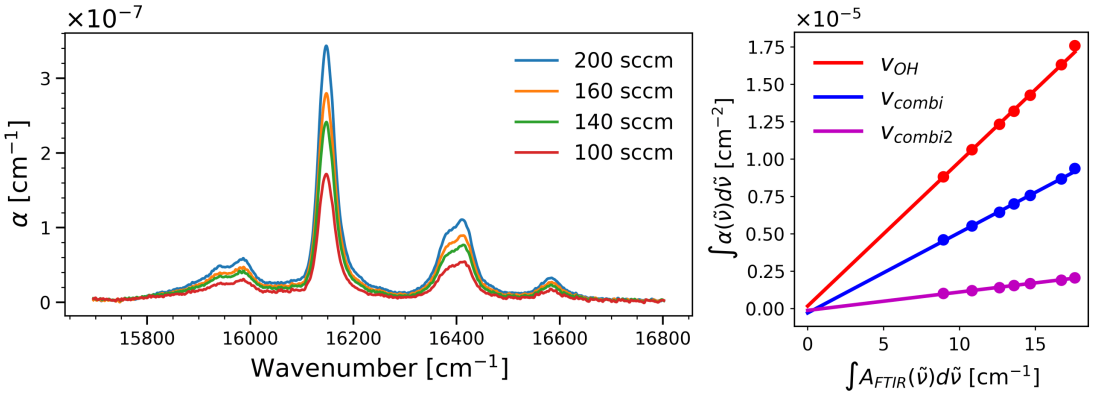

Figure 54: *t*-BuOOH $\Delta v_{OH} = 5$ mixing ratio range spectra and linear fit. To the left, the spectra are recorded with different mixing ratios of sample/carrier gas. The label denotes the flow through the sample holder. To the right, the integrated absorption coefficient is plotted against the integrated fundamental OH-stretching band recorded on the FTIR.

Each spectrum is averaged by 6 CRD scans with 60 shots at each measurement point. The region is baseline corrected by a straight line fitted between 15730 cm^{-1} - 16770 cm^{-1} and shifted upwards by $3 \cdot 10^{-9}$ cm^{-1}. The OH-stretch is integrated between 16080 cm^{-1} - 16260 cm^{-1}, the first combination band between 16315 cm^{-1} - 16480 cm^{-1} and the second combination band between 16540 cm^{-1} - 16640 cm^{-1}. The oscillator strengths are summarized in Table 7.

Table 7: Oscillator strengths for *t*-BuOOH $\Delta v_{OH} = 5$ by FTIR-CRD. Values are multiplied by $\times 10^{10}$.

	Free fit	Direct mean
Total	4.37 ± 0.25	4.43
OH	1.91 ± 0.12	1.94
Combi	1.06 ± 0.064	1.03
Combi2	0.243 ± 0.022	0.225

5.1.6 *t-BuOOH comparison of regions and calculations*

The determined oscillator strengths are summarized in Table 8 and compared to literature experimental values and a 3D local mode model. The theoretical model is

made by Emil Vogt and includes the OH-stretch, OO-stretch and OOH-bend evaluated at the equilibrium COOH torsional angle. The model uses a CCSD(T)-F12a/cc-pVDZ-F12 electronic structure. The spectroscopic techniques and experimental setup used by Wallberg[152] are identical to those used in this thesis. The only difference is that Wallberg does not correct for the solvent and impurity pressure contributions to the measured sample pressure. This results in all the reported values representing lower bounds. My reported numbers are all higher than Wallberg, ensuring no major issues with the experiments in this thesis. Homitsky[11] uses photoacustic spectroscopy with H_2O as an internal standard and estimate the vapour pressure of *t*-BuOOH from Rault's law. Surprisingly, the oscillator strengths determined by this technique is identical to the ones determined in this work. My reported standard errors are lower than Homitsky's, thus increasing the confidence in the determined number. Bassandorj[65] reports an oscillator strength for the fundamental OH-stretching transition. The value is a factor of 2 below both the experimentally determined value of this thesis and the theoretically determined value and a factor 1.5 below Wallbergs lower limit. Bassandorj uses chemical titration to determine the *t*-BuOOH partial pressure. This approach may be somewhat flawed.

Table 8: Oscillator strengths for *t*-BuOOH $\Delta v_{OH} = 1 - 5$ by FTIR-CRD and 3D local mode model. Values have been multiplied by the factor in the second row. Error is reported as 1 standard error

		$\Delta v_{OH} = 1$	$\Delta v_{OH} = 2$	$\Delta v_{OH} = 3$	$\Delta v_{OH} = 4$	$\Delta v_{OH} = 5$
		$\times 10^6$	$\times 10^7$	$\times 10^8$	$\times 10^9$	$\times 10^{10}$
Expt.	f_{OH}	4.56 ± 0.15	8.28 ± 0.24	3.50 ± 0.11	1.92 ± 0.11	1.91 ± 0.12
	f_{combi}	0.459 ± 0.058	1.08 ± 0.06	0.594 ± 0.058	1.02 ± 0.066	1.06 ± 0.064
	f_{combi2}	-	-	-	-	0.243 ± 0.022
	f_{total}	-	-	4.32 ± 0.13^a	3.29 ± 0.19	4.37 ± 0.25
Theory	f_{OH}	4.65	8.32	4.34	2.82	3.27
Wallberg[152]	f_{OH}	3.47 ± 0.23	5.75 ± 0.19	2.00 ± 0.13	1.60 ± 0.13	1.75 ± 0.18
Homitsky[11]	f_{OH}	-	-	-	1.92 ± 0.34	1.92 ± 0.56
Bassandorj[65]	f_{OH}	$2.26 \pm 5\%$				

[a]Absorbance is integrated from 10065 cm^{-1} - 10541 cm^{-1} also including the difference band and combination band.

The theoretical f-values in Table 8 are calculated with a LM model that does not include the torsion mode. With increasing number of quanta the intensity of the OH-stretch, f_{OH}, is increasingly redistributed into the surrounding combination states. In the $\Delta v_{OH} = 1 - 2$ regions, the calculated f_{OH}-values are best compared with the f_{OH}-row in the experiments. Already in $\Delta v_{OH} = 3$, the theoretical value overestimates the OH-stretching intensity by ca. 25%. The theoretical value is exactly that of the determined f_{total}-value. Calculations show that Franck-Condon sharing of intensity should not be very pronounced in this region[60] and the perfect agreement is more probable due to cancellation of error. For $\Delta v_{OH} = 4 - 5$, the theoretical number is best compared with the total integrated intensity, f_{total}. Now the calculated oscillator strength is slightly underestimated by 14% and 25%.

The relative intensities of the OH-stretching band and the combination bands are calculated with a (3+1)D LM model.[60] The comparison is summarized in Table 9. In the $\Delta v_{OH} = 1 - 3$ regions, the calculations show good agreement with experiments, but underestimate the relative intensities of the combination band(s) in the $\Delta v_{OH} = 4 - 5$ regions.

Table 9: Relative intensities for *t*-BuOOH $\Delta v_{OH} = 1 - 5$. values are reported as %.

		$\Delta v_{OH} = 1$	$\Delta v_{OH} = 2$	$\Delta v_{OH} = 3$	$\Delta v_{OH} = 4$	$\Delta v_{OH} = 5$
Expt	combi/OH	10.1	13.0	17.0	53.1	55.5
	combi2/OH	-	-	-	-	12.7
Theory	combi/OH	12.9	10.6	17.0	28.3	39.5
	combi2/OH	-	-	-	-	5.76

In conclusion, the OH-stretching bands and the OH/COOH combination band(s) are recorded in the $\Delta v_{OH} = 1 - 5$ regions using a combination of regular FTIR spectroscopy and our coupled FTIR-CRD spectrometer. The relative intensity of the combination band is observed to grow with OH quanta due to an increase in intensity sharing by the bright OH-stretching transition. The lower bounds determined by Wallberg by not removing the solvent hold for the observations in this work. Efficiently phase extracting the sample into DCM and drying it and spectrally removing trace impurities significantly improves the resulting f-values. In the $\Delta v_{OH} = 5$ region, a

second combination feature arising from two quanta excitation of the COOH torsion mode is clearly observed. This feature was not previously observable using our setup due to the insufficient S/N. The improvements made on the setup made the detection and quantification of these combination bands possible.

5.2 ISOPRENE

5.2.1 *Overview*

Isoprene spectra are recorded using a variety of experimental techniques. This thesis focuses on the experimental work associated with obtaining high quality spectra in the region covered by the JWST, 350 cm^{-1} - 16666 cm^{-1}, and at a similar resolution, $R > 1000$).[14,15] In our lab we can currently cover 600 cm^{-1} - 17050 cm^{-1} with a sufficient S/N, linear absorption and absolute intensities. This allows us to record spectra of isoprene including everything from the very intense C=CH_2 out-of-plane bending transition with two sharp peaks at 893 cm^{-1} and 906 cm^{-1}, which are often used for satellite measurements,[188] all the way up to the $\Delta v_{CH} = 6$ transition with a peak absorption at 16604 cm^{-1}. The spectral region covered by the FTIR and the region covered by the dispersive UV-Vis spectrometer with InGaAs detector were recorded by bachelor student Vera S. Hansen and the spectra are previously published in Hansen's bachelor thesis.[120] The spectra covered by the UV-Vis spectrometer with PMT detector and all the CRD spectra are recorded by myself. The dispersive spectrometer, which is described in Section 3.2.1, is hereon referred to as "UV-Vis-NIR". For this thesis all data treatment of the raw data have been done independently by myself. The spectrum of isoprene is quite complicated due to the many similar but distinct CH-stretching oscillators. Peak assignment is largely left out of this thesis but can be found in Sofie Markussen's master's thesis, which is focused on the topic of assignment using local mode theory.[189]

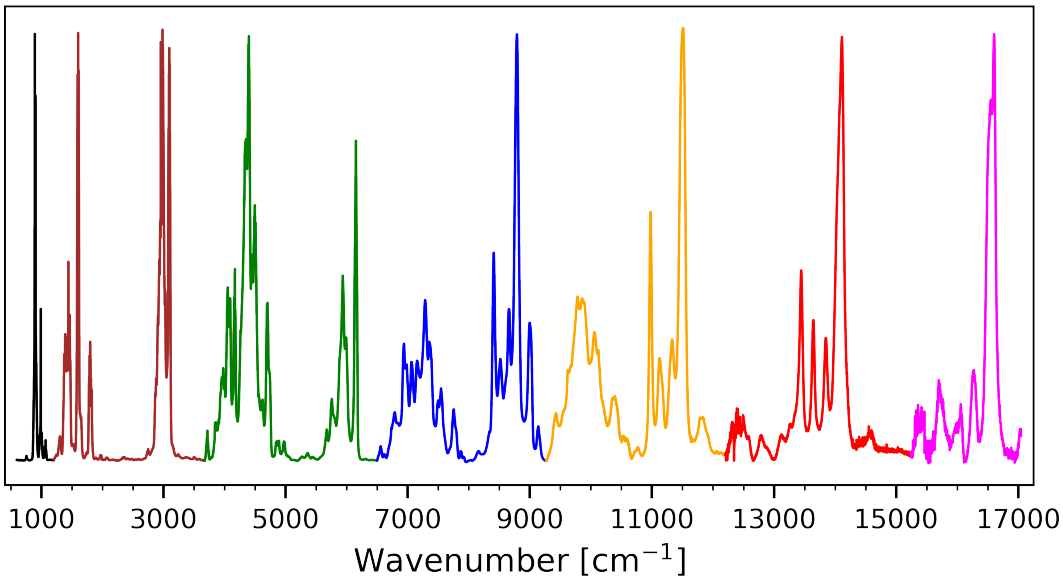

Figure 55: Isoprene full spectrum. Recorded with FTIR, UV-Vis-NIR and CRD. The colors signify the use of different scaling factors. The scaling factors are: black=1, brown=5, green=10^2, blue=2×10^3, orange=3×10^4, red=3×10^5, magenta=3×10^6.

The MIR/NIR/VIS spectrum of isoprene is recorded in the range 600 cm^{-1} to 17050 cm^{-1} and is shown in Figure 55. The CH-stretching transitions are recorded from the fundamental transition to the $\Delta v_{CH} = 6$. The CH-transitions range in intensity by six orders of magnitude. Because of this large intensity difference, several experimental procedures are needed in order to cover the range. These are summarised in Table 10.

Table 10: Isoprene experimental details

Expt. #	Effective Range [cm^{-1}]	Instrument	Light source	Beamsplitter / Detector	Cell / path length
1	600-5000	FTIR	MIR	KBr / LN-MCT	KBr / 10 cm
2	3500-10000	FTIR	NIR	CaF2 / LN-MCT	CaF2 / 100 cm
3	6300-11600	FTIR	NIR	CaF2 / LN-MCT	KBr / 1500 cm
4	10475-12265	UV-Vis-NIR	Tungsten	InGaAs	KBr / 1500 cm
5	11630-14810	UV-Vis-NIR	Tungsten	PMT	KBr / 1500 cm
6	12490-13780	CRD	Idler Beam	PMT	755 nm mirrors
7	13510-14072	CRD	Idler Beam	PMT	675 nm mirrors
8	14085-15865	CRD	Signal Beam	PMT	675 nm mirrors
9	15430-17055	CRD	Signal Beam	PMT	610 nm mirrors

As is observed from the second column, the various spectroscopic techniques and spectrometer settings are selected such that all regions overlap all the way from start to finish by at least a couple 100 cm^{-1}. In the FTIR region, this means that CH-stretching bands can be recorded using different cells with different path lengths, thus validating the assumed path lengths of the cells and the relative intensities between neighbouring manifolds. This is completely analogous to the procedure described in Section 5.1.2, although only the value from the primary experimental combination at each region is reported here.

Another important reason for achieving the overlap is to be able to stitch the spectrum together with a well-defined baseline. If a good baseline can be defined in the lower energy region, which is covered by the very robust FTIR spectrometer, then the cross-section spectra for the following regions can be baseline-corrected with the previous region as a reference, across all spectrometers, all the way up to 17050 cm^{-1}. Baseline corrections can be tricky, especially when the baseline curves in one or more directions or the absorbing species has a very densely populated spectrum as is the case for isoprene. In the FTIR and UV-Vis-NIR/InGaAs region, the baseline is corrected by 3rd order polynomials with the regions listed in Table 11 assumed as zero absorption. The UV-Vis-NIR/PMT region is corrected with both a polynomial fit and a small constant to best fit the previous spectrum. In the CRD spectra, the baselines are relatively straight and can be corrected by a constant shift. The highest energy region (expt. 9) is locally baseline-corrected in order to do the integration *(vide infra)*. In Table 11, the details regarding baseline corrections for each experiment are presented together with the intervals, which they contribute to the total spectrum.

Table 11: Experimental ranges and baseline corrections. The ranges listed are the contributions to the full spectrum (Figure 55) from each experiment.

Expt. #	Used in range [cm^{-1}]	Zero-points	Corr. type
1	600-3672	[708,718], [2240,2270], [3652,3680], [4932,4953]	3rd order pol.
2	3672-6489	[2222,2267], [3667,3680], [5177,5193], [6475,6504], [7965,8100]	3rd order pol.
3	6489-10674	[6475,6504],[7965,8100], [9243,9337],[10630,10705]	3rd order pol.
4	10674-11640	[10652,10700],[12150,12250]	3rd order pol.
5	11640-12494	[11700,12200][a],[12620,12746], [12975,13120],[9243,9337],[14300,14800]	3rd order pol.
6	12494-13600	Match UV-Vis-NIR	Const.
7	13600-14072	Match UV-Vis-NIR	Const.
8	14085-15465	Match UV-Vis-NIR + prev. CRD	Const.
9	15465-17055	Match prev. CRD	Const.

[a]Overlapping region with previous spectrum range. Contains absorbance from combination band. Baseline is fitted in this region to give best as possible overlap with previous region.

5.2.2 *Absorbance spectra* $\Delta v_{CH} = 1 - 4$

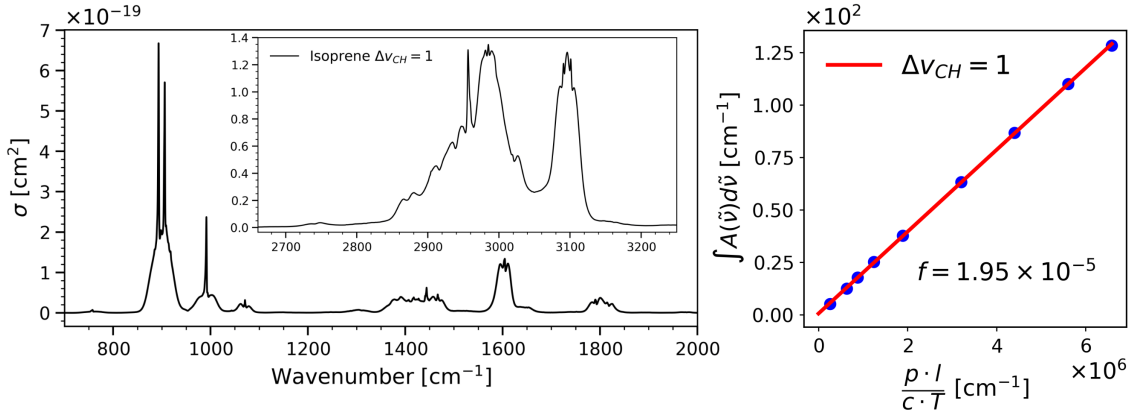

Figure 56: Isoprene fundamental region. Recorded with FTIR. CH-stretching band integrated between 2700 - 3280 cm^{-1}.

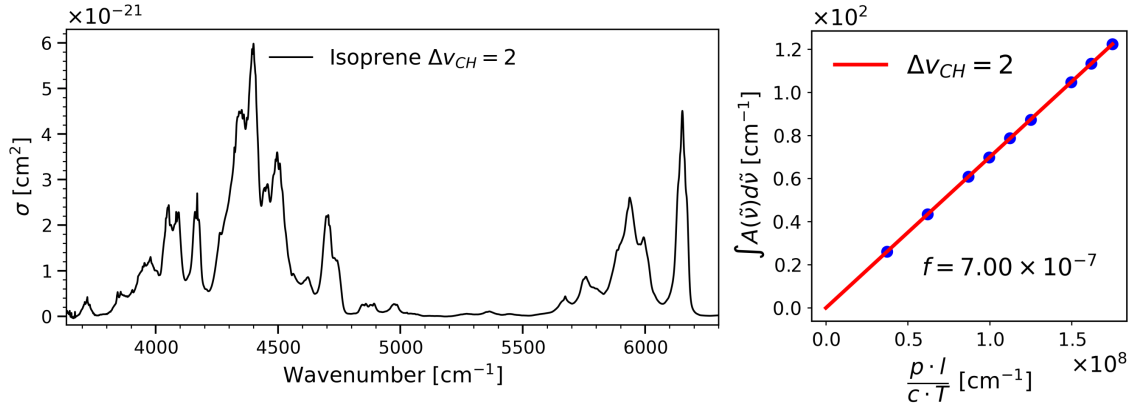

Figure 57: Isoprene $\Delta v_{CH} = 2$ region. Recorded with FTIR. CH-stretching band integrated between 5527 - 6370 cm^{-1}.

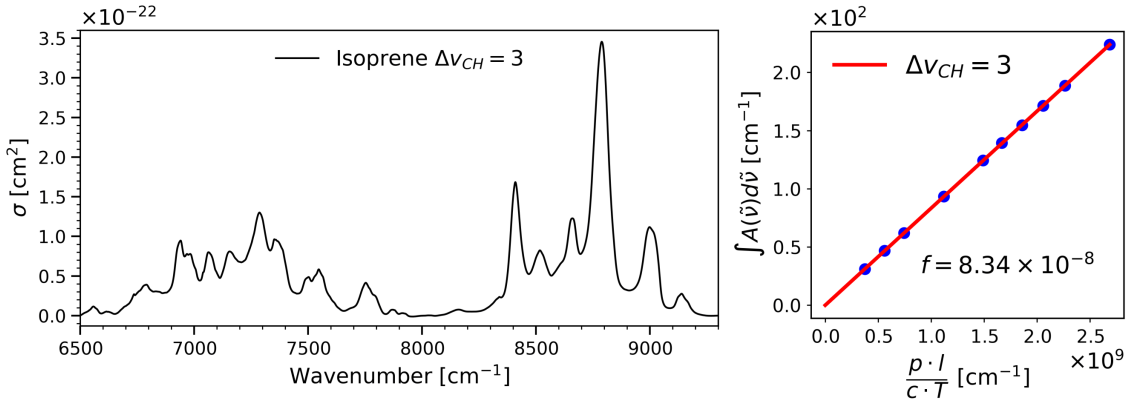

Figure 58: Isoprene $\Delta v_{CH} = 3$ region. Recorded with FTIR. CH-stretching band integrated between 8200 - 9250 cm^{-1}.

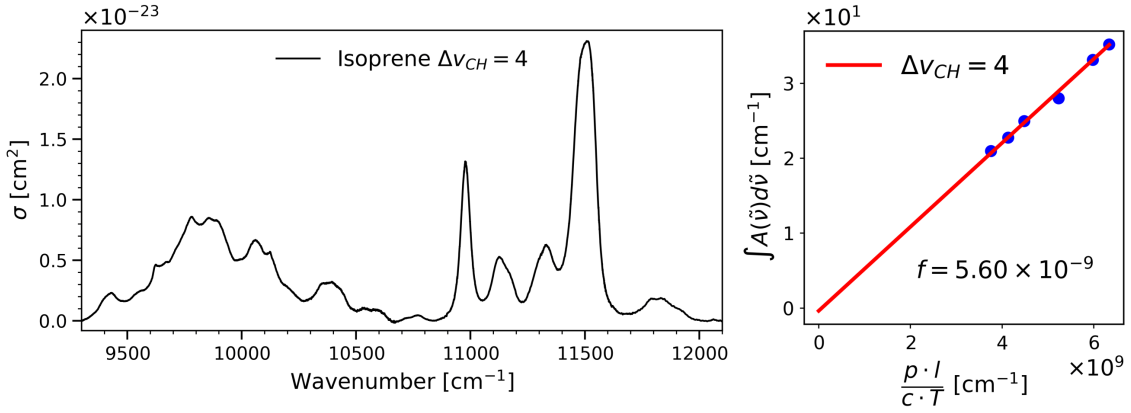

Figure 59: Isoprene $\Delta v_{CH} = 4$ region. Recorded with UV-Vis-NIR. CH-stretching band integrated between 10830 - 11680 cm^{-1}.

In Figures 56 to 59, isoprene is recorded on the FTIR and the UV-Vis-NIR spectrometer with well-defined path lengths and pressures. The S/N is within the trivial range and spectra can easily be recorded fast and with a low degree of error. The spectra are recorded with absorbance on the second axis and the integrated absorbance is fitted against pressure, path length and temperature in order to give the oscillator strength of the CH-stretching band following Equation 27. The fits all have an intercept close to zero and the difference between determining the oscillator strength with and without an intercept is minimal (*vide infra* Table 12). The linear fit is shown to the right in the aforementioned figures.

The spectra are presented as the mean of the absorption cross-sections, σ, to the left in the above figures. The spectra in the $\Delta v_{CH} = 2-4$ regions include both the v'th excited CH-stretching band and a low energy band that is a combination band consisting of $v-1$ quanta CH-stretches + 1 quantum of, primarily, HCH-bends. When increasing the CH-stretching quanta, the combination band becomes less intense relative to the CH-stretching band and moves closer in energy to the CH-strething band. The decreasing energy difference can be explained by considering the Morse oscillator (Equation 15).

The two types of transitions can be written in the notation $|v\rangle_s |v\rangle_b$ where s signifies the CH-stretching mode and b the HCH-bending modes. In the two quanta manifold region, the combination band $|1\rangle_s |1\rangle_b$ will have the Morse transition energy expression

$$\tilde{E}_{11} = \tilde{\omega}_s - 2\tilde{\omega}_s x_s + \tilde{\omega}_b - 2\tilde{\omega}_b x_b \tag{65}$$

whereas the $|2\rangle_s |0\rangle_b$ transition will have

$$\tilde{E}_{20} = \tilde{\omega}_s - 6\tilde{\omega}_s x_s \tag{66}$$

It can thus be seen that 6 vs. 4 anharmonicities, $\tilde{\omega}x$, are subtracted for the pure transition compared to the combination band with the same total quanta of excitation. This difference increases with increasing quanta. In the three quanta manifold the energy expressions are

$$\begin{aligned} \tilde{E}_{21} &= 2\tilde{\omega}_s - 6\tilde{\omega}_s x_s + \tilde{\omega}_b - 2\tilde{\omega}_b x_b \\ \tilde{E}_{30} &= 3\tilde{\omega}_s - 12\tilde{\omega}_s x_s \end{aligned} \tag{67}$$

And in the four quanta manifold

$$\begin{aligned} \tilde{E}_{31} &= 3\tilde{\omega}_s - 12\tilde{\omega}_s x_s + \tilde{\omega}_b - 2\tilde{\omega}_b x_b \\ \tilde{E}_{40} &= 4\tilde{\omega}_s - 20\tilde{\omega}_s x_s \end{aligned} \tag{68}$$

Thus the difference in added anharmonicity increases. Additionally, VPT2 calculations suggest, that the anharmonicities are larger for the CH-stretches than the CCH bends, thus increasing the observed effect. This means that the bands will converge with increasing quanta of excitation.

5.2.3 *Comparison with VPT2*

VPT2 calculations were done at the B3LYP level of theory with an AVTZ basis. The largely semi-rigid nature of isoprene makes it a reasonable candidate for this type of calculation. Isoprene has one methyl rotor, which is quite poorly described by the VPT2 model as it is a periodic triple well potential. Inspection of the force constants reveals that the mode has no cubic force constant and a very large reduced quartic force constant of 5500 cm^{-1}, which is a clear sign of a LAM mode. Modes, which do not have convergent corrections with expansion order, may cause problems in the VPT2 calculations. Calculations are done with and without this mode frozen, which turned out to have only a small effect on the resulting spectrum. The comparison with the fundamental region and the $\Delta v_{CH} = 2$ region is shown in Figures 60 and 61 for the VPT2 calculation with Me-rotor frozen.

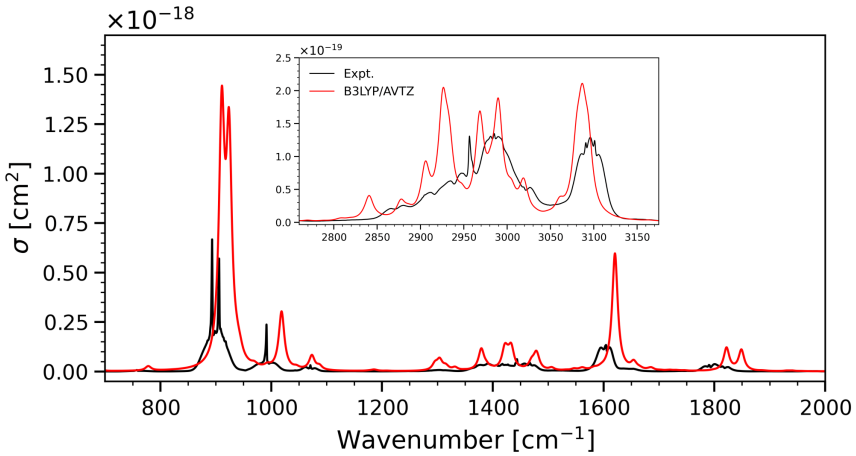

Figure 60: Isoprene comparison with VPT2 in the fundamental region

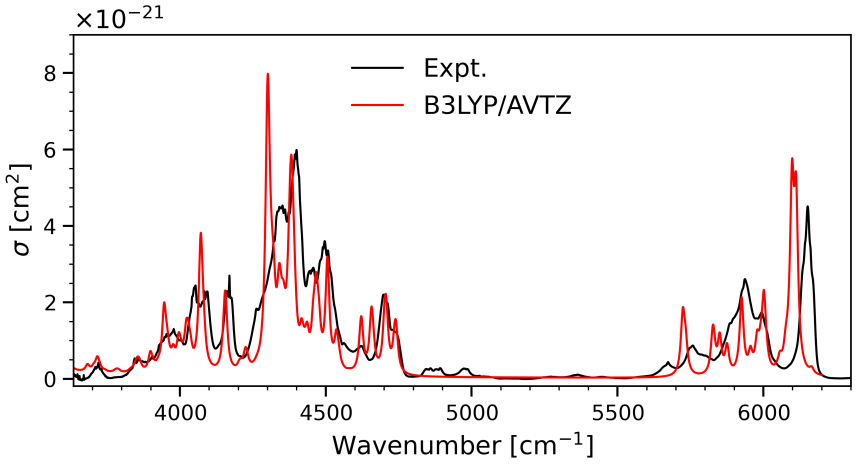

Figure 61: Isoprene comparison with VPT2 in the $\Delta v_{CH} = 2$ region

The VPT2 performs quite well in the fundamental region with a small overestimation of $\tilde{\nu}$ for most transitions in the region below 2000 cm^{-1}. The CH-stretching band is also nicely matched with some deviations. The theoretical oscillator strength for the CH band is overestimated by ca. 25%. In the 2-quanta manifold, the match of the VPT2 simulation with the experimental spectrum of the combination band is astonishing. Many peaks in the band can be assigned based on this VPT2 calculation. The CH-stretching $\Delta v_{CH} = 2$ band is also nicely matched and the theoretical oscillator strength is underestimated by ca. 15%.

5.2.4 *Spectra* $\Delta v_{CH} = 5 - 6$

In the higher overtone regions, the practical limit of absorbance spectroscopy with 15 meter path length starts to be tested. In Figure 63, the spectrum of the $\Delta v_{CH} = 5$ transition is shown as recorded with the UV-Vis-NIR spectrometer and the CRD. The difference in S/N is striking with a ca. 15:1 improvement on the CRD compared to the UV-Vis-NIR. Further, the energy resolution is measured to be ca. 5 cm^{-1} for the CRD in this region compared with the set 12 cm^{-1} resolution on the UV-Vis-NIR. The traces are co-added measurements that took ca. 12 hours to record on the CRD and ca. 160 hours on the UV-Vis-NIR. To get the same noise level of the CRD on

the UV-Vis-NIR with the same energy resolution, it would take roughly 16 years of continuous operation.

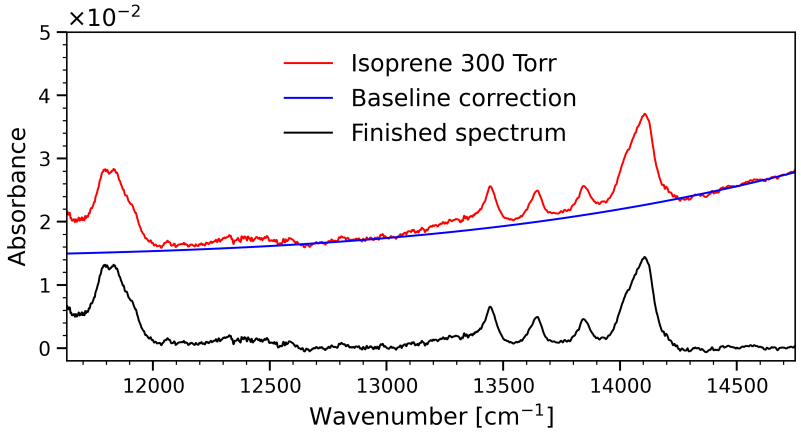

Figure 62: Isoprene $\Delta v_{CH} = 5$ region baseline correction. Recorded with UV-Vis-NIR. The red and blue trace is shifted up by 0.009 for visual purposes.

The oscillator strength is not comfortably determined in this region. On the UV-Vis-NIR, the experiments take ca. 40 hours at each pressure, limiting the practical number of experiments which can be recorded and fitted. In this work, only 3 measurements are fitted. Relatively high pressures of isoprene must be used in order to get a usable signal, which is still only 0.01 absorbance at the most. This introduces possible condensation on the optics and increased scattering, resulting in a tall and curved baseline. The UV-Vis-NIR spectrum (expt. 5) is baseline corrected by a 3rd order polynomial fit to make an acceptable baseline. My baseline fitting algorithm gets the correct shape of the baseline to a large extend, but is slightly biased to fit the baseline too high. This is due to the assumption that the zero-points listed in Table 11 are in fact zero in the spectrum. In this spectral region, the many transitions and combination bands distribute throughout the entire recorded region, and zero absorbance should, perhaps, not be expected. This is counter-acted slightly by fitting the region [11700 cm^{-1} - 12200 cm^{-1}] to overlap with the non-zero absorbance from the combination band recorded in the previous experiment 4 with the InGaAs detector. The initial linear fit of the three pressures shows a negative intercept, further suggesting that absorbance associated with isoprene is being cut off by the baseline. By shifting the baseline down by 0.000089 A units, the fit intercept became zero and the difference between integrated cross-section and free fit became $\sim$ 0. The baseline correction is shown in Figure 62 where this

minimal shift downward gives a baseline that looks completely justified, perhaps even still with regions having slightly negative absorbance.

The CRD spectra have a much more straight baseline. All CRD spectra can be perfectly aligned by shifting them down or up with a constant factor. The CRD spectra are adjusted up and down so as to match the UV-Vis-NIR spectrum as well as possible. This relies on the assumption, that the UV-Vis-NIR spectrum is accurately baseline-corrected. The CRD spectra are not perfectly in line with the UV-Vis-NIR spectrum in the entire region, so qualitative adjustments are done to best overlap the spectra. The CRD spectra and UV-Vis-NIR spectra can be seen together in Figure 63.

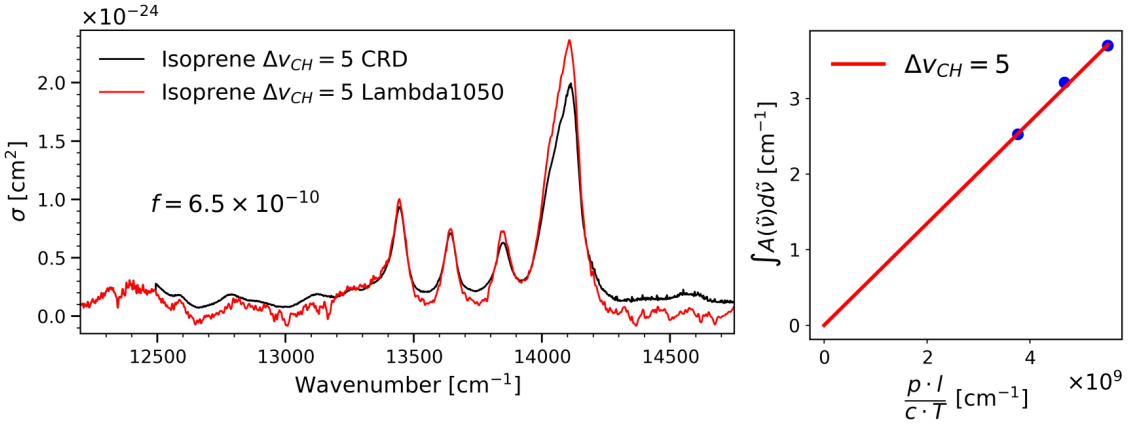

Figure 63: Isoprene $\Delta v_{CH} = 5$ region. Recorded with UV-Vis-NIR and CRD. The oscillator strength is shown in the left frame to emphasise that it is not given by the linear fit, which obtained with the UV-Vis-NIR measurements. CH-stretching band is integrated between 13245 - 14290 cm^{-1}.

Despite the limited S/N, the UV-Vis-NIR does, however, have a well-defined pressure and path length. The cavity ringdown has a less defined path length, which ultimately depends on the R_L-calibration and the operation of the mass flow controllers, which have an estimated standard error of 5%. Due to the design of the OPO-laser, the small range 14071-14085 cm^{-1} on the low energy shoulder of the main band cannot be recorded and has to be interpolated. The whole band is recorded with three different sets of optics on different days and so the only way to estimate the oscillator strength is to integrate the stitched together mean cross-section spectra.

The linear fit on the three UV-Vis-NIR data points gives $f = (6.7 \pm 0.5) \times 10^{-10}$ and the direct integrated mean cross section of the CRD spectra gives 6.5×10^{-10}. Integrating the mean cross section may introduce a bias as a 0-intercept is assumed, but the close spectral overlap with the UV-Vis-NIR instrument, which has 0 intercept, the CRD baseline is assumed to be representative. The similar f-values are in parts similar due to the adjustments to the baseline to make the spectra overlap and this should therefore not be taken as a sign of accuracy by itself. The baseline corrections needed on the CRD spectra are, however, small and it is encouraging that the numbers are not widely different. I trust the CRD measurement more due to the much higher S/N, higher resolution and more straight baseline. I report the oscillator strength as that determined by the CRD measurements and approximate the standard error as 8% which should reflect the variance in integrated cross section which I got with slightly higher or lower baselines in the CRD spectra, the intrinsic standard error on the CRD experiment (R_L and pressure) and the corroboration by the partly independent UV-Vis-NIR data. The final oscillator strength value for the $\Delta v_{CH} = 5$ band, which is further printed in bold in Table 12, is $f = (6.5 \pm 0.5) \times 10^{-10}$.

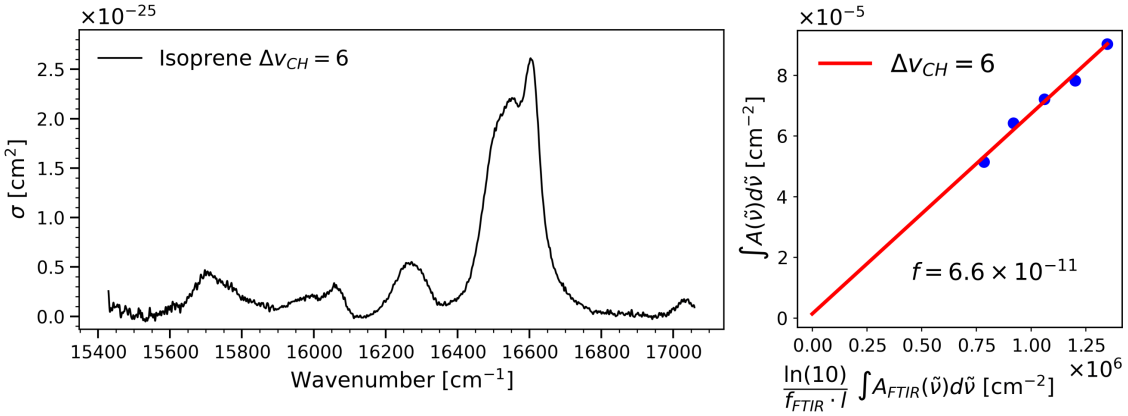

Figure 64: Isoprene $\Delta v_{CH} = 6$ region. Recorded with CRD. CH-stretching band integrated between 15540 - 16900 cm^{-1}.

In the $\Delta v_{CH} = 6$ region, which is shown in Figure 64, the entire band is recorded in the same scan with the same set of optics. The resolution is measured to be 4-5 cm^{-1} in the region, which corresponds to a resolving power of $R \sim 3300$. The signal to noise is quite good in this region despite the incredibly weak intensity of the overtone. These experiments were conducted as the very last before the 3H-crystal in the OPO

laser gave up and more than 50% of the laser shots were bad shots that were filtered away. With a new crystal the S/N could easily improve and the next overtone should be achievable with a satisfactory S/N level. As the whole spectrum was recorded in the same scan, it is possible to do a proper linear fit of the integrated absorption coefficient as a function of FTIR intensity following Equation 51. The absorbance band lies on an almost constant background of ca. $1.1 \cdot 10^{-25}$ cm^2 with slight curves up or down depending on the sample. The shifted baseline, which might be a very long tail from a higher energy electronic transition or the like, is quite high compared to the rest of the very minute signal. A local baseline correction is therefore made in order to integrate the absorption associated with the vibrational band. The baseline is corrected by a 2nd order polynomial. The linear fit has an intercept close to zero, which further corroborates the integrity of the baseline. The standard error on the reported oscillator strength is estimated from a 5% error on R_L, 4% error on the fit, and 4% collective error on the baseline and integration limits and some small contributions for pressure and temperature. This combines in a norm square to give ca. 7% standard error on the reported oscillator strength. The oscillator strengths and standard errors are summarised for all regions in Table 12.

Table 12: Isoprene oscillator strengths. Values have been multiplied with the factors in the first column. Uncertainties are reported as standard errors. The free fit value is the best value for all regions except for $\Delta v_{CH} = 5$, where the integrated cross section should be used instead.

	Free Fit	$\int \sigma$
$\Delta v_{CH} = 1$ $\times 10^5$	1.95 ± 0.03 (FTIR)	1.99 (FTIR)
$\Delta v_{CH} = 2$ $\times 10^7$	7.00 ± 0.12 (FTIR)	6.99 (FTIR)
$\Delta v_{CH} = 3$ $\times 10^8$	8.34 ± 0.15 (FTIR)	8.33 (FTIR)
$\Delta v_{CH} = 4$ $\times 10^9$	5.60 ± 0.14 (UV-Vis-NIR)	5.51 (UV-Vis-NIR)
$\Delta v_{CH} = 5$ $\times 10^{10}$	6.7 ± 0.5 (UV-Vis-NIR)	**6.5 ± 0.7 (CRD)**
$\Delta v_{CH} = 6$ $\times 10^{11}$	6.6 ± 0.5 (CRD)	6.7 (CRD)

In conclusion, the spectrum of isoprene has been recorded with 3 different instruments and we have constructed a completely overlapping spectrum from 600 cm^{-1} all the way up to 17050 cm^{-1}. The spectrum has a resolution which is comparable to the spectral instruments on the JWST. I report experimental oscillator strengths for the CH-stretching bands for the fundamental transitions and the first 5 overtones. The spectrum is shown with an absolute intensity axis and can be used not only to detect, but to quantify the amount of isoprene present in a gaseous sample at room temperature. Isoprene is one of the most promising biomarkers for chemically reduced carbon-based life and its absorption bands should be seriously considered in future work in the search for exoplanetary life. Further, isoprene, which is the most emitted biogenic hydrocarbon into the troposphere next to methane,[31] can be accurately quantified from satellite measurements, using the above oscillator strengths as reference.

6

CONCLUSION

In this PhD thesis I have shown the experimental and theoretical work that was conducted on a range of atmospherically relevant species. The hydrogen bound species include *tert*-butyl hydroperoxide dimer, methanol dimer, trimer and tetramer and water-trimethylamine. The experimental investigation of these systems show different peculiarities which can all be basis for more in-depth theoretical studies. FTIR spectroscopic experiments at cryogenic and room temperature of *tert*-butyl hydroperoxide dimer showed an interesting middle point in hydrogen bond strength between that of alcohols and organic acids and an observed redshift that was attenuated by potential energy-coupling between the two OH-oscillators. Methanol dimer was chosen as a model compound to demonstrate the temperature effects on the OH_b-stretching band shape. New considerations for spectral subtraction was needed in order to obtain usable room temperature spectra of methanol dimer. The dimer was further used as a probe for the vibrational temperature in the Gratin supersonic jet-expansion experiment in Göttingen. A calibration curve was constructed from the measurements of full width at half max and from the findings of the theoretical model. The advances in spectral subtraction enabled the acquisition of methanol dimer, trimer and tetramer spectra. Together with the implementation of a reduced dimensional VPT2 model, highly accurate Gibbs energies were obtained for the methanol clusters at room temperature. These values may be used as proxies for other atmospherically relevant species such as water clusters for which corresponding values are significantly harder to accurately obtain theoretically as well as experimentally. The water-trimethylamine complex is together with sulphuric acid one of the most important complexes in the formation of cloud condensation nuclei. The dynamics of the complex should therefore be of high interest

to the community. Spectroscopically, the room temperature band, which has previously been recorded show an unexpectedly structured OH_b-stretching band. In a combined effort of argon matrix isolation experiments and He jet-expansion experiments, we were able to identify a resonance between 3(4) different vibrational states which give rise to the complex band shape. By recording the complex in three different media we were furthermore able to tune the resonances to the point of observing avoided crossings between the states.

The absolute intensities of *tert*-butyl hydroperoxide and isoprene were obtained. This was done by rigorous experimental work using FTIR, dispersive UV-Vis-NIR and cavity ring-down spectroscopy. The latter had to be completely refurbished and improved in order to obtain the sensitivity needed for the higher overtones. Much work went into carefully coupling the light into the TEM_{00} mode of the cavity and the effective path length and the energy axis was calibrated to give the most accurate spectra. For the hydroperoxide, the intensities were determined for the fundamental OH-stretching transition all the way to the fourth overtone. The improved signal to noise made it possible to determine the oscillator strengths with high accuracy and to identify an additional combination band which was previously not detectable on our setup. The findings further corroborated earlier studies on the coupling between the OH-stretch and the COOH torsion mode. Isoprene was recorded with three different instrument and a variety of different optics to cover the entire spectral region from 600 cm^{-1} all the way to 17000 cm^{-1} covering the majority of the range of the James Webb Space Telescope. The spectrum was constructed as an unbroken spectrum and with transitions spanning 6 orders of magnitude in intensity. The recorded spectrum may be of interest to the astro-biology community as isoprene can serve as a potential biomarker for life on exoplanets.

BIBLIOGRAPHY

[1] A. J. Ångström, "Optiska Undersökningar," *Kongliga Svenska Vetenskaps-Akademiens Handlingar*, vol. 40, pp. 333–360, 1852.

[2] J. Blamer, "Notiz über die Spectrallinien des Wasserstoffs," *Annalen der Physik und Chemie*, vol. 25, pp. 80–87, 1885.

[3] J. R. Rydberg, "Researches sur la Constitution des Spectres d'Émission des Éléments Chimiques," *Kongliga Svenska Vetenskaps-Akademiens Handlingar*, vol. 23, pp. 1–177, 1885.

[4] N. Bohr, "I. On the Constitution of Atoms and Molecules," *The London, Edinburgh, and Dublin Philosophical Magazine and Journal of Science*, vol. 26, no. 151, pp. 1–25, 1913.

[5] H. G. Kjaergaard, H. Yu, B. J. Schattka, B. R. Henry, and A. W. Tarr, "Intensities in Local Mode Overtone Spectra: Propane," *J. chem. Phys.*, vol. 93, pp. 6239–6248, 11 1990.

[6] J. Wallberg and H. G. Kjaergaard, "Absolute Fundamental and Overtone OH and OD Stretching Intensities of Alcohols," *Spectrochim. Acta A Mol. Biomol. Spectrosc.*, vol. 208, pp. 315–324, 2019.

[7] B. J. Miller, L. Du, T. J. Steel, A. J. Paul, A. H. Södergren, J. R. Lane, B. R. Henry, and H. G. Kjaergaard, "Absolute Intensities of NH-Stretching Transitions in Dimethylamine and Pyrrole," *J. Phys. Chem. A*, vol. 116, no. 1, pp. 290–296, 2012.

[8] H. G. Kjaergaard, D. M. Turnbull, and B. R. Henry, "Intensities of CH- and CD-Stretching Overtones in 1,3-Butadiene and 1,3-Butadiene-d6," *J. Chem. Phys.*, vol. 99, pp. 9438–9452, 12 1993.

[9] K. R. Lange, N. P. Wells, K. S. Plegge, and J. A. Phillips, "Integrated Intensities of O-H Stretching Bands: Fundamentals and Overtones in Vapor-Phase Alcohols and Acids," *J. Phys. Chem. A*, vol. 105, no. 14, pp. 3481–3486, 2001.

[10] H. Zhang, C. M. Roehl, S. P. Sander, and P. O. Wennberg, "Intensity of the Second and Third OH Overtones of H_2O_2, HNO_3, and HO_2NO_2," *J. GeoPhys. Res. Atmos.*, vol. 105, no. D11, pp. 14593–14598, 2000.

[11] S. C. Homitsky, S. M. Dragulin, L. M. Haynes, and S. Hsieh, "O-H Stretch Overtone Excitation in Methyl and Ethyl Hydroperoxides," *J. Phys. Chem. A*, vol. 108, no. 44, pp. 9492–9499, 2004.

[12] D. L. Howard, P. Jørgensen, and H. G. Kjaergaard, "Weak Intramolecular Interactions in Ethylene Glycol Identified by Vapor Phase OH-Stretching Overtone Spectroscopy," *J. Am. Chem. Soc.*, vol. 127, no. 48, pp. 17096–17103, 2005.

[13] P. Bertran, "Study of the Vibrational Frequencies and Intensities of Pinacolyl Alcohol and Neopentyl Alcohol," Master's thesis, University of Copenhagen, Department of Chemistry, 2020.

[14] G. S. Wright, G. H. Rieke, A. Glasse, M. Ressler, M. G. Marín, J. Aguilar, S. Alberts, J. Álvarez Márquez, I. Argyriou, K. Banks, P. Baudoz, A. Boccaletti, P. Bouchet, J. Bouwman, B. R. Brandl, D. Breda, S. Bright, S. Cale, L. Colina, C. Cossou, A. Coulais, M. Cracraft, W. D. Meester, D. Dicken, M. Engesser, M. Etxaluze, O. D. Fox, S. Friedman, H. Fu, D. Gasman, A. Gáspár, R. Gastaud, V. Geers, A. M. Glauser, K. D. Gordon, T. Greene, T. R. Greve, T. Grundy, M. Güdel, P. Guillard, P. Haderlein, R. Hashimoto, T. Henning, D. Hines, B. Holler, Örs Hunor Detre, A. Jahromi, B. James, O. C. Jones, K. Justtanont, P. Kavanagh, S. Kendrew, P. Klaassen, O. Krause, A. Labiano, P.-O. Lagage, S. Lambros, K. Larson, D. Law, D. Lee, M. Libralato, J. L. Alverez, M. Meixner, J. Morrison, M. Mueller, K. Murray, M. Mycroft, R. Myers, O. Nayak, B. Naylor, B. Nickson, A. Noriega-Crespo, G. Östlin, B. O'Sullivan, R. Ottens, P. Patapis, K. Penanen, M. Pietraszkiewicz, T. Ray, M. Regan, A. Roteliuk, P. Royer, P. Samara-Ratna, B. Samuelson, B. A. Sargent, S. Scheithauer, A. Schneider, J. Schreiber, B. Shaughnessy, E. Sheehan, I. Shivaei, G. C. Sloan, L. Tamas, K. Teague, T. Temim, T. Tikkanen, S. Tustain,

E. F. van Dishoeck, B. Vandenbussche, M. Weilert, P. Whitehouse, and S. Wolff, "The Mid-infrared Instrument for JWST and Its In-flight Performance," *PASP*, vol. 135, no. 1046, p. 048003, 2023.

[15] T. Böker, T. L. Beck, S. M. Birkmann, G. Giardino, C. Keyes, N. Kumari, J. Muzerolle, T. Rawle, P. Zeidler, Y. Abul-Huda, C. A. de Oliveira, S. Arribas, K. Bechtold, R. Bhatawdekar, N. Bonaventura, A. J. Bunker, A. J. Cameron, S. Carniani, S. Charlot, M. Curti, N. Espinoza, P. Ferruit, M. Franx, P. Jakobsen, D. Karakla, M. López-Caniego, N. Lützgendorf, R. Maiolino, E. Manjavacas, A. P. Marston, S. H. Moseley, P. Ogle, M. Perna, M. Peña-Guerrero, N. Pirzkal, R. Plesha, C. R. Proffitt, B. J. Rauscher, H.-W. Rix, B. R. del Pino, Z. Rustamkulov, E. Sabbi, D. K. Sing, M. Sirianni, M. te Plate, L. Úbeda, G. M. Wahlgren, E. Wislowski, R. Wu, and C. J. Willott, "In-orbit Performance of the Near-infrared Spectrograph NIRSpec on the James Webb Space Telescope," *PASP*, vol. 135, p. 038001, mar 2023.

[16] E. Arunan, G. R. Desiraju, R. A. Klein, J. Sadlej, S. Scheiner, I. Alkorta, D. C. Clary, R. H. Crabtree, J. J. Dannenberg, P. Hobza, *et al.*, "Defining the Hydrogen Bond: An account (IUPAC Technical Report)," *Pure Appl. Chem.*, vol. 83, no. 8, pp. 1619–1636, 2011.

[17] E. Arunan, G. R. Desiraju, R. A. Klein, J. Sadlej, S. Scheiner, I. Alkorta, D. C. Clary, R. H. Crabtree, J. J. Dannenberg, P. Hobza, *et al.*, "Definition of the Hydrogen Bond (IUPAC Recommendations 2011)," *Pure Appl. Chem.*, vol. 83, no. 8, pp. 1637–1641, 2011.

[18] A. S. Hansen, E. Vogt, and H. G. Kjaergaard, "Gibbs Energy of Complex Formation–Combining Infrared Spectroscopy and Vibrational Theory," *Int. Rev. Phys. Chem.*, vol. 38, no. 1, pp. 115–148, 2019.

[19] L. Du, K. Mackeprang, and H. G. Kjaergaard, "Fundamental and Overtone Vibrational Spectroscopy, Enthalpy of Hydrogen Bond Formation and Equilibrium Constant Determination of the Methanol–Dimethylamine Complex," *Phys. Chem. Chem. Phys.*, vol. 15, pp. 10194–10206, 2013.

[20] H. G. Kjaergaard, G. R. Low, T. W. Robinson, and D. L. Howard, "Calculated OH-Stretching Vibrational Transitions in the Water-Nitrogen and Water-Oxygen Complexes," *J. Phys. Chem. A*, vol. 106, no. 38, pp. 8955–8962, 2002.

[21] R. E. Hubbard and M. K. Haider, *Hydrogen Bonds in Proteins: Role and Strength. In: Encyclopedia of Life Sciences (ELS).* John Wiley & Sons, Ltd, 2010.

[22] J. A. Ippolito, R. S. Alexander, and D. W. Christianson, "Hydrogen Bond Stereochemistry in Protein Structure and Function," *J. Mol. Biol.*, vol. 215, no. 3, pp. 457–471, 1990.

[23] R. W. Hooft, C. Sander, and G. Vriend, "Positioning Hydrogen Atoms by Optimizing Hydrogen-Bond Networks in Protein structures," *Proteins: Struct., Funct., Bioinf.*, vol. 26, no. 4, pp. 363–376, 1996.

[24] I. K. McDonald and J. M. Thornton, "Satisfying Hydrogen Bonding Potential in Proteins," *J. Mol. Biol.*, vol. 238, no. 5, pp. 777–793, 1994.

[25] T. E. Creighton, "Stability of Folded Conformations: Current Opinion in Structural Biology 1991, 1: 5–16," *Curr. Opin. Struct. Biol.*, vol. 1, no. 1, pp. 5–16, 1991.

[26] R. Zhang, A. Khalizov, L. Wang, M. Hu, and W. Xu, "Nucleation and Growth of Nanoparticles in the Atmosphere," *Chem. Rev.*, vol. 112, no. 3, pp. 1957–2011, 2012.

[27] J. Zhao, A. Khalizov, R. Zhang, and R. McGraw, "Hydrogen-Bonding Interaction in Molecular Complexes and Clusters of Aerosol Nucleation Precursors," *J. Phys. Chem. A*, vol. 113, no. 4, pp. 680–689, 2009.

[28] J. H. Seinfeld and S. N. Pandis, *Atmospheric Chemistry and Physics: From Air Pollution to Climate Change.* John Wiley & Sons, 2016.

[29] A. Guenther, C. N. Hewitt, D. Erickson, R. Fall, C. Geron, T. Graedel, P. Harley, L. Klinger, M. Lerdau, W. McKay, *et al.*, "A Global Model of Natural Volatile Organic Compound Emissions," *J. GeoPhys. Res. Atmos.*, vol. 100, no. D5, pp. 8873–8892, 1995.

[30] A. Guenther, T. Karl, P. Harley, C. Wiedinmyer, P. I. Palmer, and C. Geron, "Estimates of Global Terrestrial Isoprene Emissions using MEGAN (Model of Emissions of Gases and Aerosols from Nature)," *Atmos. Chem. Phys.*, vol. 6, no. 11, pp. 3181–3210, 2006.

[31] A. B. Guenther, X. Jiang, C. L. Heald, T. Sakulyanontvittaya, T. Duhl, L. K. Emmons, and X. Wang, "The Model of Emissions of Gases and Aerosols from Nature version 2.1 (MEGAN2.1): an Extended and Updated Framework for Modeling Biogenic Emissions," *Geosci. Model Dev.*, vol. 5, no. 6, pp. 1471–1492, 2012.

[32] K. H. Møller, K. H. Bates, and H. G. Kjaergaard, "The Importance of Peroxy Radical Hydrogen-Shift Reactions in Atmospheric Isoprene Oxidation," *J. Phys. Chem. A*, vol. 123, no. 4, pp. 920–932, 2019.

[33] K. H. Møller, E. Praske, L. Xu, J. D. Crounse, P. O. Wennberg, and H. G. Kjaergaard, "Stereoselectivity in Atmospheric Autoxidation," *J. Phys. Chem. Lett.*, vol. 10, no. 20, pp. 6260–6266, 2019.

[34] F. Bianchi, T. Kurtén, M. Riva, C. Mohr, M. P. Rissanen, P. Roldin, T. Berndt, J. D. Crounse, P. O. Wennberg, T. F. Mentel, *et al.*, "Highly Oxygenated Organic Molecules (HOM) from Gas-Phase Autoxidation Involving Peroxy Radicals: A Key Contributor to Atmospheric Aerosol," *Chem. Rev.*, vol. 119, no. 6, pp. 3472–3509, 2019.

[35] J. D. Crounse, L. B. Nielsen, S. Jørgensen, H. G. Kjaergaard, and P. O. Wennberg, "Autoxidation of Organic Compounds in the Atmosphere," *J. Phys. Chem. Lett.*, vol. 4, no. 20, pp. 3513–3520, 2013.

[36] E. Praske, R. V. Otkjær, J. D. Crounse, J. C. Hethcox, B. M. Stoltz, H. G. Kjaergaard, and P. O. Wennberg, "Intramolecular Hydrogen Shift Chemistry of Hydroperoxy-Substituted Peroxy Radicals," *J. Phys. Chem. A*, vol. 123, no. 2, pp. 590–600, 2018.

[37] B. Bonn, R. von Kuhlmann, and M. G. Lawrence, "High Contribution of Biogenic Hydroperoxides to Secondary Organic Aerosol Formation," *Geophys. Res. Lett.*, vol. 31, no. 10, 2004.

[38] Intergovernmental Panel on Climate Change (IPCC), *The Earth's Energy Budget, Climate Feedbacks and Climate Sensitivity*, p. 923–1054. Cambridge University Press, 2023.

[39] U. Pöschl, "Atmospheric Aerosols: Composition, Transformation, Climate and Health Effects," *Angew. Chem. Int. Ed.*, vol. 44, no. 46, pp. 7520–7540, 2005.

[40] M. Kanakidou, J. Seinfeld, S. Pandis, I. Barnes, F. J. Dentener, M. C. Facchini, R. V. Dingenen, B. Ervens, A. Nenes, C. Nielsen, *et al.*, "Organic Aerosol and Global Climate Modelling: A Review," *Atmos. Chem. Phys.*, vol. 5, no. 4, pp. 1053–1123, 2005.

[41] European Environment Agency, "Europe's air quality status 2023," 2023. `https://www.eea.europa.eu/publications/europes-air-quality-status-2023` visited August 2024.

[42] WHO Air quality, Energy and Health, "Air Pollution is Responsible for 6.7 Million Premature Deaths Every Year," 2023. `https://www.who.int/teams/environment-climate-change-and-health/air-quality-and-health/health-impacts/types-of-pollutants` visited August 2024.

[43] WHO, "The Top 10 Causes of Death," 2024. `https://www.who.int/news-room/fact-sheets/detail/the-top-10-causes-of-death` visited August 2024.

[44] UN Environment Programme, "Pollution Action Note – Data You Need to Know," 2023. `https://www.unep.org/interactives/air-pollution-note` visited August 2024.

[45] D. W. Dockery, C. A. Pope, X. Xu, J. D. Spengler, J. H. Ware, M. E. Fay, B. G. Ferris, and F. E. Speizer, "An Association Between Air Pollution and Mortality in Six U.S. Cities," *N. Engl. J. Med.*, vol. 329, no. 24, pp. 1753–1759, 1993.

[46] S. Weichenthal, L. Pinault, T. Christidis, R. T. Burnett, J. R. Brook, Y. Chu, D. L. Crouse, A. C. Erickson, P. Hystad, C. Li, R. V. Martin, J. Meng, A. J. Pappin, M. Tjepkema, A. van Donkelaar, C. L. Weagle, and M. Brauer, "How low can you go? Air Pollution Affects Mortality at ery low Levels," *Sci. Adv.*, vol. 8, no. 39, p. eabo3381, 2022.

[47] Y. A. Awe, B. K. Larsen, and E. Sanchez-Triana, "The Global Health Cost of PM 2.5 Air Pollution: A Case for Action Beyond 2021," 2021. http://documents.worldbank.org/curated/en/455211643691938459/The-Global-Health-Cost-of-PM-2-5-Air-Pollution-A-Case-for-Action-Beyond-2021.

[48] M. Hippler, "Quantum Chemical Study and Infrared Spectroscopy of Hydrogen-Bonded $CHCl_3$–NH_3 in the Gas Phase," *J. Chem. Phys.*, vol. 127, no. 8, p. 084306, 2007.

[49] T. Häber, U. Schmitt, and M. A. Suhm, "FTIR-Spectroscopy of Molecular Clusters in Pulsed Supersonic Slit-Jet Expansions," *Phys. Chem. Chem. Phys.*, vol. 1, pp. 5573–5582, 1999.

[50] R. Wugt Larsen and M. A. Suhm, "Cooperative Organic Hydrogen Bonds: The Librational Modes of Cyclic Methanol Clusters," *J. Chem. Phys.*, vol. 125, p. 154314, 10 2006.

[51] M. I. Sulaiman, S. Yang, and A. M. Ellis, "Infrared Spectroscopy of Methanol and Methanol/Water Clusters in Helium Nanodroplets: The OH Stretching Region," *J. Phys. Chem. A*, vol. 121, no. 4, pp. 771–776, 2017. PMID: 28060504.

[52] M. Nedić, T. N. Wassermann, R. W. Larsen, and M. A. Suhm, "A Combined Raman- and Infrared Jet Study of Mixed Methanol–Water and Ethanol–Water Clusters," *Phys. Chem. Chem. Phys.*, vol. 13, pp. 14050–14063, 2011.

[53] R. A. Provencal, J. B. Paul, K. Roth, C. Chapo, R. N. Casaes, R. J. Saykally, G. S. Tschumper, and I. Schaefer, H. F., "Infrared Cavity Ringdown Spectroscopy of Methanol Clusters: Single Donor Hydrogen Bonding," *J. Chem. Phys.*, vol. 110, pp. 4258–4267, 03 1999.

[54] I. Doroshenko, V. Pogorelov, V. Sablinskas, and V. Balevicius, "Matrix-Isolation Study of Cluster Formation in Methanol: O–H Stretching Region," *J. Mol. Liq.*, vol. 157, no. 2, pp. 142–145, 2010.

[55] M. Van Thiel, E. D. Becker, and G. C. Pimentel, "Infrared Studies of Hydrogen Bonding of Methanol by the Matrix Isolation Technique," *J. Chem. Phys.*, vol. 27, pp. 95–99, 06 1957.

[56] U. Buck and I. Ettischer, "Vibrational Predissociation Spectra of Size Selected Methanol Clusters: New Experimental Results," *J. Chem. Phys.*, vol. 108, pp. 33–38, 01 1998.

[57] U. Buck and F. Huisken, "Infrared Spectroscopy of Size-Selected Water and Methanol Clusters," *Chem. Rev.*, vol. 100, no. 11, pp. 3863–3890, 2000.

[58] F. Huisken, A. Kulcke, C. Laush, and J. M. Lisy, "Dissociation of Small Methanol Clusters after Excitation of the O–H Stretch Vibration at 2.7 μ," *J. Chem. Phys.*, vol. 95, pp. 3924–3929, 09 1991.

[59] F. Huisken, M. Kaloudis, M. Koch, and O. Werhahn, "Experimental Study of the O–H Ring Vibrations of the Methanol Trimer," *J. Chem. Phys.*, vol. 105, pp. 8965–8968, 11 1996.

[60] E. Vogt, R. M. Huchmala, C. V. Jensen, M. A. Boyer, J. Wallberg, A. S. Hansen, A. Kjærsgaard, M. I. Lester, A. B. McCoy, and H. G. Kjaergaard, "Coupling of Torsion and OH-Stretching in *tert*-Butyl Hydroperoxide. II. The OH-Stretching Fundamental and Overtone Spectra," *J. Chem. Phys.*, vol. 154, no. 16, p. 164307, 2021.

[61] A. S. Hansen, R. M. Huchmala, E. Vogt, M. A. Boyer, T. Bhagde, M. F. Vansco, C. V. Jensen, A. Kjærsgaard, H. G. Kjaergaard, A. B. McCoy, *et al.*, "Coupling of Torsion and OH-Stretching in *tert*-Butyl Hydroperoxide. I. The Cold and Warm First OH-Stretching Overtone Spectrum," *J. Chem. Phys.*, vol. 154, no. 16, p. 164306, 2021.

[62] D. W. Chandler, W. E. Farneth, and R. N. Zare, "A Search for Mode-Selective Chemistry: The Unimolecular Dissociation of *t*-Butyl Hydroperoxide Induced by Vibrational Overtone Excitation," *J. Chem. Phys.*, vol. 77, no. 9, pp. 4447–4458, 1982.

[63] M. Likar, J. Baggott, and F. Crim, "Vibrationally Mediated Photodissociation of *t*-Butyl Hydroperoxide: Vibrational Overtone Spectroscopy and Photodissociation Dynamics," *J. Chem. Phys.*, vol. 90, no. 11, pp. 6266–6274, 1989.

[64] M.-C. Chuang, J. E. Baggott, D. W. Chandler, W. E. Farneth, and R. N. Zare, "Unimolecular Decomposition of t-Butylhydroperoxide by Direct Excitation of the 6–0 O—H Stretching Overtone," *Faraday Discuss. Chem. Soc.*, vol. 75, pp. 301–313, 1983.

[65] M. Baasandorj, D. K. Papanastasiou, R. K. Talukdar, A. S. Hasson, and J. B. Burkholder, "$(CH_3)_3COOH$ (*tert*-Butyl Hydroperoxide): OH Reaction Rate Coefficients between 206 and 375 K and the OH Photolysis Quantum Yield at 248 nm," *Phys. Chem. Chem. Phys.*, vol. 12, no. 38, pp. 12101–12111, 2010.

[66] C. V. Jensen, "Experimental Absolute Intensities of OH-Stretching Vibrational Transitions of *tert*-Butyl Hydroperoxide," Master's thesis, University of Copenhagen, Department of Chemistry, 2021.

[67] K. H. Møller, C. M. Tram, and H. G. Kjaergaard, "Side-by-Side Comparison of Hydroperoxide and Corresponding Alcohol as Hydrogen-Bond Donors," *J. Phys. Chem. A*, vol. 121, no. 15, pp. 2951–2959, 2017.

[68] M. Born and R. Oppenheimer, "Zur Quantentheorie der Molekeln," *Ann. Phys.*, vol. 389, no. 20, pp. 457–484, 1927.

[69] E. Vogt, *Vibrational Models in Internal Coordinates*. PhD thesis, University of Copenhagen, Department of Chemistry, 2023.

[70] P. M. Morse, "Diatomic Molecules According to the Wave Mechanics. II. Vibrational Levels," *Phys. Rev.*, vol. 34, pp. 57–64, Jul 1929.

[71] D. S. S. Emil Vogt and H. G. Kjaergaard, "Accuracy of XH-Stretching Intensities with the Deng–Fan Potential," *Mol. Phys.*, vol. 117, no. 13, pp. 1629–1639, 2019.

[72] Z. Deng and Y. Fan, "A Potential Function of Diatomic Molecules," *Shandong Univ. J.*, vol. 7, pp. 162–166, 1957.

[73] M. J. Frisch, G. W. Trucks, H. B. Schlegel, G. E. Scuseria, M. A. Robb, J. R. Cheeseman, G. Scalmani, V. Barone, G. A. Petersson, H. Nakatsuji, X. Li, M. Caricato, A. V. Marenich, J. Bloino, B. G. Janesko, R. Gomperts, B. Mennucci, H. P. Hratchian, J. V. Ortiz, A. F. Izmaylov, J. L. Sonnenberg, D. Williams-Young,

F. Ding, F. Lipparini, F. Egidi, J. Goings, B. Peng, A. Petrone, T. Henderson, D. Ranasinghe, V. G. Zakrzewski, J. Gao, N. Rega, G. Zheng, W. Liang, M. Hada, M. Ehara, K. Toyota, R. Fukuda, J. Hasegawa, M. Ishida, T. Nakajima, Y. Honda, O. Kitao, H. Nakai, T. Vreven, K. Throssell, J. A. Montgomery, Jr., J. E. Peralta, F. Ogliaro, M. J. Bearpark, J. J. Heyd, E. N. Brothers, K. N. Kudin, V. N. Staroverov, T. A. Keith, R. Kobayashi, J. Normand, K. Raghavachari, A. P. Rendell, J. C. Burant, S. S. Iyengar, J. Tomasi, M. Cossi, J. M. Millam, M. Klene, C. Adamo, R. Cammi, J. W. Ochterski, R. L. Martin, K. Morokuma, O. Farkas, J. B. Foresman, and D. J. Fox, "Gaussian 16, Revision A," 2016. Gaussian Inc. Wallingford CT.

[74] A. Nejad, *Vibrational Dynamics of Formic Acid and its Dimer: FTIR and Raman Jet Spectroscopy and Theory.* PhD thesis, Georg-August-Universität, Göttingen, 2022.

[75] P. R. Franke, J. F. Stanton, and G. E. Douberly, "How to VPT2: Accurate and Intuitive Simulations of CH Stretching Infrared Spectra Using VPT2+K with Large Effective Hamiltonian Resonance Treatments," *J. Phys. Chem. A*, vol. 125, no. 6, pp. 1301–1324, 2021.

[76] P. Carbonniere and V. Barone, "Coriolis Couplings in Variational Computations of Vibrational Spectra Beyond the Harmonic Approximation: Implementation and Validation," *Chem. Phys. Lett.*, vol. 392, no. 4, pp. 365–371, 2004.

[77] J. K. Watson, "The Molecular Vibration–Rotation Kinetic-Energy Operator for General Internal Coordinates," *J. Mol. Spec.*, vol. 228, no. 2, pp. 645–658, 2004. Special Issue Dedicated to Dr. Jon T. Hougen on the Occasion of His 68th Birthday.

[78] M. A. Boyer and A. B. McCoy, "A Flexible Approach to Vibrational Perturbation Theory using Sparse Matrix Methods," *J. Chem. Phys.*, vol. 156, p. 054107, 02 2022.

[79] V. Barone, "Anharmonic Vibrational Properties by a Fully Automated Second-Order Perturbative Approach," *J. Chem. Phys.*, vol. 122, no. 1, pp. 14108–14108, 2005.

[80] M. Fusè, G. Mazzeo, G. Longhi, S. Abbate, Q. Yang, and J. Bloino, "Scaling-up VPT2: A Feasible Route to Include Anharmonic Correction on Large Molecules," *Spectrochim. Acta A Mol. Biomol. Spectrosc.*, vol. 311, p. 123969, 2024.

[81] M. A. Boyer and A. B. McCoy, "A Wave Function Correction-Based Approach to the Identification of Resonances for Vibrational Perturbation Theory," *J. Chem. Phys.*, vol. 157, p. 164113, 10 2022.

[82] K. Mackeprang, H. G. Kjaergaard, T. Salmi, V. Hänninen, and L. Halonen, "The Effect of Large Amplitude Motions on the Transition Frequency Redshift in Hydrogen Bonded Complexes: A Physical Picture," *J. Chem. Phys.*, vol. 140, no. 18, p. 184309, 2014.

[83] K. Mackeprang, V. Hänninen, L. Halonen, and H. G. Kjaergaard, "The Effect of Large Amplitude Motions on the Vibrational Intensities in Hydrogen Bonded Complexes," *J. Chem. Phys.*, vol. 142, no. 9, p. 094304, 2015.

[84] K. Mackeprang and H. G. Kjaergaard, "Vibrational Transitions in Hydrogen Bonded Bimolecular Complexes - A Local Mode Perturbation Theory Approach to Transition Frequencies and Intensities," *J. Mol. Spectrosc.*, vol. 334, pp. 1–9, 2017.

[85] A. Kjaersgaard, E. Vogt, A. S. Hansen, and H. G. Kjaergaard, "Room Temperature Gas-Phase Detection and Gibbs Energies of Water Amine Bimolecular Complex Formation," *J. Phys. Chem. A*, vol. 124, no. 35, pp. 7113–7122, 2020.

[86] E. Vogt, C. V. Jensen, and H. G. Kjaergaard, "Effect of Temperature on the OH-Stretching Bands of the Methanol Dimer," *J. Phys. Chem. A*, vol. 128, no. 2, pp. 392–400, 2024.

[87] E. Vogt and H. G. Kjaergaard, "Vibrational Spectroscopy of the Water Dimer at Jet-Cooled and Atmospheric Temperatures," *Annu. Rev. Phys. Chem.*, vol. 73, pp. 209–231, 2022.

[88] E. Vogt, I. Simkó, A. G. Császár, and H. G. Kjaergaard, "Reduced-Dimensional Vibrational Models of the Water Dimer," *J. Chem. Phys.*, vol. 156, 04 2022. 164304.

[89] C. V. Jensen, E. Vogt, A. S. Poulsen, and H. G. Kjaergaard, "Room Temperature Gas Phase Equilibrium Constants of the Methanol Dimer, Trimer and Tetramer," *J. Phys. Chem. A*, vol. 128, no. 31, pp. 6382–6391, 2024.

[90] V. Barone, M. Biczysko, J. Bloino, M. Borkowska-Panek, I. Carnimeo, and P. Panek, "Toward Anharmonic Computations of Vibrational Spectra for Large Molecular Systems," *Int. J. Quantum Chem.*, vol. 112, no. 9, pp. 2185–2200, 2011.

[91] V. Barone, M. Biczysko, and J. Bloino, "Fully Anharmonic IR and Raman Spectra of Medium-Size Molecular Systems: Accuracy and Interpretation," *Phys. Chem. Chem. Phys.*, vol. 16, pp. 1759–1787, 2014.

[92] T. Fornaro, I. Carnimeo, and M. Biczysko, "Toward Feasible and Comprehensive Computational Protocol for Simulation of the Spectroscopic Properties of Large Molecular Systems: The Anharmonic Infrared Spectrum of Uracil in the Solid State by the Reduced Dimensionality/Hybrid VPT2 Approach," *J. Phys. Chem. A*, vol. 119, no. 21, pp. 5313–5326, 2015.

[93] E. Vogt, P. Bertran Valls, and H. G. Kjaergaard, "Accurate Calculations of OH-Stretching Intensities with a Reduced-Dimensional Local Mode Model Including Eckart Axis Embedding," *J. Phys. Chem. A*, vol. 124, no. 5, pp. 932–942, 2020.

[94] E. Vogt, A. S. Hansen, and H. G. Kjaergaard, "Local Modes of Vibration: The Effect of Low-Frequency Vibrations," in *Molecular Spectroscopy: A Quantum Chemistry Approach* (Y. Ozaki, M. J. Wójcik, and J. Popp, eds.), ch. 14, pp. 289–424, John Wiley & Sons, 2019.

[95] E. B. Wilson Jr, J. Decius, P. C. Cross, and D. Mann, "Molecular vibrations," 1955.

[96] J. W. Ellis, "Molecular Absorption Spectra of Liquids Below 3 μ," *Trans. Faraday Soc.*, vol. 25, pp. 888–898, 1929.

[97] R. Mecke, "Absorptionsuntersuchungen an Kohlenwasserstoffen im Nahen Ultraroten: IV. Berechnung von Anharmonischen Valenzschwingungen Mehratomiger Moleküle," *Zeitschrift für Physik*, vol. 99, no. 3, pp. 217–235, 1936.

[98] R. T. Birge and H. Sponer, "The Heat of Dissociation of Non-Polar Molecules," *Phys. Rev.*, vol. 28, pp. 259–283, Aug 1926.

[99] S.-i. Ishiuchi, M. Fujii, T. W. Robinson, B. J. Miller, and H. G. Kjaergaard, "Vibrational Overtone Spectroscopy of Phenol and Its Deuterated Isotopomers," *J. Phys. Chem. A*, vol. 110, no. 23, pp. 7345–7354, 2006.

[100] P. E. Hintze, H. G. Kjaergaard, V. Vaida, and J. B. Burkholder, "Vibrational and Electronic Spectroscopy of Sulfuric Acid Vapor," *J. Phys. Chem. A*, vol. 107, no. 8, pp. 1112–1118, 2003.

[101] H. G. Kjaergaard, D. L. Howard, D. P. Schofield, T. W. Robinson, S. Ishiuchi, and M. Fujii, "OH- and CH-Stretching Overtone Spectra of Catechol," *J. Phys. Chem. A*, vol. 106, no. 2, pp. 258–266, 2002.

[102] C. V. Jensen, "GitHub Repository of 1D LM code." `https://github.com/CasperVJensen/tert-Butyl_Hydroperoxide_Dimer.git` visited July 2023.

[103] C. V. Jensen and H. G. Kjaergaard, "Gas-Phase Room-Temperature Detection of the tert-Butyl Hydroperoxide Dimer," *J. Phys. Chem. A*, vol. 127, no. 31, pp. 6476–6485, 2023.

[104] P. W. Atkins and R. S. Friedman, *Molecular Quantum Mechanics*. Oxford University Press, 2011.

[105] E. R. Johnson, S. Keinan, P. Mori-Sánchez, J. Contreras-García, A. J. Cohen, and W. Yang, "Revealing Noncovalent Interactions," *J. Am. Chem. Soc.*, vol. 132, no. 18, pp. 6498–6506, 2010.

[106] J. Contreras-García, E. R. Johnson, S. Keinan, R. Chaudret, J.-P. Piquemal, D. N. Beratan, and W. Yang, "NCIPLOT: A Program for Plotting Noncovalent Interaction Regions," *J. Chem. Theory Comput.*, vol. 7, no. 3, pp. 625–632, 2011.

[107] G. Saleh, L. Lo Presti, C. Gatti, and D. Ceresoli, "NCImilano: An Electron-Density-Based Code for the Study of Noncovalent Interactions," *J. Appl. Crystallogr.*, vol. 46, pp. 1513–1517, Oct 2013.

[108] R. A. Boto, J. Contreras-García, J. Tierny, and J.-P. Piquemal, "Interpretation of the Reduced Density Gradient," *Mol. Phys.*, vol. 114, no. 7-8, pp. 1406–1414, 2016.

[109] J. R. Lane, A. S. Hansen, K. Mackeprang, and H. G. Kjaergaard, "Kinetic Energy Density as a Predictor of Hydrogen-Bonded OH-Stretching Frequencies," *J. Phys. Chem. A*, vol. 121, no. 18, pp. 3452–3460, 2017.

[110] R. Laplaza, F. Peccati, R. A. Boto, C. Quan, A. Carbone, J.-P. Piquemal, Y. Maday, and J. Contreras-García, "NCIPLOT and the Analysis of Noncovalent Interactions using the Reduced Density Gradient," *Wiley Interdiscip. Rev.: Comput. Mol. Sci.*, vol. 11, no. 2, p. e1497, 2021.

[111] T. Berndt, J. Chen, E. R. Kjærgaard, K. H. Møller, A. Tilgner, E. H. Hoffmann, H. Herrmann, J. D. Crounse, P. O. Wennberg, and H. G. Kjaergaard, "Hydrotrioxide (ROOOH) Formation in the Atmosphere," *Science*, vol. 376, no. 6596, pp. 979–982, 2022.

[112] Y. A. Abramov, "On the Possibility of Kinetic Energy Density Evaluation from the Experimental Electron-Density Distribution," *ACTA CRYSTALLOGR A*, vol. 53, pp. 264–272, May 1997.

[113] J. Hilgevoord, "The Uncertainty Principle for Energy and Time," *Am. J. Phys.*, vol. 64, no. 12, pp. 1451–1456, 1996.

[114] P. Busch, *The Time–Energy Uncertainty Relation*, vol. 734, pp. 73–105. Springer, 01 2008.

[115] S. Agarwal, L. Seifert, D. Zhu, B. Shu, R. Fernandes, and Z. Qu, "Investigations on Pressure Broadening Coefficients of NO Lines in the 1←0 Band for N_2, CO_2, Ar, H_2, O_2 and He," *Appl. Sci.*, vol. 13, no. 3, 2023.

[116] B. Ruscic, A. F. Wagner, L. B. Harding, R. L. Asher, D. Feller, D. A. Dixon, K. A. Peterson, Y. Song, X. Qian, C.-Y. Ng, J. Liu, W. Chen, and D. W. Schwenke, "On the Enthalpy of Formation of Hydroxyl Radical and Gas-Phase Bond Dissociation Energies of Water and Hydroxyl," *J. Phys. Chem. A*, vol. 106, no. 11, pp. 2727–2747, 2002.

[117] M. Umer and K. Leonhard, "Ab Initio Calculations of Thermochemical Properties of Methanol Clusters," *J. Phys. Chem. A*, vol. 117, no. 7, pp. 1569–1582, 2013.

[118] E. Vogt, J. Langeland, C. Kjær, T. T. Lindkvist, H. G. Kjaergaard, and S. B. Nielsen, "Effect of Freezing out Vibrational Modes on Gas-Phase Fluorescence Spectra of Small Ionic Dyes," *J. Phys. Chem. Lett.*, vol. 12, no. 46, pp. 11346–11352, 2021.

[119] C. L. Andersen, C. S. Jensen, K. Mackeprang, L. Du, S. Jørgensen, and H. G. Kjaergaard, "Similar Strength of the NH$\cdots$O and NH$\cdots$S Hydrogen Bonds in Binary Complexes," *J. Phys. Chem. A*, vol. 118, no. 46, pp. 11074–11082, 2014.

[120] V. S. Hansen, "Absorption Spectroscopy and Absolute Intensities of Isoprene," Bachelor's Thesis, University of Copenhagen, Department of Chemistry, 2024.

[121] J. Irving and N. Mullineux, *Mathematics in Physics and Engineering*, vol. 6. Academic Press, 2013.

[122] The Editors of Encyclopaedia Britannica, "Michelson-Morley Experiment." `https://www.britannica.com/science/Michelson-Morley-experiment` visited August 2024.

[123] "Vertex 80 Beam path." `https://www.bruker.com/en/products-and-solutions/infrared-and-raman/ft-ir-research-spectrometers/vertex-research-ft-ir-spectrometer/vertex-80-80v-ft-ir-spectrometer.html` visited May 2024.

[124] R. G. Sellar and G. D. Boreman, "Comparison of Relative Signal-to-Noise Ratios of Different Classes of Imaging Spectrometer," *Appl. Opt.*, vol. 44, pp. 1614–1624, Mar 2005.

[125] H. Nyquist, "Certain Topics in Telegraph Transmission Theory," *Trans. AIEE*, vol. 47, no. 2, pp. 617–644, 1928.

[126] C. Shannon, "Communication in the Presence of Noise," *Proc. IRE*, vol. 37, no. 1, pp. 10–21, 1949.

[127] M. H. Michel Herman, Robert Georges and D. Hurtmans, "High Resolution Fourier Transform Spectroscopy of Jet-Cooled Molecules," *Int. Rev. Phys. Chem.*, vol. 19, no. 2, pp. 277–325, 2000.

[128] M. D. Morse, "Supersonic Beam Sources," in *Atomic, Molecular, and Optical Physics: Atoms and Molecules* (F. Dunning and R. G. Hulet, eds.), ch. 2, pp. 21–47, Academic Press, 1996.

[129] P. Atkins, J. De Paula, and R. Friedman, *Physical Chemistry: Quanta, Matter, and Change*. Oxford University Press, USA, 2nd ed., 2014.

[130] M. A. Suhm and F. Kollipost, "Femtisecond Single-Mole Infrared Spectroscopy of Molecular Clusters," *Phys. Chem. Chem. Phys.*, vol. 15, pp. 10702–10721, 2013.

[131] K. Otto, *Raman-Spektroskopie kleiner Moleküle und Molekülaggregate im Überschallstrahl nach thermischer Anregung*. PhD thesis, Georg-August-Universität Göttingen, Germany, 2015.

[132] V. Meyer, S. Eisermann, H. C. Gottschalk, R. Hildebrandt, B. Langer, U. Schmitt, M. Zippert, and M. A. Suhm, "Gratin Jet Figures," 2020. `https://doi.org/10.25625/6V6KSN` visited May 2024.

[133] H. C. Gottschalk, T. L. Fischer, V. Meyer, R. Hildebrandt, U. Schmitt, and M. A. Suhm, "A Sustainable Slit Jet FTIR Spectrometer for Hydrate Complexes and Beyond," *Instruments*, vol. 5, no. 1, 2021.

[134] T. L. Fischer, M. Bödecker, S. M. Schweer, J. Dupont, V. Lepère, A. Zehnacker-Rentien, M. A. Suhm, B. Schröder, T. Henkes, D. M. Andrada, R. M. Balabin, H. K. Singh, H. P. Bhattacharyya, M. Sarma, S. Käser, K. Töpfer, L. I. Vazquez-Salazar, E. D. Boittier, M. Meuwly, G. Mandelli, C. Lanzi, R. Conte, M. Ceotto, F. Dietrich, V. Cisternas, R. Gnanasekaran, M. Hippler, M. Jarraya, M. Hochlaf, N. Viswanathan, T. Nevolianis, G. Rath, W. A. Kopp, K. Leonhard, and R. A. Mata, "The First HyDRA Challenge for Computational Vibrational Spectroscopy," *Phys. Chem. Chem. Phys.*, vol. 25, pp. 22089–22102, 2023.

[135] K. C. Lin, T. L. Tai, and M. Tsai, "Effect of Deposition Rate on the Formation of Multimeric Species of Matrix Isolated Ethanol," *J. Chi. Chem. Soc.*, vol. 26, no. 4, pp. 141–144, 1979.

[136] "General Discussion," *Faraday Discuss.*, vol. 118, pp. 295–314, 2001.

[137] J. H. Wallberg, "Construction of a Cavity Ring Down Spectrometer for Measurements of Absolute Intensities," Master's thesis, University of Copenhagen, Department of Chemistry, 2017.

[138] M. D. Wheeler, S. M. Newman, A. J. Orr-Ewing, and M. N. R. Ashfold, "Cavity Ring-Down Spectroscopy," *J. Chem. Soc., Faraday Trans.*, vol. 94, pp. 337–351, 1998.

[139] D. Romanini and K. K. Lehmann, "Ring-Down Cavity Absorption Spectroscopy of the very Weak HCN Overtone Bands with Six, Seven, and Eight Stretching Quanta," *J. Chem. Phys.*, vol. 99, pp. 6287–6301, 11 1993.

[140] S. S. Brown, "Absorption Spectroscopy in High-Finesse Cavities for Atmospheric Studies," *Chem. Rev.*, vol. 103, no. 12, pp. 5219–5238, 2003.

[141] H. Kogelnik and T. Li, "Laser Beams and Resonators," *Appl. Opt.*, vol. 5, pp. 1550–1567, Oct 1966.

[142] H. Telfah, A. C. Paul, and J. Liu, "Aligning an Optical Cavity: With Reference to Cavity Ring-Down Spectroscopy," *Appl. Opt.*, vol. 59, pp. 9464–9468, Oct 2020.

[143] D. Z. Anderson, "Alignment of Resonant Optical Cavities," *Appl. Opt.*, vol. 23, pp. 2944–2949, Sep 1984.

[144] R. P. Giel Berden and G. Meijer, "Cavity Ring-Down Spectroscopy: Experimental Schemes and Applications," *Int. Rev. Phys. Chem.*, vol. 19, no. 4, pp. 565–607, 2000.

[145] N. Zhadnov, K. Kudeyarov, D. Kryuchkov, I. Semerikov, K. Khabarova, and N. Kolachevsky, "On the Thermal Noise Limit of Ultrastable Optical Cavities," *Quantum Electron.*, vol. 48, p. 425, may 2018.

[146] H. Huang and K. K. Lehmann, "Noise in Cavity Ring-Down Spectroscopy Caused by Transverse Mode Coupling," *Opt. Express*, vol. 15, pp. 8745–8759, Jul 2007.

[147] D.-H. Lee, Y. Yoon, B. Kim, J. Lee, Y. Yoo, and J. Hahn, "Optimization of the Mode Matching in Pulsed Cavity Ringdown Spectroscopy by Monitoring Non-Degenerate Transverse Mode Beating," *Appl. Phys. B*, vol. 74, pp. 435–440, 2002.

[148] "Laser Calculator." `https://www.lasercalculator.com/` visited August 2024.

[149] C. V. Jensen, "GitHub Repository of CRD Exp Fit Code." `https://github.com/CasperVJensen/CRD_exp_fit_raw_data` visited August 2024.

[150] Wikipedia Contributors, "Chauvenet's Criterion — Wikipedia, The Free Encyclopedia," 2024. https://en.wikipedia.org/w/index.php?title=Chauvenet%27s_criterion&oldid=1200116628 visited August 2024.

[151] L. Lin and P. D. Sherman, "Cleaning Data the Chauvenet Way," *The Proceedings of the SouthEast SAS Users Group, SESUG Proceedings, Paper SA11*, pp. 1–11, 2007.

[152] J. W. Wallberg, *Intensities of Fundamental and Overtone OH, OD and NH Stretching Transitions*. PhD thesis, University of Copenhagen, Department of Chemistry, 2019.

[153] I. Gordon, L. Rothman, R. Hargreaves, R. Hashemi, E. Karlovets, F. Skinner, E. Conway, C. Hill, R. Kochanov, Y. Tan, *et al.*, "The HITRAN2020 Molecular Spectroscopic Database," *J. Quant. Spectrosc. Radiat. Transf.*, vol. 277, p. 107949, 2022.

[154] H. L. Fang and D. A. Compton, "Vibrational Overtones of Gaseous Alcohols," *J. Phys. Chem.*, vol. 92, no. 23, pp. 6518–6527, 1988.

[155] J.-D. Chai and M. Head-Gordon, "Long-Range Corrected Hybrid Density Functionals with Damped Atom–Atom Dispersion Corrections," *Phys. Chem. Chem. Phys.*, vol. 10, no. 44, pp. 6615–6620, 2008.

[156] R. A. Kendall, T. H. Dunning Jr, and R. J. Harrison, "Electron Affinities of the First-Row Atoms Revisited. Systematic Basis Sets and Wave Functions," *J. Chem. Phys.*, vol. 96, no. 9, pp. 6796–6806, 1992.

[157] T. H. Dunning Jr, "Gaussian Basis Sets for use in Correlated Molecular Calculations. I. The Atoms Boron through Neon and Hydrogen," *J. Chem. Phys.*, vol. 90, no. 2, pp. 1007–1023, 1989.

[158] H. G. Kjaergaard, A. L. Garden, G. M. Chaban, R. B. Gerber, D. A. Matthews, and J. F. Stanton, "Calculation of Vibrational Transition Frequencies and Intensities in Water Dimer: Comparison of Different Vibrational Approaches," *J. Phys. Chem. A*, vol. 112, no. 18, pp. 4324–4335, 2008.

[159] A. Becke, "Density-Functional Thermochemistry. III. The Role of Exact Exchange," *J. Chem. Phys.*, vol. 98, p. 5648, 1993.

[160] Y. Zhao and D. G. Truhlar, "The M06 Suite of Density Functionals for Main Group Thermochemistry, Thermochemical Kinetics, Noncovalent Interactions, Excited States, and Transition Elements: Two New Functionals and Systematic Testing of Four M06-Class Functionals and 12 other Functionals," *Theor. Chem. Acc.*, vol. 120, no. 1, pp. 215–241, 2008.

[161] C. Adamo and V. Barone, "Toward Reliable Density Functional Methods Without Adjustable Parameters: The PBE0 Model," *J. Chem. Phys.*, vol. 110, no. 13, pp. 6158–6170, 1999.

[162] M. Ernzerhof and G. E. Scuseria, "Assessment of the Perdew–Burke–Ernzerhof Exchange-Correlation Functional," *J. Chem. Phys.*, vol. 110, no. 11, pp. 5029–5036, 1999.

[163] T. Yanai, D. P. Tew, and N. C. Handy, "A New Hybrid Exchange–Correlation Functional using the Coulomb-Attenuating Method (CAM-B3LYP)," *Chem. Phys. Lett.*, vol. 393, no. 1-3, pp. 51–57, 2004.

[164] S. Grimme, J. Antony, S. Ehrlich, and H. Krieg, "A Consistent and Accurate *Ab Initio* Parametrization of Density Functional Dispersion Correction (DFT-D) for the 94 Elements H-Pu," *J. Chem. Phys.*, vol. 132, no. 15, p. 154104, 2010.

[165] S. Grimme, "Semiempirical GGA-Type Density Functional Constructed with a Long-Range Dispersion Correction," *J. Comput. Chem.*, vol. 27, no. 15, pp. 1787–1799, 2006.

[166] K. A. Peterson, T. B. Adler, and H.-J. Werner, "Systematically Convergent Basis Sets for Explicitly Correlated Wavefunctions: The Atoms H, He, B–Ne, and Al–Ar," *J. Chem. Phys.*, vol. 128, no. 8, p. 084102, 2008.

[167] T. B. Adler, G. Knizia, and H.-J. Werner, "A Simple and Efficient CCSD(T)-F12 Approximation," *J. Chem. Phys.*, vol. 127, no. 22, p. 221106, 2007.

[168] H.-J. Werner, P. J. Knowles, P. Celani, W. Györffy, A. Hesselmann, D. Kats, G. Knizia, A. Köhn, T. Korona, D. Kreplin, R. Lindh, Q. Ma, F. R. Manby, A. Mitrushenkov, G. Rauhut, M. Schütz, K. R. Shamasundar, T. B. Adler, R. D. Amos, S. J. Bennie, A. Bernhardsson, A. Berning, J. A. Black, P. J. Bygrave,

R. Cimiraglia, D. L. Cooper, D. Coughtrie, M. J. O. Deegan, A. J. Dobbyn, K. Doll, M. Dornbach, F. Eckert, S. Erfort, E. Goll, C. Hampel, G. Hetzer, J. G. Hill, M. Hodges, T. Hrenar, G. Jansen, C. Köppl, C. Kollmar, S. J. R. Lee, Y. Liu, A. W. Lloyd, R. A. Mata, A. J. May, B. Mussard, S. J. McNicholas, W. Meyer, T. F. Miller III, M. E. Mura, A. Nicklass, D. P. O'Neill, P. Palmieri, D. Peng, K. A. Peterson, K. Pflüger, R. Pitzer, I. Polyak, M. Reiher, J. O. Richardson, J. B. Robinson, B. Schröder, M. Schwilk, T. Shiozaki, M. Sibaev, H. Stoll, A. J. Stone, R. Tarroni, T. Thorsteinsson, J. Toulouse, M. Wang, M. Welborn, and B. Ziegler, "MOLPRO, 12.1 , a Package of Ab Initio Programs." `https://www.molpro.net` visited July 2023.

[169] H.-J. Werner, P. J. Knowles, G. Knizia, F. R. Manby, and M. Schütz, "Molpro: a General-Purpose Quantum Chemistry Program Package," *Wiley Interdiscip. Rev.: Comput. Mol. Sci.*, vol. 2, no. 2, pp. 242–253, 2012.

[170] H.-J. Werner, P. J. Knowles, F. R. Manby, J. A. Black, K. Doll, A. Heßelmann, D. Kats, A. Köhn, T. Korona, D. A. Kreplin, Q. Ma, I. Miller, Thomas F., A. Mitrushchenkov, K. A. Peterson, I. Polyak, G. Rauhut, and M. Sibaev, "The Molpro Quantum Chemistry Package," *J. Chem. Phys.*, vol. 152, p. 144107, 04 2020.

[171] C. Colominas, J. Teixidó, J. Cemelí, F. J. Luque, and M. Orozco, "Dimerization of Carboxylic Acids: Reliability of Theoretical Calculations and the Effect of Solvent," *J. Phys. Chem. B*, vol. 102, no. 12, pp. 2269–2276, 1998.

[172] J. B. Togeas, "Acetic Acid Vapor: 2. A Statistical Mechanical Critique of Vapor Density Experiments," *J. Phys. Chem. A*, vol. 109, no. 24, pp. 5438–5444, 2005.

[173] M. Goubet, P. Soulard, O. Pirali, P. Asselin, F. Réal, S. Gruet, T. R. Huet, P. Roy, and R. Georges, "Standard Free Energy of the Equilibrium between the Trans-Monomer and the Cyclic-Dimer of Acetic Acid in the Gas Phase from Infrared Spectroscopy," *Phys. Chem. Chem. Phys.*, vol. 17, no. 11, pp. 7477–7488, 2015.

[174] O. Socha and M. Dračínskỳ, "Dimerization of Acetic Acid in the Gas Phase—NMR Experiments and Quantum-Chemical Calculations," *Molecules*, vol. 25, no. 9, p. 2150, 2020.

[175] B. F. King and F. Weinhold, "Structure and Spectroscopy of (HCN)n Clusters: Cooperative and Electronic Delocalization Effects in C-H$\cdots$N Hydrogen Bonding," *J. Chem. Phys.*, vol. 103, no. 1, pp. 333–347, 1995.

[176] L. Ojamaee and K. Hermansson, "*Ab Initio* Study of Cooperativity in Water Chains: Binding Energies and Anharmonic Frequencies," *J. Phys. Chem.*, vol. 98, no. 16, pp. 4271–4282, 1994.

[177] D. Zimmermann, T. Häber, H. Schaal, and M. A. Suhm, "Hydrogen Bonded Rings, Chains and Lassos: The Case of t-Butyl Alcohol Clusters," *Mol. Phys.*, vol. 99, no. 5, pp. 413–425, 2001.

[178] M. Masella and J. P. Flament, "Relation Between Cooperative Effects in Cyclic Water, Methanol/Water, and Methanol Trimers and Hydrogen Bonds in Methanol/Water, Ethanol/Water, and Dimethylether/Water Heterodimers," *J. Chem. Phys.*, vol. 108, no. 17, pp. 7141–7151, 1998.

[179] C. M. Western, "PGOPHER: A Program for Simulating Rotational, Vibrational and Electronic Spectra," *J. Quant. Spectrosc. Radiat. Transfer*, vol. 186, pp. 221–242, 2017. Satellite Remote Sensing and Spectroscopy: Joint ACE-Odin Meeting, October 2015.

[180] E. Vogt, "GitHub Repository of MeOH Dimer Temperature Simulation Code." `https://github.com/CasperVJensen/MeOH-dimer.git` visited August 2024.

[181] M. Rozenberg, A. Loewenschuss, and C. J. Nielsen, "H-Bonded Clusters in the Trimethylamine/Water System: A Matrix Isolation and Computational Study," *J. Phys. Chem. A*, vol. 116, no. 16, pp. 4089–4096, 2012.

[182] S. Jiang, M. Su, S. Yang, C. Wang, Q.-R. Huang, G. Li, H. Xie, J. Yang, G. Wu, W. Zhang, Z. Zhang, J.-L. Kuo, Z.-F. Liu, D. H. Zhang, X. Yang, and L. Jiang, "Vibrational Signature of Dynamic Coupling of a Strong Hydrogen Bond," *J. Phys. Chem. Lett.*, vol. 12, no. 9, pp. 2259–2265, 2021.

[183] E. Lwin, T. L. Fischer, and M. A. Suhm, "Microhydration of Tertiary Amines: Robust Resonances in Red-Shifted Water," *J. Phys. Chem. Lett.*, vol. 14, no. 45, pp. 10194–10199, 2023.

[184] B. Zhang, Y. Yu, Z. Zhang, Y.-Y. Zhang, S. Jiang, Q. Li, S. Yang, H.-S. Hu, W. Zhang, D. Dai, G. Wu, J. Li, D. H. Zhang, X. Yang, and L. Jiang, "Infrared Spectroscopy of Neutral Water Dimer Based on a Tunable Vacuum Ultraviolet Free Electron Laser," *J. Phys. Chem. Lett.*, vol. 11, no. 3, pp. 851–855, 2020.

[185] A. J. Barnes, "Matrix Isolation Studies of Hydrogen Bonding – An Historical Perspective," *J. Mol. Struc.*, vol. 1163, pp. 77–85, 2018.

[186] M. Gawrilow and M. A. Suhm, "2-Methoxyethanol: Harmonic Tricks, Anharmonic Challenges and Chirality-Sensitive Chain Aggregation," *Phys. Chem. Chem. Phys.*, vol. 22, pp. 15303–15311, 2020.

[187] R. J. Barlow, *Statistics: a Guide to the use of Statistical Methods in the Physical Sciences*, vol. 29. John Wiley & Sons, 1993.

[188] D. Fu, D. B. Millet, K. C. Wells, V. H. Payne, S. Yu, A. Guenther, and A. Eldering, "Direct Retrieval of Isoprene from Satellite-Based Infrared Measurements," *Nat. commun.*, vol. 10, no. 1, p. 3811, 2019.

[189] S. Markussen, "The CH-Stretching Fundamental and Overtone Transitions of Isoprene," Master's thesis, University of Copenhagen, Department of Chemistry, 2021.

7

PUBLISHED PAPERS

A PAPER 1

Gas-Phase Room-Temperature Detection of the *tert*-Butyl Hydroperoxide Dimer

Casper Vindahl Jensen and Henrik G. Kjaergaard*.

The Journal of Physical Chemistry A, 2023, 127(31), 6476-6485

THE JOURNAL OF PHYSICAL CHEMISTRY A
A JOURNAL OF THE AMERICAN CHEMICAL SOCIETY

pubs.acs.org/JPCA Article

Gas-Phase Room-Temperature Detection of the *tert*-Butyl Hydroperoxide Dimer

Published as part of The Journal of Physical Chemistry virtual special issue "Marsha I. Lester Festschrift".

Casper Vindahl Jensen and Henrik G. Kjaergaard*

Cite This: *J. Phys. Chem. A* 2023, 127, 6476–6485 Read Online

ACCESS | Metrics & More | Article Recommendations | Supporting Information

ABSTRACT: We have detected the *tert*-butyl hydroperoxide dimer, $(t\text{-BuOOH})_2$, in the gas phase at room temperature using conventional FTIR techniques. The dimer is identified by an asymmetric absorbance band assigned to the fundamental hydrogen-bound OH_b-stretch. The weighted band maximum of the dimer OH_b-stretch is located at ~3452 cm^{-1}, red-shifted by ~145 cm^{-1} from the monomer OH-stretching band. The gas-phase dimer assignment is supported by Ar matrix isolation FTIR experiments at 12 K and experiments with a partially deuterated sample. Computationally, we find the lowest energy structure of $(t\text{-BuOOH})_2$ to be a doubly hydrogen bound six-membered ring with non-optimal hydrogen bond angles. We estimate the gas-phase constant of dimer formation, K, to be 0.4 (standard pressure of 1 bar) using the experimental integrated absorbance and a theoretically determined oscillator strength of the OH_b-stretching band.

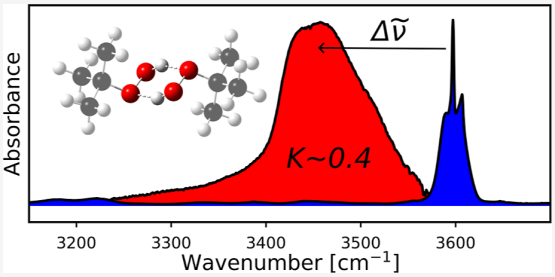

INTRODUCTION

Hydrogen bonds are of general interest and the formation of hydrogen bound complexes are important in a myriad of chemical systems. These range from particle formation and aerosol growth in the atmosphere to biological processes where inter- and intramolecular hydrogen bonds are key to the shape and functionality of proteins.[1−5] In the atmosphere, volatile organic compounds are emitted and subsequently oxidized, leading to a large presence of highly oxygenated organic molecules (HOMs) capable of acting as hydrogen bond donors and/or acceptors. These HOMs include functionalities such as alcohols, hydroperoxides, organic acids, ethers, carbonyls, etc.[6] Hydrogen bonds play a crucial role in the formation of the initial bimolecular complexes that grow to form larger clusters, which ultimately condense into aerosols and particles in the atmosphere.[7,8] Formation of bimolecular complexes with a single hydrogen bond are usually energetically disfavored compared to the monomers at room temperature due to the small binding enthalpies and low entropy of the complexes. This results in relatively small unitless formation constants (standard pressure of 1 bar), typically $K < 1$.[9] In contrast, carboxylic acids form doubly hydrogen bound dimers with geometries that allow for optimal hydrogen bonding angles of ca. 180° in a planar eight-membered ring.[10,11] Carboxylic acids therefore have significantly larger constants of dimer formation of $K > 100$.[12−21]

Previously, it has been shown that the organic hydroperoxide, *tert*-butyl hydroperoxide (*t*-BuOOH) forms stronger hydrogen bonds, compared to the corresponding alcohol *tert*-butanol (*t*-BuOH).[22] In the complexes with di-methyl ether (DME) as acceptor (O-atom), the observed room temperature gas phase OH-stretching redshift increased from ~100 cm^{-1} for the *t*-BuOH·DME complex to ~170 cm^{-1} for the *t*-BuOOH·DME complex, and K was found to be 5.5 times higher for the *t*-BuOOH·DME complex. Bimolecular complexes consisting of two hydroperoxide units have been detected in cold matrix isolation experiments and ab initio calculations have suggested a doubly hydrogen-bound structure.[23−29] These complexes include H_2O_2 dimer, HO_2 dimer, and the H_2O_2−HO_2 complex. The geometry of these doubly bound complexes are suggested to have a ring-type structure similar to that of the organic acids; however, with a non-planar six-membered ring. In CCl_4 solution, $(t\text{-BuOOH})_2$ has been detected with the same suggested doubly bound cyclic structure and an equilibrium constant of $K = 1.9$.[30]

Organic hydroperoxides are known to be unstable and even explosive under ambient conditions and therefore warrant concerns when handled.[31] *t*-BuOOH is a somewhat stable organic hydroperoxide, which makes it well-suited for experimental studies. It has been used as a model compound

Received: June 1, 2023
Revised: July 13, 2023
Published: August 1, 2023

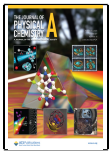

https://doi.org/10.1021/acs.jpca.3c03702
J. Phys. Chem. A 2023, 127, 6476−6485

for the organic hydroperoxide functionality in studies of properties such as the OH-stretching overtone spectroscopy, OH-stretch coupling to the COOH torsion and photodissociation of the OO-bond, with various gas phase infrared (IR) and ultra violet-visible spectroscopic techniques as well as with theoretical simulations.[32−38]

In this study, we detect the *t*-BuOOH dimer $(t\text{-BuOOH})_2$ in the gas phase at room temperature. To the best of our knowledge, this is the first gas phase detection of an organic hydroperoxide dimer at room temperature. The low vapor pressure of *t*-BuOOH (∼5 Torr) present an experimental challenge, as the formation of dimer scales with its formation constant and the monomer pressure squared. The absorbance band associated with the hydrogen bound OH_b-stretching fundamental transition in the dimer is assigned and quantified. We estimate the constant of dimer formation, *K*, by an approach that combines spectroscopic measurements and a calculated oscillator strength of the associated OH_b-stretching band.[9] We compare the results to that previously reported for $(t\text{-BuOOH})_2$ in CCl_4 solution, the singly bound *t*-BuOOH·DME complex and acetic acid dimer and complex to elucidate the effects of the number of hydrogen bonds as well as the functional groups involved in the bonding.[9,12−22,39] Additionally, the weak interactions between the two *t*-BuOOH units in the dimer are illustrated by a non-covalent interaction (NCI) analysis.[40−43]

EXPERIMENTAL SECTION

The compounds *t*-BuOOH in water (70 wt %), *t*-BuOOH in decane (5.0−6.0 M), *t*-BuOH (anhydrous, ≥99.5%), DCM (anhydrous, ≥99.8%), $MgSO_4$ (anhydrous, ≥99.5%), and molecular sieves (3 Å) were purchased from Sigma-Aldrich. Deuterium oxide was purchased from Eurisotop. The water solvated *t*-BuOOH sample was extracted into DCM by a liquid−liquid phase extraction. The DCM phase was then dried by adding $MgSO_4$. To make the partially deuterated sample, the water solvated *t*-BuOOH sample was mixed with deuterium oxide in volume ratio 1:2 by stirring for 2 h and the DCM phase extraction was performed afterward. All samples were kept in sample holders sealed by PRODURAN Teflon stoppers. All samples, except for *t*-BuOH, which was semi-solid at the working temperatures, were ensured dry by adding activated 3 Å molecular sieves to the sample holders. The samples were connected via Swagelok UltraTorr fittings to a J. Young vacuum line with a background pressure of 10^{-4} Torr and were degassed repeatedly by freeze-pump-thaw-cycles until no bubbles were observed upon thawing.

The sample gas was introduced directly via a flexible metal tube into a 1 m optical pathlength cell (Tornado Series T5, Specac White-cell). The cell was fitted with CaF_2 windows and Au-coated internal and Al external mirrors and was placed in a Fourier transform IR (FTIR) (Bruker Vertex 80) spectrometer. The vacuum system and cell was flushed with D_2O before conducting the deuterium experiments to limit the rapid H/D exchange with trace amounts of H_2O. The cell compartment was continuously purged with N_2 during measurements to limit absorption from ambient H_2O and CO_2. The sample holders were covered with duct tape and the glass vacuum line and sample cells were covered in black plastic at all times to reduce photo-degradation of *t*-BuOOH. The pressure was measured in 10 s intervals by a diaphragm pressure gauge (Agilent, CDG500—10 Torr) attached directly to the cell. From this measurement, the monomer pressure was obtained by subtracting the estimated partial pressures of the solvent and impurities (vide infra). The temperature around the sample cells was kept at 298.2 ± 0.2 K during the recording of the spectra.

All spectra were recorded with a KBr beam splitter, a liquid nitrogen cooled HgCdTe (LN-MCT) detector with scanning velocity of 80 kHz and were averaged over 2000 scans with a 1 cm^{-1} resolution. We used a near IR (NIR) light source with a 3 mm aperture. This light source/beamsplitter/detector combination gave the highest S/N ratio for the OH_b-stretch region and the higher wavenumber region of the DCM reference band facilitating its subtraction (vide infra).

A low pressure reference spectrum of the *t*-BuOOH monomer was recorded with a longer optical pathlength cell (16 PA, IR Analysis, Inc. White-cell). The cell had a measured optical pathlength of 15 m and was fitted with KBr windows and Au-coated internal and Al external mirrors. The low sample pressure (∼0.3 Torr) ensured minimal dimer formation in the monomer reference spectrum. The reference spectrum was corrected for DCM and *t*-BuOH impurities.

At equilibrium, the unitless constant of dimer formation can be expressed by

$$K = \frac{p_{\mathrm{dim}} \cdot p^{\ominus}}{p_{\mathrm{mon}}^{\ 2}} \tag{1}$$

where *K* is the constant of dimer formation, p_{dim} is the dimer pressure, p_{mon} is the monomer pressure, and $p^{\ominus}$ is the standard pressure of 1 bar (750 Torr). To estimate the dimer pressure in the gas mixture we use an experimental and theoretical hybrid technique, which has been described previously.[9,44] We integrate the absorbance of the observed band associated with the OH_b-stretch and relate this to a calculated oscillator strength of the transition, f_{calc}, to determine the dimer pressure

$$p_{\mathrm{dim}} = 2.6935 \cdot 10^{-9} \frac{\text{Torr m cm}}{\text{K}} \frac{T}{f_{\mathrm{calc}} \cdot l} \cdot \int A(\tilde{\nu}) \mathrm{d}\tilde{\nu} \tag{2}$$

where l is the pathlength in units of m, *T* is the temperature, and $A(\tilde{\nu})$ is the wavenumber-dependent base 10 absorbance.

The dimer pressure is usually hard to obtain directly by experiments as it is insignificant compared to the total pressure of the gas mixture.[9] The hybrid method described has proven efficient at quantifying very small dimer pressures provided a unique absorption band can be detected. The technique takes advantage of the redshift and intensity enhancement of the OH_b-stretching band, which typically occurs upon hydrogen bonding.[9−11,45,46]

Matrix isolation experiments were performed to identify complex formation and aid the assignment of the weak $(t\text{-BuOOH})_2$ gas phase signal. The *t*-BuOOH sample was diluted 1:1790 in Ar and deposited on a CsI window at 12 K. A total of 11.7 mmol was deposited at a rate of 0.112 mmol/min. Spectra were recorded at 0.5 cm^{-1} resolution with a FTIR spectrometer (Bruker Vertex 70) with a MIR light source using a 3.0 mm aperture, a CaF_2 beamsplitter and a LN-MCT detector with a scanning velocity of 80 kHz. The bandwidth was restricted to 5266 cm^{-1} and a 20 kHz acquisition filter with a low-pass cutoff at 3950 cm^{-1} was used. Spectra were averaged over 2000 scans at 12 K. The matrix was annealed by raising the temperature to 20, 25, and 30 K for 10 min each and finally 30 K again for 20 min, with a spectrum recorded after each annealing cycle. This allowed for diffusion of the

https://doi.org/10.1021/acs.jpca.3c03702
J. Phys. Chem. A 2023, 127, 6476−6485

molecules within the Ar matrix promoting further cluster formation as well as relaxation of meta-stable matrix sites.[47−49]

COMPUTATIONAL DETAILS

Electronic structure calculations were performed with density functional theory (DFT) functionals B3LYP,[50] M06-2X,[51] PBE0,[52,53] and CAM-B3LYP[54] including the Grimme D3 empirical dispersion,[55] and ωB97X-D,[56] which includes the Grimme D2 empirical dispersion.[57] All DFT calculations were performed with Gaussian 16 using the aug-cc-pVTZ (AVTZ) basis set[58,59] and the "verytight" convergence criteria and the "ultrafine" integration grid.[60] A normal mode harmonic oscillator frequency calculation (NM HO) of the optimized geometries ensured convergence to a minimum. Finally, CCSD(T)-F12a/cc-pVDZ-F12 single-point energy calculations were performed on the ωB97X-D/AVTZ optimized geometries using Molpro12.1.[61−65]

A manual conformer search for alternative $(t\text{-BuOOH})_2$ structures was performed by varying the starting structure angles, dihedral angles, and number of hydrogen bonds and optimizing all generated structures at the ωB97X-D/AVTZ level of theory with the default optimization criteria in Gaussian 16. If a new conformer was found, it was reoptimized with the "verytight" convergence criteria and a NM HO calculation was performed.

The NCIs of the lowest energy optimized $(t\text{-BuOOH})_2$ structure was analyzed using NCIPLOT4.0 software.[40] The programme is used to calculate and visualize the reduced density gradient $s(\mathbf{r}) = 0.5$ a.u. isosurfaces[41−43] where $\mathbf{r}$ is a spatial coordinate. The surfaces are constructed from the CCSD(T)-F12a/cc-pVDZ-F12//ωB97X-D/AVTZ wave function using the "ultrafine" keyword for integration. The isosurfaces are color coded for the range -0.015 a.u. $< \mathrm{sign}(\lambda_2)\cdot\rho(\mathbf{r}) < 0.015$ a.u. where λ_2 is the second eigenvalue of the electron density Hessian and $\rho(\mathbf{r})$ is the electron density.

The frequency and oscillator strength of the OH_b-stretching transition were calculated with a one-dimensional local mode model (1D LM) programmed in Python 3.[66] The potential energy surface (PES) was sampled along the OH bond displacement coordinate: $q = [-0.45; 1.475$ Å] in 0.025 Å increments from the ωB97X-D/AVTZ equilibrium geometry. The points were interpolated to $\Delta q = 0.00002$ Å using a cubic spline to ensure convergence within the used Simpson's integration method. The vibrational Schrödinger equation was solved in a basis of the first 50 associated Legendre $m = 1$ polynomials. The Cartesian components of the dipole moment function were sampled and interpolated in the same way along the coordinate q.

The unitless oscillator strength was calculated as[67,68]

$$f = 4.702\cdot10^{-7}\frac{\mathrm{cm}}{D^2}\cdot\tilde{\nu}_{10}\cdot|\vec{\mu}_{10}|^2 \tag{3}$$

where $\tilde{\nu}_{10}$ is the transition wavenumber in cm^{-1} and $\vec{\mu}_{10}$ the transition dipole moment in Debye ($1\mathrm{D} = 3.33564\times10^{-30}$ C·m). The oscillator strength can be converted to units of km/mol by the multiplication factor 5.3313×10^6 km/mol.

The coupling between the two OH-stretching oscillators in $(t\text{-BuOOH})_2$ was estimated using a two-dimensional (2D) harmonically coupled anharmonic oscillator LM (HCAO LM) model.[69,70] The 2D PES was sampled along the displacement coordinates of the two chemically equivalent oscillators: q_1, $q_2 = [-0.075; 0.075$ Å] in 0.025 Å increments around the ωB97X-D/AVTZ equilibrium geometry. The force constants were determined by fitting the 7×7 PES grid to a 2D polynomial to the sixth order. The harmonic coupling was then estimated from the second-order force constants by[69,70]

$$\gamma' = -\frac{1}{2}\frac{F_{12}}{\sqrt{F_{11}}\sqrt{F_{22}}}\cdot\tilde{\omega} \tag{4}$$

where γ' is the coupling parameter, F_{ij} is the second-order derivative of the PES with respect to the displacement coordinates, $\tilde{\omega} = \sqrt{\frac{F_{11}}{\mu_{OH}}}/(2\pi c)$ is the harmonic transition wavenumber of the OH_b-stretch, and μ_{OH} is the reduced mass of the oscillator.

RESULTS AND DISCUSSION

Matrix Isolation FTIR Spectroscopy. Initially, we use matrix isolation FTIR spectra of *t*-BuOOH deposited in an Ar matrix to detect the formation of its clusters. Cold experiments give the optimal conditions for cluster formation as the entropic penalty of losing three vibrational and three rotational degrees of freedom upon cluster formation is minimized. In the top panel of Figure 1, we show the spectrum of the initial deposited sample. An intense and narrow band from the OH-stretch in *t*-BuOOH monomer is observed at 3579 cm^{-1}. We assign the broader and stronger band at ~3400 cm^{-1} to the OH_b-stretch of $(t\text{-BuOOH})_2$. A broad tail to lower wavenumbers is assigned as multiple OH_b-stretching bands of larger *t*-BuOOH clusters (multimers). In the bottom panel of Figure 1, we show the difference spectra after each annealing cycle with the initial deposit spectrum subtracted. In the difference spectra, the bands associated with $(t\text{-BuOOH})_2$ and larger clusters increase with each annealing cycle, while those of the monomer becomes increasingly negative as free monomer is

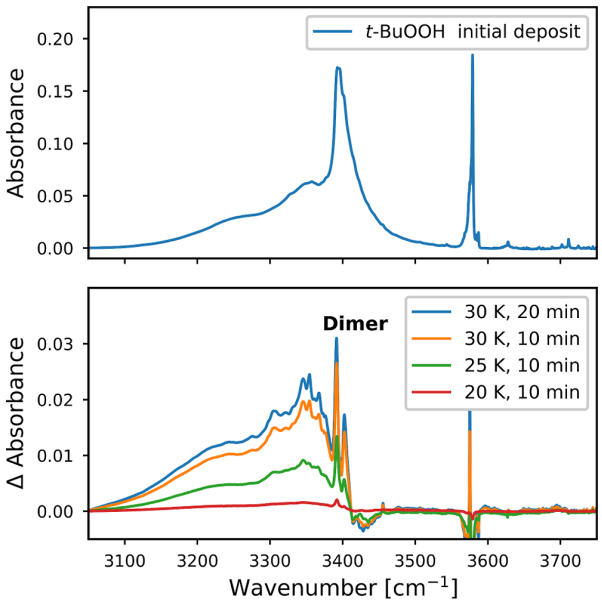

Figure 1. FTIR spectrum of *t*-BuOOH in a frozen Ar matrix. *t*-BuOOH is diluted 1:1790 in Ar and deposited on a CsI window at 12 K. Upper panel: spectrum immediately after the *t*-BuOOH/Ar mixture is deposited. Lower panel: difference spectra after each of the annealing cycles. Spectra are recorded between cycles and the initial deposit spectrum is subtracted.

https://doi.org/10.1021/acs.jpca.3c03702
J. Phys. Chem. A 2023, 127, 6476−6485

used to form the clusters. Two peaks associated with the dimer are observed to grow with each annealing cycle at 3392 and 3402 cm^{-1}, respectively. The appearance of two peaks is most probable due to the clusters getting trapped in different sites in the matrix with varying stabilization.[47−49] At 3628 cm^{-1}, the OH-stretching band from trace amounts of *t*-BuOH present in the sample can be seen. The minor sharp absorbance peaks at higher energies are from trace amounts of water in the sample compartment.

Theoretically, we identify five conformers of $(t\text{-BuOOH})_2$ (Section S16). The lowest energy conformer of $(t\text{-BuOOH})_2$ is shown to the left in Figure 2. The structure has a doubly

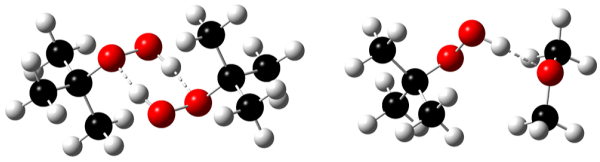

Figure 2. Calculated lowest energy ωB97X-D/AVTZ structures. Left: doubly hydrogen bound $(t\text{-BuOOH})_2$. Right: singly bound *t*-BuOOH·DME.

hydrogen bound six-membered ring in agreement with earlier findings for other hydroperoxide complexes.[23−29,31] At the ωB97X-D/AVTZ and B3LYP-D3/AVTZ levels of theory, all high-energy conformers have zero point corrected electronic formation energies, ΔE (ΔH at 0 K), that are 15−20 kJ/mol higher than the most stable conformer found, and Gibbs formation energies, ΔG, about 9−14 kJ/mol higher at 298 K (Table S6). This makes population of the high-energy conformers highly unlikely both in the matrix and the gas phase room temperature experiments. The difference, $\Delta H - \Delta G$, between the lowest energy conformer and the four other found conformers, highlights the entropic energy penalty of ca. 5 kJ/mol at 298 K associated with forming the rigid ring in the lowest energy structure. In the cold experiment, we find that formation of $(t\text{-BuOOH})_2$ is favored over that of larger clusters. Thus, in the gas phase at room temperature, clusters larger than the dimer are very unlikely to form. In contrast, alcohols have previously been reported to favor larger clusters.[71−74] The matrix isolation spectra show that formation of $(t\text{-BuOOH})_2$ is possible and provides an estimate of the OH-stretching redshift of ∼180 cm^{-1}.

Gas Phase Spectral Subtraction. In the gas phase, isolation of the $(t\text{-BuOOH})_2$ spectrum relies on accurate spectral subtraction of the *t*-BuOOH monomer, solvents, and impurities. Quantification of *K* relies on determination of the *t*-BuOOH monomer and dimer pressures. Within the approach we use, the measured integrated absorbance of the OH_b-stretching band and a calculated oscillator strength of the OH_b-stretching transition is used to determine the dimer pressure. We assume that the observed band only gains intensity from the OH_b-stretching transition in $(t\text{-BuOOH})_2$.

Due to its limited stability, *t*-BuOOH is commercially available only as solutions in decane and water, two solvents that are difficult to quantify and subtract from the measured spectrum of the gas mixture. For water, this is due to its rotational fine-structure, which is sensitive to pressure and temperature changes. For decane, it is due to its broad CH-stretching and HCH-bending bands, which overlap the bands from *t*-BuOOH. To avoid the challenge of quantifying these solvents in the gas mixture, we exchange the solvent to DCM. DCM has a very clear and characteristic CH-stretching/HCH-bending combination band with visible rotational fine-structure centered at 4467 cm^{-1} that facilitate accurate spectral subtraction (Figure 3B). In addition, DCM absorbance

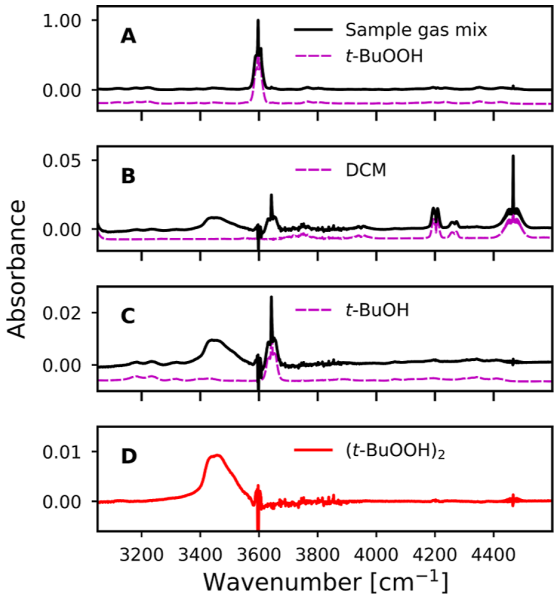

Figure 3. In panel A, the spectrum of the original sample is shown. In panel B, the *t*-BuOOH monomer has been subtracted leaving a spectrum of $(t\text{-BuOOH})_2$ with DCM and *t*-BuOH impurities. In panel C, we have subtracted DCM, and in panel D, *t*-BuOH has been subtracted, leaving a spectrum of pure $(t\text{-BuOOH})_2$. In frames A, B, and C, the reference spectrum of the largest impurity is shown with a dashed line underneath the spectrum of the sample gas mix.

bands are very weak in the OH-stretching region. The most prevalent impurity in the *t*-BuOOH sample, apart from the solvent, is its degradation product *t*-BuOH[75,76] with an OH-stretching band at 3643 cm^{-1} (Figure 3C). We record reference spectra of *t*-BuOH and DCM with known pressures and subtract these reference spectra from the sample mix spectra to estimate their respective partial pressures in the sample. This leaves a spectrum of only *t*-BuOOH + $(t\text{-BuOOH})_2$ and gives an accurate estimate of the *t*-BuOOH monomer partial pressure as the partial pressure of the dimer is negligible. The *t*-BuOOH monomer pressure is corrected for the partial pressure contributions from the solvent and impurities to the total pressure.

In Figure 3, we show the progression from the initial sample spectrum to the final $(t\text{-BuOOH})_2$ spectrum by subtraction of *t*-BuOOH monomer-, DCM-, and *t*-BuOH reference spectra, respectively. The amount of *t*-BuOH and especially DCM that is subtracted varies significantly between the different experiments. The spectrum shown has a measured total sample pressure of 6.51 Torr. Reference spectra of DCM corresponding to 2.83 Torr and *t*-BuOH corresponding to 0.19 Torr is subtracted. This leaves a determined *t*-BuOOH monomer pressure of 3.49 Torr. The estimated pressure of $(t\text{-BuOOH})_2$ present in the sample is about 3 orders of magnitude smaller than that of the *t*-BuOOH monomer and can be ignored in the determination of the monomer pressure. Due to the low partial pressure of $(t\text{-BuOOH})_2$, its associated OH_b-stretching band is very weak in comparison to the OH-stretch of the *t*-BuOOH

https://doi.org/10.1021/acs.jpca.3c03702
J. Phys. Chem. A 2023, 127, 6476−6485

monomer. This is noticeable in the change in absorbance-axis from panel A to the other panels. The spectra have been refined by subtracting the reference spectra of ambient water in the cell compartment of the spectrometer. We also correct for a slight ice build-up on the LN-MCT detector (Sections S5 and S6).

In the $(t\text{-BuOOH})_2$ spectrum (Figure 3D), we observe small residuals from imperfect subtraction of the intense *t*-BuOOH monomer signal at around 3597 cm^{-1}. Small residual signals from DCM subtraction is also observed at 4467 cm^{-1} and finally signals from water impurities are observed in the region 3600−3950 cm^{-1}. This is primarily due to differences in pressure-broadening of the sharp rotational-vibrational lines between the spectra of the samples and the references. We also recorded spectra of the decane solvated *t*-BuOOH sample and obtained a spectrum of $(t\text{-BuOOH})_2$ with a band profile indistinguishable to that of the DCM solvated sample (Section S11).

Band Shape and Position. In Figure 4, we show the OH_b-stretching band of $(t\text{-BuOOH})_2$ measured for different *t*-BuOOH monomer pressures. The absorbance band is asymmetric with a full width at half maximum (fwhm) of ~110 cm^{-1}. The intensity-weighted center of the band is 3452 cm^{-1}, which corresponds to an OH-stretching band redshift of 145 cm^{-1} from the *t*-BuOOH monomer (Table 1). However,

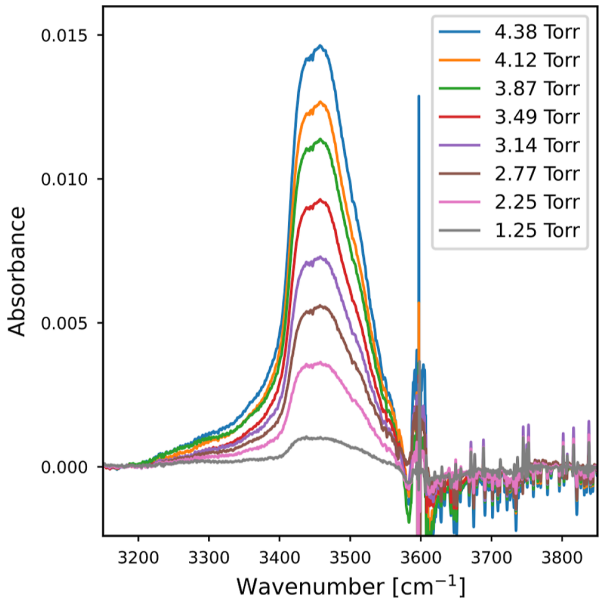

Figure 4. Subset of the recorded $(t\text{-BuOOH})_2$ spectra. Labels denote *t*-BuOOH monomer pressure in each experiment.

the two OH_b-stretching modes in $(t\text{-BuOOH})_2$ couple, leading to an IR-inactive symmetric transition and an IR-active antisymmetric transition, the latter of which gives rise to the observed band. The splitting of the two transitions are calculated to be 35 cm^{-1} with the HCAO LM model (32 cm^{-1} with NM HO model) with the antisymmetric transition at the highest energy. A decoupled OH_b-stretching transition would be located in between the symmetric/antisymmetric transitions or about 18 cm^{-1} lower than that observed. The coupling between the two modes thus attenuate the observed redshift. In addition, the maximum of the OH_b-stretching band in hydrogen bound complexes shift to higher wavenumbers as the temperature increases due to coupling and population of the low-frequency intermolecular modes. In methanol dimer, for example, the cold OH_b-stretching band is located at the onset of the warm OH_b-stretching band.[9,77] In general, the OH_b-stretching band maximum occurs ca. 25 cm^{-1} lower in cold spectra compared to the corresponding band maximum at room temperature. This is illustrated in a few examples for different hydrogen bound complexes.[9,73,77]

To experimentally decouple the two OH_b-stretching oscillators, we record spectra of a partially deuterated *t*-BuOOH sample. The sample is deuterated to roughly 50% atom D. Thus, the spectrum will contain a mix of dimers formed with either 0, 1, or 2H replaced by D, roughly in ratio 1:2:1. The formed *t*-BuOOH·*t*-BuOOD dimer is observed in both matrix experiments and in gas phase room temperature experiments. In the 12 K matrix isolation difference spectra of the partly deuterated sample (Figure S15), we determine a 17 cm^{-1} shift of the two observed OH_b-stretching bands in good agreement with the calculated shift expected from decoupling the two OH_b-stretching transitions. Due to temperature effects, the observed shift under cold conditions of ca. 17 cm^{-1} is a more direct measure of the decoupling of the two OH_b-stretching oscillators. If we include the additional shift of 17 cm^{-1}, the redshift of the isolated OH_b-stretching band in $(t\text{-BuOOH})_2$ becomes 162 cm^{-1}, which is comparable to the 170 cm^{-1} redshift found for *t*-BuOOH·DME.[22]

In Figure 5, the OH_b-stretching band position in the gas phase spectrum of $(t\text{-BuOOH})_2$ is compared to that of the partially deuterated dimer *t*-BuOOH·*t*-BuOOD. We subtract the spectrum of the non-deuterated dimer from the spectrum of the mixture to obtain the spectrum of the singly- and doubly deuterated dimers *t*-BuOOH·*t*-BuOOD and $(t\text{-BuOOD})_2$. The latter is expected to have no intensity in the OH-stretching region. We observe an OH_b-stretching band maximum of *t*-BuOOH·*t*-BuOOD at ~3415 cm^{-1}, which is shifted ~37 cm^{-1} from the intensity weighted maximum of the non-deuterated $(t\text{-BuOOH})_2$. The 37 cm^{-1} shift in the gas phase is ca. 20 cm^{-1} larger than that found in the matrix isolation experiment. We attribute the width and shape of the OH_b-stretching band of (*t*-

Table 1. Calculated ωB97X-D/AVTZ Geometric Parameters and Room-Temperature Observed Redshifts[a]

	$\theta_{OH\cdots O}$ [°]	$R_{OH\cdots O}$ [Å]	ΔR_{OH} [Å]	calc $\tilde{\nu}$	obs $\tilde{\nu}^b$	obs $\Delta\tilde{\nu}$
t-BuOOH				3669[c]	3597	
$(t\text{-BuOOH})_2$	154.2	1.90	0.0115	3413[c]	3452	145 (162)[f]
t-BuOOH·DME[d]	168.4	1.81	0.0123	3363[e]	3428	170
	163.1	1.83	0.0126	3356[e]		

[a]All $\tilde{\nu}$ are in units of cm^{-1}. [b]Band maximum. Intensity weighted band maximum for $(t\text{-BuOOH})_2$. [c]Calculated with 1D LM model. [d]Values from Møller et al.[22] includes two conformers. [e]1D LM model assuming Morse potential from Møller et al.[22] [f]Redshift including the 17 cm^{-1} shift from decoupling the OH_b-stretch in the dimer.

https://doi.org/10.1021/acs.jpca.3c03702
J. Phys. Chem. A 2023, 127, 6476−6485

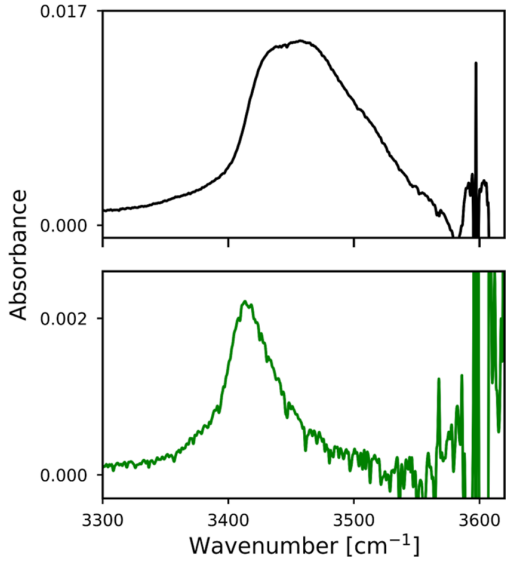

Figure 5. Gas-phase spectra at 298 K of non-deuterated $(t\text{-BuOOH})_2$ and partly deuterated *t*-BuOOH·*t*-BuOOD. Top panel: the spectrum of the non-deuterated $(t\text{-BuOOH})_2$ at 4.38 Torr monomer pressure, equivalent to the highest trace in Figure 4. Bottom panel: the band associated with the OH_b-stretch in the singly deuterated dimer (*t*-BuOOH·*t*-BuOOD). The spectrum is recorded at a measured total pressure of 4.7 Torr. The band has a maximum at 3415 cm^{-1}.

$(t\text{-BuOOH})_2$ to the coupling of the OH_b-stretching mode with the low frequency intermolecular modes. Previous studies of weakly hydrogen bound complexes have shown that the low frequency intermolecular modes can significantly widen and change the overall shape of the observed OH_b-stretching band at room temperature.[9,44,73,78,79] The OH_b-stretching transition occurs from a manifold of thermally populated low lying vibrational states, translating into many hot transitions that all contribute intensity to the observed band.[78] The band shape of *t*-BuOOH·*t*-BuOOD is more narrow with a fwhm ∼45 cm^{-1}. This reduced width is likely due to changes in frequencies and population of the intermolecular modes upon deuteration. No clear combination bands are observed in the cold experiments and it is therefore unlikely that these will contribute significantly to the band at room temperature.

It is difficult to calculate accurately the frequencies and oscillator strengths of OH_b-stretching transitions in weakly bound complexes.[78,80−82] We use a 1D LM model to calculate the frequency and oscillator strength of the OH_b-stretching transitions in $(t\text{-BuOOH})_2$. In the 1D LM model, the OH_b-stretch is not coupled to the intermolecular modes and thus gives reasonable results for the OH_b-stretching transition with a minimum of variables. The 1D LM model predicts a transition wavenumber of 3413 cm^{-1} with ωB97X-D/AVTZ, which is fairly close to the observed band maximum. The simplistic 1D LM model overestimates the redshift of the OH_b-stretch due to the omission of coupling to the low frequency intermolecular modes.[82,83]

In Table 1, the calculated geometric parameters and redshifts are compared with the observed redshifts for $(t\text{-BuOOH})_2$ and for the bi-molecular complex *t*-BuOOH·DME (Figure 2, Right). Smaller hydrogen bond angles, smaller elongation of O−H intramolecular bonds and longer hydrogen bonds are all indicative of weaker hydrogen bonds in $(t\text{-BuOOH})_2$ compared to *t*-BuOOH·DME.[10,11] The slightly smaller redshift in $(t\text{-BuOOH})_2$ compared to that in *t*-BuOOH·DME also suggests weaker individual OOH···O hydrogen bonds in $(t\text{-BuOOH})_2$. The ring strain in the $(t\text{-BuOOH})_2$ structure leads to non-optimal hydrogen bond angles of 154.2°, smaller than that found in *t*-BuOOH·DME and is in line with the smaller redshift.

Constant of Dimer Formation. To determine the constant of dimer formation, the amount of $(t\text{-BuOOH})_2$ present in the gas mixture must be determined. The $(t\text{-BuOOH})_2$ partial pressure is determined from eq 2, where the OH_b-stretching band is integrated between 3250 and 3577 cm^{-1}. We estimate the theoretical oscillator strength (f_{calc}) of the entire OH_b-stretching band in $(t\text{-BuOOH})_2$ to be 1.4 × 10^{-4}. This arises from two times the oscillator strength of one OH_b-stretching transition, which is calculated with the 1D LM model to be 9.1 × 10^{-5} (ωB97X-D/AVTZ) and empirically corrected for the effect of the coupling to the intermolecular modes.[83] The empirical correction comes from a relatively robust discrepancy found between the 1D LM model and a LM perturbation theory model, which includes coupling to the intermolecular modes. The two models were applied to a range of hydrogen bound complexes, for which a reduction in intensity of ∼25% was observed when introducing coupling to the intermolecular modes.[81−83]

In Figure 6, the estimated pressure of $(t\text{-BuOOH})_2$ is fitted to the square of the *t*-BuOOH monomer pressure for a number

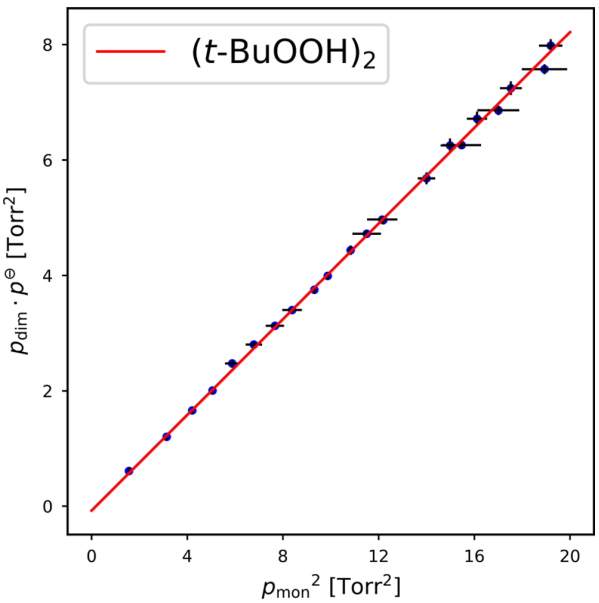

Figure 6. Determined $(t\text{-BuOOH})_2$ pressure fitted against *t*-BuOOH monomer pressure squared. The linear fit is performed by minimizing a χ^2 taking into consideration the error on each individual measurement. The error bars indicate errors in monomer pressure and integrated absorbance in the horizontal and vertical direction, respectively.

of experiments. The determined monomer- and dimer pressures for all measurements are shown in Table S1. The constant of dimer formation for $(t\text{-BuOOH})_2$ is estimated to be K = 0.41 ± 0.017 following eq 1, with the uncertainty reported as one standard error (σ_{std}) including all experimental errors. The statistical χ^2-fit uncertainty is 0.0054 and reflects a

https://doi.org/10.1021/acs.jpca.3c03702
J. Phys. Chem. A 2023, 127, 6476−6485

Table 2. Equilibrium Constants and ΔG-Values at Room Temperature

	K	ΔG [kJ/mol]	T [K]	refs
$(t\text{-BuOOH})_2$[a]	0.41	2.2	298	this work
t-BuOOH·DME[a]	0.17	4.4	295−298	Møller et al.[22]
t-BuOH·DME[a]	0.031	8.6	295−298	Møller et al.[22]
$(t\text{-BuOOH})_2$[b]	1.90	−1.6	303	Walling & Heaton[30]
$(t\text{-BuOOD})_2$[b]	1.65	−1.3	303	Walling & Heaton[30]
$(CH_3COOH)_2$	[30, 2000]	[−8,−18]		various sources.[17,19−21]
CH_3COOH·MeOH[a]	1.1	−0.24	308	Wagner et al.[39]

[a]Gas-phase experiment. [b]In solution of CCl_4.

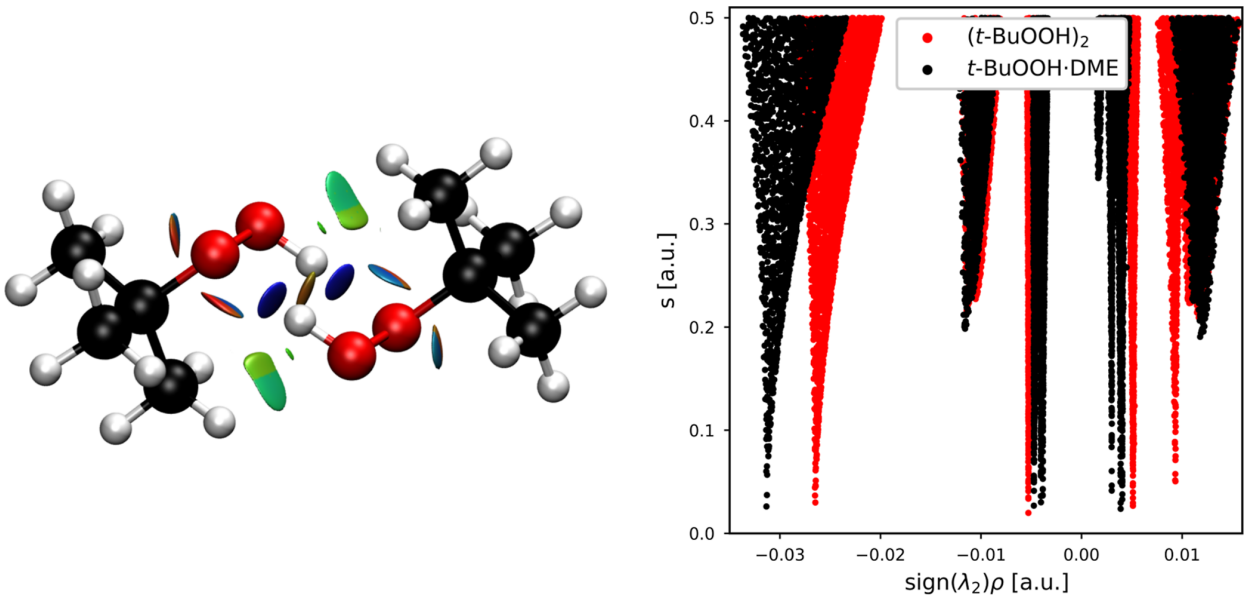

Figure 7. NCI analyses of $(t\text{-BuOOH})_2$. Left: the NCI $s(\mathbf{r}) = 0.5$ a.u. isosurfaces in $(t\text{-BuOOH})_2$. Right: the $s(\mathbf{r})$ plotted vs $\text{sign}(\lambda_2)\cdot\rho(\mathbf{r})$ for $(t\text{-BuOOH})_2$ (red) and t-BuOOH·DME (black).

very certain quadratic correlation between the integrated absorbance of the OH_b-stretching band and the monomer pressure as is expected for dimer formation. The quadratic correlation further rules out significant intensity contribution from a t-BuOOH trimer, which would introduce a cubic correlation between the integrated absorbance and the t-BuOOH monomer pressure. The $K = 0.41$ corresponds to a $\Delta G = 2.2$ kJ/mol at 298 K. The accuracy of the quantification of K is limited by the estimated oscillator strength, which we expect to be accurate to better than a factor of 2. K is inversely proportional to f_{calc} and ΔG scales logarithmically with K. Thus, we expect an accuracy of K to be within a factor 2 corresponding to an accuracy of ΔG of better than ±1.7 kJ/mol at 298 K.

We also calculated ΔG directly with different DFT functionals within the harmonic oscillator and rigid rotor approximations. The difference between the ωB97X-D and B3LYP-D3 functionals are 2.9 kJ/mol corresponding to a factor 3.2 difference in K, underlining the sensitivity to the electronic structure method used in the purely theoretical approach (Table S10). In comparison, the calculated 1D LM oscillator strength of the OH_b-stretch, and by extension K, varies less than 20% between the ωB97X-D and the B3LYP-D3 methods (Section S12). This insensitivity of f_{calc} to electronic structure method is in agreement with results for other hydrogen bound complexes.[9] For example, the f_{calc} of the OH_b-stretch varies less than 10% between the ωB97X-D and CCSD(T)-F12a methods for the MeOH·DMA complex. Thus, K determined with this hybrid method is relatively insensitive to the choice of the electronic structure method.

In Table 2, we compare K for various hydrogen bound complexes and dimers. The experimentally determined constant of dimer formation and corresponding ΔG value at 298 K for t-BuOOH·DME is 0.17 and 4.4 kJ/mol, respectively. $(t\text{-BuOOH})_2$ thus has an increased stabilization of ca. 2.2 kJ/mol at 298 K compared to t-BuOOH·DME. The modest increase in stabilization was surprising, as we expected the binding-enthalpy from forming an additional hydrogen bond to shift the ΔG value significantly. This phenomenon is observed for carboxylic acids, where constants of dimer formation of the doubly bound dimers are orders of magnitude larger than that of the singly bound complexes. For acetic acid, the constants of dimer formation of the singly hydrogen bound complexes with methanol and ethanol were experimentally estimated to $K \sim 1$.[39] The fluorinated version, trifluoroacetic acid, also forms complexes with various ketones with $K < 1$.[84] However, upon forming two hydrogen bonds in an eight-membered ring in an acetic acid dimer, theoretical studies report $K \sim 30-860$[17] and IR-, NMR-, and vapor density experiments estimate values in the order of $K \sim 1000-2000$.[19−21] For formic acid with a similar eight-membered ring, K is estimated from theory and experiments in the order of ∼300.[12−16] In $(t\text{-BuOOH})_2$, the

https://doi.org/10.1021/acs.jpca.3c03702
J. Phys. Chem. A 2023, 127, 6476−6485

weakening of the individual hydrogen bonds, as well as an additional entropic energy penalty from forming a rigid ring, results in the modest additional stabilization of ca. 2.2 kJ/mol at room temperature. Previously, K has been determined for $(t\text{-BuOOH})_2$ and $(t\text{-BuOOD})_2$ in CCl_4 solution to be 1.90 and 1.65, respectively.[30] These values are significantly higher than the gas-phase value presented here. In the CCl_4 experiment, the reported K is lower for the deuterated dimer, which is opposing the common trend of deuterated species forming stronger bound complexes.[85]

In Figure 7, we show the NCI analysis of the intermolecular electron densities and the reduced electron density gradients. To the left is shown the spatial analysis illustrated as $s(\mathbf{r}) = 0.5$ a.u. isosurfaces and to the right the $s(\mathbf{r})$ is plotted versus $\text{sign}(\lambda_2)\cdot\rho(\mathbf{r})$. The isosurfaces to the left are on a color gradient from strong attractive (blue) to weak secondary (green) to strong repulsive interactions (red). The hydrogen bonds are clearly visible as two deep blue-colored circular surfaces located close to the hydrogen atoms of each OOH group. In the 2D plot to the right, the $s(\mathbf{r})$ minima corresponding to the hydrogen bonds are located at $\text{sign}(\lambda_2)\cdot\rho(\mathbf{r}) = -0.0265$ a.u. and -0.0313 a.u. for $(t\text{-BuOOH})_2$ and t-BuOOH·DME, respectively, signifying weaker individual hydrogen bonds in $(t\text{-BuOOH})_2$. An additional interaction in $(t\text{-BuOOH})_2$, which is not present in the t-BuOOH·DME, is the repulsive interaction in the middle of the ring. This is seen as a red-brown isosurface in the center of $(t\text{-BuOOH})_2$ and corresponds to the $s(\mathbf{r})$ extremum at $\text{sign}(\lambda_2)\cdot\rho(\mathbf{r}) = 0.0093$ a.u. in the 2D plot.

CONCLUSIONS

We have detected $(t\text{-BuOOH})_2$ in the gas phase at room temperature from its fundamental OH_b-stretching band. The band profile is wide and asymmetric with an intensity weighted maximum at 3452 cm^{-1}. We decoupled the two OH-stretching oscillators by partially deuterating the dimer. This facilitated direct comparison with the redshift of the singly bound t-BuOOH·DME complex which was found to be similar to that of $(t\text{-BuOOH})_2$. The matrix isolation spectrum of t-BuOOH·t-BuOOD dimer provided an estimate of the HCAO LM coupling parameter, γ', of 17 cm^{-1} between the two OH_b-stretching vibrations. The calculated lowest energy structure of the dimer is a closed 6-membered ring structure, which imposes non-optimal angles for the hydrogen bonds. Other conformers were found energetically unfavorable and were not detected at room temperature. The constant of dimer formation is determined to be ∼0.4, which is roughly twice that found for the singly bound t-BuOOH·DME complex. This rough factor two increase from a singly to a doubly hydrogen bound complex is significantly smaller than that found for carboxylic acids.

ASSOCIATED CONTENT

Supporting Information

The Supporting Information is available free of charge at https://pubs.acs.org/doi/10.1021/acs.jpca.3c03702.

Protocol of the t-BuOOH sample phase extracted from H_2O into DCM; H-NMR and C-NMR spectra of finished samples confirming purity and estimating residual DCM and H_2O content; measured and estimated pressures of all experiments; spectral refinement by subtracting water vapor- and ice signals from the spectra; details on baseline corrections and integration limits; estimation of experimental errors and procedure of propagation of error; data treatment of commercially available t-BuOOH solvated in decane; oscillator strengths and transition wavenumbers calculated with different models for t-BuOOH and $(t\text{-BuOOH})_2$; deuteration of t-BuOOH sample is shown and the 12 K matrix spectra of the partly deuterated sample; integrated kinetic energy densities $G(s_{0.5})$ of the NCI analyses; alternative conformers found and thermodynamic properties; Mulliken charge distributions in the t-BuOOH monomer, dimer, and the t-BuOOH·DME complex; and calculated thermodynamic properties for the most stable conformer are reported with different DFT functionals (PDF)

AUTHOR INFORMATION

Corresponding Author

Henrik G. Kjaergaard − *Department of Chemistry, University of Copenhagen, 2100 Copenhagen-Ø, Denmark;* orcid.org/0000-0002-7275-8297; Phone: +45 35320334; Email: hgk@chem.ku.dk; Fax: +45 35320322

Author

Casper Vindahl Jensen − *Department of Chemistry, University of Copenhagen, 2100 Copenhagen-Ø, Denmark;* orcid.org/0000-0002-9102-1223

Complete contact information is available at: https://pubs.acs.org/10.1021/acs.jpca.3c03702

Notes

The authors declare no competing financial interest.

ACKNOWLEDGMENTS

The authors thank Emil Vogt and Timothy Zwier for helpful discussions. The authors thank Joseph Lane for providing the Bonder calculations and Mathias Dowds for assisting the sample preparation and NMR analysis. The authors thank The Novo Nordisk Foundation, grant numbers NNF19OC0057374 and NNF22OC0080193 for financial support.

REFERENCES

(1) Hubbard, R. E.; Haider, M. K. Hydrogen Bonds in Proteins: Role and Strength. In *Encyclopedia of Life Sciences (ELS)*; John Wiley & Sons, Ltd, 2010.

(2) Ippolito, J. A.; Alexander, R. S.; Christianson, D. W. Hydrogen Bond Stereochemistry in Protein Structure and Function. *J. Mol. Biol.* **1990**, *215*, 457−471.

(3) Hooft, R. W.; Sander, C.; Vriend, G. Positioning Hydrogen Atoms by Optimizing Hydrogen-Bond Networks in Protein structures. *Proteins: Struct., Funct., Bioinf.* **1996**, *26*, 363−376.

(4) McDonald, I. K.; Thornton, J. M. Satisfying Hydrogen Bonding Potential in Proteins. *J. Mol. Biol.* **1994**, *238*, 777−793.

(5) Creighton, T. E. Stability of Folded Conformations: Current Opinion in Structural Biology 1991, 1: 5−16. *Curr. Opin. Struct. Biol.* **1991**, *1*, 5−16.

(6) Bianchi, F.; Kurtén, T.; Riva, M.; Mohr, C.; Rissanen, M. P.; Roldin, P.; Berndt, T.; Crounse, J. D.; Wennberg, P. O.; Mentel, T. F.; et al. Highly Oxygenated Organic Molecules (HOM) from Gas-Phase Autoxidation involving Peroxy Radicals: A Key Contributor to Atmospheric Aerosol. *Chem. Rev.* **2019**, *119*, 3472−3509.

(7) Zhang, R.; Khalizov, A.; Wang, L.; Hu, M.; Xu, W. Nucleation and Growth of Nanoparticles in the Atmosphere. *Chem. Rev.* **2012**, *112*, 1957−2011.
(8) Zhao, J.; Khalizov, A.; Zhang, R.; McGraw, R. Hydrogen-Bonding Interaction in Molecular Complexes and Clusters of Aerosol Nucleation Precursors. *J. Phys. Chem. A* **2009**, *113*, 680−689.
(9) Hansen, A. S.; Vogt, E.; Kjaergaard, H. G. Gibbs Energy of Complex Formation−Combining Infrared Spectroscopy and Vibrational Theory. *Int. Rev. Phys. Chem.* **2019**, *38*, 115−148.
(10) Arunan, E.; Desiraju, G. R.; Klein, R. A.; Sadlej, J.; Scheiner, S.; Alkorta, I.; Clary, D. C.; Crabtree, R. H.; Dannenberg, J. J.; Hobza, P.; et al. Defining the Hydrogen Bond: An account (IUPAC Technical Report). *Pure Appl. Chem.* **2011**, *83*, 1619−1636.
(11) Arunan, E.; Desiraju, G. R.; Klein, R. A.; Sadlej, J.; Scheiner, S.; Alkorta, I.; Clary, D. C.; Crabtree, R. H.; Dannenberg, J. J.; Hobza, P.; et al. Definition of the Hydrogen Bond (IUPAC Recommendations 2011). *Pure Appl. Chem.* **2011**, *83*, 1637−1641.
(12) Mackeprang, K.; Xu, Z.-H.; Maroun, Z.; Meuwly, M.; Kjaergaard, H. G. Spectroscopy and Dynamics of Double Proton Transfer in Formic Acid Dimer. *Phys. Chem. Chem. Phys.* **2016**, *18*, 24654−24662.
(13) Barton, J. R.; Hsu, C. PVTX Properties of Associated Vapors of Formic and Acetic Acids. *J. Chem. Eng. Data* **1969**, *14*, 184−187.
(14) Vander Auwera, J.; Didriche, K.; Perrin, A.; Keller, F. Absolute Line Intensities for Formic Acid and Dissociation Constant of the Dimer. *J. Chem. Phys.* **2007**, *126*, 124311.
(15) Winkler, A.; Hess, P. Study of the Energetics and Dynamics of Hydrogen Bond Formation in Aliphatic Carboxylic Acid Vapors by Resonant Photoacoustic Spectroscopy. *J. Am. Chem. Soc.* **1994**, *116*, 9233−9240.
(16) Miyamoto, S.; Nakamura, S.; Iwai, Y.; Arai, Y. Measurement of Vapor-Phase Compressibility Factors of Monocarboxylic Acids using a Flow-Type Apparatus and their Association Constants. *J. Chem. Eng. Data* **1999**, *44*, 48−51.
(17) Colominas, C.; Teixidó, J.; Cemelí, J.; Luque, F. J.; Orozco, M. Dimerization of Carboxylic Acids: Reliability of Theoretical Calculations and the Effect of Solvent. *J. Phys. Chem. B* **1998**, *102*, 2269−2276.
(18) Chocholoušová, J.; Vacek, J.; Hobza, P. Acetic Acid Dimer in the Gas Phase, Nonpolar Solvent, Microhydrated Environment, and Dilute and Concentrated Acetic Acid: Ab Initio Quantum Chemical and Molecular Dynamics Simulations. *J. Phys. Chem. A* **2003**, *107*, 3086−3092.
(19) Togeas, J. B. Acetic Acid Vapor: 2. A Statistical Mechanical Critique of Vapor Density Experiments. *J. Phys. Chem. A* **2005**, *109*, 5438−5444.
(20) Goubet, M.; Soulard, P.; Pirali, O.; Asselin, P.; Réal, F.; Gruet, S.; Huet, T. R.; Roy, P.; Georges, R. Standard Free Energy of the Equilibrium between the Trans-Monomer and the Cyclic-Dimer of Acetic Acid in the Gas Phase from Infrared Spectroscopy. *Phys. Chem. Chem. Phys.* **2015**, *17*, 7477−7488.
(21) Socha, O.; Dračínský, M. Dimerization of Acetic Acid in the Gas Phase—NMR Experiments and Quantum-Chemical Calculations. *Molecules* **2020**, *25*, 2150.
(22) Møller, K. H.; Tram, C. M.; Kjaergaard, H. G. Side-by-Side Comparison of Hydroperoxide and Corresponding Alcohol as Hydrogen-Bond Donors. *J. Phys. Chem. A* **2017**, *121*, 2951−2959.
(23) Giguère, P. A.; Srinivasan, T. Raman Study of Matrix Isolated H_2O_2 and D_2O_2. *Chem. Phys. Lett.* **1975**, *33*, 479−482.
(24) Giguere, P. A. Intermediates in the Gas-Phase Disproportionation of HO_2 Radicals. *J. Phys. Chem.* **1981**, *85*, 3733−3734.
(25) Diem, M.; Tso, T.-L.; Lee, E. K. On the Bonding and Structure in Dihydroperoxyl $(HO_2)_2$ and H_2O_4. *J. Chem. Phys.* **1982**, *76*, 6452−6454.
(26) Dobado, J.; Molina, J. M. Ab Initio Molecular Orbital Calculation of the Hydrogen Peroxide Dimer: Study of Basis set Superposition Error. *J. Phys. Chem.* **1993**, *97*, 7499−7504.
(27) Engdahl, A.; Nelander, B.; Karlström, G. A Matrix Isolation and Ab Initio Study of the Hydrogen Peroxide Dimer. *J. Phys. Chem. A* **2001**, *105*, 8393−8398.
(28) Engdahl, A.; Nelander, B. The HOOH−HOO Complex. A Matrix Isolation Study. *Phys. Chem. Chem. Phys.* **2004**, *6*, 730−734.
(29) Qu, Y.; Bian, X.; Zhou, Z.; Gao, H. Existence of Hydroperoxy and Hydrogen Peroxide Radical Complex ($HO_2 \cdot H_2O_2$). *Chem. Phys. Lett.* **2002**, *366*, 260−266.
(30) Walling, C.; Heaton, L. Hydrogen Bonding and Complex Formation in Solutions of t-Butyl Hydroperoxide. *J. Am. Chem. Soc.* **1965**, *87*, 48−51.
(31) Duh, Y.-S.; Kao, C.-S.; Hwang, H.-H.; Lee, W. W.-L. Thermal Decomposition Kinetics of Cumene Hydroperoxide. *Process Saf. Environ. Prot.* **1998**, *76*, 271−276.
(32) Hansen, A. S.; Huchmala, R. M.; Vogt, E.; Boyer, M. A.; Bhagde, T.; Vansco, M. F.; Jensen, C. V.; Kjærsgaard, A.; Kjaergaard, H. G.; McCoy, A. B.; et al. Coupling of Torsion and OH-Stretching in tert-Butyl Hydroperoxide. I. The Cold and Warm First OH-Stretching Overtone Spectrum. *J. Chem. Phys.* **2021**, *154*, 164306.
(33) Vogt, E.; Huchmala, R. M.; Jensen, C. V.; Boyer, M. A.; Wallberg, J.; Hansen, A. S.; Kjærsgaard, A.; Lester, M. I.; McCoy, A. B.; Kjaergaard, H. G. Coupling of Torsion and OH-Stretching in tert-Butyl Hydroperoxide. II. The OH-Stretching Fundamental and Overtone Spectra. *J. Chem. Phys.* **2021**, *154*, 164307.
(34) Chandler, D. W.; Farneth, W. E.; Zare, R. N. A Search for Mode-Selective Chemistry: The Unimolecular Dissociation of t-Butyl Hydroperoxide Induced by Vibrational Overtone Excitation. *J. Chem. Phys.* **1982**, *77*, 4447−4458.
(35) Likar, M.; Baggott, J.; Crim, F. Vibrationally Mediated Photodissociation of t-Butyl Hydroperoxide: Vibrational Overtone Spectroscopy and Photodissociation Dynamics. *J. Chem. Phys.* **1989**, *90*, 6266−6274.
(36) Homitsky, S. C.; Dragulin, S. M.; Haynes, L. M.; Hsieh, S. O−H Stretch Overtone Excitation in Methyl and Ethyl Hydroperoxides. *J. Phys. Chem. A* **2004**, *108*, 9492−9499.
(37) Chuang, M.-C.; Baggott, J. E.; Chandler, D. W.; Farneth, W. E.; Zare, R. N. Unimolecular Decomposition of t-Butylhydroperoxide by Direct Excitation of the 6−0 O—H Stretching Overtone. *Faraday Discuss. Chem. Soc.* **1983**, *75*, 301−313.
(38) Baasandorj, M.; Papanastasiou, D. K.; Talukdar, R. K.; Hasson, A. S.; Burkholder, J. B. $(CH_3)_3COOH$ (tert-Butyl Hydroperoxide): OH Reaction Rate Coefficients between 206 and 375 K and the OH Photolysis Quantum Yield at 248 nm. *Phys. Chem. Chem. Phys.* **2010**, *12*, 12101−12111.
(39) Wagner, M.; Apelblat, A.; Tamir, A. Excess Gibbs Free Energy in Methanol + Acetic Acid and Ethanol + Acetic Acid. *J. Chem. Thermodyn.* **1980**, *12*, 181−186.
(40) Contreras-García, J.; Johnson, E. R.; Keinan, S.; Chaudret, R.; Piquemal, J.-P.; Beratan, D. N.; Yang, W. NCIPLOT: A Program for Plotting Noncovalent Interaction Regions. *J. Chem. Theory Comput.* **2011**, *7*, 625−632.
(41) Johnson, E. R.; Keinan, S.; Mori-Sánchez, P.; Contreras-García, J.; Cohen, A. J.; Yang, W. Revealing Noncovalent Interactions. *J. Am. Chem. Soc.* **2010**, *132*, 6498−6506.
(42) Boto, R. A.; Contreras-García, J.; Tierny, J.; Piquemal, J.-P. Interpretation of the Reduced Density Gradient. *Mol. Phys.* **2016**, *114*, 1406−1414.
(43) Laplaza, R.; Peccati, F.; Boto, A.; Quan, C.; Carbone, A.; Piquemal, J.-P.; Maday, Y.; Contreras-García, J. NCIPLOT and the Analysis of Noncovalent Interactions using the Reduced Density Gradient. *Wiley Interdiscip. Rev.: Comput. Mol. Sci.* **2021**, *11*, No. e1497.
(44) Hippler, M. Quantum Chemical Study and Infrared Spectroscopy of Hydrogen-Bonded $CHCl_3$−NH_3 in the Gas Phase. *J. Chem. Phys.* **2007**, *127*, 084306.
(45) Kjaergaard, H. G.; Low, G. R.; Robinson, T. W.; Howard, D. L. Calculated OH-Stretching Vibrational Transitions in the Water-Nitrogen and Water-Oxygen Complexes. *J. Phys. Chem. A* **2002**, *106*, 8955−8962.

https://doi.org/10.1021/acs.jpca.3c03702
J. Phys. Chem. A 2023, 127, 6476−6485

(46) Hippler, M.; Hesse, S.; Suhm, M. A. Quantum-Chemical Study and FTIR Jet Spectroscopy of $CHCl_3$−NH_3 Association in the Gas Phase. *Phys. Chem. Chem. Phys.* **2010**, *12*, 13555−13565.
(47) Redington, R. L. Matrix Trapping Sites and Interactions with LiF Monomer. *J. Chem. Phys.* **1995**, *102*, 7332−7340.
(48) Kappe, C. O.; Wong, M. W.; Wentrup, C. Acetylketene: Conformational Isomerism and Photochemistry. Matrix Isolation Infrared and Ab Initio Studies. *J. Org. Chem.* **1995**, *60*, 1686−1695.
(49) Barnes, A. Matrix Isolation Vibrational Spectroscopy as a Tool for Studying Conformational Isomerism. *J. Mol. Struct.* **1984**, *113*, 161−174.
(50) Becke, A. Density-Functional Thermochemistry. III. The Role of Exact Exchange. *J. Chem. Phys.* **1993**, *98*, 5648−5652.
(51) Zhao, Y.; Truhlar, D. G. The M06 Suite of Density Functionals for Main Group Thermochemistry, Thermochemical Kinetics, Noncovalent Interactions, Excited States, and Transition Elements: Two New Functionals and Systematic Testing of Four M06-Class Functionals and 12 other Functionals. *Theor. Chem. Acc.* **2008**, *120*, 215−241.
(52) Adamo, C.; Barone, V. Toward Reliable Density Functional Methods Without Adjustable Parameters: The PBE0 Model. *J. Chem. Phys.* **1999**, *110*, 6158−6170.
(53) Ernzerhof, M.; Scuseria, G. E. Assessment of the Perdew−Burke−Ernzerhof Exchange-Correlation Functional. *J. Chem. Phys.* **1999**, *110*, 5029−5036.
(54) Yanai, T.; Tew, D. P.; Handy, N. C. A New Hybrid Exchange−Correlation Functional using the Coulomb-Attenuating Method (CAM-B3LYP). *Chem. Phys. Lett.* **2004**, *393*, 51−57.
(55) Grimme, S.; Antony, J.; Ehrlich, S.; Krieg, H. A Consistent and Accurate Ab Initio Parametrization of Density Functional Dispersion Correction (DFT-D) for the 94 Elements H-Pu. *J. Chem. Phys.* **2010**, *132*, 154104.
(56) Chai, J.-D.; Head-Gordon, M. Long-Range Corrected Hybrid Density Functionals with Damped Atom−Atom Dispersion Corrections. *Phys. Chem. Chem. Phys.* **2008**, *10*, 6615−6620.
(57) Grimme, S. Semiempirical GGA-Type Density Functional Constructed with a Long-Range Dispersion Correction. *J. Comput. Chem.* **2006**, *27*, 1787−1799.
(58) Dunning, T. H., Jr Gaussian Basis Sets for use in Correlated Molecular Calculations. I. The Atoms Boron through Neon and Hydrogen. *J. Chem. Phys.* **1989**, *90*, 1007−1023.
(59) Kendall, R. A.; Dunning, T. H., Jr; Harrison, R. J. Electron Affinities of the First-Row Atoms Revisited. Systematic Basis Sets and Wave Functions. *J. Chem. Phys.* **1992**, *96*, 6796−6806.
(60) Frisch, M. J.; Trucks, G. W.; Schlegel, H. B.; Scuseria, G. E.; Robb, M. A.; Cheeseman, J. R.; Scalmani, G.; Barone, V.; Petersson, G. A.; Nakatsuji, H. et al. *Gaussian 16*, Revision C.01.; Gaussian Inc: Wallingford CT, 2016.
(61) Adler, T. B.; Knizia, G.; Werner, H.-J. A Simple and Efficient CCSD(T)-F12 Approximation. *J. Chem. Phys.* **2007**, *127*, 221106.
(62) Peterson, K. A.; Adler, T. B.; Werner, H.-J. Systematically Convergent Basis Sets for Explicitly Correlated Wavefunctions: The Atoms H, He, B−Ne, and Al−Ar. *J. Chem. Phys.* **2008**, *128*, 084102.
(63) Werner, H.-J.; Knowles, P. J.; Celani, P.; Györffy, W.; Hesselmann, A.; Kats, D.; Knizia, G.; Köhn, A.; Korona, T.; Kreplin, D.; et al. MOLPRO, 12.1, a package of ab initio programs. URL visited July 2023. https://www.molpro.net (accessed July 12, 2023).
(64) Werner, H.-J.; Knowles, P. J.; Knizia, G.; Manby, F. R.; Schütz, M. Molpro: a General-Purpose Quantum Chemistry Program Package. *Wiley Interdiscip. Rev.: Comput. Mol. Sci.* **2012**, *2*, 242−253.
(65) Werner, H.-J.; Knowles, P. J.; Manby, F. R.; Black, J. A.; Doll, K.; Heßelmann, A.; Kats, D.; Köhn, A.; Korona, T.; Kreplin, D. A.; et al. The Molpro Quantum Chemistry Package. *J. Chem. Phys.* **2020**, *152*, 144107.
(66) Jensen, C. V. GitHub Repository of 1D LM code. URL visited July 2023. https://github.com/CasperVJensen/tert-Butyl_Hydroperoxide_Dimer.git (accessed July 12, 2023).
(67) Kjaergaard, H. G.; Yu, H.; Schattka, B. J.; Henry, B. R.; Tarr, A. W. Intensities in Local Mode Overtone Spectra: Propane. *J. Chem. Phys.* **1990**, *93*, 6239−6248.
(68) Atkins, P. W.; Friedman, R. S. *Molecular Quantum Mechanics*; Oxford University Press, 2011.
(69) Vogt, E.; Hansen, A. S.; Kjaergaard, H. G. *Molecular Spectroscopy: A Quantum Chemistry Approach*; Ozaki, Y., Wójcik, M. J., Popp, J., Eds.; John Wiley & Sons, 2019; Chapter 14, pp 289−424.
(70) Kjaergaard, H. G.; Garden, A. L.; Chaban, G. M.; Gerber, R. B.; Matthews, D. A.; Stanton, J. F. Calculation of Vibrational Transition Frequencies and Intensities in Water Dimer: Comparison of Different Vibrational Approaches. *J. Phys. Chem. A* **2008**, *112*, 4324−4335.
(71) Zimmermann, D.; Häber, T.; Schaal, H.; Suhm, M. A. Hydrogen Bonded Rings, Chains and Lassos: The Case of t-Butyl Alcohol Clusters. *Mol. Phys.* **2001**, *99*, 413−425.
(72) Hansen, A. S.; Du, L.; Kjaergaard, H. G. Positively Charged Phosphorus as a Hydrogen Bond Acceptor. *J. Phys. Chem. Lett.* **2014**, *5*, 4225−4231.
(73) Häber, T.; Schmitt, U.; Suhm, M. A. FTIR-Spectroscopy of Molecular Clusters in Pulsed Supersonic Slit-Jet Expansions. *Phys. Chem. Chem. Phys.* **1999**, *1*, 5573−5582.
(74) Larsen, R. W.; Zielke, P.; Suhm, M. A. Hydrogen-Bonded OH Stretching Modes of Methanol Clusters: A Combined IR and Raman Isotopomer Study. *J. Chem. Phys.* **2007**, *126*, 194307.
(75) Hiatt, R.; Clipsham, J.; Visser, T. The Induced Decomposition of tert-Butyl Hydroperoxide. *Can. J. Chem.* **1964**, *42*, 2754−2757.
(76) Hiatt, R. R.; Mill, T.; Mayo, F. R. Homolytic Decompositions of Hydroperoxides. I. Summary and Implications for Autoxidation. *J. Org. Chem.* **1968**, *33*, 1416−1420.
(77) Oswald, S.; Wallrabe, M.; Suhm, M. A. Cooperativity in Alcohol−Nitrogen Complexes: Understanding Cryomatrices through Slit Jet Expansions. *J. Phys. Chem. A* **2017**, *121*, 3411−3422.
(78) Vogt, E.; Kjaergaard, H. G. Vibrational Spectroscopy of the Water Dimer at Jet-Cooled and Atmospheric Temperatures. *Annu. Rev. Phys. Chem.* **2022**, *73*, 209−231.
(79) Bulychev, V.; Gromova, E.; Tokhadze, K. Experimental and Theoretical Study of the ν(HF) Absorption Band structure in the H2O...HF Complex. *Opt. Spectrosc.* **2004**, *96*, 774−788.
(80) Vogt, E.; Simkó, I.; Császár, A. G.; Kjaergaard, H. G. Reduced-Dimensional Vibrational Models of the Water Dimer. *J. Chem. Phys.* **2022**, *156*, 164304.
(81) Mackeprang, K.; Kjaergaard, H. G.; Salmi, T.; Hänninen, V.; Halonen, L. The Effect of Large Amplitude Motions on the Transition Frequency Redshift in Hydrogen Bonded Complexes: A Physical Picture. *J. Chem. Phys.* **2014**, *140*, 184309.
(82) Mackeprang, K.; Hänninen, V.; Halonen, L.; Kjaergaard, H. G. The Effect of Large Amplitude Motions on the Vibrational Intensities in Hydrogen Bonded Complexes. *J. Chem. Phys.* **2015**, *142*, 094304.
(83) Mackeprang, K.; Kjaergaard, H. G. Vibrational Transitions in Hydrogen Bonded Bimolecular Complexes - A Local Mode Perturbation Theory Approach to Transition Frequencies and Intensities. *J. Mol. Spectrosc.* **2017**, *334*, 1−9.
(84) Ling, C.; Christian, S. D.; Affsprung, H. E. Vapor Phase Association of Trifluoroacetic Acid with Acetone and Cyclopentanone. *J. Phys. Chem.* **1966**, *70*, 901−904.
(85) Kjaersgaard, A.; Vogt, E.; Christensen, N. F.; Kjaergaard, H. G. Attenuated Deuterium Stabilization of Hydrogen-Bound Complexes at Room Temperature. *J. Phys. Chem. A* **2020**, *124*, 1763−1774.

https://doi.org/10.1021/acs.jpca.3c03702
J. Phys. Chem. A 2023, 127, 6476−6485

B PAPER 2

Effect of Temperature on the OH-Stretching Bands of the Methanol Dimer.

Emil Vogt, **Casper Vindahl Jensen** and Henrik G. Kjaergaard*.

The Journal of Physical Chemistry A, 2024, 128(2), 392-400

THE JOURNAL OF PHYSICAL CHEMISTRY A
A JOURNAL OF THE AMERICAN CHEMICAL SOCIETY

pubs.acs.org/JPCA Article

Effect of Temperature on the OH-Stretching Bands of the Methanol Dimer

Emil Vogt, Casper Vindahl Jensen, and Henrik G. Kjaergaard*

Cite This: J. Phys. Chem. A 2024, 128, 392−400 Read Online

ABSTRACT: We present a conceptually simple model for understanding the significant spectral changes that occur with the temperature in the infrared spectra of hydrogen-bound complexes. We have measured room-temperature spectra of the methanol dimer and two deuterated isotopologues in the OH(D)-stretching region. We correctly predict spectral changes observed in the gas phase for the bound OH stretch in the methanol dimer from jet-cooled to room temperature and corroborate this with experimental and theoretical results for deuterated isotopologues. The origin of the observed spectral features is explained based on a reduced-dimensional vibrational model, which includes the two high-frequency OH stretches, the two methyl torsions, and the six intermolecular low-frequency vibrations. Key to the success of the model is a new coordinate definition to describe the intrinsic large-amplitude curvilinear motion of low-frequency vibrations. Despite the deceivingly simple appearance of the room temperature bound OH-stretching fundamental band, it consists of ∼10^7 vibrational transitions.

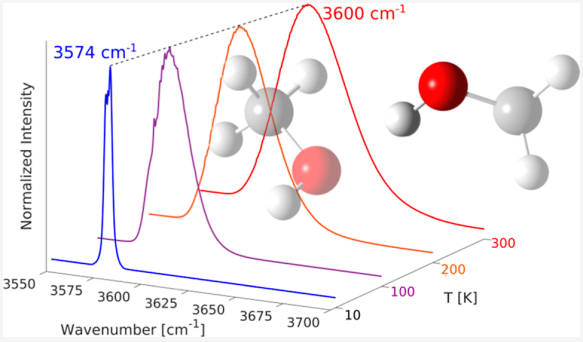

INTRODUCTION

Hydrogen-bound complexes are important in the atmosphere for both nucleation and radiative transfer processes, and it is therefore essential to obtain and simulate their spectra to advance our understanding and modeling of the atmosphere.[1,2] Much work has been devoted to the spectroscopy of hydrogen-bound complexes formed in supersonic expansions at low temperatures that favor complex formation. However, these temperatures are far from those of the atmosphere (from about 260 to 320 K). Infrared spectra of complexes in the gas phase at ambient temperatures are inherently difficult to measure due to the small equilibrium constants that govern their formation.[3] These spectra are also difficult to simulate due to the large number of populated vibrational states that arise from the low-frequency large-amplitude intermolecular vibrations. Here, we focus on the hydrogen-bound methanol dimer as a model system that shares some characteristics with the atmospherically prevalent water dimer.

The comparison of cold and warm infrared spectra is straightforward for isolated semirigid molecules. At elevated temperatures, the increased number of ro-vibrational transitions from thermally populated excited rotational states leads to well-understood changes in the rotational structure of vibrational bands. These changes can be simulated based on ro-vibrational models with parameters extracted from cold spectra or ab initio calculations. Only a few transitions from thermally excited vibrational states are likely to also contribute, and the spectral contribution from these transitions is generally limited for semirigid molecules. Thus, the jet-expansion spectra can be used to understand and model the corresponding spectra at elevated temperatures.

For floppy systems (systems with low-frequency vibrations) like hydrogen-bound bimolecular complexes, the comparison of cold and warm spectra is complicated and even the interpretation of cold spectra requires advanced ro-vibrational models.[4−13] For a bimolecular complex, six low-frequency, large-amplitude intermolecular vibrations are formed upon complex formation. At ambient temperatures, the thermal energy (∼200 cm^{-1}) is typically comparable to the energy scale of these intermolecular vibrations, and therefore, many excited vibrational states are populated. The spectra thus consist of transitions from the vibrational ground state as well as from excited vibrational states. As the temperature increases, the transitions from the excited vibrational states grow in importance, and eventually, the contribution from the vibrational ground-state becomes negligible.[3,14]

The low gas-phase equilibrium constants of formation for weakly bound complexes at ambient temperatures limits the

Received: September 27, 2023
Revised: November 30, 2023
Accepted: December 11, 2023
Published: January 5, 2024

https://doi.org/10.1021/acs.jpca.3c06456
J. Phys. Chem. A 2024, 128, 392−400

obtainable partial pressure.[3] In practice, the spectrum of the complex is therefore mixed with much stronger signals arising from the more abundant monomers, which have to be accurately subtracted. This accurate spectral subtraction tends to be more difficult to accomplish for homodimers, compared with heterodimers, as the spectral features of the monomers quickly lead to saturation, and one cannot vary the pressure of the two monomers individually. The hydrogen-bound XH stretch (where X = O, N, etc.) is often used to detect the complex of interest as this band redshifts away from the corresponding monomer XH stretch and increases in intensity upon complex formation.[3,15] In a few examples, other bands have also been detected.[3,16−20] Bands associated with the bound XH stretch lose the rotational fine structure and often become asymmetric with a tail extending toward higher energies, and the band maximum shifts to higher wavenumbers with increasing temperature. The bands are typically broader than what can be accounted for solely by the temperature-dependent rotational profiles. Interestingly, bands in these complexes associated with vibrations not directly affected by hydrogen bond formation tend to show a traditional rotational fine structure. One clear example of these characteristics is seen in the infrared spectrum of the water−trimethylamine (H_2O−TMA) complex (Figure 1), in which the H_2O unit acts as the donor unit of the hydrogen

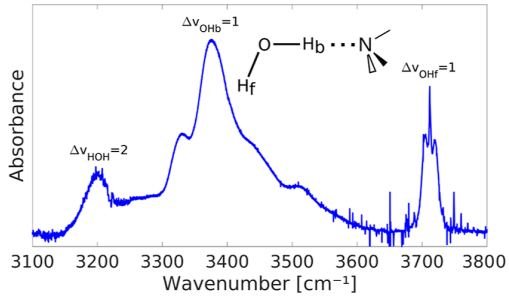

Figure 1. Gas-phase room-temperature infrared spectrum of the water−TMA complex in the OH-stretching fundamental region.[20] The HOH-bending overtone is clearly observed due to Fermi resonance coupling with the OH_b stretch.

bond and nitrogen acts as the acceptor atom.[20] The H_2O−TMA complex is relatively strongly bound, with a Gibbs energy of 3.8 ± 0.2 kJ/mol at room temperature, corresponding to an equilibrium constant of 0.21 ± 0.02. This facilitates detection, and several infrared and near-infrared bands have been observed at room temperature.[3,20] The bound OH-stretching fundamental band ($\Delta v_{OHb} = 1$) is significantly red-shifted, very broad (full width at half maximum of ∼130 cm^{-1}), asymmetric and has an additional structure. In comparison, the free OH stretching fundamental band ($\Delta v_{OHf} = 1$) has a transition wavenumber close to that of the decoupled OH stretch of H_2O (3715 cm^{-1} versus 3706.5 cm^{-1}) and shows a clear P,Q,R structure.[20,21] The full width at half maximum of the OH_f-stretching band is ∼30 cm^{-1}, in agreement with predictions based on the rotational constants of the complex.[20]

To extrapolate information from jet-expansion conditions to ambient conditions and to prevent misinterpretations of observed band structures in the ambient-temperature spectra, it is imperative to understand the spectral variations with temperature. However, calculation of accurate spectra of hydrogen-bound complexes is difficult due to the intrinsic curvilinear motion of the large-amplitude intermolecular vibrations.[22,23] In addition, both intermolecular and XH-stretching vibrations are sensitive to the level of electronic structure theory. A hypothesis for the mechanism responsible for the observed spectral temperature variations in hydrogen-bound complexes has previously been proposed by Thomas and Thompson[24,25] and has been used to interpret infrared spectra of relatively strongly bound complexes.[19,26−28] For the methanol dimer, $(CH_3OH)_2$, infrared spectra in the OH-stretching region exist at both jet-cooled and ambient temperatures.[3,29] We have developed a reduced-dimensional vibrational model to understand the temperature variations of the OH-stretching bands. Improved room-temperature spectra of the OH_b-stretching band are also recorded to facilitate a comparison of theory and experiments. We corroborate our investigation with additional calculated and measured spectra of the bound OD-stretching band of two deuterated isotopologues, $(CH_3OD)_2$ and $(CD_3OD)_2$, for which subtle, but noticeable, spectral changes should occur due to the change of masses. Based on our model, we provide a physical interpretation of the observed spectral temperature variation, which is general for hydrogen-bound complexes and consistent with the original hypothesis of Thomas and Thompson.[24,25]

THEORETICAL SECTION

The reduced dimensionality of our model limits the number of electronic energies to be evaluated, which allows for the use of accurate electronic structure methods. We have used CCSD(T)-F12a/cc-pVDZ-F12 as implemented in the Molpro2020 program both for the geometry optimization and to calculate the single points needed to represent the potential energy surface and the dipole moment surface.[30−32] We have previously shown that accurate OH-stretching fundamental and overtone transition wavenumbers and intensities can be obtained with CCSD(T)-F12a/cc-pVDZ-F12 surfaces.[33] The CCSD(T)-F12a/cc-pVDZ-F12 calculations were performed with the recommended correlation factor of $\beta = 0.9$ and with the frozen core approximation.[31] The vibrational model includes the two OH stretches and all eight large-amplitude, low-frequency vibrations (methyl torsions and intermolecular vibrations). The coordinates of the two OH stretches were defined as the two OH-bond lengths. The methyl torsions and the intermolecular vibrations have comparable frequencies and are known to couple strongly and hence are all included.[34]

An essential part of this model is a new definition of the low-frequency vibrational coordinates to be able to describe the intrinsic large-amplitude curvilinear motion. This is done by first obtaining an effective normal mode description of the low-frequency vibrational coordinates from the Hessian of the complex, by excluding (projecting out) the high-frequency (≥1000 cm^{-1}) intramolecular vibrations of both methanol units. Then, the displacements along these new effective normal coordinates are adapted to facilitate curvilinear motion, as illustrated in Figure 2.

The intramolecular vibrations were defined from the normal vibrations of the methanol monomer, rotated to the orientation of either the donor or acceptor methanol units in the methanol dimer. An Eckart embedding algorithm was used to calculate the required rotation matrices ($\boldsymbol{U}_i$).[35] The projection operator is defined as

$$\boldsymbol{P} = \prod_{i=1}^{2} \prod_{j=2}^{12} [\boldsymbol{I} - (\boldsymbol{U}_i \vec{Q}_{i,j})^T (\boldsymbol{U}_i \vec{Q}_{i,j})] \quad (1)$$

https://doi.org/10.1021/acs.jpca.3c06456
J. Phys. Chem. A 2024, 128, 392−400

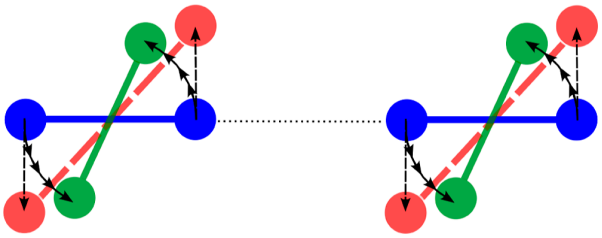

Figure 2. Sketch of displaced geometries with effective rectilinear normal coordinates (red) and with the new coordinate definition (green) for a model complex. The equilibrium geometry is shown in blue. In this example, the new coordinate definition avoids elongating the bond in each unit, i.e., it avoids deformations of the monomers.

where the two products run over the 12 vibrational normal coordinates, $\vec{Q}_{i,j}$, excluding methyl torsion, $j = 1$, for each of the methanol units, $i = 1$ and 2. The reduced Hessian was diagonalized to yield effective normal coordinates for the low-frequency vibrations, τ. The aforementioned strong coupling between the intermolecular and methyl torsion modes manifests itself in the change of the effective normal coordinates upon inclusion of the latter (Section S1). As a consequence, the highest frequency of the low-frequency modes changes from ~300 to ~650 cm^{-1} upon including methyl torsion, highlighting that including methyl torsion is essential for the description of the low-frequency vibrations. The obtained effective normal coordinates are still rectilinear coordinates, which are not appropriate for describing the inherent curvilinear motion of these large-amplitude vibrations. Thus, each effective normal coordinate was partitioned into a set of displacements of the donor unit and a set of displacements of the acceptor unit. Displacements along the low-frequency vibrational coordinates were defined from a sequence of infinitesimal displacements and separate reorientations of the donor and acceptor units, i.e., curvilinear coordinates. The sequential reorientations enable the sampling of the large displacement along a single (effective) normal coordinate without the sampling of high-energy (unphysical) geometries that are otherwise inherently generated from large displacements along each of the original rectilinear normal coordinates. The harmonic frequencies calculated with the new coordinates are equivalent to the harmonic frequencies calculated with the effective normal coordinates (Tables S2 and S3).

A 2D model for each OH stretch with each low-frequency vibration is defined as

$$\hat{H} = \hat{H}_{OH} + \hat{H}_{\tau} + \sum_{n,m}^{n+m\leq 6} \frac{1}{n!m!} \frac{\partial^{n+m} V(q_{OH}, q_{\tau})}{\partial q_{OH}^{n} \partial q_{\tau}^{m}}\bigg|_{eq} q_{OH}^{n} q_{\tau}^{m} \tag{2}$$

where q_i is the displacement coordinate of the ith mode and eq denotes the equilibrium geometry. The kinetic energy coupling between OH stretches and the low-frequency modes have previously been shown to have limited impact on calculated energies of the water dimer, and we therefore exclude this coupling in our model.[36] The 1D Hamiltonian for the OH stretch is of the form

$$\hat{H}_{OH} = \frac{\hat{p}_{OH}^{2}}{2\mu_{OH}} + V_{OH}(q_{OH}) \tag{3}$$

where $\hat{p}_{OH} = \frac{\hbar}{i}\frac{\partial}{\partial q_{OH}}$ and $V_{OH}(q_{OH})$ is the OH-stretching potential energy curve, calculated from the equilibrium geometry. The 1D Hamiltonian for the low-frequency vibrations is of the form

$$\hat{H}_{\tau} = \frac{1}{2}\hat{p}_{\tau}^{\dagger} G_{\tau\tau} \hat{p}_{\tau} + V_{\tau}(q_{\tau}) \tag{4}$$

where $G_{\tau\tau}$ is the G-matrix element for the vibration τ and $V_{\tau}(q_{\tau})$ is the potential energy curve along q_{τ}, calculated from the equilibrium geometry. The new coordinates resemble normal coordinates, and $G_{\tau\tau}$ is kept constant. The 1D potential energy curves and dipole moment functions were represented with cubic splines with single points calculated from −0.5 to 0.9 Å in steps of 0.05 Å for the OH stretches and from $-3q_{c,\tau}$ to $3q_{c,\tau}$ in steps of $0.5q_{c,\tau}$ for the low-frequency vibrations, where $q_{c,\tau}$ is the classical turning point of mode τ (Table S5). The two-dimensional potential energy and dipole moment surfaces were calculated with equidistant 9 × 9 grids with the same step sizes as those used for the 1D grids. The 2D Hamiltonians were constructed in a product basis of the associated 1D anharmonic eigenfunctions, which were found by diagonalizing the 1D Hamiltonian setup with Hermite basis functions (parameterized based on the calculated harmonic frequencies). Further theoretical information is provided in the Supporting Information.

EXPERIMENTAL SECTION

Methanol, ≥99.9%, spectroscopic grade, and methanol-d_1, 99.5% atom D, were purchased from Sigma-Aldrich. Methanol-d_4, 99.8% atom D, and D_2O, 99.9%, were purchased from Eurisotop. The samples were kept in sample holders fitted with Produran Teflon stoppers and degassed by repeated freeze−pump−thaw cycles until no change in pressure was observed. The samples were prepared on a J. Young glass vacuum system, which was connected by flexible metal tubing to a 10 cm gas cell fitted with CaF_2 windows and a diaphragm pressure gauge. The gas cell was seated in a Bruker Vertex 80 FTIR spectrometer with the sample compartment continuously purged with dry N_2 to minimize signals from ambient CO_2 and H_2O. The spectrometer was fitted with a mid-infrared light source with the aperture set at 4 mm, a CaF_2 beamsplitter, and a liquid nitrogen cooled Hg−Cd−Te (LN-MCT) detector. The resolution was set at 1 cm^{-1}, and the spectra were averaged over 2000 scans. All spectra were recorded at 298 ± 0.3 K.

The dimer spectra were obtained by subtracting spectra recorded at a low pressure from those recorded at a higher pressure with a suitable scaling factor. As the formation of the dimer scales with the square of the monomer pressure, intensity of the OH-stretching band from the dimer remains after subtracting the monomer signals.[37,38] An example of subtraction is shown for the OH-stretching region of CH_3OH in Figure 3. Apart from the bound OH-stretching band associated with the dimer, the subtraction leaves some monomer residuals in the high-energy tail of the observed dimer band due to differences in the pressure broadening of the individual ro-vibrational transitions in the monomer OH-stretching band. The measured high and low pressures for the three methanol isotopologues were about 25 and 7 Torr (1 bar = 750.06 Torr), respectively (Table S9). The high pressure was limited to about 25 Torr to minimize the formation of the methanol trimer and tetramer, which form at higher pressures and partly overlap with the dimer band.[39,40] The pressure of the reference spectrum was kept large

https://doi.org/10.1021/acs.jpca.3c06456
J. Phys. Chem. A 2024, 128, 392−400

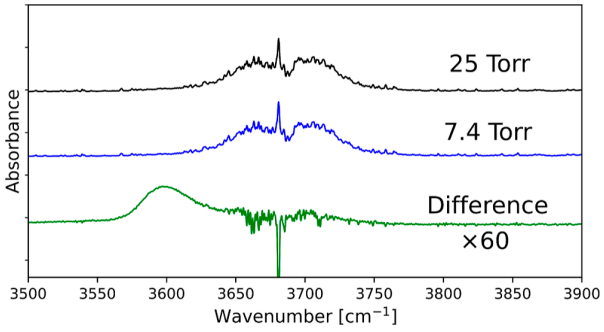

Figure 3. Spectra of CH_3OH and $(CH_3OH)_2$. Upper trace (black): CH_3OH sample spectrum was recorded with a measured pressure of 25 Torr. Middle trace (blue): CH_3OH sample spectrum with a measured pressure of 7.4 Torr, multiplied by a scaling factor of 3.37. Lower trace (green): spectrum of $(CH_3OH)_2$ was obtained by subtracting the middle trace from the upper trace. The spectrum of $(CH_3OH)_2$ is multiplied by 60 for visual purposes.

enough to allow for some self-broadening of the sharp ro-vibrational transitions of the monomer. The pressure difference between the sample and the reference spectra was sufficient to produce spectra of the dimer. As seen in Figure 3, at 25 Torr, only a small amount of the dimer is formed, and the scaled low-pressure spectrum looks virtually identical to the high-pressure spectrum. The OH_b-stretching band from the dimer becomes evident in the difference spectrum after magnification. The $(CH_3OH)_2$ spectrum was refined by subtracting an ambient air reference spectrum to remove small signals from H_2O in the OH-stretching region. A larger spectral region is shown for all three methanol dimer isotopologues in Figure S4. We report the experimentally observed full width at half maximum values for the bound OH(D)-stretching bands of all three isotopologues at room temperature. The reported values are sensitive to the choice of the baseline and monomer scaling factor, and we estimate an associated uncertainty of ±3 cm^{-1} for the presented band profiles.

RESULTS AND DISCUSSION

Coupling of the OH Stretch and Low-Frequency Vibrations. The optimized geometry of a hydrogen-bound complex is a balance between orienting and distancing the two units to optimize the hydrogen bond and the weak secondary interactions, while minimizing the deformation energy. For $(CH_3OH)_2$, the hydrogen bond is the dominant interaction. Displacements along the intermolecular coordinates change the relative orientation and distance between the donor and acceptor units and tend to weaken the hydrogen bond. As a consequence, the predicted red shift of the OH_b stretch is systematically overestimated in models that do not include the intermolecular vibrations. Thus, inclusion of each intermolecular vibration generally shifts the OH_b stretch to higher wavenumbers (smaller red shift).[36,41,42]

In the upper panel of Figure 4, we illustrate the effect of each of the low-frequency vibrations on the two OH-stretching transitions $|0\rangle_b \rightarrow |1\rangle_b$ and $|0\rangle_f \rightarrow |1\rangle_f$. The vibrational mode eight (ν_8), which partially breaks the hydrogen bond for both positive and negative displacements, results in the largest shift in the OH_b stretch of 28 cm^{-1}. The seven remaining vibrations each result in shifts of less than 5 cm^{-1}. In contrast, the OH_f stretch is almost completely unaffected by the low-frequency vibrations, with the largest shift being less than 1.5 cm^{-1}.

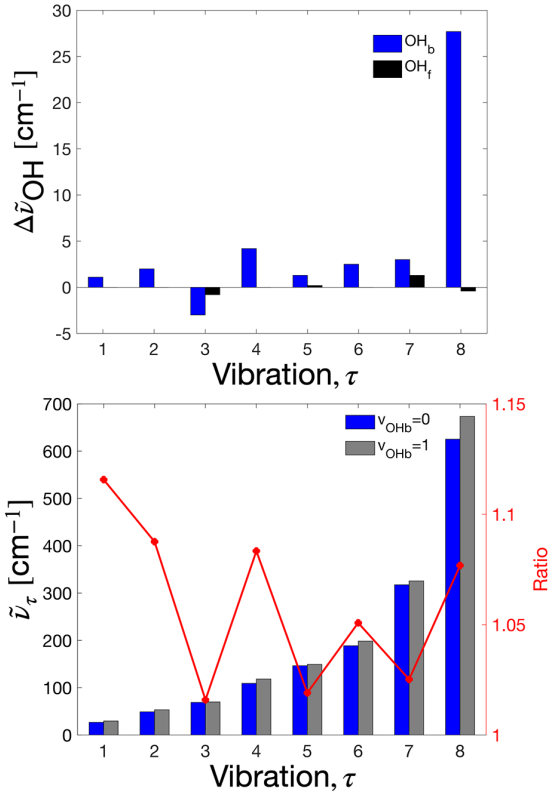

Figure 4. Shift in OH-stretching fundamental transition wavenumbers due to coupling with one of the eight low-frequency vibrations (upper panel). The low-frequency vibrations, τ, are constructed from the intermolecular and methyl torsion vibrations and are numbered by increasing transition wavenumbers. Wavenumbers for the $|\nu\rangle_b|0\rangle_\tau \rightarrow |\nu\rangle_b|1\rangle_\tau$ transitions with the OH_b stretch in either the ground ($\nu_{OHb} = 0$, blue bars) or first excited ($\nu_{OHb} = 1$, gray bars) state (lower panel). The ratio between the two transition wavenumbers for each vibration is shown with connected red circles.

Recently, the shifts in the calculated OH-stretching transition wavenumbers, induced by the low-frequency vibrations, have been found to be almost completely additive for the four OH stretches of the water dimer.[36] Thus, accurate OH-stretching transition wavenumbers could be calculated by adding the shifts induced by each of the low-frequency vibrations. The sum of the shifts shown in the upper panel of Figure 4 is 38.8 cm^{-1} for the OH_b stretch and 0.3 cm^{-1} for the OH_f stretch. If the sum of the shifts is added to the calculated 1D fundamental transition wavenumbers, the values are (3541.1 + 38.8) cm^{-1} = 3579.9 cm^{-1} for the OH_b stretch and (3692.5 + 0.3) cm^{-1} = 3692.8 cm^{-1} for the OH_f stretch, which compares well with the observed values of 3575 and 3684.1 cm^{-1}, respectively, at jet-cooled conditions.[29]

The frequencies of low-frequency vibrations often depend on the quantum number of a high-frequency vibration to which they are coupled. This is seen, for example, between methyl torsion and CH-stretching vibrations in xylenes and between the COOH torsion and the OH-stretching vibration in hydroperoxides.[43,44] Likewise, the frequencies of the low-frequency vibrations of the methanol dimer depend on the OH_b-stretching quantum number, as also shown for other hydrogen bound complexes.[12,45,46] In the lower panel of Figure 4, we show the calculated wavenumber of the $|\nu\rangle_b|0\rangle_\tau \rightarrow |\nu\rangle_b|1\rangle_\tau$ transition for

https://doi.org/10.1021/acs.jpca.3c06456
J. Phys. Chem. A 2024, 128, 392−400

each of the eight low-frequency vibrations with the OH_b stretch in either the ground ($v_{OHb} = 0$) or first excited ($v_{OHb} = 1$) state. The wavenumbers of the $|1\rangle_b|0\rangle_\tau \rightarrow |1\rangle_b|1\rangle_\tau$ transitions are 2–11% larger than those of the $|0\rangle_b|0\rangle_\tau \rightarrow |0\rangle_b|1\rangle_\tau$ transitions. The change in the frequency of the low-frequency vibrations between $v_{OH} = 0$ and $v_{OH} = 1$ directly impacts the pure OH-stretching transition wavenumbers as hot transitions of the type $|0\rangle_b|m\rangle_\Sigma \rightarrow |v\rangle_b|m\rangle_\Sigma$ (where m_Σ denotes the collection of quantum numbers for the eight low-frequency vibrations) contribute to the OH-stretching band. Hot OH_b-stretching transitions, $|0\rangle_b|m\rangle_\Sigma \rightarrow |v\rangle_b|m\rangle_\Sigma$, will thus have larger transition wavenumbers than those of cold OH_b-stretching transitions.

The increases in vibrational frequencies of the low-frequency vibrations with excitations of the OH_b stretch can be understood from the correlation between the strength of the hydrogen bond and the frequencies of the intermolecular vibrations. In the limit of dissociation, the hydrogen bond strength and the frequencies of the intermolecular vibrations approach zero. The frequencies of the intermolecular vibrations increase as the hydrogen bond strengthens. In $v_{OHb} = 1$, the OH bond is elongated, and the hydrogen bond is slightly stronger. The methyl torsion vibrations are only weakly affected by excitations of the OH stretches. However, the eight low-frequency vibrations all contain a fraction of the intermolecular vibrations; thus, the frequency of each low-frequency vibration increases with excitations of the OH_b stretch. The eight low-frequency vibrations are barely affected by excitations of the OH_f stretch as this vibration is not directly associated with the hydrogen bond (Table S2).

Simulation of Spectra. In Figure 5, we present room-temperature populations (smoothed over 15 cm^{-1} for visual purposes) and the cumulative density of (vibrational) states for the three methanol dimer isotopologues. The density of states is calculated with the fundamental transition wavenumbers for the low-frequency vibrations, shown in Tables S2 and S3, assuming a harmonic progression of the energy levels and using an iterative algorithm based on the coin change problem as described elsewhere.[47,48] The populations are normalized to one. The number of vibrational states needed to converge the room-temperature population to 99% is 0.75×10^7 for $(CH_3OH)_2$, 0.97×10^7 for $(CH_3OD)_2$, and 3.5×10^7 for $(CD_3OD)_2$. This means that there are about 4.5 times more transitions in the OD-stretching bands of $(CD_3OD)_2$ than in the OH-stretching bands of $(CH_3OH)_2$, if all combination transitions are excluded.

To calculate the OH-stretching band profile at elevated temperatures, including the effect of all eight low-frequency vibrations, while providing a simple physical picture, we introduce the following approximations:

1. The calculated shifts in the OH-stretching transition wavenumber from the coupling to each of the eight low-frequency vibrations are assumed to be additive.
2. The eight low-frequency vibrations are assumed not to couple with each other.
3. All $\Delta v_{OHb} = 1$ transitions are given equal transition dipole moments, and no combination transitions are included.

The first approximation is justified, as discussed, based on the results of ref 36. The second approximation is necessary to allow calculations with a large number of states needed to converge the room-temperature spectrum. This approximation is crude; however, it likely has a limited effect on the simulated band profiles as the high number of populated states, and thus

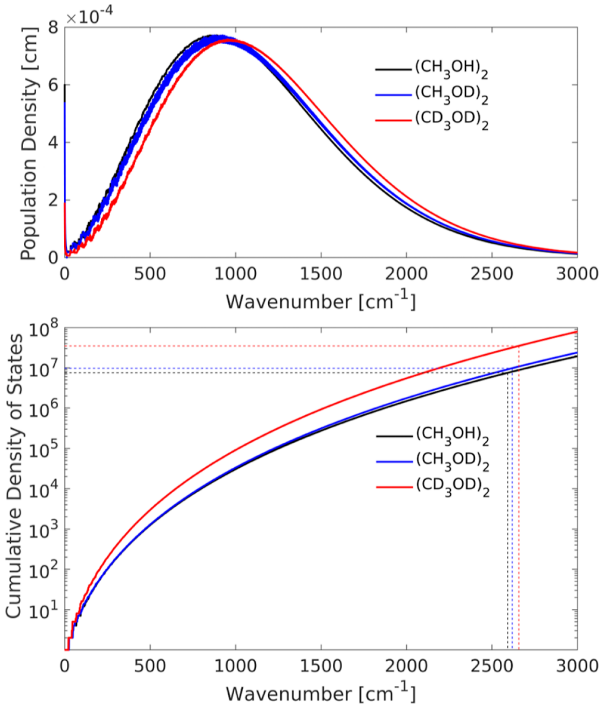

Figure 5. Room-temperature populations for the methanol dimer isotopologues (upper panel). The population are converged to 99% at 2592 cm^{-1} for $(CH_3OH)_2$, at 2618 cm^{-1} for $(CH_3OD)_2$, and at 2657 cm^{-1} for $(CD_3OD)_2$. These values are used to draw the dashed lines in the lower panel, which shows the cumulative density of states for the different methanol dimer isotopologues.

transitions, lead to averaging of the manifestation of coupling. The third approximation is justified based on the calculated transition dipole moments for the $|0\rangle_b|n\rangle_\tau \rightarrow |1\rangle_b|n\rangle_\tau$ transitions in Table S6 and from the fact that no combination transitions (e.g., $|0\rangle_b|0\rangle_\tau \rightarrow |1\rangle_b|n\rangle_\tau$) are observed in the jet-cooled spectrum of $(CH_3OH)_2$ in the OH-stretching region (vide infra, Figure 7). In agreement with this observation, the calculated intensities of the $|0\rangle_b|0\rangle_\tau \rightarrow |1\rangle_b|n\rangle_\tau$ combination transitions are at most 1% of those of the $|0\rangle_b|0\rangle_\tau \rightarrow |1\rangle_b|0\rangle_\tau$ transition, as shown in Table S7. Not including combination transitions means that each

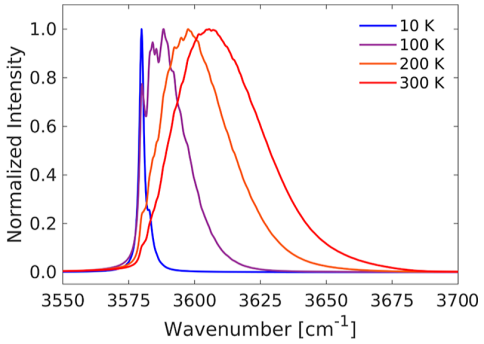

Figure 6. Calculated OH_b-stretching band profiles at various temperatures. For visual purposes, the individual profiles are normalized so that the intensity at the band maximum is 1.0. The vibrational transitions are convoluted with Lorentzian profiles with a full width at half maximum of 2 cm^{-1} at all temperatures.

https://doi.org/10.1021/acs.jpca.3c06456
J. Phys. Chem. A 2024, 128, 392−400

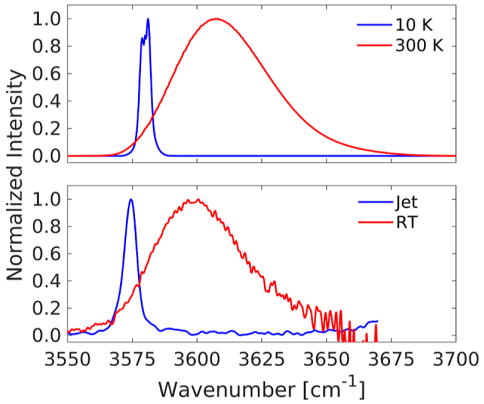

Figure 7. Comparison of calculated (upper panel) and experimental (lower panel) OH_b-stretching band profiles at jet-cooled conditions (blue traces, ref 29) and at room temperature (298 K, red traces). The calculated and experimental band maxima are 3581.1 and 3575 cm^{-1} at jet-cooled conditions and 3608.1 and ~3601 cm^{-1} at room temperature, respectively.

thermally populated state contributes only one transition to an OH-stretching band, which simplifies the calculations while maintaining the majority of the intensity.

In Figure 6, we show the calculated OH_b-stretching fundamental band at various temperatures, with each band maximum set to one. With the applied approximations, the integrated intensities of the bands are equivalent. The vibrational transitions are convoluted with Lorentzian profiles with a full width at half maximum of 2 cm^{-1} at all temperatures to highlight the changes in the vibrational band profile solely due to the $|0\rangle_b|m\rangle_\Sigma \rightarrow |v\rangle_b|m\rangle_\Sigma$ hot transitions. In Figure S1, we show the calculated OH_b-stretching band with the individual vibrational transitions convoluted with rotational profiles at the respective temperatures. Overall, the rotational profiles have little impact on the OH_b-stretching band profile at ambient temperatures. The number of populated states needed to account for 99% of the population is only 5 at 10 K but rapidly increases with increasing temperature and is ~10^3 at 100 K, ~10^5 at 200 K, and ~10^7 at 300 K. At elevated temperatures, the band maximum clearly shifts to higher wavenumbers, the band profile loses structure associated with individual vibrational transitions, and it becomes asymmetric with a tail extending toward higher wavenumbers. The increasing number of transitions with increasing temperature and the systematic energy increase of these explain the observed systematic changes in the OH_b-stretching band. The overall width of the band changes from 3 cm^{-1} at 10 K to 42 cm^{-1} at 300 K. In Figure S3, we show the calculated OH_f-stretching fundamental band at various temperatures. The shape of this band originates almost exclusively from the rotational profiles as the wavenumbers of the transitions from the ground and thermally excited states are similar due to the weak coupling between the OH_f stretch and the low-frequency vibrations.

Cold and Warm Spectra. In Figure 7, we compare calculated and experimental gas-phase spectra in the OH_b-stretching region at jet-cooled and ambient temperatures.[29] In the simulated spectra, the vibrational transitions are convoluted with rigid-rotor rotational profiles calculated with PGOPHER at the respective temperatures.[49] The individual ro-vibrational transitions are convoluted with Lorentzian profiles with a full width at half maximum of 1 cm^{-1} to reflect the resolution of the experiments. The resemblance between the calculated and experimental spectra is remarkable, especially considering the simplicity of the theoretical model. The calculated shift in the band maximum is 27 cm^{-1}, compared with the experimental shift of ~26 cm^{-1}. The calculations contain no empirical scaling or shift, and even the absolute agreement is excellent. Combination bands between the OH_b stretch and one of the four lowest frequency vibrations ($\tilde{\nu}_i \leq 150$ cm^{-1}) can, in principle, contribute to the OH_b-stretching band profile. However, as seen from the experimental jet-cooled spectrum in Figure 7,[29] no strong combination bands are observed in the OH_b-stretching region (3550−3675 cm^{-1}), and none of these transitions are predicted to have a significant intensity (Table S7). In Figure S2, we show the OH_b-stretching band profiles calculated with B3LYP-D3/aug-cc-pVTZ to highlight the sensitivity of the results to the level of the electronic structure theory.[50−52] This sensitivity is also evident by comparing the values tabulated in Tables S2 and S4. The appearance of the OH_b-stretching band calculated with the B3LYP-D3/aug-cc-pVTZ potential energy surface is similar to that obtained with the CCSD(T)-F12a/cc-pVDZ-F12 potential energy surface, but the quantitative agreement with both cold and warm spectra is significantly worse. For example, with our model, the band maximum wavenumber of the OH_b-stretching band at 10 K is 3504 cm^{-1} with B3LYP-D3/aug-cc-pVTZ and 3581 cm^{-1} with CCSD(T)-F12a/cc-pVDZ-F12, compared with 3575 cm^{-1} observed experimentally.[29]

It is clear that changes in the low-frequency vibrations will impact the OH_b-stretching band profile. To investigate the impact of such changes and to test the sensitivity of the applied theoretical model, we calculated and measured room-temperature OD_b-stretching spectra of two deuterated methanol dimer isotopologues, $(CH_3OD)_2$ and $(CD_3OD)_2$. Upon deuteration, the low-frequency vibrations generally decrease in frequency, which leads to a significant increase in the number of vibrational transitions that constitute the room-temperature band.

In Figure 8, we present measured and calculated OD_b-stretching bands for $(CH_3OD)_2$ and $(CD_3OD)_2$. The calculated OD_b-stretching band maximum for $(CD_3OD)_2$ is located at

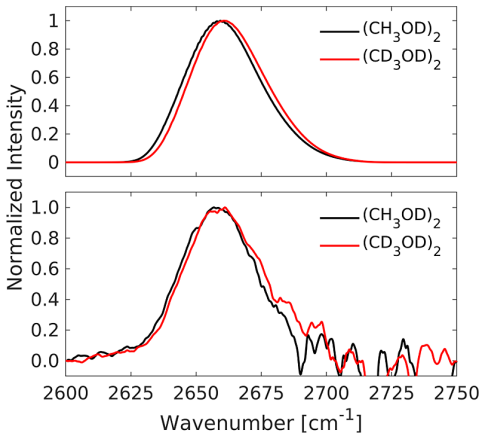

Figure 8. Comparison of the calculated (upper panel) and experimental (lower panel) OD_b-stretching band profiles of $(CH_3OD)_2$ (black trace) and $(CD_3OD)_2$ (red trace) at room temperature. The dimer spectra were smoothed by a 3 cm^{-1} rolling average to minimize the residuals that remain from imperfect subtraction of the narrow ro-vibrational transitions of the methanol monomer.

https://doi.org/10.1021/acs.jpca.3c06456
J. Phys. Chem. A 2024, 128, 392−400

Table 1. Calculated and Experimental Bound OH(D)-Stretching Band Maxima ($\tilde{\nu}$) and Full Widths at Half Maximum (Γ) of the Three Methanol Dimer Isotopologues at Jet-Cooled Conditions and at Room Temperature[a]

	jet-cooled		room temperature			
isotopologue	$\tilde{\nu}$ (Expt.[b])	$\tilde{\nu}$ (Calc.)	$\tilde{\nu}$ (Expt.)	$\tilde{\nu}$ (Calc.)	Γ (Expt.)	Γ (Calc.)
$(CH_3OH)_2$	3575[c]	3581.1	3601	3608.1	47 ± 3	42
$(CH_3OD)_2$	2637	2638.6	2657	2659.3	37 ± 3	34
$(CD_3OD)_2$	-	2638.0	2661	2660.7	37 ± 3	34

[a]All values are given in cm^{-1}. [b]From ref 29. [c]Observed at 3574.4 cm^{-1} in a jet-expansion molecular beam depletion experiment.[54]

slightly higher wavenumbers (~1.5 cm^{-1}) than that of the corresponding profile for $(CH_3OD)_2$. This subtle change is also observed in the experimental spectra, with both the low- and high-energy sides of the band moved to slightly higher wavenumbers. These OD_b-stretching fundamental bands are narrower than the OH_b-stretching fundamental band of $(CH_3OH)_2$ (Figure 7). The observed full width at half maximum is 37 ± 3 cm^{-1} for both $(CH_3OD)_2$ and $(CD_3OD)_2$, in agreement with the calculated widths of 34 cm^{-1} for both isotopologues. The observed and calculated widths are 47 ± 3 and 42 cm^{-1}, respectively, for $(CH_3OH)_2$. The narrower OD_b-stretching fundamental bands, compared with the OH_b-stretching fundamental band, has also been observed for singly deuterated isotopologues of other hydrogen-bound complexes.[53] Our theoretical model clearly captures the observed spectral changes upon isotopic substitution, which supports the idea that the applied approximations in the model are reasonable. A summary of the observed and calculated vibrational properties for the three methanol dimer isotopologues is shown in Table 1.

CONCLUSIONS

We have experimentally and theoretically illustrated the effect of the temperature on the infrared band shapes of the hydrogen-bound methanol dimer and two of its deuterated isotopologues. Bands associated with vibrations directly affected by the hydrogen bond formation can change substantially with increasing temperature, as illustrated for the OH_b-stretching (and OD_b-stretching) fundamental band. At ambient temperatures, this band is broad, asymmetric, with a tail extending to higher wavenumbers, and its maximum is shifted to higher wavenumbers than that observed under jet-cooled conditions. For hydrogen-bound complexes, the six low-frequency intermolecular vibrations that arise upon complex formation give rise to many states that are thermally accessible. For the methanol dimer, the two methyl torsions couple with the intermolecular vibrations and also have to be included. The OH_b-stretching fundamental band observed for the methanol dimer at ambient temperatures consists of a large number of hot transitions of the type, $|0\rangle_b|m\rangle_\Sigma \rightarrow |\nu\rangle_b|m\rangle_\Sigma$, which shift to higher wavenumbers as m_Σ increases. We have shown that the band shape arising from the hot transitions can be accurately simulated with a relatively simple vibrational model. Key to the success of our model is a new definition of the coordinates for the low-frequency, large-amplitude vibrations that undergo curvilinear motion and the use of an accurate (CCSD(T)-F12a/cc-pVDZ-F12) potential energy surface. The model not only qualitatively reproduces the observed temperature variations but also quantitatively captures the broadening, change in shape, and shift in the band maximum. The quantitative agreement with experiments is somewhat surprising and could reflect some cancellation of errors in the approximations made in our model. Nevertheless, we anticipate that this agreement is not merely a coincidence but rather reflects the robustness of the physical framework inherent to our model.

The effect of temperature on the infrared bands of atmospheric complexes alters their absorption of incoming and outgoing radiation. Thus, these effects are important to take into account to accurately model the contribution of complexes to radiative transfer in Earth's atmosphere. The physical interpretation for the changes in band shapes with the temperature is likely applicable to numerous complexes.

ASSOCIATED CONTENT

Data Availability Statement

The data that support the findings of this study are available within the article and its Supporting Information. The calculated coordinates, CCSD(T)-F12a/cc-pVDZ-F12 potential energy surfaces, and experimental spectra, are available online at https://erda.ku.dk/archives/2f8c23d1e1a21fdcc7152655e617bdd1/published-archive.html.

Supporting Information

The Supporting Information is available free of charge at https://pubs.acs.org/doi/10.1021/acs.jpca.3c06456.

Theoretical data and experimental details including spectral subtraction (PDF)

AUTHOR INFORMATION

Corresponding Author

Henrik G. Kjaergaard − *Department of Chemistry, University of Copenhagen, DK-2100 Copenhagen Ø, Denmark;* orcid.org/0000-0002-7275-8297; Email: hgk@chem.ku.dk

Authors

Emil Vogt − *Department of Chemistry, University of Copenhagen, DK-2100 Copenhagen Ø, Denmark;* orcid.org/0000-0003-3335-9813

Casper Vindahl Jensen − *Department of Chemistry, University of Copenhagen, DK-2100 Copenhagen Ø, Denmark;* orcid.org/0000-0002-9102-1223

Complete contact information is available at: https://pubs.acs.org/10.1021/acs.jpca.3c06456

Notes

The authors declare no competing financial interest.

ACKNOWLEDGMENTS

We are grateful for funding from the Independent Research Fund Denmark (grant no. 9040-00142B) and the Novo Nordisk Foundation (grant nos. NNF19OC0057374 and NNF220C0080193) and for computer time from the High Performance Computer Centre at University of Copenhagen.

REFERENCES

(1) Vaida, V.; Daniel, J. S.; Kjaergaard, H. G.; Goss, L. M.; Tuck, A. F. Atmospheric absorption of near infrared and visible solar radiation by the hydrogen bonded water dimer. *Q. J. R. Meteorol. Soc.* **2001**, *127*, 1627−1643.

(2) Vaida, V.; Kjaergaard, H. G.; Feierabend, K. J. Hydrated complexes: relevance to atmospheric chemistry and climate. *Int. Rev. Phys. Chem.* **2003**, *22*, 203−219.

(3) Hansen, A. S.; Vogt, E.; Kjaergaard, H. G. Gibbs energy of complex formation − combining infrared spectroscopy and vibrational theory. *Int. Rev. Phys. Chem.* **2019**, *38*, 115−148.

(4) Wormer, P. E. S.; van der Avoird, A. Intermolecular potentials, internal motions, and spectra of van der Waals and hydrogen-bonded complexes. *Chem. Rev.* **2000**, *100*, 4109−4144.

(5) Spaun, B.; Changala, P. B.; Patterson, D.; Bjork, B. J.; Heckl, O. H.; Doyle, J. M.; Ye, J. Continuous probing of cold complex molecules with infrared frequency comb spectroscopy. *Nature* **2016**, *533*, 517−520.

(6) Sarka, J.; Császár, A. G.; Mátyus, E. Rovibrational quantum dynamical computations for deuterated isotopologues of the methane-water dimer. *Phys. Chem. Chem. Phys.* **2017**, *19*, 15335−15345.

(7) Fischer, T. L.; Bödecker, M.; Zehnacker-Rentien, A.; Mata, R. A.; Suhm, M. A. Setting up the HyDRA blind challenge for the microhydration of organic molecules. *Phys. Chem. Chem. Phys.* **2022**, *24*, 11442−11454.

(8) Wang, X.-G.; Carrington, T. J. Computing excited OH stretch states of water dimer in 12D using contracted intermolecular and intramolecular basis functions. *J. Chem. Phys.* **2023**, *158*, 084107.

(9) Glorieux, R.; Hays, B. M.; Bogomolov, A. S.; Herman, M.; Vanfleteren, T.; Moazzen-Ahmadi, N.; Lauzin, C. Understanding the high-resolution spectral signature of the N_2−H_2O van der Waals complex in the 2OH stretch region. *J. Chem. Phys.* **2023**, *158*, 224302.

(10) Vogt, E.; Simkó, I.; Császár, A. G.; Kjaergaard, H. G. Quantum chemical investigation of the cold water dimer spectrum in the first OH-stretching overtone region provides a new interpretation. *J. Phys. Chem. A* **2023**, *127*, 9409−9418.

(11) Felker, P. M.; Bačić, Z. H_2O−CO and D_2O−CO complexes: Intra- and intermolecular rovibrational states from full-dimensional and fully coupled quantum calculations. *J. Chem. Phys.* **2020**, *153*, 074107.

(12) Liu, Y.; Li, J.; Felker, P. M.; Bačić, Z. HCl−H_2O dimer: an accurate full-dimensional potential energy surface and fully coupled quantum calculations of intra- and intermolecular vibrational states and frequency shifts. *Phys. Chem. Chem. Phys.* **2021**, *23*, 7101−7114.

(13) Felker, P. M.; Bačić, Z. Noncovalently bound molecular complexes beyond diatom−diatom systems: full-dimensional, fully coupled quantum calculations of rovibrational states. *Phys. Chem. Chem. Phys.* **2022**, *24*, 24655−24676.

(14) Vigasin, A. Bound, metastable and free states of bimolecular complexes. *Infrared Phys.* **1991**, *32*, 461−470.

(15) Arunan, E.; Desiraju, G. R.; Klein, R. A.; Sadlej, J.; Scheiner, S.; Alkorta, I.; Clary, D. C.; Crabtree, R. H.; Dannenberg, J. J.; Hobza, P.; Kjaergaard, H. G.; Legon, A. C.; Mennucci, B.; Nesbitt, D. J. Definition of the hydrogen bond (IUPAC Recommendations 2011). *Pure Appl. Chem.* **2011**, *83*, 1637−1641.

(16) Hippler, M. Quantum chemical study and infrared spectroscopy of hydrogen-bonded $CHCl_3$−NH_3 in the gas phase. *J. Chem. Phys.* **2007**, *127*, 084306.

(17) Du, L.; Mackeprang, K.; Kjaergaard, H. G. Fundamental and overtone vibrational spectroscopy, enthalpy of hydrogen bond formation and equilibrium constant determination of the methanol−dimethylamine complex. *Phys. Chem. Chem. Phys.* **2013**, *15*, 10194−10206.

(18) Hansen, A. S.; Du, L.; Kjaergaard, H. G. The effect of fluorine substitution in alcohol−amine complexes. *Phys. Chem. Chem. Phys.* **2014**, *16*, 22882−22891.

(19) Bulychev, V. P.; Svishcheva, E. A.; Tokhadze, K. G. Experimental and theoretical study of absorption spectrum of the $(CH_3)_2CO$· HF complex. Influence of anharmonic interactions on the frequency and intensity of the CO and H−F stretching bands. *Spectrochim. Acta, Part A* **2014**, *117*, 679−685.

(20) Kjaersgaard, A.; Vogt, E.; Hansen, A. S.; Kjaergaard, H. G. Room temperature gas-phase detection and Gibbs energies of water amine bimolecular complex formation. *J. Phys. Chem. A* **2020**, *124*, 7113−7122.

(21) Gordon, I.; Rothman, L.; Hargreaves, R.; Hashemi, R.; Karlovets, E.; Skinner, F.; Conway, E.; Hill, C.; Kochanov, R.; Tan, Y.; et al. The HITRAN2020 molecular spectroscopic database. *J. Quant. Spectrosc. Radiat. Transfer* **2022**, *277*, 107949.

(22) Császár, A. G.; Fábri, C.; Szidarovszky, T. Exact Numerical Methods for Stationary-State-Based Quantum Dynamics of Complex Polyatomic Molecules. *Molecular Spectroscopy and Quantum Dynamics*; Elsevier, 2021; pp 43−78.

(23) Vogt, E.; Kjaergaard, H. G. Vibrational Spectroscopy of the Water Dimer at Jet-Cooled and Atmospheric Temperatures. *Annu. Rev. Phys. Chem.* **2022**, *73*, 209−231.

(24) Thomas, R. K.; Thompson, H. W. Hydrogen bonding in the vapour phase: an unusual type of infrared band. *Proc. R. Soc. London, A* **1970**, *316*, 303−313.

(25) Thomas, R. K. Hydrogen bonding in the gas phase: the infrared spectra of complexes of hydrogen fluoride with hydrogen cyanide and methyl cyanide. *Proc. R. Soc. London, A* **1971**, *325*, 133−149.

(26) Shchepkin, D. N. The low-frequency vibrations and the origin of hydrogen-bonded band profiles. *J. Mol. Struct.* **1987**, *156*, 303−314.

(27) Bulychev, V. P.; Gromova, E. I.; Tokhadze, K. G. Experimental and theoretical study of the ν(HF) absorption band structure in the H_2O· HF complex. *Opt. Spectrosc.* **2004**, *96*, 774−788.

(28) Bulychev, V. P.; Grigoriev, I. M.; Gromova, E. I.; Tokhadze, K. G. Study of the ν_1 band shape of the H_2O· HF, H_2O· DF, and H_2O· HCl complexes in the gas phase. *Phys. Chem. Chem. Phys.* **2005**, *7*, 2266−2278.

(29) Oswald, S.; Wallrabe, M.; Suhm, M. A. Cooperativity in alcohol−nitrogen complexes: understanding cryomatrices through slit jet expansions. *J. Phys. Chem. A* **2017**, *121*, 3411−3422.

(30) Adler, T. B.; Knizia, G.; Werner, H.-J. A simple and efficient CCSD(T)-F12 approximation. *J. Chem. Phys.* **2007**, *127*, 221106.

(31) Peterson, K. A.; Adler, T. B.; Werner, H.-J. Systematically convergent basis sets for explicitly correlated wavefunctions: The atoms H, He, B−Ne, and Al−Ar. *J. Chem. Phys.* **2008**, *128*, 084102.

(32) Werner, H.-J.; Knowles, P. J.; Manby, F. R.; Black, J. A.; Doll, K.; Heßelmann, A.; Kats, D.; Köhn, A.; Korona, T.; Kreplin, D. A.; et al. The Molpro quantum chemistry package. *J. Chem. Phys.* **2020**, *152*, 144107.

(33) Vogt, E.; Bertran Valls, P.; Kjaergaard, H. G. Accurate calculations of OH-Stretching intensities with a reduced-dimensional local mode model including Eckart axis embedding. *J. Phys. Chem. A* **2020**, *124*, 932−942.

(34) Kollipost, F.; Andersen, J.; Mahler, D. W.; Heimdal, J.; Heger, M.; Suhm, M. A.; Wugt Larsen, R. The effect of hydrogen bonding on torsional dynamics: A combined far-infrared jet and matrix isolation study of methanol dimer. *J. Chem. Phys.* **2014**, *141*, 174314.

(35) Krasnoshchekov, S. V.; Isayeva, E. V.; Stepanov, N. F. Determination of the Eckart molecule-fixed frame by use of the apparatus of quaternion algebra. *J. Chem. Phys.* **2014**, *140*, 154104.

(36) Vogt, E.; Simkó, I.; Császár, A. G.; Kjaergaard, H. G. Reduced-dimensional vibrational models of the water dimer. *J. Chem. Phys.* **2022**, *156*, 164304.

(37) Du, L.; Kjaergaard, H. G. Fourier transform infrared spectroscopy and theoretical study of dimethylamine dimer in the gas phase. *J. Phys. Chem. A* **2011**, *115*, 12097−12104.

(38) Jensen, C. V.; Kjaergaard, H. G. Gas-phase room-temperature detection of the tert-butyl hydroperoxide dimer. *J. Phys. Chem. A* **2023**, *127*, 6476−6485.

(39) Renner, T. A.; Kucera, G. H.; Blander, M. A study of hydrogen bonding in methanol vapor by measurement of thermal conductivity. *J. Chem. Phys.* **1977**, *66*, 177−184.

(40) Sulaiman, M. I.; Yang, S.; Ellis, A. M. Infrared spectroscopy of methanol and methanol/water clusters in helium nanodroplets: The OH stretching region. *J. Phys. Chem. A* **2017**, *121*, 771−776.

https://doi.org/10.1021/acs.jpca.3c06456
J. Phys. Chem. A 2024, 128, 392−400

(41) Wang, Y.; Carter, S.; Braams, B. J.; Bowman, J. M. MULTIMODE quantum calculations of intramolecular vibrational energies of the water dimer and trimer using ab initio-based potential energy surfaces. *J. Chem. Phys.* **2008**, *128*, 071101.
(42) Mackeprang, K.; Kjaergaard, H. G.; Salmi, T.; Hänninen, V.; Halonen, L. The effect of large amplitude motions on the transition frequency redshift in hydrogen bonded complexes: A physical picture. *J. Chem. Phys.* **2014**, *140*, 184309.
(43) Rong, Z.; Kjaergaard, H. G. Internal methyl rotation in the CH stretching overtone spectra of ortho-meta-and para-Xylene. *J. Phys. Chem. A* **2002**, *106*, 6242−6253.
(44) Vogt, E.; Huchmala, R. M.; Jensen, C. V.; Boyer, M. A.; Wallberg, J.; Hansen, A. S.; Kjærsgaard, A.; Lester, M. I.; McCoy, A. B.; Kjaergaard, H. G. Coupling of torsion and OH-stretching in tert-butyl hydroperoxide. II. The OH-stretching fundamental and overtone spectra. *J. Chem. Phys.* **2021**, *154*, 164307.
(45) Garden, A. L.; Halonen, L.; Kjaergaard, H. G. Calculated band profiles of the OH-Stretching Transitions in water dimer. *J. Phys. Chem. A* **2008**, *112*, 7439−7447.
(46) Felker, P. M.; Bačić, Z. HF trimer: 12D fully coupled quantum calculations of HF-stretch excited intramolecular and intermolecular vibrational states using contracted bases of intramolecular and intermolecular eigenstates. *J. Chem. Phys.* **2023**, *158*, 234109.
(47) Beyer, T.; Swinehart, D. F. Algorithm 448: Number of multiply-restricted partitions. *Commun. ACM* **1973**, *16*, 379.
(48) Vogt, E.; Langeland, J.; Kjær, C.; Lindkvist, T. T.; Kjaergaard, H. G.; Nielsen, S. B. Effect of freezing out vibrational modes on gas-phase fluorescence spectra of small ionic dyes. *J. Phys. Chem. Lett.* **2021**, *12*, 11346−11352.
(49) Western, C. M. PGOPHER A program for simulating rotational, vibrational and electronic spectra. *J. Quant. Spectrosc. Radiat. Transfer* **2017**, *186*, 221−242.
(50) Kendall, R. A.; Dunning, T. H.; Harrison, R. J. Electron affinities of the first-row atoms revisited. Systematic basis sets and wave functions. *J. Chem. Phys.* **1992**, *96*, 6796−6806.
(51) Becke, A. D. Density-functional thermochemistry. III. The role of exact exchange. *J. Chem. Phys.* **1993**, *98*, 5648−5652.
(52) Grimme, S.; Antony, J.; Ehrlich, S.; Krieg, H. A consistent and accurate ab initio parametrization of density functional dispersion correction (DFT-D) for the 94 elements H-Pu. *J. Chem. Phys.* **2010**, *132*, 154104.
(53) Kjaersgaard, A.; Vogt, E.; Christensen, N. F.; Kjaergaard, H. G. Attenuated deuterium stabilization of hydrogen-bound complexes at room temperature. *J. Phys. Chem. A* **2020**, *124*, 1763−1774.
(54) Huisken, F.; Kulcke, A.; Laush, C.; Lisy, J. M. Dissociation of small methanol clusters after excitation of the O−H stretch vibration at 2.7 μ. *J. Chem. Phys.* **1991**, *95*, 3924−3929.

https://doi.org/10.1021/acs.jpca.3c06456
J. Phys. Chem. A 2024, 128, 392−400

C PAPER 3

Room Temperature Gas Phase Equilibrium Constants of the Methanol Dimer, Trimer and Tetramer.

Casper Vindahl Jensen, Emil Vogt, Andras Sun Poulsen and Henrik G. Kjaergaard*.

The Journal of Physical Chemistry A, 2024, 128(31), 6382-6391

THE JOURNAL OF PHYSICAL CHEMISTRY A
A JOURNAL OF THE AMERICAN CHEMICAL SOCIETY

pubs.acs.org/JPCA Article

Room Temperature Gas Phase Equilibrium Constants of the Methanol Dimer, Trimer, and Tetramer

Casper Vindahl Jensen, Emil Vogt, Andras Sun Poulsen, and Henrik G. Kjaergaard*

Cite This: J. Phys. Chem. A 2024, 128, 6382−6391 Read Online

ACCESS | Metrics & More | Article Recommendations | Supporting Information

ABSTRACT: We have detected the methanol dimer, trimer, and tetramer at equilibrium conditions at room temperature in the gas phase using direct absorption Fourier transform infrared spectroscopy. The infrared intensity of the OH-stretching transitions are enhanced upon hydrogen bonding and are increasingly red-shifted with increasing cluster size, facilitating identification and quantification of the various clusters. We calculate the intensities of the bound OH-stretches, OH_b, for all clusters with a range of reduced dimensional vibrational models with different levels of electronic structure theory. Partial pressures of the clusters are obtained by scaling the measured integrated absorbance of the OH_b-stretching bands by the calculated intensities of the associated vibrational transitions. We estimate the methanol dimer equilibrium constant, K_D, to be 0.033, at 298.15 K, which is comparable to that of the water dimer. For the methanol trimer and tetramer, we estimate equilibrium constants for aggregation of monomers of $K_T \sim 0.04$ and $K_Q \sim 0.6$, respectively.

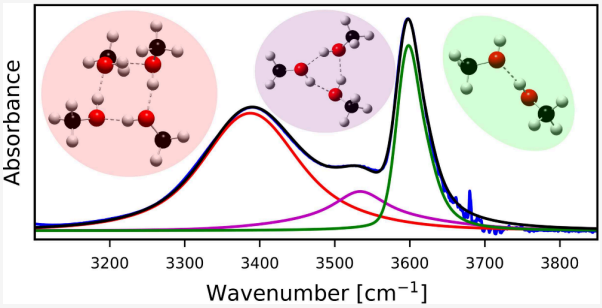

INTRODUCTION

The OH-functional group is prevalent in the troposphere in both water (H_2O) and alcohols. Alcohols are emitted directly into the atmosphere from both biogenic and anthropogenic sources on Earth's surface, and oxidation of emitted hydrocarbons by reaction with hydroxyl radicals also leads to formation of compounds with OH-functional groups.[1] Since the OH-functional group is both an intermediately strong hydrogen bond donor and acceptor[2] it is important in formation of clusters in the atmosphere. The formation of bimolecular complexes and sequentially small clusters is often the initial and rate-limiting step toward forming condensed aerosol droplets.[3−6] The formation and presence of aerosols in the atmosphere accounts for one of the largest anthropogenic impacts on the change of Earths radiative budget, but is at the same time associated with a relatively large uncertainty, mainly due to the poorly understood mechanisms of clustering and cloud-seeding.[7] We investigate methanol (MeOH) clusters (Figure 1) to further our understanding of OH···O interactions of small clusters.

Molecular clusters of MeOH have previously been studied with various theoretical and experimental techniques under different conditions. The majority of the experimental infrared (IR) spectroscopic work have focused on the characterization of clusters at cold and nonequilibrium conditions using techniques such as helium droplet,[8] supersonic jet-expansion,[9−12] and Ar and N_2 matrix isolation.[13,14] Further, IR spectra of size selected clusters $(MeOH)_{2-9}$ have been recorded using molecular beam depletion spectroscopy.[15−18]

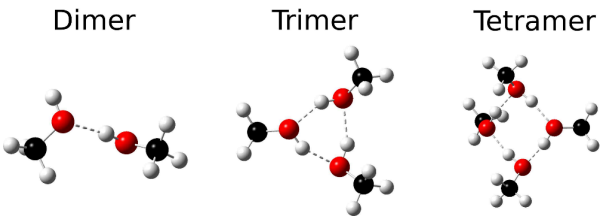

Figure 1. Structure of methanol dimer, trimer, and tetramer optimized with the B3LYP-D3/aug-cc-pVTZ method.

The cold techniques have the advantage of favoring cluster formation and producing IR spectra predominantly consisting of vibrational ground-state transitions with limited rotational structure. These spectra are invaluable for the studies of isolated cold clusters and as benchmarks for vibrational calculations.[19] However, they are far from the thermal conditions relevant for the atmosphere (∼260−320 K) and do not provide information on the equilibrium energetics.

Different experimental studies have approached the challenge of quantifying the formation of MeOH clusters at

Received: April 26, 2024
Revised: June 28, 2024
Accepted: July 1, 2024
Published: July 31, 2024

https://doi.org/10.1021/acs.jpca.4c02730
J. Phys. Chem. A 2024, 128, 6382−6391

thermal equilibrium. These include methods such as thermal conductivity[20−22] and measurements of heat capacity, which can be used to fit real gas virial coefficients.[23,24] These approaches usually probe temperatures and pressures much higher than what is atmospherically relevant and rely on fitting, including constrained thermodynamic parameters. Spectroscopic methods have also been used in different approaches including fitting the change in MeOH monomer absorbance with pressure to an i^{th} order polynomial with the coefficients being proportional to the i^{th} order cluster equilibrium constants. The authors estimate uncertainties of about a factor 100 in this approach.[25] Common to the previous studies is the assumption that only the dimer and tetramer of MeOH form in measurable amounts and that the MeOH trimer is neglected in the analyses.

An alternative hybrid approach is to obtain the partial pressure of the clusters from a combination of experimental spectra and theoretical oscillator strengths.[2,26] The ratio of the measured integrated absorption band and the corresponding calculated oscillator strength of the band is proportional to the partial pressure of the cluster. This approach is especially suited for the detection and quantification of hydrogen bound complexes.[2,27−29] Upon hydrogen bonding, the OH-stretching band is red-shifted and the intensity of the band is enhanced, typically by a factor 20 or more.[2,30,31] The detection of an isolated OH_b-stretching band usually relies on accurate spectral subtraction of the monomer species.[27,28,32,33] The OH_b-stretching band is a very sensitive and quantitative probe for the minute amounts of complex that forms at room temperature. Recently, this approach was used to quantify equilibrium constants of $(MeOH)_{2-4}$, but oversaturation of the monomer signal drastically influenced the band shape and area of the clusters.[34] The equilibrium constant for the MeOH dimer was found to be 2 orders of magnitude smaller than that of the H_2O dimer.[35] In this study, we use this hybrid method to quantify the equilibrium constants of the MeOH dimer, trimer, and tetramer in the gas phase at room temperature. We use a variety of reduced dimensionality normal mode and local mode vibrational models with different levels of electronic structure theory to determine reliable oscillator strengths of the OH_b-stretches in the clusters. This allows us to determine the standard formation Gibbs energies for these clusters under conditions relevant for atmospheric processes.

EXPERIMENTAL SECTION

The experimental setup and approach has been described previously[2,27,28,36] and is summarized. Spectroscopic grade methanol, MeOH ≥ 99.9%, was purchased from Sigma-Aldrich. The MeOH sample was kept in a sample holder fitted with a Produran Teflon stopper and was degassed by repeated freeze−pump−thaw cycles. The samples were prepared on a J. Young glass vacuum system, which was connected by flexible metal tubing to a 10 cm gas cell fitted with CaF_2 windows and a diaphragm pressure gauge. The chosen path length gave a maximum absorbance below 0.8 for the monomer OH-stretching band. This ensured linearity in absorbance, which allowed for accurate spectral subtraction. A reference MeOH monomer spectrum was recorded using a Specac Tornado series White-cell with a path length of 100 cm. The cell is equipped with CaF_2 windows and Au internal and Al external mirrors. The low pressure (9.9 Torr) reference spectrum was pressure-broadened by adding ∼300 Torr N_2 to better match the ro-vibrational lines of the spectra recorded at higher pressures. The gas cells were seated in a Bruker Vertex 80 FTIR spectrometer with the sample compartment continuously purged with dry N_2 to minimize signals from ambient CO_2 and H_2O. The spectrometer was fitted with a SiC Mid-IR light-source with the aperture set at 4 mm, a CaF_2 beamsplitter, and a liquid nitrogen cooled Hg−Cd−Te (LN-MCT) detector. The resolution was set at 1 cm^{-1}, and the spectra were averaged over 2000 scans. All spectra were recorded at 298.2 ± 0.3 K.

At thermodynamic equilibrium, the formation of homomolecular clusters scales with the monomer pressure raised to a power equal to the order of the cluster. We express the unitless equilibrium constants for the formation of clusters in terms of cluster and monomer pressures as follows:

$$K_D = \frac{p_D \cdot p^{\ominus}}{p_M^2},\quad K_T = \frac{p_T \cdot p^{\ominus 2}}{p_M^3},\quad K_Q = \frac{p_Q \cdot p^{\ominus 3}}{p_M^4} \tag{1}$$

where K_Z and p_Z is the equilibrium constant and partial pressure of the Z'th order MeOH cluster, and p_M is the pressure of the monomer. $p^{\ominus}$ is the standard pressure of 750.06 Torr (1 bar). Although the expressions in eq 1 could imply 3- and 4-body reactions, we emphasize that this is not the case. Rather, higher order clusters are most likely formed from sequential additions of monomer units.[3] At the pressures investigated in this work, the monomer pressure can, to a good approximation, be taken as the total sample pressure, which is directly read from the pressure gauge attached to the cell. The error of this approximation is less than 0.5% as the partial pressures of the clusters are small (*vide infra*). The main challenge in obtaining equilibrium constants is to determine the small partial pressures of the clusters. To do this, we use a hybrid theoretical/experimental spectroscopic approach,[2,26] which we have used previously to determine small partial pressures of molecular complexes in gas mixtures.[27,28,32,33,37,38] The partial pressure of a cluster can be determined from the ratio of a measured integrated absorbance and the corresponding calculated oscillator strength of the band:

$$p_{cluster} = 2.6935 \times 10^{-9} \frac{\text{Torr m cm}}{\text{K}} \frac{T}{f_{calc} \cdot l} \cdot \int A(\tilde{\nu})\, \mathrm{d}\tilde{\nu} \tag{2}$$

where $p_{cluster}$ is the cluster partial pressure, f_{calc} is the calculated oscillator strength, l the path length of the cell, and $A(\tilde{\nu})$ the wavenumber dependent base-10 absorbance of the band. We focus on the absorption band associated with the bound OH_b-stretch, thus taking advantage of the OH-stretching redshift and intensity enhancement upon hydrogen bonding.[30,31] We approximate the oscillator strength of the band as the oscillator strength of the ground-state OH-stretching transition.[36] The clusters are expected to be progressively more red-shifted with the size of the cluster due to the increasing cooperative effects in the cyclic hydrogen bonding networks.[39−41] This aids the separation and identification of the different clusters. We make the assumption that only the dimer, trimer, and tetramer form in measurable amounts at the pressures and temperature of our experiments.

The OH_b-stretching band from each of the three clusters is fitted with the sum of two normalized Voight profiles. The two Voight profiles are shifted slightly from each other simply to allow for some asymmetry in the absorbance band profiles, which has been observed for the MeOH dimer at room temperature.[2,36] In total, 21 parameters (Gaussian and

https://doi.org/10.1021/acs.jpca.4c02730
J. Phys. Chem. A 2024, 128, 6382−6391

Lorentzian widths, peak positions, and pairwise relative amplitudes) are optimized for the 3 pairs of Voight profiles by fitting the sum of the profiles to the recorded spectra. The parameters are fitted to the spectra recorded at all different pressures in parallel by letting the absolute amplitudes relax for each pressure with a set of fixed profile parameters. A loss function is constructed as a sum of squared absorbance residuals in the spectral range 3150−3650 cm^{-1}, with a larger weight given to the spectra recorded at higher pressures. When all band shape parameters are optimized, the absolute amplitudes of each pair of Voigt profiles give the integrated band areas at each sample pressure for the three clusters. The optimization is performed first by the Nelder−Mead "Simplex" algorithm followed by the gradient decent "Migrad" algorithm all implemented in the library Minuit2 in Python 3.[42] The loss function and optimized parameters are provided in Section S4.

THEORETICAL AND COMPUTATIONAL DETAILS

The $(MeOH)_{2-4}$ structures are optimized in Gaussian16[43] with the B3LYP-D3[44,45] and ωB97X-D[46] functionals using the aug-cc-pVTZ (AVTZ) basis set.[47,48] The $(MeOH)_2$ structure was also optimized in Molpro12.1 with CCSD(T)-F12a/cc-pVDZ-F12[49−53] using the recommended correlation factor β = 0.9. For $(MeOH)_2$ there is only one conformer. For the MeOH trimer and tetramer, we only consider the theoretically determined global minimum energy structures (Figure 1) with closed ring configurations and methyl groups in alternating up and down positions relative to the approximate plane of the OH-ring.[34] The transition wavenumber $\tilde{\nu}$ and unitless oscillator strength f_{calc} were calculated with normal and local mode approaches.

In the normal mode approach, we perform a range of reduced dimensionality VPT2 calculations. The reduced dimensionality scheme ensures that the potential energy surface (PES) and dipole moment surface (DMF) are expanded and evaluated along only the selected set of anharmonically active vibrational modes. Selecting a subset of active modes also reduces the computational effort, as numerical derivatives of the Hessian along the active normal modes are the most expensive step in the calculation. Various protocols have been proposed in reducing the dimensionality of normal mode VPT2 calculations.[54−57] Quantitative approaches to selecting active modes by evaluating cross-cubic force constants,[54] as well as more chemical intuitive approaches, where modes are selected based on the spatial vicinity of the functional group of interest[55−57] have been used with some success. The remaining modes can be set as "inactive", where they are treated harmonically and still contribute with cross-cubic and some cross-quartic force constants in the anharmonic correction to the active modes, or as "frozen", where they are completely turned off in the VPT2 treatment.[54] We chose the latter to emphasize the reduced dimensionality and to ensure predictable and reliable results for the calculated OH-stretching modes. In the various clusters, we include the 3 intramolecular modes: OH-stretch, CO-stretch, and COH-bend for each MeOH unit, and the two intermolecular modes that resemble in- and out-of-plane OH···O-bends (donor rock and twist) for each hydrogen bond. This corresponds to 8 vibrational modes for $(MeOH)_2$.

In the local mode approach, for all clusters, we use a reduced dimensional model that includes only the OH-stretching local modes and treats them as uncoupled, i.e., a simple 1D model for each OH-stretching local mode. The coupling leads to mixing of the OH-stretching modes and a redistribution of intensity, but does not have a large effect on the intensity of the total OH_b-stretching band. The frequency and oscillator strength of the OH_b-stretching transition were calculated with a 1D local mode model programmed in Python 3.[27,58] The PES was sampled along the OH-bond displacement coordinate: q = [−0.5 Å ; 1.5 Å] in 0.05 Å increments from the equilibrium geometry. The points were interpolated to Δq = 0.00002 Å using a cubic spline to ensure convergence within the used Simpson's integration method. The vibrational Schrödinger equation was solved in a basis of the first 50 associated Legendre m = 1 polynomials. The Cartesian components of the dipole moment function (DMF) were sampled and interpolated in the same way along coordinate q. These local mode calculations were done with both DFT methods.

In addition, for the MeOH dimer, we also performed a higher dimensional local mode variational calculation using the B3LYP-D3/AVTZ and CCSD(T)-F12a/cc-pVDZ-F12 methods. We include the bound OH_b-stretch, the OO-stretch (donor−acceptor intermolecular stretch), the donor rock and the donor twist and coupling between these in a 4D model.[28] The donor rock and twist modes partially break the hydrogen bond for both positive and negative displacements, and have previously been found to be important for describing the OH_b-stretch.[28,59−62] The OH_f-stretch is only weakly affected by these modes, and we use the 1D local mode model for it. The internal curvilinear coordinates are described in the Z-matrix in Table S1. The potential energy surface is approximated with an n-mode representation limited to pairwise (2D) coupling. The dipole moment single points were calculated with an Eckart axis embedding with the equilibrium structure as the reference geometry.[63,64] Details of the range of potential energy and dipole moment single points are provided in Table S3. The 4D Hamiltonian is set up in a direct product basis of 1D eigenfunctions contracted from 71 associated Legendre primitive basis functions. The 1D potential energy and G-matrix cuts are calculated with the equilibrium geometry as the reference structure. All integrals are calculated with Gauss-Legendre quadrature with 101 points per mode. We limit the size of the basis with a maximum polyadd truncation number of 8 for the three intermolecular modes and 5 for the OH-stretch. In addition, we employ an energy cutoff based on the sum of computed 1D energies of 18000 cm^{-1}. This approach, although good, is not feasible for larger clusters. We used the reduced dimensionality VPT2 calculated oscillator strengths obtained with the B3LYP-D3/AVTZ level PES and DMF to determine the cluster partial pressures. We scale these oscillator strengths by a factor of 0.664 obtained from the ratio of the 4D LM CCSD(T)-F12a/cc-pVDZ-F12 and the reduced dimensionality VPT2 (B3LYP-D3/AVTZ) calculated oscillator strengths for the OH_b-stretch in MeOH dimer (*vide infra*).

RESULTS AND DISCUSSION

MeOH Cluster Spectra. The spectra of MeOH clusters were obtained from MeOH spectra recorded at 20 different pressures in the range of 40−87 Torr. A MeOH monomer reference spectrum was recorded at an increased path length with a reduced MeOH pressure of 9.9 Torr and pressure-broadened with 300 Torr N_2. The low pressure of 9.9 Torr ensured limited cluster formation in the monomer reference spectrum. The additional N_2 broadening of the narrow ro-

https://doi.org/10.1021/acs.jpca.4c02730
J. Phys. Chem. A 2024, 128, 6382−6391

vibrational lines of MeOH turned out to be paramount in the subtraction of the monomer signal. To highlight the importance of pressure broadening, we show in Figure S6 how a reference spectrum recorded at very low pressures and not pressure broadened by N_2 results in insufficient subtraction of the monomer. In Figure 2, we show the spectral subtraction

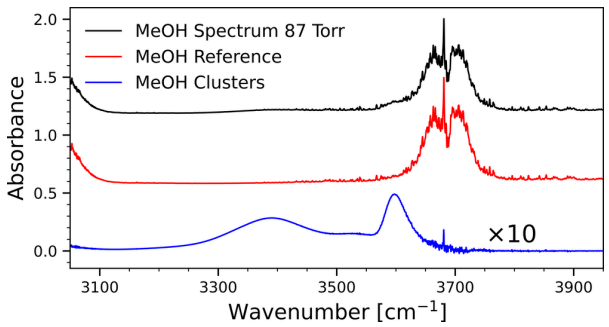

Figure 2. Reference spectrum of MeOH monomer recorded at 9.9 Torr and increased path length (red trace) is subtracted from the high pressure MeOH spectrum (black trace) with scaling factor of 0.88 resulting in the spectrum of MeOH clusters (blue trace). For visual purposes, the blue trace is magnified by a factor 10 and the red and black trace are shifted in absorbance by 0.6 and 1.2, respectively. All spectra are baseline corrected linearly between 2660 and 4141 cm^{-1}. The full spectral range is shown in Figure S4.

of the monomer reference from a high pressure MeOH spectrum, leaving behind signal from the MeOH clusters. The monomer reference spectrum is subtracted from the range of spectra recorded at different pressures to give spectra with various amounts of cluster signal.

The change in absorbance between the high pressure spectrum and the low pressure reference spectrum becomes apparent when magnified by a factor of 10, and clearly reveals a wide cluster absorption band with three maxima located at 3390, 3526, and 3598 cm^{-1}, respectively. The spectrum resembles previous spectra recorded at room temperature[9] and consists of absorbance contributions from OH_b-stretching transitions in the MeOH dimer, trimer and tetramer.[9,34] We deconvolute the band by fitting three band profiles, one for each order of cluster, with each cluster band profile consisting of the sum of two Voight profiles slightly shifted from each other to allow for asymmetric band-shapes.[36]

In Figure 3, we show the fit to the spectrum recorded at 87 Torr. The three fitted band profiles representing the dimer, trimer, and tetramer add up to a trace that closely follows that of the recorded spectrum. The largest deviation between the fit and the spectrum is seen below 3150 cm^{-1} and above 3650 cm^{-1} where residual CH-stretch and OH-stretch signals interfere. The band profiles are not fitted outside these boundaries. In a cold pulsed jet-expansion FTIR experiment of MeOH, OH_b-stretching bands were observed with maxima at 3293, 3474, and 3575 cm^{-1}, and were assigned to the tetramer, trimer and dimer, respectively.[9] The peak location of the cold clusters are supported by other studies including cavity ringdown and predissociative size selected molecular beam depletion experiments.[12,15,17,18] These three maxima all appear at the onset of the fitted band profiles in our room temperature spectra, which we assign as the MeOH tetramer, trimer, and dimer. In general, it has been observed that cold OH_b-stretching absorption bands are positioned at the low energy

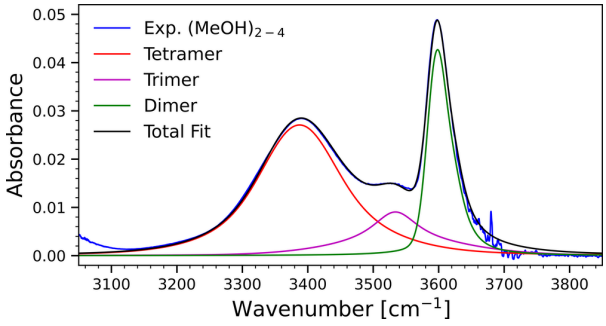

Figure 3. Fitted band profiles are plotted together with the summed fit in black overlaid with the spectrum recorded at 87 Torr total pressure in blue. Peak maxima of the fitted profiles from left to right: (red) tetramer 3388 cm^{-1}, (magenta) trimer 3534 cm^{-1}, and (green) dimer 3598 cm^{-1}.

onset of the thermal band counterparts in bimolecular hydrogen bound complexes.[2,9,36,65] For $(MeOH)_2$, spectra at both cold and warm conditions are available with limited interfering absorbance from other clusters,[2,9,36] and *ab initio* simulated band profiles at various temperatures have recently been presented.[36] In Figure 4, we show a comparison between

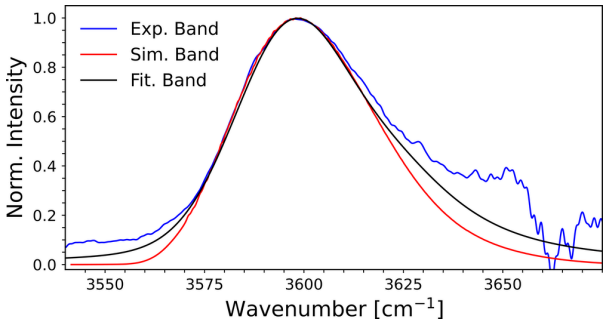

Figure 4. Experimental (blue) and simulated (red) band profiles of the isolated $(MeOH)_2$ at room temperature from ref 36 are compared with the fitted band profile of this work (black). The three normalized profiles are congruent, supporting the shape of the fitted $(MeOH)_2$ profile determined in this work.

our fitted $(MeOH)_2$ band profile and an experimental and simulated band profile at room temperature from ref 36. The resulting fitted $(MeOH)_2$ band profile of this work closely resembles the asymmetric band profile with a tailing toward high energy as observed and simulated in previous work,[36] thus supporting the shape of the fitted band profile. Here, we have assumed that the cluster band intensities can be approximated from only ground-state transitions, i.e. that the calculated band intensities are independent of temperature.[36] Transitions from quasi-bound states could have some effect on the cluster spectra.[66] The contributions from quasi-bound states are difficult to quantify and depend on temperature.

Calculated OH_b-Stretching Intensities. The measured integrated absorbances of the fitted profiles are scaled by calculated oscillator strengths, f_{calc}, to determine the partial pressure of the individual clusters in the gas mixture. To obtain reliable f_{calc} for the OH_b-stretching vibrations in the clusters, we compare results of normal mode and local mode approaches at two different DFT electronic structure methods and, for the MeOH dimer, also at the CCSD(T)-F12a level. The VPT2

https://doi.org/10.1021/acs.jpca.4c02730
J. Phys. Chem. A 2024, 128, 6382−6391

method is one of the most commonly used vibrational methods for including anharmonic corrections and is implemented in quantum chemical softwares such as Gaussian16.[43] The pertubative approach used in VPT2 relies on small corrections in a convergent power expansion of the harmonic oscillator approximation of the PES. However, the PES of especially the low energy, large amplitude motion (LAM) vibrational modes can be highly deviant from a harmonic oscillator in the normal mode coordinates conventionally used. This results in very large perturbations of the harmonic potentials that can give unphysical $\tilde{\nu}$ and f_{calc} for the LAM modes and modes to which they are coupled.[54−56] For this reason, the VPT2 treatment should be used with caution in the description of hydrogen bound complexes as the lowest frequency intermolecular modes are often characterized as LAMs.

Within the local mode framework, we have previously shown that both the frequency and intensity of the OH_b-stretch in a hydrogen bound bimolecular complex are affected by some of the intermolecular modes. In particular, the two local modes "rock" and "twist", which partially break the hydrogen bond for both positive and negative displacement, are important to include to accurately describe the OH_b-stretch.[36,59−62,67] The low frequency modes are, in other words, potentially important for the OH_b-stretch description and are likely to cause problems in a normal mode VPT2 calculation. In Figure S13 we show a scan of the PES along the normal coordinate of a problematic LAM mode with the corresponding harmonic and VPT2 potentials to highlight the problem of the lowest frequency modes. We also show that the most important modes resembling the "twist" and "rock" intermolecular local modes are well-behaved in the VPT2 description and can therefore be included in the reduced dimensional VPT2 model. In Table S17, we show a 1D VPT2 calculation for all of the modes of the MeOH dimer of which some give unphysical $\tilde{\nu}$ and f_{calc}, highlighting some problematic modes. By limiting our vibrational system in a reduced dimensionality VPT2 scheme, we avoid inclusion of problematic LAM modes and limit the number of potential resonant states, that may cause problems as resonances are often not correctly identified and treated in some VPT2 routines.[54,68] We include the modes that are in the direct spatial vicinity and/or directly perturb the hydrogen bond(s) in the clusters based on our previous results within the local mode model for bimolecular complexes.[28,36,59−62]

In Tables 1 and 2, we show calculated transition wavenumbers $\tilde{\nu}$ and oscillator strengths f_{calc} for MeOH dimer, trimer, and tetramer at the B3LYP-D3/AVTZ level. The results of NM VPT2 models with various dimensionality are compared with 1D local mode calculations only including the OH-stretches and ignoring coupling to other modes, and with previously assigned experimental values.[9,12] The column "Coupled OH" signifies reduced dimensionality of VPT2 models, including only the OH-stretching modes. The "+intra" column includes the CO-stretch and COH-bend and the "+intra +inter" columns includes also the two modes resembling the intermolecular "twist" and "rock" modes. The results of the coupled OH models are similar to the results of the 1D LM models, owing to the high degree of localization of the OH-stretches in the normal mode coordinates. It is important to include all OH-stretches in the reduced dimensionality VPT2 models (see Tables S13 to S16). Inclusion of the two intramolecular modes (CO-stretch and COH-bend) for each MeOH unit has a minimal effect on both the transition wavenumber and intensity as expected.[64] However, including the two intermolecular "twist" and "rock" modes for each hydrogen bond changes the transition wavenumber and intensity substantially for all OH_b-stretches in all the clusters as expected.[59−62] The transition wavenumber increases by ca. 25 cm^{-1} for the dimer and trimer and 35−60 cm^{-1} for the tetramer. The sum of OH_b-stretching intensities drops by 14%, 4%, and 13% for the dimer, trimer, and tetramer, respectively. This increase in transition wavenumber and decrease in intensity is expected as the intermolecular modes partially break the hydrogen bond, attenuating the red shift and intensity enhancement effect of the hydrogen bond.[30,31,61] We observe that our reduced dimensional VPT2 calculation (OH_b + intra + inter) with B3LYP-D3/AVTZ predicts $\tilde{\nu}$ values that are systematically underestimated by ca. 100−150 cm^{-1} compared to experimental values. It is previously described that B3LYP-D3 performs well in a similar reduced dimensionality VPT2 model[57] and that B3LYP-D3 in

Table 1. B3LYP-D3/AVTZ Calculated OH_b-Stretching Transition Wavenumbers, $\tilde{\nu}$, for MeOH Clusters[a]

	NM VPT2				
	Coupled OH	+intra	+intra +inter	LM OH	Expt.
$(MeOH)_2$					
ν_{OHf}	3663	3648	3646	3662	3684[b]
ν_{OHb}	3463	3454	3481	3452	3574[c]
$(MeOH)_3$					
ν_{OH1}	3360	3353	3379	3312	3473[b]
ν_{OH2}	3340	3333	3355	3301	3467[b]
ν_{OH3}	3239	3232	3258	3295	3432[b]
$(MeOH)_4$					
ν_{OH1}	3159	3154	3190	3072	3293[c]
ν_{OH2}	3106	3101	3144	3072	
ν_{OH3}	3106	3101	3144	3072	
ν_{OH4}	2974	2971	3037	3072	

[a]All values in cm^{-1}. [b]Taken from ref 12. [c]Taken from ref 9.

Table 2. B3LYP-D3/AVTZ Calculated OH_b-Stretching Oscillator Strengths, f_{calc}, for MeOH Clusters[a]

	NM VPT2			
	Coupled OH	+intra	+intra +inter	LM OH
$(MeOH)_2$				
OH_f	0.675	0.670	0.666	0.606
OH_b	11.1	11.1	9.49	11.3
$(MeOH)_3$				
ν_{OH1}	16.5	16.4	15.1	11.9
ν_{OH2}	17.8	17.7	16.9	13.1
ν_{OH3}	2.76	2.87	3.52	13.4
$\sum\nu_{OH}$	37.1	37.0	35.5	38.4
$(MeOH)_4$				
ν_{OH1}	5.11	5.10	4.62	23.5
ν_{OH2}	42.2	42.0	36.3	23.5
ν_{OH3}	42.2	42.0	36.3	23.5
ν_{OH4}	0.00	0.00	0.00	23.5
$\sum\nu_{OH}$	89.5	89.1	77.2	94.0

[a]All f_{calc} have been multiplied by a factor 10^5.

https://doi.org/10.1021/acs.jpca.4c02730
J. Phys. Chem. A 2024, 128, 6382−6391

general slightly overestimates hydrogen bonding energies,[69] which may cause underestimation of $\tilde{\nu}$ and overestimation of f_{calc}. We observe the same underestimation of $\tilde{\nu}$ in the LM models for the clusters with B3LYP-D3/AVTZ. Comparison with results with the ωB97X-D functional (Table S16) shows calculated oscillator strengths within ca. 10% of the B3LYP-D3 results, underlining the relative insensitivity of f_{calc} to electronic structure methods. Although calculated at different levels of electronic structure theory and with different vibrational models, we obtain oscillator strengths of the OH_b-stretches in the three clusters similar to those obtained by a full dimensional VPT2 calculation with MP2 electronic structure by Behera et al.[34]

To compensate for deficiencies in both the B3LYP-D3 electronic structure method and the VPT2 vibrational model, we compare the results of the MeOH dimer with 4D LM calculations using B3LYP-D3/AVTZ and CCSD(T)-F12a/VDZ-F12. A local mode calculation with the CCSD(T)-F12a/VDZ-F12 method leads to accurate transition wavenumbers and oscillator strengths for MeOH (see Table S30). For the MeOH dimer, a 1D LM calculation at this level gives a $\tilde{\nu}$ that is close for OH_f and slightly too low for OH_b when compared with experiments, as expected. The CCSD(T)-F12a 1D intensities are lower than the B3LYP-D3 values for both, recapitulating the argument that B3LYP-D3 overestimates the H-bonding energies. To include the effect of the intermolecular modes, we calculated the oscillator strength of the dimer OH_b-stretch with a 4D local mode model, where the OH_b-stretch and three of the intermolecular modes are included. At the CCSD(T)-F12a/VDZ-F12 level, the 4D model gives the OH_b-stretch $\tilde{\nu}$ = 3579 cm^{-1}, only 5 cm^{-1} from the experimental value. The oscillator strength decrease by about 30% from the 1D LM value in line with results from other bimolecular complexes[28,60,61] and is found to be f_{calc} = 6.30 × 10^{-5}. This value is 33% lower than that found with the best reduced dimensionality VPT2 B3LYP-D3/AVTZ calculation of 9.49 × 10^{-5}. With B3LYP-D3/AVTZ, the 4D LM model gives $\tilde{\nu}$ = 3501 cm^{-1} and f_{calc} = 8.51 × 10^{-5}, showing similar shifts from 1D to 4D as the CCSD(T)-F12a method. By comparison of the 8D VPT2 model with the 4D LM model at the same B3LYP-D3/AVTZ electronic structure, a difference of about 10% further supports the use of the reduced dimensionality VPT2 approach. CCSD(T) methods are unfeasible for the trimer and tetramer, and the local mode coordinates are not easily defined for the intermolecular vibrations. To provide the best oscillator strengths for the trimer and tetramer, we instead scaled the VPT2 intensities with the same factor (0.664) as that found for the dimer between the 8D VPT2 B3LYP-D3 model and the 4D LM CCSD(T)-F12a model. The scaling factor is not necessarily the same for all clusters, but the deficiencies of the model and electronic structure should give deviations of the same magnitude and direction. Thus, our best estimates of the summed OH_b-stretching oscillator strenghts in the dimer, trimer and tetramer are 6.30 × 10^{-5}, 23.5 × 10^{-5}, and 51.2 × 10^{-5}, respectively. The oscillator strengths can be converted to kilometers per mole by the multiplication factor 5.3313 × 10^6.

The red shift and intensity enhancement of the OH_b-stretches in the clusters increases as a function of the hydrogen bonding strength.[27,30,31] The strength of the hydrogen bonds in the clusters are increased by cooperative effects, meaning an XH-group, which is acting as a H-bond acceptor, becomes a better hydrogen bond donor.[39−41] Especially in closed ring type structures, the increasing number of hydrogen bonds acts to contract the ring, decreasing the intermolecular OO-distance, and increasing the hydrogen bond strength. In the trimer, the calculated intensity only increases 23% per hydrogen bond, compared to the dimer, and the calculated red shift increases by ∼100 cm^{-1}. This limited effect of tripling the number of H-bonds is due to the difficulty of obtaining optimal H-bond angles of 180° in the triangular structure. In the tetramer, the additional hydrogen bond allows for close to optimal hydrogen bonding angles, and the calculated intensity per hydrogen bond is doubled compared to the dimer. The red shift is calculated to be ∼300 cm^{-1} larger than that of the dimer. Geometric parameters for the cluster hydrogen bonds are listed in Table S31.

Equilibrium Constants. In Figure 5, we show a representative excerpt of spectra from the range of measured

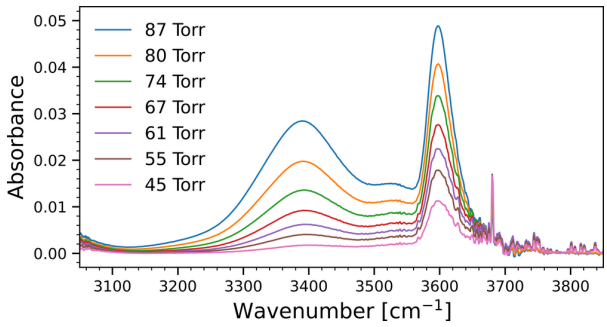

Figure 5. Spectra of methanol clusters recorded at different pressures. As the different orders of clusters grow with pressure at different rates, the bands from the individual clusters appear in different ratios to each other. At low pressures, the band from $(MeOH)_2$ dominates, while at higher pressures the bands from $(MeOH)_3$ and $(MeOH)_4$ are seen to grow in. The spectra are smoothed by a 3 cm^{-1} rolling average.

sample pressures. It is seen that in the low pressure spectra, the $(MeOH)_2$ band dominates with very limited intensity observed corresponding to trimer or tetramer formation. As the pressure increases, the bands from the larger clusters increase relative to that of the dimer. To determine the equilibrium constants of cluster formation, we fit the partial pressure of each cluster as a function of the monomer pressure raised to the power equal to the order of cluster. The MeOH monomer pressure is approximated as the total measured pressure. In Figure 6, we show the fit of the dimer pressure as a function of the monomer pressure squared. Each blue dot represents an experiment at a measured MeOH monomer pressure and a cluster pressure determined from the integrated band area and the calculated oscillator strength. Pressures and integrated areas are listed in Section S5.

The linearity in the pressure fit in Figure 6 confirms that the fitted profile represents the formation of a dimer. The slope of the fit corresponds to the unitless equilibrium constant of dimer formation and is K_D = 0.033 ± 0.007. The errors reported on the equilibrium constants are expressed as a 95% confidence interval, assuming a Gaussian probability distribution. The errors are combined from the individually estimated errors on primarily f_{calc} and the integrated band areas, as well as minor uncertainties from the linear fit and measured pressure and temperature. The estimated error in the calculated oscillator strength is 20% for the dimer and 40% for the

https://doi.org/10.1021/acs.jpca.4c02730
J. Phys. Chem. A 2024, 128, 6382−6391

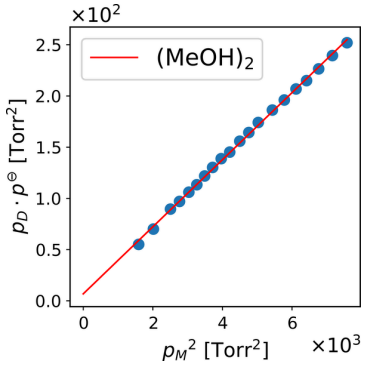

Figure 6. $(MeOH)_2$ partial pressures for each spectrum are fitted against the monomer pressure squared.

trimer and tetramer. For the dimer and tetramer, the OH_b-stretching bands are strong and clearly separated, which makes fitting simple, and we therefore estimate an error of 10%. The trimer OH_b-stretching band is much weaker and is buried between the dimer and tetramer bands. The fitting is therefore quite uncertain, and some fitting parameters are at their limits. We therefore associate an error of 40% with the determined trimer band area. The linear fits for $(MeOH)_3$ and $(MeOH)_4$ are included in Section S6, where we also compare them to fits against different orders of monomer pressure. The trimer fit shows some deflection downward for low pressure samples suggesting that the integrated absorbance of the trimer band may include contributions from dimer formation at these low pressures, and we exclude the 3 lowest pressure measurements in the final fit. The tetramer deflects upward in the high pressure samples, which is most likely due to some formation of higher order clusters as observed at jet-cooled conditions where the tetramer peak is superimposed on a wide multimer band.[9,15,18] We exclude the 4 highest pressure samples in the final fit. In both cases, the linearity is improved and we obtain K_T = 0.041 ± 0.023 and K_Q = 0.57 ± 0.25 using the scaled reduced dimensional VPT2 oscillator strenghts given in the previous section. Following eq 1, we can now determine the cluster composition at 298.2 K given a MeOH monomer pressure. For example, at 70 Torr MeOH, we determine 0.21 Torr $(MeOH)_2$, 0.025 Torr $(MeOH)_3$, and 0.033 Torr $(MeOH)_4$ at equilibrium. Thus, the dimer dominates, and the trimer and tetramer abundances are comparable. This corresponds to the clusters cumulatively making up ∼0.4% of the total pressure, and it is therefore a reasonable assumption to ignore this pressure contribution in measurements of p_M. At p_M = 10 Torr, the cluster partial pressures are 4×10^{-3} Torr, 7×10^{-5} Torr, and 1×10^{-5} Torr for the dimer, trimer and tetramer, respectively, confirming limited cluster formation in the monomer reference spectrum.

In Table 3, we compare our determined equilibrium constants with the previous results. Our work is in agreement with that of Frurip et al.[20] and Weltner et al.[23] with equilibrium constants for both dimer and tetramer within a factor of 2. Inskeep et al.[25] also obtain a K_D very close to ours but get a K_Q about 10 times larger than our value. The work in refs 20, 23, and 25 all depend on a fitting expression including only the monomer, dimer, and tetramer, intentionally leaving out a trimer fitting term, and Frurip et al.[20] and Weltner et al.[23] further sample partial pressures close to saturation and at temperatures in the range 330−520 K. The equilibrium

Table 3. Reported Cluster Equilibrium Constants under Standard Conditions

refs	K_D	K_T	K_Q	Method
This Work	3.3×10^{-2}	4.1×10^{-2}	5.7×10^{-1}	Spectroscopic
Behera[34]	3.8×10^{-4}	6.9×10^{-3}	3.2×10^{-1}	Spectroscopic
Frurip[20]	5.8×10^{-2}	–	6×10^{-1}	Thermal Conductivity[a]
Inskeep[25]	3.5×10^{-2}	–	9	Spectroscopic
Weltner[23]	5.7×10^{-2}	–	9.5×10^{-1}	Heat Capacity[a]

[a]Extrapolated from high temperature experiments.

constants are temperature sensitive, and the lack of sampling at ambient temperatures makes the extrapolation to standard conditions associated with a larger uncertainty. Behera et al. attempts to quantify dimer, trimer, and tetramer partial pressures in their gas using a spectroscopic approach similar to this work and at ambient temperatures.[34] Unfortunately, their spectra are visibly oversaturated by the monomer OH-stretching absorbance band, which results in a large error in the subtraction of the monomer signal. The oversaturation further burries the dimer and, to some extent, the trimer signals, which are accidentally subtracted out together with the monomer resulting in an underestimation of the dimer and trimer partial pressures. As a result, they report a K_D value, which is 2 orders of magnitude smaller than the previously reported and present value and far from the likely comparable value for water dimer.

The theoretical/experimental hybrid method deployed in this work provides equilibrium constants with 20−60% relative error. Although the calculation of the oscillator strengths f_{calc} is associated with the largest error, it is relatively robust with respect to electronic structure theory and the vibrational model. The relative error of K_{eq} scales linearly with that of f_{calc}. In the direct computational approach, K_{eq} is determined from the calculated standard Gibbs energy of formation by $K_{eq} = exp(-\Delta G^\ominus/RT)$. $\Delta G^\ominus$ is difficult to calculate accurately due to the large uncertainty in the frequencies, in particular the low frequency vibrational modes, which are often poorly described by harmonic potentials. The error in K_{eq} scales exponentially with the error in $\Delta G^\ominus$. In Table 4, we show the thermodynamic parameters calculated using the two DFT functionals within the rigid rotor and harmonic oscillator approximations. Between the two DFT methods, the differences in K_{eq} for especially the trimer and tetramer are substantial with a factor of 3 and 6 difference, respectively. In comparison, the determined f_{calc} and, by extension of the theoretical/experimental hybrid method, the equilibrium constants differ by ca. 10% between the two methods. In ref 70, a more advanced hindered rotor approach is implemented for each of the LAM modes in the clusters and the theoretical values are in very good agreement with the theoretical/experimental results of this work. This recapitulates the important contribution the LAM modes have in the vibrational partition function and the error that the rigid rotor and harmonic oscillator approximations may cause in the determination of the entropy of hydrogen bound complexes. With the limited uncertainty in our results we obtain a K_D that is in good agreement with previous results and we provide equilibrium constants of the trimer and tetramer with a limited spread.

https://doi.org/10.1021/acs.jpca.4c02730
J. Phys. Chem. A 2024, 128, 6382−6391

Table 4. Electronic Energies and Thermodynamic Values at T = 298 K Calculated with the B3LYP-D3/AVTZ and ωB97X-D/AVTZ Methods in Gaussian16[a]

Cluster	Method	ΔE	ΔZPVE	$\Delta H^{\ominus}$	$T \times \Delta S^{\ominus}$	$\Delta G^{\ominus}$	Expt. $\Delta G^{\ominus}$ This work
$(MeOH)_2$	B3LYP-D3	−25.4	5.5	−18.7	−28.4	9.7	
	ωB97X-D	−23.8	5.3	−17.3	−27.1	9.8	8.5 [8.0, 9.1]
	ref 70	–	–	−16.0	−22.2	6.2	
$(MeOH)_3$	B3LYP-D3	−76.8	14.5	−62.5	−74.4	11.9	
	ωB97X-D	−72.9	14.4	−58.6	−73.6	15.0	8.0 [6.8, 10]
	ref 70	–	–	−56.1	−64.8	8.7	
$(MeOH)_4$	B3LYP-D3	−136.1	21.4	−115.2	−115.7	0.5	
	ωB97X-D	−129.0	21.3	−107.7	−112.5	4.9	1.4 [0.47, 2.8]
	ref 70	–	–	−107.6	−109.2	1.6	

[a]The values are all reported in kJ/mol and signify the values of the n-sized cluster minus n × the optimized monomer values. ΔE is the electronic energy, ΔZPVE is the formation zero point vibrational energy correction, $\Delta H^{\ominus}$ is the formation enthalpy, $\Delta S^{\ominus}$ is the formation entropy, and $\Delta G^{\ominus}$ is the formation Gibbs energy. The experimental $\Delta G^{\ominus}$ values in this work are given with a ±2 standard error interval. Reference 70 uses RIMP2/aug-cc-pV(TQ)Z//B3LYP/TZVP and a hindered rotor approach to describe the LAM modes in the clusters.

CONCLUSION

We have investigated the formation of MeOH clusters under equilibrium conditions at room temperature. We measured the gas phase FTIR spectra of MeOH at a range of pressures. By accurately subtracting the MeOH monomer spectrum, we were able to fit and quantify the areas of the OH_b-stretching bands associated with the individual MeOH dimer, trimer, and tetramer. The clusters were observed as a broad feature spanning from ca. 3150 cm^{-1} to 3700 cm^{-1} with maxima at 3598, 3527, and 3390 cm^{-1} for the dimer, trimer, and tetramer, respectively. Intensity from the dimer and tetramer dominate the IR spectrum, but a broad feature from the trimer is also visible. Various vibrational models including a reduced dimensionality VPT2 model were used to provide reliable oscillator strengths used to quantify the partial pressures of the clusters in the sample gas. We determine equilibrium constants of $K_D = 0.033 \pm 0.007$, $K_T = 0.041 \pm 0.023$, and $K_Q = 0.57 \pm 0.25$. MeOH is the alcohol that most closely resembles H_2O in its hydrogen bonding strength and structure. The equilibrium constant found for MeOH dimer formation is close to that of the H_2O dimer (0.03−0.06),[35] and in hydrogen bound complexes with trimethylamine and dimethylamine at room temperature, the formation constants are similar between MeOH and H_2O.[2,28] The hydrogen bonding structure in the H_2O dimer, trimer and tetramer[71] is similar to that in the MeOH clusters. We therefore propose that the equilibrium constants for the H_2O trimer and tetramer are similar to our determined MeOH trimer and tetramer equilibrium constants.

ASSOCIATED CONTENT

Data Availability Statement

Gaussian files and raw spectra are available online at: https://erda.ku.dk/archives/0bafb187ff3a0245e4a0c676bd5a945c/published-archive.html.

Supporting Information

The Supporting Information is available free of charge at https://pubs.acs.org/doi/10.1021/acs.jpca.4c02730.

Description of local mode coordinates. Cartesian coordinates of optimized MeOH monomer and clusters. Full spectral range of methanol cluster. Small corrections due to deuterium impurity. Example of insufficient spectral subtraction and pressure broadening. Details on cluster band fitting. Measured temperatures and pressures. Determined cluster pressures. Adjustment of integrated area due to spectral subtraction. Confirmation of linear scaling of cluster pressures. Analysis on reduced dimensional VPT2 model with inclusion of 1D normal mode PES and DMF scans. Local mode model results. Geometric parameters of hydrogen bonds in the MeOH clusters. Harmonic wavenumbers and rotational constants for MeOH clusters. (PDF)

AUTHOR INFORMATION

Corresponding Author

Henrik G. Kjaergaard − *Department of Chemistry, University of Copenhagen, 2100 Copenhagen-Ø, Denmark;* orcid.org/0000-0002-7275-8297; Phone: +45 35320334; Email: hgk@chem.ku.dk; Fax: +45 35320322

Authors

Casper Vindahl Jensen − *Department of Chemistry, University of Copenhagen, 2100 Copenhagen-Ø, Denmark;* orcid.org/0000-0002-9102-1223

Emil Vogt − *Department of Chemistry, University of Copenhagen, 2100 Copenhagen-Ø, Denmark;* orcid.org/0000-0003-3335-9813

Andras Sun Poulsen − *Department of Chemistry, University of Copenhagen, 2100 Copenhagen-Ø, Denmark*

Complete contact information is available at: https://pubs.acs.org/10.1021/acs.jpca.4c02730

Notes

The authors declare no competing financial interest.

ACKNOWLEDGMENTS

The authors thank The Novo Nordisk Foundation, grant numbers NNF19OC0057374 and NNF22OC0080193 for financial support. We thank Andreas Thirstrup Simonsen for contributing preliminary work.

REFERENCES

(1) Galloway, M. M.; Huisman, A. J.; Yee, L. D.; Chan, A. W. H.; Loza, C. L.; Seinfeld, J. H.; Keutsch, F. N. Yields of oxidized volatile organic compounds during the OH radical initiated oxidation of isoprene, methyl vinyl ketone, and methacrolein under high-NO_x conditions. *Atmos. Chem. and Phys.* **2011**, *11*, 10779−10790.

(2) Hansen, A. S.; Vogt, E.; Kjaergaard, H. G. Gibbs Energy of Complex Formation−Combining Infrared Spectroscopy and Vibrational Theory. *Int. Rev. Phys. Chem.* **2019**, *38*, 115−148.

(3) Seinfeld, J. H.; Pandis, S. N. *Atmospheric Chemistry and Physics: From Air Pollution to Climate Change*; John Wiley & Sons: 2016; Chapter 11.
(4) Zhang, R.; Khalizov, A.; Wang, L.; Hu, M.; Xu, W. Nucleation and Growth of Nanoparticles in the Atmosphere. *Chem. Rev.* **2012**, *112*, 1957−2011.
(5) Zhao, J.; Khalizov, A.; Zhang, R.; McGraw, R. Hydrogen-Bonding Interaction in Molecular Complexes and Clusters of Aerosol Nucleation Precursors. *J. Phys. Chem. A* **2009**, *113*, 680−689.
(6) Tröstl, J.; Chuang, W. K.; Gordon, H.; Heinritzi, M.; Yan, C.; Molteni, U.; Ahlm, L.; Frege, C.; Bianchi, F.; Wagner, R.; et al. The Role of Low-Volatility Organic Compounds in Initial Particle Growth in the Atmosphere. *Nature* **2016**, *533*, 527−531.
(7) Intergovernmental Panel on Climate Change (IPCC) *Climate Change 2021 − The Physical Science Basis: Working Group I Contribution to the Sixth Assessment Report of the Intergovernmental Panel on Climate Change*; Cambridge University Press: 2023; pp 923−1054.
(8) Sulaiman, M. I.; Yang, S.; Ellis, A. M. Infrared Spectroscopy of Methanol and Methanol/Water Clusters in Helium Nanodroplets: The OH Stretching Region. *J. Phys. Chem. A* **2017**, *121*, 771−776. PMID: 28060504.
(9) Haber, T.; Schmitt, U.; Suhm, M. A. FTIR-Spectroscopy of Molecular Clusters in Pulsed Supersonic Slit-Jet Expansions. *Phys. Chem. Chem. Phys.* **1999**, *1*, 5573−5582.
(10) Nedić, M.; Wassermann, T. N.; Larsen, R. W.; Suhm, M. A. A combined Raman- and infrared jet study of mixed methanol−water and ethanol−water clusters. *Phys. Chem. Chem. Phys.* **2011**, *13*, 14050−14063.
(11) Wugt Larsen, R.; Suhm, M. A. Cooperative organic hydrogen bonds: The librational modes of cyclic methanol clusters. *J. Chem. Phys.* **2006**, *125*, 154314.
(12) Provencal, R. A.; Paul, J. B.; Roth, K.; Chapo, C.; Casaes, R. N.; Saykally, R. J.; Tschumper, G. S.; Schaefer, I.; Schaefer, I.; H. F. Infrared Cavity Ringdown Spectroscopy of Methanol Clusters: Single Donor Hydrogen Bonding. *J. Chem. Phys.* **1999**, *110*, 4258−4267.
(13) Doroshenko, I.; Pogorelov, V.; Sablinskas, V.; Balevicius, V. Matrix-Isolation Study of Cluster Formation in Methanol: O−H Stretching Region. *J. Mol. Liq.* **2010**, *157*, 142−145.
(14) Van Thiel, M.; Becker, E. D.; Pimentel, G. C. Infrared Studies of Hydrogen Bonding of Methanol by the Matrix Isolation Technique. *J. Chem. Phys.* **1957**, *27*, 95−99.
(15) Buck, U.; Huisken, F. Infrared Spectroscopy of Size-Selected Water and Methanol Clusters. *Chem. Rev.* **2000**, *100*, 3863−3890.
(16) Huisken, F.; Kulcke, A.; Laush, C.; Lisy, J. M. Dissociation of small methanol clusters after excitation of the O−H stretch vibration at 2.7 μ. *J. Chem. Phys.* **1991**, *95*, 3924−3929.
(17) Huisken, F.; Kaloudis, M.; Koch, M.; Werhahn, O. Experimental Study of the O−H Ring Vibrations of the Methanol Trimer. *J. Chem. Phys.* **1996**, *105*, 8965−8968.
(18) Buck, U.; Ettischer, I. Vibrational predissociation spectra of size selected methanol clusters: New experimental results. *J. Chem. Phys.* **1998**, *108*, 33−38.
(19) Fischer, T. L.; Bödecker, M.; Schweer, S. M.; Dupont, J.; Lepère, V.; Zehnacker-Rentien, A.; Suhm, M. A.; Schröder, B.; Henkes, T.; Andrada, D. M.; et al. The First HyDRA Challenge for Computational Vibrational Spectroscopy. *Phys. Chem. Chem. Phys.* **2023**, *25*, 22089−22102.
(20) Frurip, D.; Curtiss, L.; Blander, M. Thermal Conductivity Measurements and Molecular Association in a Series of Alcohol Vapors: Methanol, Ethanol, Isopropanol, and t-Butanol. *Int. J. Thermophys.* **1981**, *2*, 115−132.
(21) Butler, J. N.; Brokaw, R. S. Thermal Conductivity of Gas Mixtures in Chemical Equilibrium. *J. Chem. Phys.* **1957**, *26*, 1636−1643.
(22) Brokaw, R. S. Thermal Conductivity of Gas Mixtures in Chemical Equilibrium. II. *J. Chem. Phys.* **1960**, *32*, 1005−1006.
(23) Weltner, W., Jr; Pitzer, K. S. Methyl Alcohol: The Entropy, Heat Capacity and Polymerization Equilibria in the Vapor, and Potential Barrier to Internal Rotation. *J. Am. Chem. Soc.* **1951**, *73*, 2606−2610.
(24) Kretschmer, C. B.; Wiebe, R. Pressure-Volume-Temperature Relationships of Alcohol Vapors. *J. Am. Chem. Soc.* **1954**, *76*, 2579−2583.
(25) Inskeep, R. G.; Kelliher, J. M.; McMahon, P. E.; Somers, B. G. Molecular Association of Methanol Vapor. *J. Chem. Phys.* **1958**, *28*, 1033−1036.
(26) Hippler, M. Quantum Chemical Study and Infrared Spectroscopy of Hydrogen-Bonded $CHCl_3$−NH_3 in the Gas Phase. *J. Chem. Phys.* **2007**, *127*, 084306.
(27) Jensen, C. V.; Kjaergaard, H. G. Gas-Phase Room-Temperature Detection of the tert-Butyl Hydroperoxide Dimer. *J. Phys. Chem. A* **2023**, *127*, 6476−6485.
(28) Kjaersgaard, A.; Vogt, E.; Hansen, A. S.; Kjaergaard, H. G. Room Temperature Gas-Phase Detection and Gibbs Energies of Water Amine Bimolecular Complex Formation. *J. Phys. Chem. A* **2020**, *124*, 7113−7122.
(29) Howard, D. L.; Kjaergaard, H. G. Vapor Phase near Infrared Spectroscopy of the Hydrogen Bonded Methanol-Trimethylamine Complex. *J. Phys. Chem. A* **2006**, *110*, 9597−9601.
(30) Arunan, E.; Desiraju, G. R.; Klein, R. A.; Sadlej, J.; Scheiner, S.; Alkorta, I.; Clary, D. C.; Crabtree, R. H.; Dannenberg, J. J.; Hobza, P.; et al. Defining the Hydrogen Bond: An account (IUPAC Technical Report). *Pure Appl. Chem.* **2011**, *83*, 1619−1636.
(31) Arunan, E.; Desiraju, G. R.; Klein, R. A.; Sadlej, J.; Scheiner, S.; Alkorta, I.; Clary, D. C.; Crabtree, R. H.; Dannenberg, J. J.; Hobza, P.; et al. Definition of the Hydrogen Bond (IUPAC Recommendations 2011). *Pure Appl. Chem.* **2011**, *83*, 1637−1641.
(32) Kjaersgaard, A.; Vogt, E.; Christensen, N. F.; Kjaergaard, H. G. Attenuated Deuterium Stabilization of Hydrogen-Bound Complexes at Room Temperature. *J. Phys. Chem. A* **2020**, *124*, 1763−1774.
(33) Møller, K. H.; Tram, C. M.; Kjaergaard, H. G. Side-by-Side Comparison of Hydroperoxide and Corresponding Alcohol as Hydrogen-Bond Donors. *J. Phys. Chem. A* **2017**, *121*, 2951−2959.
(34) Behera, B.; Chakraborty, S. Room Temperature Gas Phase Infrared Spectra of H-bonded Oligomers of Methanol. *Vib. Spec.* **2020**, *106*, 102981.
(35) Leforestier, C. Water Dimer Equilibrium Constant Calculation: A Quantum Formulation Including Metastable States. *J. Chem. Phys.* **2014**, *140*, 074106.
(36) Vogt, E.; Jensen, C. V.; Kjaergaard, H. G. Effect of Temperature on the OH-Stretching Bands of the Methanol Dimer. *J. Phys. Chem. A* **2024**, *128*, 392−400.
(37) Hansen, A. S.; Du, L.; Kjaergaard, H. G. Positively Charged Phosphorus as a Hydrogen Bond Acceptor. *J. Phys. Chem. Lett.* **2014**, *5*, 4225−4231.
(38) Du, L.; Kjaergaard, H. G. Fourier Transform Infrared Spectroscopy and Theoretical Study of Dimethylamine Dimer in the Gas Phase. *J. Phys. Chem. A* **2011**, *115*, 12097−12104.
(39) King, B. F.; Weinhold, F. Structure and Spectroscopy of (HCN)n Clusters: Cooperative and Electronic Delocalization Effects in C-H···N Hydrogen Bonding. *J. Chem. Phys.* **1995**, *103*, 333−347.
(40) Ojamaee, L.; Hermansson, K. *Ab Initio* Study of Cooperativity in Water Chains: Binding Energies and Anharmonic Frequencies. *J. Phys. Chem.* **1994**, *98*, 4271−4282.
(41) Zimmermann, D.; Häber, T.; Schaal, H.; Suhm, M. A. Hydrogen Bonded Rings, Chains and Lassos: The Case of t-Butyl Alcohol Clusters. *Mol. Phys.* **2001**, *99*, 413−425.
(42) James, F.; et al. Minuit. *CERN Program Library Long Writeup D* **1994**, *506*, 1993.
(43) Frisch, M. J.; Trucks, G. W.; Schlegel, H. B.; Scuseria, G. E.; Robb, M. A.; Cheeseman, J. R.; Scalmani, G.; Barone, V.; Petersson, G. A.; Nakatsuji, H. et al. *Gaussian 16*, Revision C.01. 2016; Gaussian Inc.: Wallingford CT.
(44) Becke, A. Density-Functional Thermochemistry. III. The Role of Exact Exchange. *J. Chem. Phys.* **1993**, *98*, 5648.
(45) Grimme, S.; Antony, J.; Ehrlich, S.; Krieg, H. A Consistent and Accurate *Ab Initio* Parametrization of Density Functional Dispersion

https://doi.org/10.1021/acs.jpca.4c02730
J. Phys. Chem. A 2024, 128, 6382−6391

Correction (DFT-D) for the 94 Elements H-Pu. *J. Chem. Phys.* **2010**, *132*, 154104.
(46) Chai, J.-D.; Head-Gordon, M. Long-Range Corrected Hybrid Density Functionals with Damped Atom-Atom Dispersion Corrections. *Phys. Chem. Chem. Phys.* **2008**, *10*, 6615−6620.
(47) Dunning, T. H., Jr Gaussian Basis Sets for use in Correlated Molecular Calculations. I. The Atoms Boron through Neon and Hydrogen. *J. Chem. Phys.* **1989**, *90*, 1007−1023.
(48) Kendall, R. A.; Dunning, T. H., Jr; Harrison, R. J. Electron Affinities of the First-Row Atoms Revisited. Systematic Basis Sets and Wave Functions. *J. Chem. Phys.* **1992**, *96*, 6796−6806.
(49) Adler, T. B.; Knizia, G.; Werner, H.-J. A Simple and Efficient CCSD(T)-F12 Approximation. *J. Chem. Phys.* **2007**, *127*, 221106.
(50) Peterson, K. A.; Adler, T. B.; Werner, H.-J. Systematically Convergent Basis Sets for Explicitly Correlated Wavefunctions: The Atoms H, He, B−Ne, and Al−Ar. *J. Chem. Phys.* **2008**, *128*, 084102.
(51) Werner, H.-J.; Knowles, P. J.; Celani, P.; Györffy, W.; Hesselmann, A.; Kats, D.; Knizia, G.; Köhn, A.; Korona, T.; Kreplin, D. et al. MOLPRO, 12.1, a package of ab initio programs. URL visited July 2023: https://www.molpro.net.
(52) Werner, H.-J.; Knowles, P. J.; Knizia, G.; Manby, F. R.; Schütz, M. Molpro: a General-Purpose Quantum Chemistry Program Package. *Wiley Interdiscip. Rev.: Comput. Mol. Sci.* **2012**, *2*, 242−253.
(53) Werner, H.-J.; Knowles, P. J.; Manby, F. R.; Black, J. A.; Doll, K.; Heßelmann, A.; Kats, D.; Köhn, A.; Korona, T.; Kreplin, D. A.; et al. The Molpro Quantum Chemistry Package. *J. Chem. Phys.* **2020**, *152*, 144107.
(54) Fusè, M.; Mazzeo, G.; Longhi, G.; Abbate, S.; Yang, Q.; Bloino, J. Scaling-up VPT2: AFeasible Route to Include Anharmonic Correction on Large Molecules. *Spectrochimica Acta Part A: Molecular and Biomolecular Spectroscopy* **2024**, *311*, 123969.
(55) Barone, V.; Biczysko, M.; Bloino, J.; Borkowska-Panek, M.; Carnimeo, I.; Panek, P. Toward Anharmonic Computations of Vibrational Spectra for Large Molecular Systems. *Int. J. Quantum Chem.* **2012**, *112*, 2185−2200.
(56) Barone, V.; Biczysko, M.; Bloino, J. Fully Anharmonic IR and Raman Spectra of Medium-Size Molecular Systems: Accuracy and Interpretation. *Phys. Chem. Chem. Phys.* **2014**, *16*, 1759−1787.
(57) Fornaro, T.; Carnimeo, I.; Biczysko, M. Toward Feasible and Comprehensive Computational Protocol for Simulation of the Spectroscopic Properties of Large Molecular Systems: The Anharmonic Infrared Spectrum of Uracil in the Solid State by the Reduced Dimensionality/Hybrid VPT2 Approach. *J. Phys. Chem. A* **2015**, *119*, 5313−5326.
(58) Jensen, C. V. GitHub Repository of 1D LM code. URL visited July 2023: https://github.com/CasperVJensen/tert-Butyl_Hydroperoxide_Dimer.git.
(59) Mackeprang, K.; Kjaergaard, H. G.; Salmi, T.; Hänninen, V.; Halonen, L. The Effect of Large Amplitude Motions on the Transition Frequency Redshift in Hydrogen Bonded Complexes: A Physical Picture. *J. Chem. Phys.* **2014**, *140*, 184309.
(60) Mackeprang, K.; Hänninen, V.; Halonen, L.; Kjaergaard, H. G. The Effect of Large Amplitude Motions on the Vibrational Intensities in Hydrogen Bonded Complexes. *J. Chem. Phys.* **2015**, *142*, 094304.
(61) Mackeprang, K.; Kjaergaard, H. G. Vibrational Transitions in Hydrogen Bonded Bimolecular Complexes - A Local Mode Perturbation Theory Approach to Transition Frequencies and Intensities. *J. Mol. Spectrosc.* **2017**, *334*, 1−9.
(62) Vogt, E.; Kjaergaard, H. G. Vibrational Spectroscopy of the Water Dimer at Jet-Cooled and Atmospheric Temperatures. *Annu. Rev. Phys. Chem.* **2022**, *73*, 209−231.
(63) Krasnoshchekov, S. V.; Isayeva, E. V.; Stepanov, N. F. Determination of the Eckart Molecule-Fixed Frame by use of the Apparatus of Quaternion Algebra. *J. Chem. Phys.* **2014**, *140*, 154104.
(64) Vogt, E.; Bertran Valls, P.; Kjaergaard, H. G. Accurate Calculations of OH-Stretching Intensities with a Reduced-Dimensional Local Mode Model Including Eckart Axis Embedding. *J. Phys. Chem. A* **2020**, *124*, 932−942.
(65) Schaal, H.; Häber, T.; Suhm, M. A. Hydrogen Bonding in 2-Propanol. The Effect of Fluorination. *J. Phys. Chem. A* **2000**, *104*, 265−274.
(66) Bound, Metastable and Free States of Bimolecular Complexes. *Infrared. Phys.* **1991**, *32*, 461−470.
(67) Vogt, E.; Simkó, I.; Császár, A. G.; Kjaergaard, H. G. Reduced-Dimensional Vibrational Models of the Water Dimer. *J. Chem. Phys.* **2022**, *156*, 164304.
(68) Boyer, M. A.; McCoy, A. B. A Wave Function Correction-Based Approach to the Identification of Resonances for Vibrational Perturbation Theory. *J. Chem. Phys.* **2022**, *157*, 164113.
(69) Thanthiriwatte, K. S.; Hohenstein, E. G.; Burns, L. A.; Sherrill, C. D. Assessment of the Performance of DFT and DFT-D Methods for Describing Distance Dependence of Hydrogen-Bonded Interactions. *J. Chem. Theory Comput.* **2011**, *7*, 88−96. PMID: 26606221.
(70) Umer, M.; Leonhard, K. Ab Initio Calculations of Thermochemical Properties of Methanol Clusters. *J. Phys. Chem. A* **2013**, *117*, 1569−1582.
(71) Maheshwary, S.; Patel, N.; Sathyamurthy, N.; Kulkarni, A. D.; Gadre, S. R. Structure and Stability of Water Clusters $(H_2O)_n$, n = 8−20: An Ab Initio Investigation. *J. Phys. Chem. A* **2001**, *105*, 10525−10537.

https://doi.org/10.1021/acs.jpca.4c02730
J. Phys. Chem. A 2024, 128, 6382−6391